Air Force Institute of Technology
AFIT Scholar

Theses and Dissertations | Student Graduate Works

12-1996

Electrical Characterization of Intrinsic and Induced Deep Level Defects in Hexagonal SiC

James D. Scofield

Follow this and additional works at: https://scholar.afit.edu/etd

Part of the Atomic, Molecular and Optical Physics Commons

Recommended Citation
Scofield, James D., "Electrical Characterization of Intrinsic and Induced Deep Level Defects in Hexagonal SiC" (1996). *Theses and Dissertations*. 5824.
https://scholar.afit.edu/etd/5824

This Dissertation is brought to you for free and open access by the Student Graduate Works at AFIT Scholar. It has been accepted for inclusion in Theses and Dissertations by an authorized administrator of AFIT Scholar. For more information, please contact AFIT.ENWL.Repository@us.af.mil.

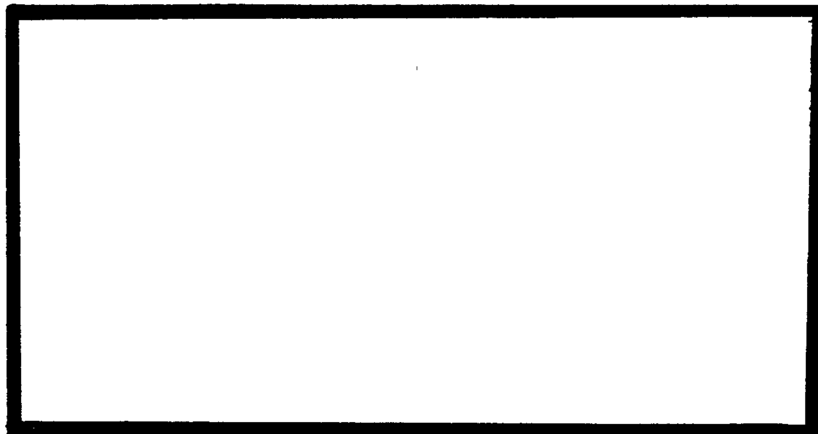

DISTRIBUTION STATEMENT A
Approved for public release;
Distribution Unlimited

DTIC QUALITY INSPECTED 4

19970520 199

DEPARTMENT OF THE AIR FORCE

AIR UNIVERSITY

AIR FORCE INSTITUTE OF TECHNOLOGY

Wright-Patterson Air Force Base, Ohio

Electrical Characterization of Intrinsic and Induced Deep Level Defects in Hexagonal SiC

Dissertation

James D. Scofield, GS-12, USAF

AFIT/DS/ENP/96-08

Approved for public release; distribution unlimited

"The views expressed in this dissertation are those of the author and do not reflect the official policy or position of the Department of Defense or the U. S. Government."

ELECTRICAL CHARACTERIZATION OF INTRINSIC AND INDUCED DEEP LEVEL DEFECTS IN HEXAGONAL SiC

DISSERTATION

Presented to the Faculty of the Graduate School of Engineering

of the Air Force Institute of Technology

Air University

In Partial Fulfillment of the Requirements

for the Degree of

Doctor of Philosophy

James D. Scofield, B.S., M.S.

AFIT/DS/ENP/96-08

November 1996

Approved for public release; distribution unlimited

AFIT/DS/ENP/96-08

ELECTRICAL CHARACTERIZATION OF INTRINSIC AND INDUCED DEEP LEVEL DEFECTS IN HEXAGONAL SiC

James D. Scofield, B.S., M.S.

Approved:

YUNG KEE YEO
Professor of Physics
Chairman, Advisory Committee

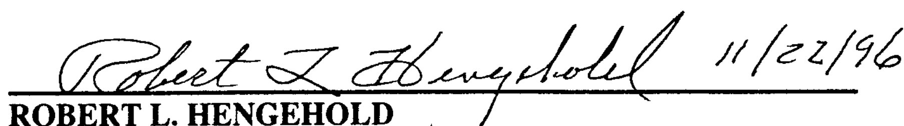

ROBERT L. HENGEHOLD
Professor of Physics and Head
Department of Engineering Physics
Member, Advisory Committee

DENNIS W. QUINN
Professor, Department of Mathematics and Statistics
Member, Advisory Committee

Major MICHAEL A. MARCINIAK
WL/POO
Member, Advisory Committee

KENNETH W. BAUER
Professor, Department of Operational Sciences
Deans Representative

Accepted:

Robert A. Calico, Jr.
Dean, Graduate School of Engineering

PREFACE

The research outlined and summarized in the following text has been motivated by recent advances made in both wide bandgap material quality and device development technologies utilizing these material systems for electronic and optoelectronic applications. Specifically, bulk growth of hexagonal silicon carbide substrate boules was realized in 1989 as a result of breakthroughs made at North Carolina State University, CREE Research Inc., and the Naval Research Laboratory. Although the material quality was initially very poor with high concentrations of stacking voids, inclusions of undesired polytypes, and significant transition metal densities resulting from the extremely high (2500 °C) growth temperature, continued progress and improvements were made in the succeeding five years. Commercialized substrate products have increased in size from one inch diameters to the present two inch wafer with significantly improved crystalline quality. The availability of these products is the primary reason that silicon carbide enjoys a large advantage over the III-Nitrides and diamond materials for high temperature, high power, wide bandgap applications. However, while silicon carbide is the most highly developed of the large energy gap materials at the time of writing, it is only comparable in quality to early GaAs substrates which were available in the late 1960's and early 1970's. Thus, the majority of efforts to develop and commercialize electronic products based in this material system have been of limited success, due largely to the high concentrations, unknown origins, and device degrading effects of impurity related and intrinsic defects in the SiC crystal. Large variabilities of material quality between runs or even across the same wafer/boule, as was observed for most of the material and state-of-the-art devices obtained and characterized during this study, is indicative of a material technology still in its infancy. This variability presents enormous difficulty in obtaining consistent data with which to predict trends, describe phenomenon, and draw conclusions regarding the nature and sources of the large numbers of defects observed in this material. Despite the limitations of current materials, blue light emitting diodes and ultraviolet photodetectors have been developed as commercial products, although quantum efficiencies are very low. High temperature and power devices, which are the near-term applications and real impetus for the current level of support for this technology, have yet to be realized in any significant capacity. This is due almost entirely to the quality of the material, meaning high point and extended defect concentrations which limit and degrade device potentiality and performance. Thus, as was true for Si and GaAs, an understanding of the nature and sources of defects in a material, which present allowed carrier quantum states in the nominally forbidden energy gap and dominate device performance, will be fundamental to actualization of the performance potential of SiC. Additional benefits to be realized from an intimate knowledge between electronic carrier affecting behavior and impurity or defect type are the attainment of insulating or semi-insulating material, and donor/acceptor impurities exhibiting ionization potentials with lower magnitudes than those currently being utilized. This research project represents one of the initial studies of the intrinsic, unintentional impurity, and induced deep level defects in this material using a non-optical technique. The results are intended

to expand the very limited knowledge base in the area of SiC deep level defects, and will provide a basis for additional efforts ultimately aimed at improving material quality and enabling SiC to attain the status of a mature technology.

I would like to acknowledge the support granted by the Aeropropulsion and Power Directorate of Wright Laboratory, without which this project would not have been possible. Professor Yung Kee Yeo is recognized as providing me with the wisdom, guidance, and academic and experimental framework within which this research project was realized. As my mentor he has been an invaluable source of direction and motivation, for which I am sincerely thankful. I am extremely grateful for the opportunity to have worked closely with Dr. Daniel Johnstone for the past three years and have benefited immeasurably as a result of our interactions and discussions. He was responsible for identifying my interest in defect characterization and physics, and guided my initial forays into the transient spectroscopy world. I would also like to recognize Dr. Edward Ingham for his significant theoretical contributions, which complimented and enhanced my experimental efforts and eventually resulted in a very successful collaborative effort. Finally, the largest share of gratitude is given to my parents for providing the environment which cultivates wonder and inquisition, and to my wife and children, without whose presence and continuing support over the past four years, none of these accomplishments have any significance.

James D. Scofield

Table of Contents

Page

Preface ... iv

List of Figures ... vi

List of Tables ... vii

Abstract ... viii

I. Introduction ... I-1

I-I. Background:Wide Bandgap Semiconductors ... I-1
I-II. High Temperature High Power Electronics ... I-9

II. Silicon Carbide ... II-1

II-I. Material Properties ... II-1
II-I-1. History ... II-1
II-I-2. Polymorphism ... II-2
II-I-3. SiC Crystal Anomalies and Polytypism ... II-5
II-I-4. Crystallographic Notation ... II-10
II-I-5. Electrical and Optical Properties of SiC ... II-11

III. Defect Induced Bandgap States ... III-1

III-I. Impurities and Deep Defect Levels ... III-1
III-I-1. SiC Shallow Levels ... III-2
III-I-2. Unintentional Impurities and Deep Levels ... III-4
III-II Defect Classification:Traps and Recombination Centers ... III-11
III-II-1. Energy Conservation and Relative Recombination Probabilities ... III-13
III-II-2. Electronic Lattice Coupling ... III-19

IV. SiC Defect Characterization ... IV-1

IV-I. Deep Level Transient Spectroscopy IV-1
IV-I-1. Principles and Physics of DLTS Measurements IV-1
IV-I-2. Specific System Hardware and Implementation IV-12

V. DLTS Transient Analysis V-1

V-I. Transient Data Fitting: Modulating Functions and Generalized Least Squares V-1
V-I-1. Modulating Functions V-2
V-I-2. Linear Prediction and Generalized Least Squares V-7
V-I-3. Improved Linear Prediction Applied to Empirical DLTS Signals V-29

VI. Simulation and Model Analysis VI-1

VI-I. Modeling of Capture and Emission Processes in SiC VI-4
VI-II. Dominant SiC Capture Mechanism VI-21
VI-III. Modeled Capture Cross Section Trends from Deep Level Emission Data VI-24

VII. Nonradiative Capture in SiC VII-1

VII-I. Evidence for Capture by Multi-Phonon Emission in SiC VII-1
VII-II. SiC Capture Events in Neutral Material VII-18
VII-III. Deep Level Pairs Attributable to Inequivalent Lattice Sites VII-28
VII-III-1. N-type 6H-SiC Deep Electron Trap VII-30
VII-III-2. 6H-SiC:Mg Deep Level Pair VII-46

VIII. SiC Deep Levels VIII-1

VIII-I. Intrinsic Deep Levels Identified VIII-1
VIII-II. Deep Levels in Bulk 6H-SiC VIII-6
VIII-III. Deep Levels in Epitaxial 6H-SiC VIII-21
VIII-IV. Deep Level Sources VIII-25
VIII-V. Defect Dominant Junction Characteristics of 4H-SiC p^+/n Diodes VIII-30
VIII-V-1. Forward I-V-T of 4H-SiC p^+/n Diodes VIII-36
VIII-V-2. Reverse I-V, I-V-T and Breakdown Behavior VIII-44
VIII-V-3. DLTS Characterization of 4H-SiC p^+/n Diodes VIII-53
VIII-V-4. Electroluminescence of

4H-SiC p^+/n Junctions VIII-61

IX. Conclusions and Recommendations IX-1

Appendix A: Publication Summary A-1

Appendix B: Secondary Experimental Techniques B-1

B-I-1. Photoluminescence and Electroluminescence B-1
B-I-2. Temperature Dependent Hall Effect Measurement B-5
B-I-3. Current Voltage (I-V) and I-V-Temperature Measurements B-9

Appendix C: Sample Processes for Chemical Preparation of SiC Samples C-1

Appendix D. I-V Data Acquisition and Experiment Automation Software D-1

Bibliography .... a

List of Figures

Figure **Page**

I-1. Conceptual configuration of a more electric aircraft showing subsystems targeted for conversion from hydraulic to electric motor actuation I-11

I-2. Calculated skin temperatures for a supersonic F-15 aircraft I-14

I-3. Temperature distribution for an F-100 class afterburner fighter engine I-15

I-4. Intrinsic carrier concentration as a function of temperature for several semiconductors. I-17

II-1. Representation of the close packing of atomic layers using the spherical approximation illustrating the Si and C site occupation positions defining general polytypes of SiC II-9

II-2. Graphical representation of the Ramsdell zigzag notation of 4 SiC polytypes ... II-12

II-3. Brillouin zone of a wurtzite crystal. Illustrated are points of high symmetry. A point not at the intersection of two or more lines is meant to represent a general point along the line. II-15

III-1. 6H-SiC nitrogen donor model of Suttrop *et al.* concluded from analysis of observed IR absorption transitions. III-3

III-2. Graphical representation between traps and recombination centers as related to a deep level bandgap state E_T. III-12

III-3. Pictoral representation of several possible Auger recombination paths. The figure illustrates both expected band-to-band and band-to-defect state three body recombinations. III-16

III-4. Graphic representation of Lax's cascade capture mechanism for a coulombically attractive defect potential with a ground state ionization energy E_T. III-22

III-5. Configuration coordinate diagram for a deep trap level illustrating the origin of the exponentially varying capture cross section $\sigma(T)$. III-25

III-6. Illustration of the three primary defect potential types associated with traps

and recombination centers in semiconductors. III-33

IV-1. Simplified band diagram of an n-type Schottky barrier diode with a single deep level (ET) present under conditions of I) quiescent zero bias, II) forward bias trap filling, and III) reverse bias trap emission illustrating the DLTS measurement cycle. IV-7

IV-2. a) Capacitance transient thermal evolution showing DC and three rate window definitions, and b) resulting rate window spectral peak. IV-9

IV-3. Schematic diagram of the DLTS system implemented and used to perform the characterization of SiC deep levels. IV-15

V-1. Inverse mean square error vs. SNR plot for the IGLS and OLS estimates of the exponential component λ_1. Illustrated comparisons for the results of the two fitting algorithms on 2-mode decay transients without a baseline constant. V-20

V-2. Inverse mean square error vs. SNR plot for the IGLS and OLS estimates of the exponential component λ_2. Illustrated comparisons for the results of the two fitting algorithms on the same 2-mode decay transients used for Fig. V-1. V-21

V-3. Inverse mean square error vs. SNR plot for the DIGLS and DOLS estimates of the exponential component λ_1. Illustrated comparisons for the results of the two fitting algorithms on 2-mode decay transients with a baseline C_0. V-26

V-4. Inverse mean square error vs. SNR plot for the IGLS and OLS estimates of the exponential component λ_2. Illustrated comparisons for the results of the two fitting algorithms on the same 2-mode decay transients used for Fig. V-3. V-27

V-5. Comparison of the IGLS and DIGLS estimates of l1 in a plot of inverse MSE vs. SNR. Performance is compared on simulated 2-mode decay transients. V-28

V-6. Flatband idealization of an n-type Schottky barrier illustrating the positional dependencies of the depletion layer edge as a function of applied bias. V-31

V-7. Arrhenius plot comparison of the GaAs EL2 deep level emission rate estimates using DOLS and DIGLS under maximal SNR conditions. V-33

V-8. DDLTS results of the GaAs EL2 deep level emission rate estimates when SNR was severely degraded. Plot compares the DOLS and DIGLS estimates showing superiority of DIGLS over DOLS. V-35

V-9. Rate window plot of the EL2 emission rate thermal evolution under the maximal SNR scenario used for DIGLS and DOLS comparison. V-36

V-10. EL2 rate window plot with artificially degraded SNR used for estimator comparison experiments. V-37

V-11. Rate window spectral characteristic of an electron trapping center in n-type 6H-SiC bulk material. V-39

V-12. Arrhenius plots of the DIGLS fitting results showing convincing evidence for the presence of two exponential components in the decay transients. V-41

V-13. Arrhenius plot comparison of the DIGLS and DOLS fitting results on a vacancy or crystalline damage related hole trap in p-6H-SiC. V-43

V-14. Arrhenius plot of the EL2 data under maximal SNR conditions showing both the MF and DIGLS results. Under these conditions the methods yield identical estimates of the decay emission rate. V-45

V-15. Arrhenius plot of the artificially degraded SNR data from the EL2 center comparing the MF and DIGLS algorithms. V-47

VI-1. Calculated free carrier concentrations as a function of temperature for n- and p-type 4H- and 6H-SiC. A comparison to temperature dependent Hall effect data is illustrated for the 6H-SiC n-type material. VI-12

VI-2. Calculated Fermi level position for a) n-type and b) p-type 6H- and 4H-SiC with donor and acceptor ionization energy levels illustrated as horizontal lines. VI-14

VI-3. Rate window a), and Arrhenius representation of DIGLS fitted and reduced simulation data for a single deep level in n-type 6H-SiC. VI-16

VI-4. Illustration of the electric field barrier lowering of an attractive Coulombic defect potential. VI-18

VI-5. Simulated data plots of the a) prefactor, b) exponential factor, and c) the resulting product associated with carrier capture at a 748 meV electron trap in n-6H-SiC. VI-26

VI-6. Normalized trap occupation prefactor and rate window for a 450 meV electron trap in n-type 6H-SiC with the inclusion of MPE capture kinetics. VI-28

VI-7. Normalized, MPE captured carrier concentration in 6H-SiC as a function of

filling pulse duration for a fixed E_b/E_T ratio of 0.2, where E_T=750 meV. VI-31

VI-8. Normalized, MPE captured carrier concentration in 6H-SiC as a function of filling pulse duration for a fixed E_b/E_T ratio of 0.43, where E_T=750 meV. VI-32

VI-9. Normalized, MPE captured carrier concentration in 6H-SiC as a function of filling pulse duration for a fixed E_b/E_T ratio of 0.65, where E_T=750 meV. VI-33

VI-10. Capacitance transient amplitude data plotted as a function of 1/kT. Data was obtained from simulated and DIGLS fitted transients, which were generated with the inclusion of MPE kinetics. VI-38

VII-1. Empirical transient amplitude data for a 1.04 eV hole trap in p-6H-SiC bulk material. Included in the figure are the fits used to estimate E_b and the effects of the incomplete acceptor ionization condition. VII-4

VII-2. Transient amplitude data and associated fits for various pre-convergent E_b values for an 861 meV hole trap in p-6H-SiC. VII-7

VII-3. a) DLTS rate window spectral plots for two electron traps in n-type 6H-SiC bulk and epitaxial material. b) these levels are characterized by MPE capture kinetics as revealed by the transient amplitude fits. VII-9

VII-4. Plots illustrating the agreement of experimental data with the MPE capture mechanism for three additional majority carrier traps in bulk and epitaxial 4H- and 6H-SiC. VII-10

VII-5. Trap occupation distribution of a minority carrier hole trap found in asymmetrically doped, epitaxially formed p^+/n diodes. VII-11

VII-6. Arrhenius analysis of the capture rate estimates for the 253 and 612 meV electron traps observed in epitaxial 6H and 4H-SiC. VII-22

VII-7. Rate window capture spectrum of the 612 meV electron trap frequently observed in n-type epitaxially grown 6H-SiC. VII-24

VII-8. Capture spectrum for six rate window temporal ratios (t2/t1) of the 253 meV electron trap observed in n-type epitaxially grown 4H-SiC. VII-25

VII-9. a) Rate window spectrum and b) Arrhenius plot for the deep electron trap commonly observed in bulk n-type 6H-SiC and related to vanadium. VII-32

VII-10. Arrhenius plot of the emission rate estimate obtained by considering only a single decay mode for the DLTS data associated with Fig. VII-9. ..... VII-34

VII-11. Emission transient amplitude profiles for the electron trap illustrated in Fig. VII-9. VII-35

VII-12. Rate window spectral plots illustrating results of self-consistency experiments for the electron trapping center shown in Fig. VII-9. VII-38

VII-13. Simulated rate window spectra for an electron trap in n-type 6H-SiC illustrating the capture barrier effect on rate window symmetry for $E_b/E_T>0.47$. VII-42

VII-14. Simulated rate window data for an electron trap in n-type 6H-SiC designed to exhibit a low temperature spectral peak to illustrate Eb and n(T) effects on DLTS results in SiC. VII-44

VII-15. Simulated rate window data for an electron trap in n-type 6H-SiC designed to exhibit a high temperature spectral peak to illustrate Eb and n(T) effects on DLTS results in SiC. VII-45

VII-16. a) DLTS rate window spectra and b) Arrhenius plots for data associated with Mg implanted n-type 6H-SiC. VII-47

VII-17. Transient amplitude variation with temperature for the energetic pair associated with the data of Fig. VII-16. VII-51

VII-18. Rate window plots illustrating self-consistency between the experimental DLTS data and numerically simulated data for the Mg levels of Fig. VII-16. VII-53

VIII-1. Rate window DDLTS spectrum of the most commonly observed deep level in n-type 6H-SiC bulk material. VIII-9

VIII-2. Natural log of the DIGLS fitted emission rates for both the one and two mode estimates for the electron trap of Fig. VIII-1. VIII-11

VIII-3. Plots illustrating the effects of screening on a Coulomb potential using the Thomas-Fermi wavevector of $3.1x10^7$ cm^{-1}. VIII-14

VIII-4. Conventional DLTS rate window spectrum for a p-type bulk 6H-SiC sample containing the three frequently observed deep levels in this material VIII-17

VIII-5. a) Rate window spectra and b) Arrhenius analysis illustrating minority carrier hole trapping phenomenon in n-type 6H-SiC bulk material. VIII-19

VIII-6. Conventional DLTS rate window spectrum of the p-type bulk 6H-SiC Schottky diodes fabricated using an alternative sample cleaning

process detailed in Appendix C. VIII-22

VIII-7. CVDLTS rate window representation of the deep electron trapping centers observed in n-type epitaxial 6H-SiC. VIII-24

VIII-8. Epitaxial p-type 6H-SiC deep level rate window spectra illustrating three closely spaced emission peaks frequently observed in this material. VIII-26

VIII-9. Arrhenius activation energy summary plot of the newly identified and unreported deep traps found in the 6H-SiC bulk and epitaxial materials. VIII-29

VIII-10. Layer structure of the 4H-SiC p^+/n diodes investigated. VIII-32

VIII-11. Forward I-V-T characteristics for typical near ideal and strongly shunted p^+/n 4H-SiC diodes. Data was obtained at 300 K. VIII-38

VIII-12. Temperature dependent forward bias I-V family of curves for a typical well-behaved 4H-SiC p^+/n rectifier. VIII-40

VIII-13. Forward I-V-T curves for a series of shunted or leaky 4H-SiC p^+/n diodes. A well-behaved I-V characteristic is included in the figure for comparison. VIII-41

VIII-14. Forward I-V-T activation energy Arrhenius analysis of the recombination mechanism for six well-behaved 4H-SiC p^+/n diodes. VIII-43

VIII-15. Typical reverse bias I-V-T series of data sets for a well-behaved 4H-SiC p^+/n diodes without a shunted forward characteristic. VIII-45

VIII-16. Reverse I-V-T data curves for a 4H-SiC p^+/n diode that exhibited a forward bias shunting characteristic. VIII-46

VIII-17. Reverse activation energy plot typical of the 4H-SiC p^+/n diodes with non-ideal reverse I-V characteristics. VIII-48

VIII-18. Arrhenius plot of the three consistently observed generation centers in the 4H-SiC p^+/n diodes. VIII-49

VIII-19. Reverse bias series of data sets for a diode with a forward bias shunting characteristic illustrating the negative TCBV. VIII-52

VIII-20. Temperature dependent breakdown voltage data showing the negative TCBV effect for well-behaved and leaky diodes. VIII-54

VIII-21. DLTS rate window spectra of the consistently observed deep trapping centers in the 4H-SiC p^+/n diodes. VIII-56

VIII-22. DLTS spectral features of frequently observed traps in the 4H-SiC p^+/n diodes. These centers represent the low density defects identified. VIII-58

VIII-23. Injection dependent series of electroluminescence curves collected on 4H-SiC p^+/n diodes with well-behaved I-V characteristics. VIII-62

VIII-24. More commonly observed electroluminescence spectra for the 4H-SiC p+/n diodes illustrating the dominance of the violet DAP recombination feature. VIII-64

VIII-25. Electroluminescence spectra observed only for diodes possessing high concentrations of the deep level labeled F in Fig. VIII-21. .... VIII-66

VIII-26. Forward I-V-T family of curves for the diode exhibiting the green electroluminescence in Fig. VIII-25. .... VIII-67

B-1. Photoluminescence experimental hardware schematic diagram. B-4

B-2. Diagram illustrating the magnetic field, current flow, and Lorentz force which characterizes the Hall effect. B-6

B-3. Automated Hall effect experimental setup block diagram. B-10

B-4. The four basic current transport processes in a Schottky diode. B-14

B-5. Device structures used to perform electrical characterizations. B-18

List of Tables

Table **Page**

I-1. Comparison of important semiconductor properties for high temperature I-19

I-2. Johnson's and Keyes' figures of merit for power and frequency performance I-21

I-3. 600 volt MOSFET design comparison between Si and SiC I-24

II-1. Energy gap for several SiC polytypes including hexagonal fraction II-13

II-2. Energy gap for several SiC polytypes including hexagonal fraction II-13

IV-1. Energy gap for several SiC polytypes including hexagonal fraction IV-13

VI-1. Ionization energies for 6H- and 4H-SiC nitrogen donor and aluminum acceptor impurities and relative concentration distributions on each lattice site. VI-10

VII-1. Deep level trap parameters and multi-phonon emission capture barrier, cross section, and defect concentrations obtained by fitting the DLTS trap emission transient amplitude profiles. VII-14

VII-2. Estimated trap emission and MPE capture parameters for the deep level electron trapping pair associated with 1200 °C annealed 6H-SiC samples that were implanted with Mg. VII-50

VIII-1. Summary of all defects and deep levels identified in the 6H polytype of SiC. VIII-4

VIII-2. Summary of all defects and deep levels identified in the 4H polytype of SiC. VIII-5

VIII-3. Atomic concentrations of impurity species identified in the 6H-SiC wafers using secondary ion mass spectrometry. VIII-27

VIII-4. Summary of the deep level traps identified in the 4H-SiC p^+/n diodes. VIII-59

VIII-5. Atomic concentrations of impurity species identified in the 6H-SiC wafers using secondary ion mass spectrometry. VIII-27

IX-1. Summary of the deep level traps identified in the 4H-SiC epitaxial material. .. IX-5

IX-2. Summary of the deep level traps identified in the 6H-SiC bulk and epitaxial material. IX-6

Abstract

Deep level defect centers were investigated and characterized using digital deep level transient spectroscopy (DLTS) methods on hexagonal silicon carbide (SiC) polytypes of 4H and 6H, which can be utilized for high power, high temperature, and high frequency electronic device applications. Additionally, capacitance-voltage (C-V), current-voltage-temperature (I-V-T), electroluminescence (EL), and temperature dependent Hall effect measurements were also performed to support DLTS characterization. Modifications to the experimental hardware enabled DLTS characterization of the wide bandgap SiC semiconductors to temperatures approaching 800 K for the first time. As a result, several new deep trapping centers were identified and studied in both 4H- and 6H-SiC polytypes. Ten new deep level traps were found in bulk and epitaxial 6H-SiC ranging in energy from 0.380 to 1.3 eV, and eight new levels were cataloged in epitaxial 4H-SiC with thermal binding potentials of 0.2 to 0.856 eV. The observation of deep levels in large concentrations ($>10^{15}$ cm^{-3}) in the epitaxial samples was an implication of the significant role played by lattice imperfections, which are known to plague these materials. A direct correlation to lattice site inequivalencies was demonstrated for a vanadium center and two levels induced by Mg ion implantation for the first time using DLTS methods. The connection to distinct SiC lattice sites was made possible by the development of a novel parameter estimation algorithm, which also enabled the identification of a dominant non-radiative carrier capture mechanism in SiC. The ability to identify multi-exponential capacitance transient decay was significantly extended by the collaborative development of a differenced, iterative, generalized least

squares (DIGLS) parameter estimation routine. Superior fidelity to resolve closely spaced exponentials was demonstrated on both simulated and challenging real DLTS transient data for the DIGLS algorithm. Non-radiative carrier capture for several deep levels in the SiC material studied was for the first time found to proceed via lattice-relaxation multi-phonon emission (MPE). In addition, the thermal capture barrier to emission energy ratios (E_b/E_T) for these centers were found to be large and in the range of 0.6, indicating an extremely efficient electronic lattice coupling. Extensive modeling of the capture and emission kinetics of deep level defects in SiC resulted in an identification of the large errors that occur when estimating trap parameters without consideration for the incomplete shallow impurity ionization. This condition is unique to SiC, and the errors which would result from an inconsideration of this effect were demonstrated for simulated and real DLTS trap data. The junction transport characteristics of 4H-SiC p^+/n rectifiers were found to be dominated by the presence of numerous deep levels with large densities. A correlation was demonstrated between the deep levels and a significant tunneling component of carrier transport in these devices. In addition, the identification of a luminescence activator was demonstrated for a 680 meV deep hole trap measured by DLTS in the 4H-SiC p^+/n diodes. This center was found exclusively in diodes exhibiting a bright green (2.4 eV) donor-acceptor-pair (DAP) electroluminescence.

ELECTRICAL CHARACTERIZATION OF INTRINSIC AND INDUCED DEEP LEVEL DEFECTS IN HEXAGONAL SILICON CARBIDE

I. Introduction

I-I. Background: Wide Bandgap Semiconductors

The discovery of semiconducting properties in silver sulfide (Ag_2S) by Michael Faraday in 1833 [1839:122] did not stimulate a technological revolution leading to the current state of modern electronics some 160 years later. The advances in electronic technology, which have so profoundly altered our lives and fundamentally changed the world in which we live, have almost totally occurred since World War II. In fact, in the succeeding forty years following Faraday's discovery of the negative temperature coefficient of resistance in Ag_2S and other "poor conductor" crystals, progress was not great. There were, however, occasional but significant discoveries of anomalous behaviors associated with metallic (Zn, Cu, Pb, Ag, etc) sulfides, oxides, and the element silicon. Becquerel [1839:711] is credited with the first recorded observation of the photovoltaic effect. In 1873, Smith [1873:31] discovered that the conductivity of selenium (Se) could be increased by shining light on the material, which subsequently led to the fabrication of the first Se photocell three years later [Adams and Day, 1876:113].

The first recorded observation of what was to become the fundamental building block of all modern solid state electronic devices; rectification or non-linear, junction behavior, was accomplished independently by Braun [1874:556] and Schuster [1874:251] on galena (PbS), and pyrites and copper oxides, respectively. Even this important discovery would not come into prominence for another thirty years, even though the first large area dry rectifier was made using Se in 1883 [Fritts, 1883:465]. The rectification properties of semiconductors finally became fully appreciated when it was demonstrated that wire whiskers in contact with a crystal of galena or silicon created an excellent rectifier of the high frequency currents created by radio waves in an electronic circuit [Bose, 1904], and greatly increased the sensitivity of radio receivers. These wireless "crystal" receivers were prominent until the late 1930's when they were completely supplanted by vacuum tube technology. During this time, rectifiers of selenium and copper oxide became commercially important, and motivated the development of a number of discrete devices such as thermistors, varistors, and photocells [Burford and Verner, 1965:2]. By this time roughly a hundred years had passed since Faraday's discovery, yet the extent of all knowledge regarding semiconductor materials was empirical in nature. A theoretical foundation for the electronic behavior of semiconductor materials had been lacking and could only now be developed due to the emergence of quantum wave mechanics. The impetus which initiated the development of the theories necessary for a fundamental understanding was the desperate need to significantly improve the performance of microwave radar detection systems in Great Britain during the early days of World War II. The high frequency signals generated by the ten centimeter radar waves could not be

efficiently rectified and converted by existing vacuum tube technologies. Thus, the point contact crystal diode reemerged, eventually supplanting the vacuum tube, and subsequently motivated the theoretical developments leading to the monumental discovery of the point contact transistor by Brattain, Bardeen, Shockley and others at Bell Telephone Laboratories in 1948 [Bardeen and Brattain, 1948:230; Brattain and Bardeen, 1948:232; Shockley and Pearson, 1948:233].

The ultimate relation of semiconductor phenomenon to first principles requires the use of quantum mechanics, and significant progress in the theoretical picture was made starting about 1930. The questions of how to regard the tightly bound inner electrons of the atoms which make up a solid, and what occurs when an electric field is applied to the crystal were considered by Wilson [1931:458], and subsequently led to his theory of semiconductors.

Wilson correctly deduced that both the tightly bound core electrons and the bonding valence electrons, constituting the atomic structure of the crystal, cannot be associated with a single lattice point atom. They are in fact free to move unimpeded through a perfect crystal. This was the important result of Bloch's theory, which showed quantum mechanically that particles confined to a potential well have an increasing probability to occupy levels in adjacent wells as the separation distance becomes small, as is the case in a crystal lattice. However, Wilson showed that they may not all take part in electrical conduction, and construed the concepts of filled and unoccupied or partially filled bands. Thus, there finally existed a theoretical foundation upon which electronic

motion, and therefore the electronic properties of semiconductors, insulators, and metals could be differentiated and described accurately.

The concept of allowed bands of quantum states was a natural result of applying a periodic potential to the free electron states of Sommerfeld's model, in which the core electron levels of the individual atoms remained unperturbed, and the valence electron states are the energetically closely spaced plane-wave solutions of free particles. When the notion of a periodic potential is introduced, the resulting quantum solutions are confined to allowed bands of closely spaced levels separated by regions in which no energy levels are allowed. These regions void of allowed electronic states were described as forbidden bands or energy bandgaps. The manner in which these bands are formed is dependent critically upon the valencey of the constituent atoms and the interatomic spacing of the atoms in a crystal lattice. The resulting band structure determines the electronic properties of the material, and completely describes its behavior as metallic, insulating, or semiconducting. The formation of forbidden energy bands, void of electronic states, is not unique to any of the three macroscopic electronic classifications of solids. Now if there is a forbidden energy gap between a completely filled band and the next highest band presenting allowed levels, no conduction should take place. Thus, we should then have a situation in which a material might be an insulator.

The situation envisaged for an insulator does occur for solids formed from atoms having four valence electrons. Carbon (in the form of diamond), Si, Ge, and α-Sn (the low temperature hexagonal phase) form bands in which the highest occupied band is completely filled and the next highest band is separated from it by a forbidden energy

gap. This condition also occurs for numerous compound materials (SiO_2, Si_3N_4, GaAs, InP, SiC, AlGaAs, etc) and is more complex, however, the common feature is that the number of valence electrons is even for the individual molecules in each case.

The distinction between insulators and semiconductors is somewhat arbitrary and is actually dependent upon the purity of material, technical application, temperature range, and even empirical characterization method used. The common identifying characteristic of both materials is, however, the existence of a forbidden band of energies lying between the highest occupied band and the next highest band of completely unoccupied levels. The nomenclature which has been universally adopted to describe specifically the energetic magnitude of the gap between the highest occupied band and the next highest band of allowed energies is that of the energy-band gap. This characteristic energy has become the single most universally adopted parameter by which semiconductors and insulators are identified. The distinction between the two types of materials is simply one of magnitude. If the energetic spacing between the filled band and the next band presenting unoccupied levels is large, electrons will be very unlikely to be accelerated into the empty states, and the material is classified as an insulator. On the other hand, if the bandgap energy, E_G, is small, there is the possibility that electrons may be thermally excited into the band above and contribute to electrical conduction. The number of electrons excited would increase with temperature in a manner governed by statistical processes and an activation energy E_G, and we should expect an increase in conductivity with temperature. This is the phenomenon observed by Faraday, which was ascribed as a material possessing a negative temperature coefficient of resistivity. Until

recently, the range of activation energies or bandgaps which were used to discriminate between semiconductors and insulators was taken to be roughly $0 < E_G < 2$ electron volts (eV) for semiconductor assignment of a pure material.

The ability to control the conductivity of these materials, through the introduction of small concentrations of certain atomic species into the crystal lattice, is the basis for all modern electronic devices. This development is also attributable to Wilson.

Introduction of dopant chemical species into materials with bandgaps larger than 2 eV enables significant conduction in materials previously defined as insulators. This class of materials has become known as *wide-bandgap* semiconductors. The range of bandgap energies encompassed in this class of materials is from roughly 2.2 eV to over 6 eV. Until recently, this group of materials was not very technologically important, except in a few cases some of which involving intrinsic-insulating rather than semiconducting properties. This situation was not due to any fundamental device performance advantages afforded by the materials with bandgaps of lesser magnitude but rather as a result of two primary conditions. Firstly, the rapid success that was realized with Ge and Si in terms of material growth and especially purification techniques quickly eliminated all other competitors. These developments were further enhanced by the mechanical and chemical properties of these materials in terms of robustness of thin wafer slices and ease of device fabrication including etching and electrical contact metallurgy. Materials with wider bandgaps than Ge (0.65 eV) and Si (1.12 eV) are all molecular or compound solids with the exception of the diamond crystal structure of C. Fabrication of large perfect crystals in bulk volumes is considerably more difficult for molecular compounds than elemental

solids due to the additional constraints of lattice ordering and phase equilibria control of a binary system undergoing transitions between gaseous, liquid, and solid phases. As a result, Si technology has developed into the dominant device industry of today, and is the basis for virtually all integrated circuit (IC) manufacture and the majority of discrete device components. Owing to this maturity, Si based electronics can be manufactured with reproducibly high yields, excellent reliability, and extremely low-cost. Thus, developing material systems have realistic opportunities only in niche markets in which they may become commercially viable. These markets are identified by desired electronic functions which cannot be satisfied by Si-based devices due to the fundamental physical limitations of the electronic properties of Si. For example, an efficient light emitting device has never been realized with Si semiconducting material. This led to the development of light emitting diodes (LEDs) and solid state lasers in a wide range of wavelengths using compound semiconductors such as GaAs, GaP, and compounds between the two with Al added. GaAs, which is characterized by a large electron saturation drift velocity, soon found applications in the microwave device market as superior emitters and detectors of the short wavelength frequencies used in communication and radar applications. Satellite electrical-generating photovoltaic arrays, which have been manufactured using low-cost Si solar cells for 40 years, are now being replaced by GaAs, $GaInP_2$, and other IIIa-Va compounds. This was motivated by a superior resistance to damage caused by the natural radiation environment in space and higher electrical conversion efficiencies for solar cells fabricated from these materials. Although more costly to manufacture, the compound solar cells yield a significant net

cost savings by extending useful satellite lifetimes and reducing solar array mass and volume because of the higher conversion efficiencies.

Improved efficiency, longer device lifetimes, extended performance ranges, and low cost are still the drivers of modern electronic device development as they were in the 1950's. With an increasing level of device sophistication, larger numbers of mechanized functions have become electronically controlled or performed, eliminating everything from mechanical relays for electrical switching to the human labor associated with many dangerous and tedious manufacturing functions. These developments have translated into improved reliability and a reduction in manufacturing costs by eliminating sources of mechanical failure with more reliable electronic functions. As the marriage between automated mechanization and electronic device functionality becomes more deeply rooted, there has become increasingly greater demands placed upon electronic device and circuit performance and physical robustness. With these increasing electronic automation and control requirements comes an associated increase in the level of electrical power being handled by the devices and circuitry. Additionally, there are also increasing demands for electronic sensors and control circuits to be de-centralized and located near the function being performed to improve reliability and to provide more autonomous real-time feedback. This often has the undesirable effect of locating the sensor/control electronic devices or circuits in harsh environments which can seriously degrade performance. Automotive and aircraft engine controls and sensors, oil and gas well logging instrumentation, and electronics for spacecraft applications are examples of high temperature environments in which electronic functions are desired or currently being

used. As was the case during World War II, which saw the resurrection of the point contact rectifier, the Department of Defense (DOD) and specifically Air Force requirements are driving the development of electronic technologies which satisfy these high power and high temperature requirements. As will be shown in the following subsection, Si-based electronic devices are physically incapable of satisfying the specifications for devices which will be operable in the high temperature and high power regimes required by many of these applications. The approach being pursued to solve this deficiency is to develop alternative semiconductor materials with the physical properties necessary to fabricate devices which will satisfy these high power and high temperature requirements. The class of materials being developed which can potentially meet the previously mentioned demands are characterized by a single thread of commonality; their *large bandgap*. In addition to the advantages afforded by wide bandgap semiconductors in the areas mentioned above, these materials are also resistant to caustic chemicals and radiation damage owing to their large cohesive energies. They are also finding applications as optical materials which are active in the blue and ultraviolet wavelengths, especially as emitters, and can be used to develop higher density optical storage media and for full color display technologies.

I-II. High Temperature High Power Electronics

The ability of solid state electronic devices to operate under extreme thermal conditions is limited to a great extent by the physical properties of the semiconductor such as the intrinsic carrier concentration, metallurgical stability, thermal conductivity, and carrier mobility. Thermal-mechanical considerations such as heat sinking and device

packaging also determine the ability of electronic devices to remain functional during periods of extreme thermal cycling or short duration, single event, excursions to temperatures exceeding normal or specified operating conditions. The mechanism or mode of failure is many times device dependent. Deleterious reductions in reverse breakdown voltage, transistor gain, high frequency cutoff, and switching speed as well as increases in leakage currents, device resistance, and latch-up events in switching and logic devices are all typical high temperature failure mechanisms. Additionally, there may be mechanical failures associated with degraded electrical contact metallizations and electrically insulating dielectric layer liftoff and peeling effects.

To ensure electronics reliability and longevity, the junction temperature of conventional Si-based devices is currently military standard (MIL-STD) rated to operate over the temperature range of -55 °C to 125 °C. Many of the potential users of high temperature electronics call for device specifications that exceed the existing 125 °C rated Si technology. The majority of high temperature device applications are specified at or below 250 °C for automotive (75%), commercial aircraft (50%), and all oil and gas well logging except where steam recovery is utilized. In contrast, a majority of DOD/DOE space and terrestrial military applications have requirements for electronic systems to operate at temperatures up to 500 °C and beyond [Thome and King, 1988].

The primary impetus that has been pushing the development of robust device technologies is the U.S. Air Force and Navy efforts to replace bulky aircraft hydraulics and mechanical control systems with heat tolerant *in situ* control electronics. On-site electronics, actuators, and sensors will reduce complexity and increase reliability.

Subsystems such as hydraulic-driven flight control actuators, engine-gearbox driven fuel pumps, and air-driven environmental control systems would be powered electrically via electric motors. Studies on several fighter aircraft have shown that a conversion to this "more-electric" concept offers many subsystem level benefits in the areas of reliability, maintainability, supportability, and overall cost [Eike *et al.*, 1992; Shah and Rohr, 1992]. The primary subsystems being considered for conversion to a more electric functionality are shown in Figure I-1. In this concept, aircraft power is produced by an internal starter generator (ISG) that is directly driven by the main engine. The ISG power is fed to the fault tolerant power management and distribution (PMAD) electronics which powers all aircraft electrical subsystems as shown in the figure. In this design, conventional hydraulic-driven flight control actuators will be replaced by electric motor driven actuators and a distributed flight control electrical system. Electrical flight control

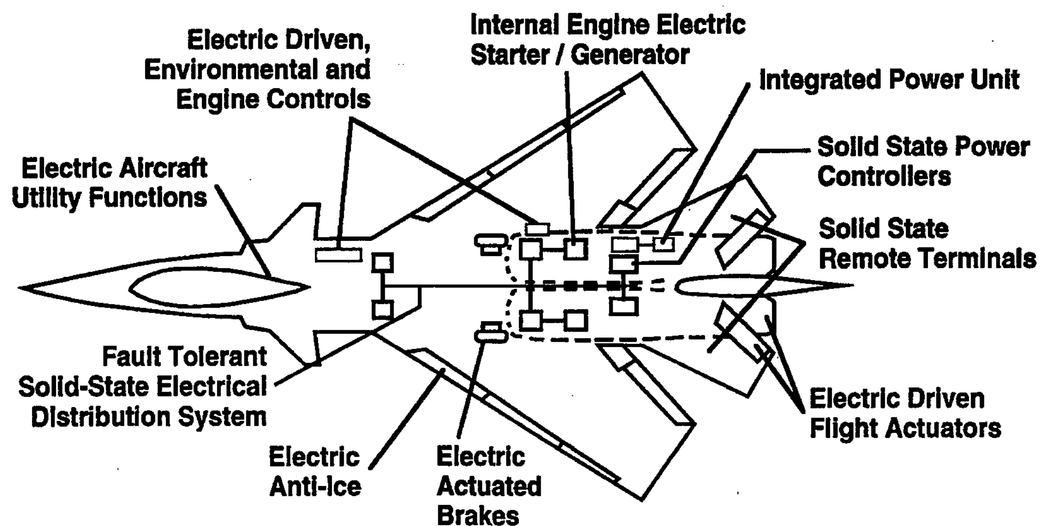

Figure I-1. Conceptual configuration of a more electric aircraft showing subsystems targeted for conversion from hydraulic actuation to electric motor driven actuation.

actuation offers subsystem benefits in fault tolerance, redundancy, reliability, and power density. The distributed control concept eliminates the major drawbacks of a centralized system in which all power and control electronics are displaced from their functions and centrally located in the aircraft. In a distributed architecture, autonomy is achieved for each function thereby improving aircraft survivability compared to a centralized control system. The elimination of hydraulic systems in aircraft will yield significant safety, reliability and maintainability, and cost advantages by removing hydraulic-oil fire hazards, mechanical complexity, and weight penalties. However, the hydraulic system serves a passive function by acting as a thermal transport medium to remove heat from flight control actuators. Thus, in the distributed control scheme, power control electronics will be located on or near the actuators without the benefit of hydraulic fluid cooling. The intermediate solution is to employ a centralized, closed-loop, environmental control system (ECS). This will considerably offset the benefits realized by eliminating the aircraft control hydraulics. One of the systems being considered for the ECS function involves using a poly-alfa olefin conducting transport medium coupled to a vapor-phase heat exchanger, similar to the system being used for electronics cooling on the advanced F-22 fighter aircraft. The optimal solution to the problem of an increased operating temperature environment is obviously to increase the heat tolerance of the control and power electronics. This can be accomplished through the development of alternative device technologies such as wide bandgap semiconductors.

In a passively cooled environment, the entire heat load from the electronics and associated actuation and mechanical functions must be coupled to the external aircraft

structure, which acts as the heat sink to the external ambient. The magnitude of the heat load, and thus the device operating temperature will depend on many factors such as physical location, aircraft speed, duration of flight at speed, altitude and ambient air conditions, electronics efficiency, and electronics packaging. However, assuming the aircraft skin as the terminal heat sink, external ambient temperature maximums can be estimated for specific performance envelopes. From these estimates, the operating temperature of the actuator flight control, PMAD, and other electronics may be projected. Figure I-2 illustrates just such a calculation of the skin temperatures for an F-15 fighter aircraft for 1.0 g flight at the three altitudes and speeds indicated. Ignoring the environment around the engines, the temperatures shown range from between approximately 90 °C and 200 °C.

As previously mentioned, in the absence of active cooling measures, these temperatures represent the ambient heat sink values. Recalling that the heat transfer rate, g, is dependent upon the difference in temperatures between the sink and source, and is given as $g = h(T_2 - T_1)$, where h is the transfer coefficient. We see that the electronic device operating temperature required to ensure adequate heat removal must necessarily be higher than the ambient. Due to the thermal resistances between the device packaging, electronics box, aircraft frame/support structure, and aircraft skin, solid state devices capable of operating at temperatures of at least 250 °C have been specified in order to support the electrification of actuator and other flight control functions in the absence of active cooling measures.

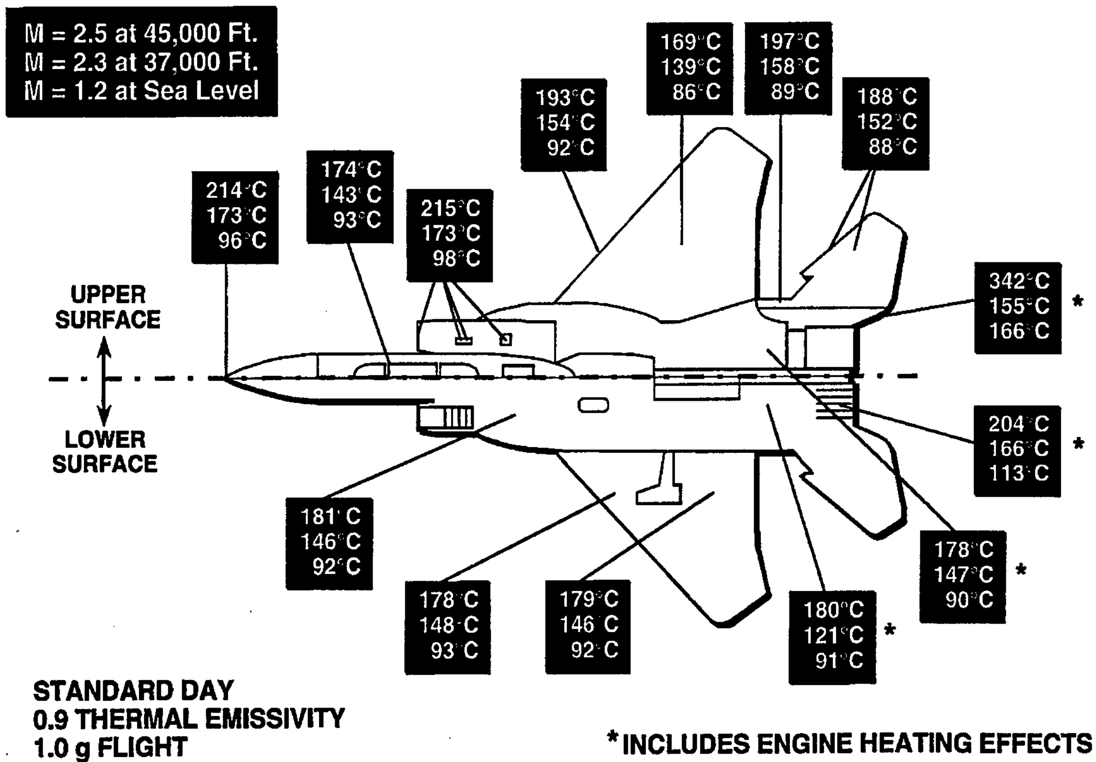

Figure I-2. Calculated skin temperatures for a supersonic F-15 aircraft.

High temperature electronics are also being proposed to provide the same hydraulic function elimination on aircraft engines [Pryzbylko, 1993]. The design seeks to utilize electro-mechanical hardware for nozzle, guide-vane, and metering valve actuators, and for fuel pumps. In this environment, the engine case temperatures will require electronics which will operate reliably up to 350 °C and above. Figure I-3 shows the projected engine case temperatures for an F-100 class afterburner fighter engine for two air speed scenarios (0.9M and 2.5M) at 40,000 and 50,000 foot altitudes. Case temperatures at locations which would house control electronics range from 175 °F (80 °C) to over 600 °F (315 °C).

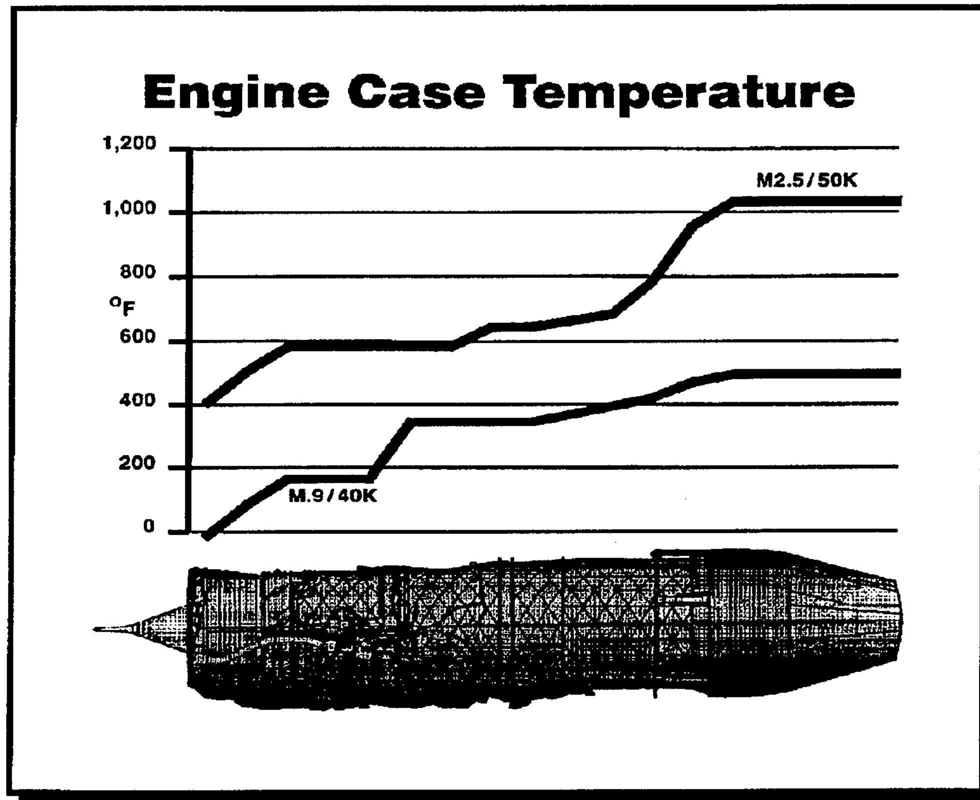

Figure I-3. Temperature distribution for an F-100 class afterburner fighter engine [Przybylko, 1995].

In order to implement these advances in aircraft subsystem performance, a wide variety of components capable of high temperature operation must be developed. Capacitors, switches (MOSFETS, IGBT's, and BJT's), and rectifying devices (p/n and Schottky diodes) are the types of discrete components required for power control and conditioning. Expected power requirements range from 50 to 800 amps at voltages up to 1000 V. Aircraft, automotive, and other high temperature electronics users have also specified needs for heat tolerant sensors ranging from flame detectors to pressure transducers. Fortuitously, in addition to high temperature tolerances, wide bandgap

semiconductors can also provide significant performance improvements over Si-based devices in the high power and high frequency areas as will be shown below.

When considering the temperature ranges of proposed operation, it becomes apparent that Si-based semiconductor device technologies rated at 125 °C are not feasible. This is due primarily to the uncontrolled generation of intrinsic carriers, poor thermal conductivities, and material instabilities. Equations I-1 and I-2 represent the analytic expressions for the intrinsic free-carrier concentration, $n_i(T)$, in a semiconductor given

$$n_i(T) = \sqrt{N_C \cdot N_V} \cdot \exp(-\frac{E_g}{2kT}) \quad \text{[I-1]}$$

by and the reverse saturation or leakage current density, $J_0(T)$, given by

$$J_0(T) = q[\frac{D_n n_i^2(T)}{L_n N_A} + \frac{D_p n_i^2(T)}{L_p N_D}] \quad \text{[I-2]}$$

associated with a simple bipolar (p-n) junction, respectively. N_C and N_V are the effective mass density of states for the conduction and valence bands, respectively. D_n, D_p and L_n, L_p are the diffusion coefficients and diffusion lengths of electrons (n) and holes (p), respectively, N_A and N_D are the acceptor (A) and donor (D) doping concentrations, k =8.617x10^{-5} eV/K is Boltzmann's constant, q=1.602x10^{-19} C is the electronic charge, and T is the absolute temperature. The exponential dependence of $n_i(T)$ on E_g, and subsequently the square law dependence of the diode leakage current upon the intrinsic concentration highlight the fundamental advantage afforded by semiconductors with wide bandgaps, for high temperature applications. The magnitude of the advantage is illustrated explicitly for several semiconductor materials ranging in bandgap from 0.65

eV to 3.1 eV in Figure I-4 in which $n_i(T)$ is plotted as a function of temperature. As seen in the figure, there is negligible intrinsic generation for the wide bandgap materials with $E_g > 2$ eV even at temperatures exceeding 500 K. Thus, in terms of reverse leakage currents, it becomes obvious that wide bandgap semiconductors can eliminate this high

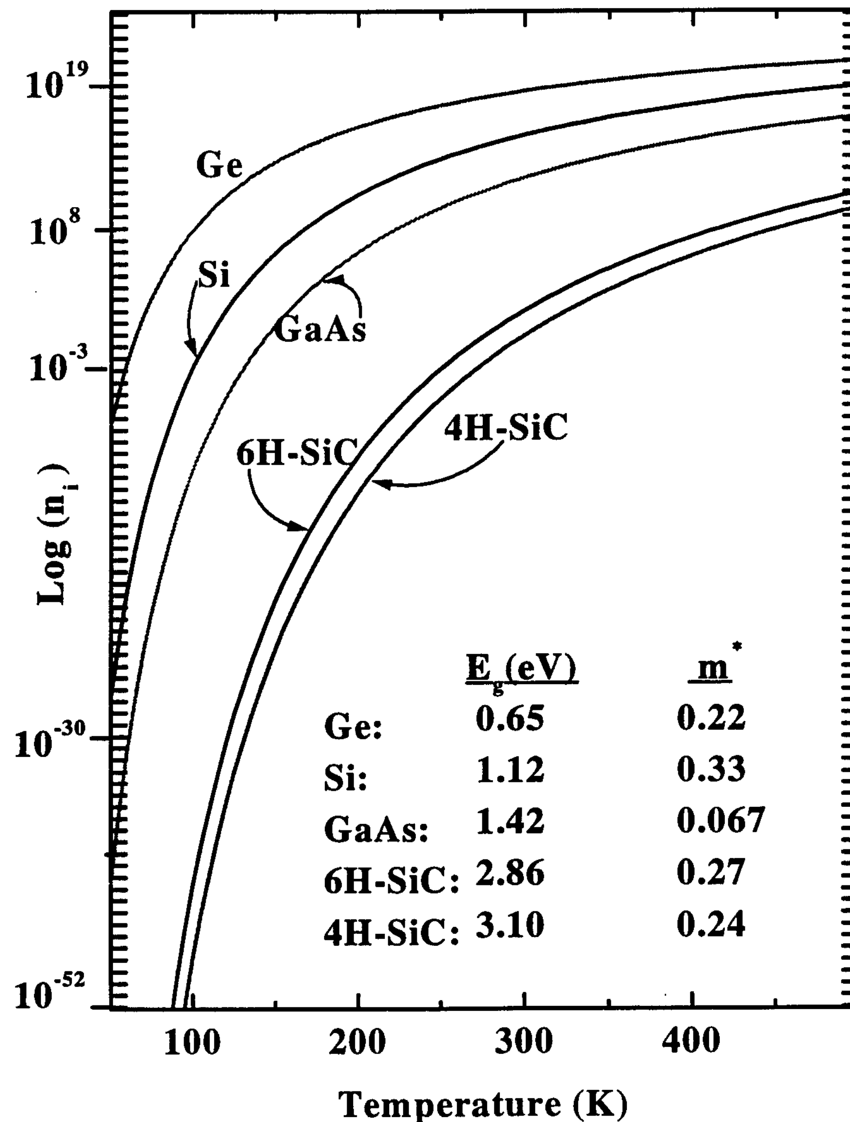

Figure I-4. Intrinsic carrier concentration as a function of temperature for several semiconductors with bandgap and effective mass values listed.

temperature device degradation mechanism completely. In fact, since the intrinsic carrier concentration is a fundamental semiconductor property, this is the only means by which it may be made negligible, and thus extend the safe operating temperature range of devices fabricated on these materials.

As previously noted, leakage currents resulting from intrinsic thermal generation of unwanted carriers is not the only consideration for determining the suitability of a material system to extend the operating temperature range of electronic devices. Carrier lifetimes and mobilities, critical breakdown field strength, saturated drift velocities, operating efficiency, and thermal conductivities are all crucial to the performance of devices subsequently built on a given material. Therefore, a judicious selection of alternative material systems must consider every contributing aspect to device performance. These factors have led to the development and characterization of promising material systems for high temperature, high power device applications. TABLE I-1 lists the important physical properties of several semiconductors being proposed as solutions to the demand for increasingly heat tolerant electronics with Si included as a comparison [Morkoc *et al.*, 1994:1365]. The maximum operating temperature values are obtained by calculating the temperature at which the intrinsic carrier concentration would be roughly 10^{15} cm^{-3}, and illustrates the highest possible temperature of device operation based only on bandgap considerations. In practice, the physical stability of a material is a more important criteria in determining suitability for heat tolerant electronics. It is this property which effectively eliminates GaAs and GaP as candidates for high temperature device applications in spite of their larger bandgaps.

TABLE I-1. Comparison of important properties for semiconductors proposed for high temperature operation

Property	Si	GaAs	GaP	3C-SiC (6H-SiC)	Diamond	GaN
Bandgap, E_g (eV) @ 300K	1.12	1.42	2.3	2.2 (2.86)	5.5	3.39
Maximum Operating Temp (°C)	327?	487?	977?	927 (1307)	1150?	-
Melting Point (°C)	1417	1237	1467	Sublimes T > 1827	Phase Change	-
Physical Stability	Good	Fair	Fair	Excellent	Very Good	Good
Electron Mobility @ 300K, μ_n (cm^2/Vs)	1400	8500	350	1000 (600)	2200	900
Hole Mobility @ 300K, μ_n (cm^2/Vs)	600	400	100	40	1600	150
Breakdown Field, E_b (V/cm)	$0.3x10^6$	$0.4\ x10^6$	-	$4\ x10^6$	$10\ x10^6$	$5\ x10^6$?
Thermal Conductivity, σ_T (W/cm)	1.5	0.5	0.8	5	20	1.3
Saturated e^- Velocity, v_s (cm/sec)	$1x10^7$	$2\ x10^7$	-	$2\ x10^7$	$2.7\ x10^7$	$2.5\ x10^7$
Dielectric Constant, κ	1138	12.8	11.1	9.7	5.5	9

The very high metallurgical reactivity of Ga and the low vapor pressures of As and P in these compounds create electrical-contact and bulk material instabilities over the higher temperature ranges of interest. The most notable data in TABLE I-1, after the maximum operating temperature entries, are the saturated electron drift velocity, thermal

conductivity, and breakdown voltage values for the wide bandgap materials diamond, GaN, and the two crystal structures of SiC. In addition to the high temperature potential of these materials, these properties result in predicted device performance for high frequency and high power applications which far exceeds those of Si or GaAs. The much larger breakdown electric field is an intrinsic material property, which is proportional to the bandgap ($V_{br} \propto E_g^{3/2}$), and translates into the ability to fabricate switching and rectifying devices capable of handling much greater power levels. An additional benefit related to the large bandgap magnitude is an inherent resistance to corrosive chemical environments owing to the large cohesive energies of the atoms in these crystals. This physical property is also responsible for the significant resistance to radiation damage exhibited by wide bandgap materials. Their excellent thermal conductivity enables efficient heat rejection when coupled to active or passive cooling systems, resulting in lower device junction temperatures and allowing higher power density operation. A large saturated electron drift velocity allows devices to achieve higher frequencies, since the transit time in a microwave field effect transistor (FET) is inversely proportional to v_s, and the maximum operating frequency is proportional to $(v_s)^{1/2}$.

To further illustrate the advantages afforded by the wide bandgap semiconductors in terms of power and frequency performance, TABLE I-2 shows a compilation of the calculated figures of merit (FOM) for two different performance metrics [Davis, 1994:162]. The Johnson FOM is based on the idea that the basic limitation of the high frequency and high power capabilities of discrete devices is set by the product of the breakdown electric field, E_b, and the saturated electron drift velocity ($J_{FOM} = (E_b v_s/\pi)^2$).

TABLE I-2. Johnson's and Keyes' figures of merit for power and frequency performance

Material	E_b (V/cm)	Johnson ($W\Omega/s^2$)	Keyes ($W/cm^{0.5}$ $s^{0.5}$)	J_{FOM}/J_{FOM}^{Si}	K_{FOM}/K_{FOM}^{Si}	E_b/E_b^{Si}
Si	$3x10^5$	$9x10^{23}$	$1.38x10^3$	1.0	1.0	1.0
GaAs	$4x10^5$	$6.25x10^{24}$	$6.3x10^2$	6.9	0.456	1.25
3C-SiC	$40x10^5$	$1x10^{27}$	$8x10^3$	1137.8	5.8	7.5
6H-SiC	$40\ x10^5$	$6.2x10^{26}$	$7x10^3$	694.4	5.12	10
Diamond	$100\ x10^5$	$7.4x10^{27}$	$4.4x10^4$	8206	32.2	25
GaN	$20\ x10^5$	$2.5x10^{26}$	$2.4x10^3$	281.6	1.76	10

Alternatively, the Keyes FOM ($K_{FOM} = \sigma_T(v_s/\kappa)^{1/2}$) considers the switching speed of transistors in integrated circuits, where a large saturated electron velocity allows high speed operation. Additionally, the Keyes quantity considers the lower limit on the size of individual devices, which is set by the thermal conductivity, σ_T. Included in the table are the ratios of the two FOM quantities for each semiconductor in terms of the Si values as well as E_b ratios.

The advantages of wide bandgap materials illustrated in the previous tables and discussion have been studied in detail, and theoretical modeling of potential device performance has been accomplished by several groups. Bhatnar and Baliga [1991:176] performed numerical simulations of SiC power rectifier and MOSFET performance comparing the results to Si devices. They found that the output characteristics of the SiC devices would outperform the entire spectrum of Si-based devices, and would handle up to 13 times the power. Similar results were realized for GaN and diamond [Morkoc *et*

al., 1994:1369], [Davis *et al.*, 1988:77] in terms of demonstrating performance advantages.

Understanding the requirements motivating the intense interest in the development of high temperature, high power, and high frequency devices leads to the selection of candidate technologies to satisfy these needs. The scientific/technical maturity of SiC far exceeds that of any other competitor, due primarily to the availability of reasonably good quality bulk substrates, which has enabled advances in epitaxial chemical-vapor-deposition (CVD) growth of device structures. Diamond, GaN, and other candidate III-nitride semiconductors (AlN, InN, etc.) have similar or potentially better device characteristics in some instances, but are seriously hindered by the lack of suitable lattice matched substrate material upon which to grow high quality device epitaxy. For example, GaN has far superior optoelectronic potential for blue and UV applications than any of the other systems due to its large direct bandgap. However, epilayer growth has been restricted to sapphire substrates, which results in material with significant concentrations of dislocations, stacking faults, grain boundaries and other crystal defects.

As a result of the technical advantages, much progress has been made toward the development of a SiC-based device technology to satisfy the need for heat tolerant electronics with high power capabilities. Metal-semiconductor and metal-oxide-semiconductor transistors as well as Schottky and p-n junction rectifiers have all been demonstrated with excellent high temperature characteristics [Palmour *et al.*, 1991:491], [Edmond *et al.*, 1991:487]. In addition to being capable of operating at higher power densities, SiC devices are projected to operate at higher efficiency levels than comparable

Si electronics. This is also a consequence of realizing a reduction in both conduction and switching losses. In the case of a power FET for example, the resistive losses depend upon the thickness (W) and doping level (N_S) of the semiconductor layers used for blocking reverse voltages, and in some instances provide the drift region across which current must flow. These losses are proportional to N_b and inversely proportional to W, which in turn depend on E_b^2 and E_b^{-1}, respectively. Thus, since E_b increases with bandgap as shown earlier, both loss parameters benefit from an increase in energy gap. Similarly, conduction losses can be reduced by taking advantage of the higher power density potential of SiC to fabricate devices with smaller areas than required for Si devices performing the same function. The result is a reduction in device capacitance, which is the primary switching loss parameter. TABLE I-3 summarizes this aspect of SiC-based device electronics advantages over Si by illustrating the design parameters of a 600 volt MOSFET for each semiconductor. The data shows an 80 fold decrease in resistive losses and a reduction in device capacitance by a factor of 5 for SiC over Si. These results are typical of the type and magnitude of performance gains which may be realized by building devices on SiC semiconducting material.

The development of higher bandgap semiconductors along with novel fabrication techniques can effectively circumvent many of the performance detracting mechanisms intrinsic to a particular device or material system when operated in the regimes of high temperature, power, or frequency. However, wide bandgap semiconductors being developed for these applications present difficulties similar to those experienced during the evolution of Si or GaAs technologies, as well as problems unique unto themselves.

TABLE I-3. 600 V MOSFET design comparison between Si and SiC

Parameter	Evaluation	SiC	Si	Units
Critical Field E_b	$\propto E_g^{3/2}$	$2.2x10^6$	$2.7x10^5$	V/cm
Thickness (W)	$2V_b/E_b$	5.4	44.9	μm
Doping (N_D)	$\varepsilon E_b^2/2qV_b$	$2.3x10^{16}$	$3.9x10^{14}$	cm^{-3}
Mobility (μ)	Characteristic	250	1500	$cm^2/V \cdot s$
Resistance (R_d)	$4V_b^2/\mu\varepsilon E_b^3$	0.58	47.6	$m\Omega \cdot cm^2$
Area	-	A	5·A	cm^2

SiC, the nitrides, and diamond are all very chemically inert with wide energy gaps, owing to their large cohesive energies. These properties make them excellent candidates for the applications and extreme operating environments outline above, but also result in poor contact metal adhesion, device processing/fabrication complications, and difficulty in doping. Ohmic contact formation can be a formidable task on wide bandgap materials due to the potentially large barrier height which may exist at the metal-semiconductor interface. Additionally, growth temperatures may sometimes exceed 1500 °C, which enhances unintentional atomic impurity incorporation.

The ability of SiC to effectively realize its performance potential has been limited by material quality, difficulty in processing, contact metallization, the lack of a suitable acceptor dopant implantation process, and especially by large concentrations of device degrading deep level defects of unknown origin. This final area has been the focus of this dissertation. Previous efforts in these areas have been very limited, and have only

recently been initiated or accomplished. Therefore, valuable feedback to growers and device manufacturers, as to the nature of the electrically active defects in this material, has not been forthcoming. This research represents one of the initial efforts to begin to identify and catalog the deep level defects present in SiC. The ultimate goal of this and other studies in this area will be to ascertain both the mechanisms of trapping and emission kinetics as related to device performance, and the physico-chemical nature or sources of the defects in this material.

The following chapters describe the crystallographic peculiarities and specifics of the SiC crystal structure, defect physics, experimental procedures, and summarize the highlights of the investigation which was undertaken.

II. Silicon Carbide

II-I. Material Properties

II-I-1. History. SiC was one of the earliest semiconductors to be discovered, and because of its large cohesive energy, was initially mistaken as an element. Although rarely found to occur in nature, except in trace amounts discovered in meteorite fragments, volcanic residue, and in some diamond pipes, SiC is easily constituted in high temperature environments such as coal furnaces. Silicon carbide had been observed in laboratory experiments by a number of investigators between 1824 and 1881 [Knippenberg, 1963:161]. The technical importance of this hard stable compound for grinding and cutting purposes, was not appreciated until the last decade of the 19th century when the observation that SiC could scratch ruby was made. Hardness analysis placed SiC at 9 on the Mohs scale between diamond (10) and topaz (8). The compound also has a large resistance to wear, and has the figure 9.15 when diamond is taken as 10.0 and corundum (Al_2O_3) as 9.0. Laboratory preparation of SiC in quantity was first accomplished by Acheson while attempting to crystallize carbon by dissolving it in aluminum silicate ($Al_2O_3SiO_2$) under the influence of an electric arc [Acheson, 1893:179]. As a result, the large scale production and use of this compound for industrial purposes, using the Acheson process, began in earnest. The long narrow (0.1 cm) bundles of SiC crystallites appearing at the end of the Acheson process were crushed into powder for practical applications. Optical and x-ray crystallographic investigation of the Acheson SiC crystals identified the presence of several different crystal modifications to

be occurring simultaneously [Hull, 1919:292], [Ott, 1926:515]. Among these modifications, one type (hexagonal) was found to be dominant.

II-I-2. Polymorphism. The ability of the same chemical compound to exist in more than one crystalline form has been given the name polymorphism. The development of thermodynamics in the nineteenth century led to the identification of polymorphic substances as different phases of the same compound. Phase theory explained the occurrence of different polymorphic modifications in terms of their relative thermodynamic stabilities. The modification with the least Gibbs free energy being the most stable under given conditions of temperature and pressure. It was soon discovered that the majority of substances which are not polymorphic at ordinary pressures undergo polymorphic transitions under high pressures, and it was realized that this was a far more general phenomenon than was originally believed.

Just as a substance can exist in the solid, liquid, or gaseous state, depending upon the temperature and pressure, so also a solid formed from solution, melt, or vapor phase can crystallize in more than one form depending upon the conditions of state at the time of condensation. Calcium carbonate ($CaCO_3$), silica (SiO_2), and tin (Sn) are common examples of solids which form different crystal structures when precipitated under various conditions of temperature and pressure. $CaCO_3$ will form orthorhombic biaxial crystals with a density of 2.94 gm/cm^3 if formation occurs below 30 ^oC, otherwise a uniaxial rhombohedral structure with a density of 2.71 gm/cm^3 is formed. Similarly, silica and tin can both exist in three structural modifications, and of course, the best known polymorphic substance, carbon, exists in the cubic and hexagonal modifications.

Since two polymorphic substances constitute two homogeneous phases, which can establish equilibrium with each other, they must conform to the Gibbs phase rule defining the degrees of freedom of the system, which is given as

$$F = C - P + 2, \qquad \text{[II-1]}$$

where F is the degrees of freedom, C is the number of components, and P is the number of phases in the system. The transition of one polymorphic modification to another is identified with C = 1 and P = 2 so that the system has 1 degree of freedom. This means that if the pressure is kept constant then the transition must occur at a definite temperature, usually called the transition point. The converse must also be true. Additionally, there can never be more than three phases in equilibrium at the same time, since F cannot be negative. Observations and experiment have indeed shown that polymorphic transitions obey the Gibbs phase rule, and are a close analogy of the transition to the liquid phase from the solid phase, the systems in both cases possessing one degree of freedom.

There is only one essential difference between the two analogous phase-transition phenomena described above. In the case of polymorphic transitions, the change is much slower than in the solid to liquid transformation. This is due to the fact that rearrangement of atoms in a solid is a significantly slower process, and the rate at which it occurs depends upon the atomic structural bonds that have to be disrupted and rearranged in the process. The result is that it is possible to superheat a polymorph without any transition taking place, while it is almost impossible to superheat a solid above its melting point at a constant pressure. Therefore, there is a structural aspect to polymorphism

which differentiates it from analogous changes of state. This fact is borne out by the presence of many metastable crystal structures, which may be present over the same temperature ranges, and in fact may also be present in the same sample along with the stable phase. The most common example being the metastable diamond phase of carbon, which does not by itself undergo a transition to the stable graphite modification, and occurs in nature as a mineral. This phenomenon cannot be explained by thermodynamic considerations alone, and requires a knowledge of the energy barrier opposing these transitions, *i.e.,* the structural atomic bonding aspects. These scientific developments were only able to occur after the development of x-ray diffraction techniques by von Laue [Verma and Krishna, 1966:33-58] and the subsequent knowledge gained about atomic groupings in crystals.

In the structural bonding aspect of polymorphic theory, groups of atomic clusters are viewed as coupled oscillators in which the propagation of heat is resolved into the vibrations of the individual clusters. The appearance of a polymorph is related by two complimentary physical conditions. First, the thermodynamic condition of realizing a stable configuration is related to minimization of the Gibbs free energy given by

$$G = E - TS + PV, \qquad \text{[II-2]}$$

where E is the internal energy of the system, S is the entropy, T, P, and V are the temperature, pressure, and volume variables of state. Secondly, the excited vibrational modes of the oscillating atomic clusters, dictated by the environmental symmetry, must maximize the kinetic capacity. In effect, this is tantamount to reducing the free energy through an increase in the entropy, S, by maximizing the thermal disorder in the solid.

The conditions of structural change resulting in the transition between polymorphic states is as follows. At absolute zero, the structure which has the lowest configuration energy is the most stable. At slightly higher temperatures, the symmetry of the thermal vibrations is consistent with the stable form, so it persists. As the temperature is further increased, the amplitude of the oscillations increases, producing increasingly strained bonds. These vibrational amplitudes will continue to increase with temperature, resulting in an increasing vapor pressure until the solid melts. If, however, there exists an alternative arrangement of atoms in which a higher energy mode of thermal vibrations is allowed ***and*** the bond strain is reduced, the transformation to this new structure will tend to occur.

The rate at which these polymorphic transitions proceed depends upon the mobility of the atoms in the crystal, which is related to the nature of the chemical bonding, that in turn determines the activation energy of the process. If the activation energy of the transformation process is low enough, and the energy barrier to the transformation large enough, the associated rate can be negligible.

II-I-3. SiC Crystal Anomalies and Polytypism. Since 1912, SiC has been known to exist in a large number of polymorphic crystal structures. It was however, found that none of the numerous observed polymorphs appeared to be related through a structural modifying transition. This was found to be true over the entire temperature range at which the solid phase occurs ($T < 2600$ °C). One of the few exceptions of any technical importance is associated with the cubic, zinc-blende modification. This crystal is thought by some to be a low temperature ($T < 2000$ °C) metastable phase of the hexagonal structure, which does transform above the transition point [Harris, 1995:9].

However, others have presented data which indicates that the cubic form is metastable over the entire temperature range of solid composition [Knippenberg and Verspui, 1966:113].

Extensive crystallographic investigations led to the discovery that SiC exhibited a special kind of one dimensional polymorphism called polytypism [Ott, 1926:515]. Subsequently, other compounds were found to possess this 1-D structural characteristic, such as ZnS and CdI_2. Polytypism is defined as the propensity of a substance to crystallize into a number of different modifications in which two dimensions of the unit cell are equivalent but which differ in a third variable dimension. Thus, polytypic crystal structures are built from identical layers of atomic structure, and differ only in the manner in which these layers are stacked. A consequence of this atomic arrangement is that all polytypes of a given substance have unit cell dimensions which are constant in two directions, and vary only in the direction normal to the identical layers. The magnitude of this third unit cell dimension is obviously an integral multiple of the spacing between successive layers, and depends simply upon the number of layers in the structure. Different stacking sequences of the identical 2-D layers can actually result in different lattice types and space groups. Polytypism can occur only in structures for which any specific lattice atom's first coordination can be satisfied in more than one way, usually cubic versus hexagonal close packing. As a result, the first nearest-neighbor relationships are the same in all polytypes of a substance, and differ only in the second and higher order coordinations. As a result of the close similarities in atomic arrangement, all polytypes have nearly the same potential energies, and differ very little in their physical properties.

It is this similarity in configuration energies which identifies polytypism as a very special kind of polymorphism. It allows the formation of many modifications under identical conditions of temperature and pressure, often existing in coalescence. If we consider that SiC is formed at temperatures greater than 2000 °C, and that the internal energies and densities are very similar, then the primary mechanism by which the free energy may be minimized is through the entropy, S (Equation II-2). We would therefore expect that a completely disordered arrangement of layers would result in the configuration of minimum free energy. But this is not observed, and so the appearance of ordered polytypes appears anomalous. As such, polytypism is very different than the polymorphism usually encountered. Jagodzinski [1954:49] pointed out that minimum free energy does not necessarily imply maximum disorder. This is true because the entropy of the system actually consists of two components, the configurational and vibrational entropys. While the configurational entropy will increase with disorder, the vibrational entropy will decrease. The vibrational entropy will favor ordered states since this will maximize the number of frequency distributions within a given energy interval, *i.e.*, larger vibrational entropy. Jagodzinski elegantly showed that there will exist two peaks in the total entropy curves corresponding to the dominance of each term over differing conditions of disorder. He further showed that the absolute value of the total entropy peak corresponding to the completely ordered condition exceeded the second order peak dominated by the configurational term. He showed that for short period polytypes, formation is governed by potential energy considerations, and as the stacking

order becomes larger (internal energy differences become negligible), the vibrational entropy becomes the dominant mechanism determining structural formation.

As the first substance identified as being polytypic, SiC has probably been the most widely investigated. It provides an excellent example of polytypism in that it has been identified in over 170 different modifications with stacking periods of up to 594 layers. The most commonly occurring polytype is the six layer stacked hexagonal structure denoted 6H-SiC. In fact, all structures are hexagonal or rhombohedral, with the lone cubic (3C-SiC) exception, and have unit cell heights ranging from 5 Å to 1500 Å.

The crystalline structure of all SiC polytypes consists of a close packing of Si and C atomic double layers in which each successive layer occupies one of two voids not occupied by the preceding layer atoms. In this arrangement, each atom is tetrahedrally bonded to four atoms of the opposite type, and has twelve second-nearest neighbors of the same type. The differences between SiC polytypes can be observed only in third or higher nearest neighbor arrangements. It is the ordered stacking of identical Si-C double layers that identifies each polytype, and results in a lattice that consists of two monoatomic (Si or C) interpenetrating close packings, with one displaced relative to the other along the c-axis (hexagonal) or the <111> direction (cubic). Thus, the Si and C layers are stacked alternately, each layer occupying the tetrahedral voids of the close packed layer on either side of it. Figure II-1 illustrates this atomic arrangement with the close packed position designators labeled as A, B, and C. In Figure II-1 (a) we see the spherical approximation to the close- packed arrangement of atoms in a solid, illustrating the atomic positions including the unoccupied voids of Layer 1. In part (b) of the figure,

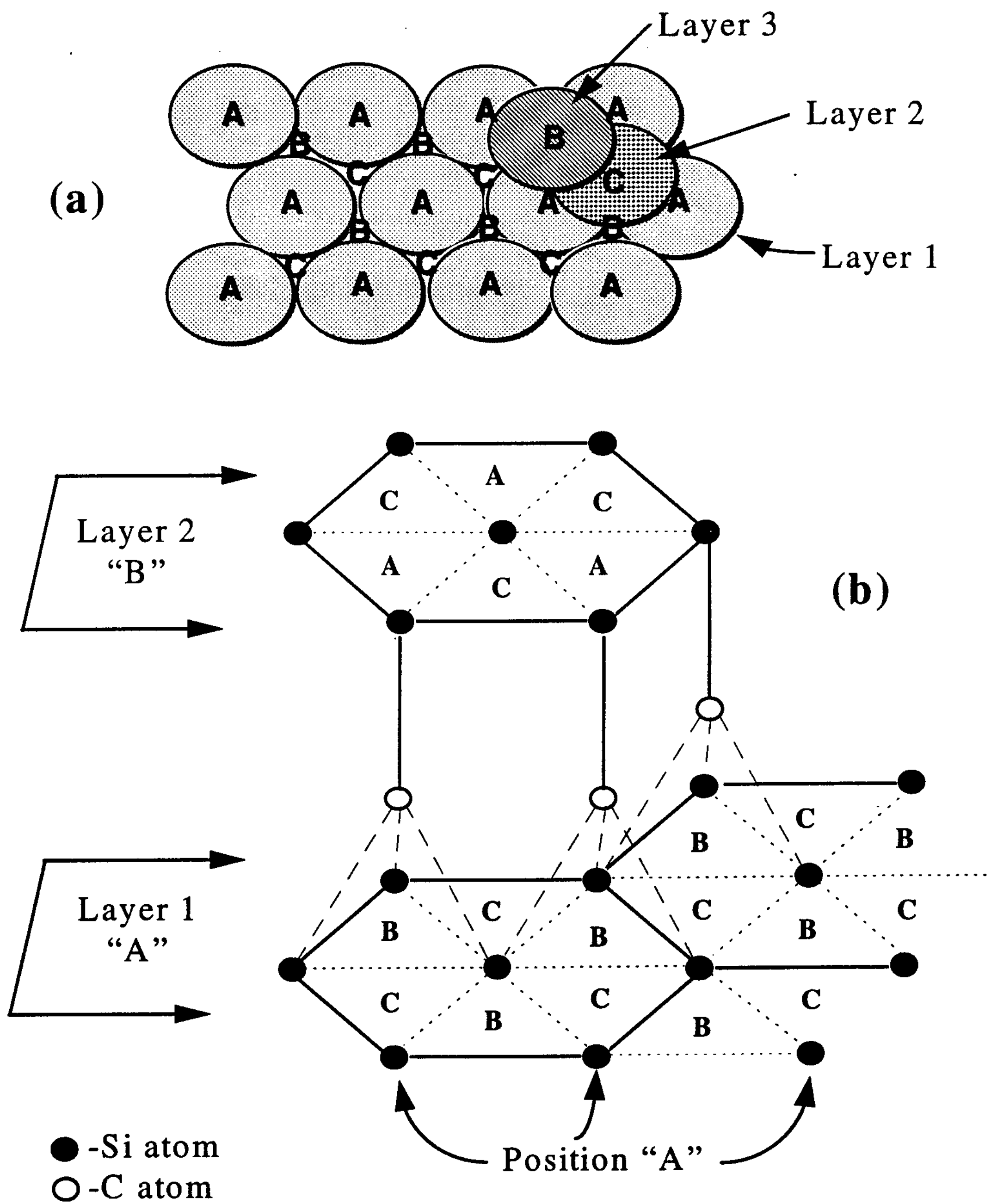

Figure II-1. (a) spherical representation of the close packing of atomic layers. (b) illustration of the Si and C site occupation positions of an arbitrary SiC polytype. The structure is arbitrary since a minimum of one additional layer is required to define the crystal. If the repeating pattern were "AB" then the wurtzite structure would result.

for the yet undefined arbitrary polytype, we see that Layer 1 is arranged so that the Si atoms occupy the "A" positions, and the carbon atoms occupy the "B" voids. As a result, the second layer Si atoms are forced to occupy the "B" positions dictated both by the tetrahedral bonding scheme and the "B" position of the carbon-atoms in Layer 1 to which they are bonded. The Layer 2 carbon atoms (not shown) can occupy either the "C" voids or the "A" voids. Stacking will continue in this manner until a periodicity is established which characterizes a specific polytype. As previously mentioned, this may require up to several hundred layers to accomplish the required repeating pattern. The repeating sequences associated with the most electronically relevant polytypes are ABC for 3C, ABCB and ABCACB for the hexagonal structures 4H and 6H, respectively. The spacing between the C and Si atoms in the same bi-layer is 1.89 Å, which is one quarter of the distance between successive Si-C layers. The bonding of SiC tetrahedra is approximately 88% covalent as estimated from their differences in electronegativity, with Si behaving as the cation species. This estimate has been confirmed using infrared reflectivity and X-ray emission spectral data [Knippenberg, 1963:168].

II-I-4. Crystallographic Notation. Several notational systems have been developed to identify the various polytypes. The ABC notation used above and in Figure II-1 is seen to be related to the atomic placement in the tetrahedral voids of the preceding layers, and was the first nomenclature developed. It becomes extremely cumbersome as the stacking order increases, and thus has been subordinated by various other systems of identification. The same is true of the Jagodzinski notation which takes advantage of the fact that all atomic sites in close packings have either cubic (k) or hexagonal (h) point

symmetry, and thus the A,B, or C layer symbols are replaced by h or k. The Ramsdell notation [Ramsdell, 1947:64] has become the most widely used system, and has been alluded to already in this dissertation. In this system, each polytype is given a representation based upon the number of layers in the stacking sequence and the symmetry of the space group characterizing the crystal. Thus, for the wurtzite structure which is purely hexagonal with a two layer repeat sequence AB, the Ramsdell notation associates with this polytype the symbol 2H. We now see that 3C is the cubic modification with a three layer stacking sequence ABC, 6H is the hexagonal structure previously designated as ABCACB, and 594R is a rhombohedral structure with the largest observed stacking order. An elegant method of geometrically representing the various polytypes was also developed by Ramsdell [1947:64], and is illustrated in Figure II-2. This system beautifully incorporates all of the information contained in the other notations, including the ABC and h,k sequential symbolism, along with an easy identification of the crystal space group symmetry. As with other notational devices, this approach can be seen to be limited to structures with low stacking orders.

II-I-5. Electrical and Optical Properties of Semiconducting SiC. Some of the electronic advantages afforded by SiC for high temperature and high power device applications have been described in the previous chapter. The bandgap of all SiC polytypes is characterized by phonon-assisted, indirect, electronic transitions. The magnitude of the energy characterizing the forbidden gap in SiC varies with polytype from approximately 2.3 to 3.3 eV. TABLE II-1 lists these magnitudes for several polytypes as determined by optical absorption methods [Verma and Krishna, 1966:101].

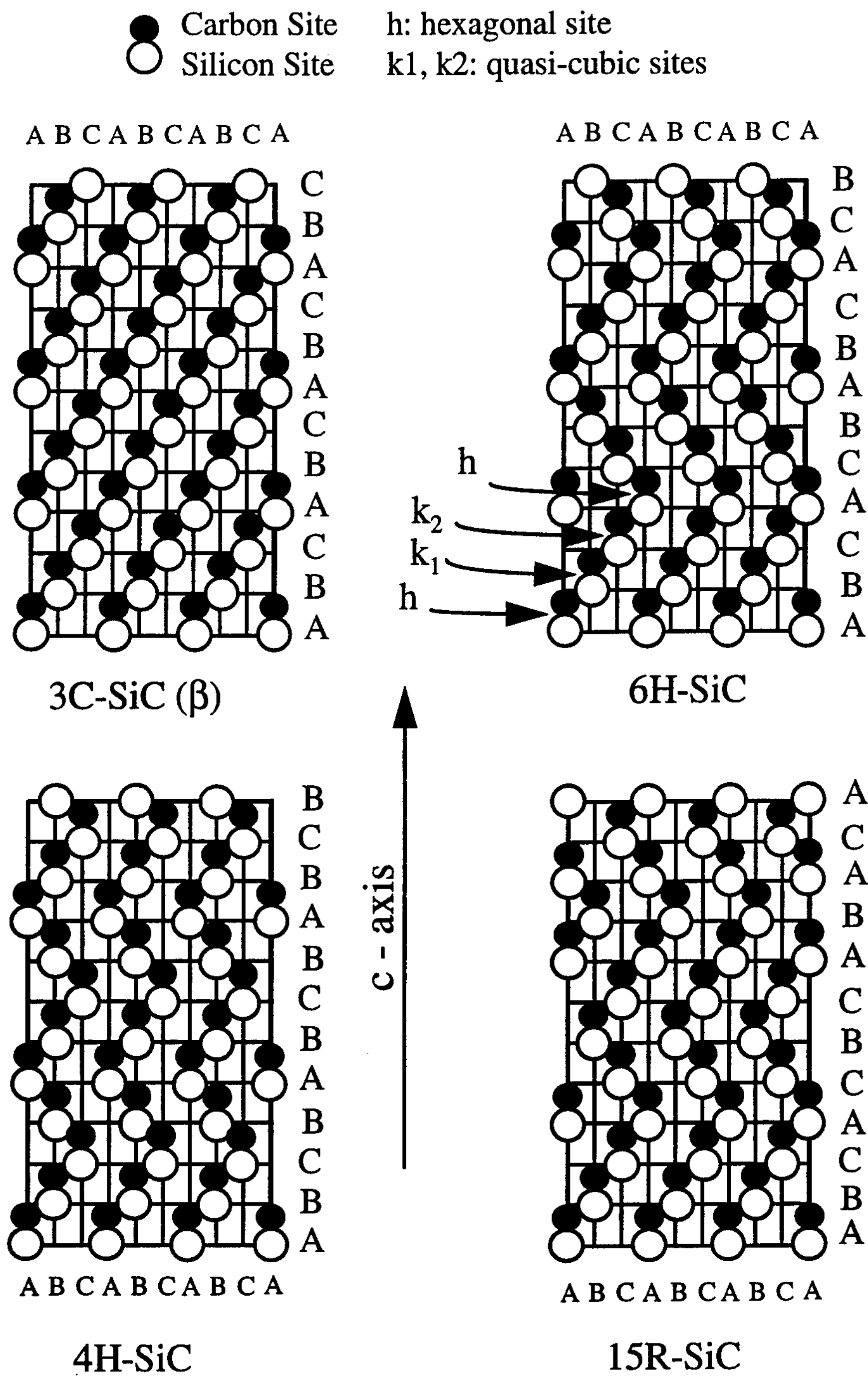

Figure II-2. Graphical representation of the Ramsdell zigzag notation of four SiC polytypes. Included are indications of the hexagonal and cubic symmetry lattice points and the ABC notational stacking sequence representations.

A unique manifestation of the polytypic nature of SiC crystals is related to the symmetry of the various lattice sites in the crystal. As previously mentioned, the close packing of atoms in the various tetrahedral and octahedral voids results in a cubic or hexagonal arrangement. In order to facilitate long range stacking sequences for crystals of orders greater than three, there must exist an intermixing of both cubic and hexagonal lattice site occupation. This is the basis for the Jagodzinski h-k notation, and is illustrated in TABLE II-1. The arrangement of first nearest-neighbors for any lattice point is the same for all polytypes, and higher order coordinations must be considered to realize differences in the local environment. If the second order coordination is considered, we obtain the hexagonal and cubic type points previously discussed. Now as the stacking order increases beyond three, the varied arrangement of stacked layers creates an environment in which the local environment, between multiple hexagonal or cubic lattice sites in the same crystal, can also be shown to be inequivalent. Thus, in the Jagodzinski nomenclature, the h-k symbols do not correspond to the individual layers but rather to unique lattice sites in the crystal. So the hkk symbol used to denote the 6H-SiC polytype

TABLE II-1. Energy gap for several SiC polytypes including "hexagonal" fraction

Polytype	h,k notation	Excitonic gap (eV)	% hexagonal
3C	k	2.39	0
2H	h	3.3	100
6H	hkk	3.023	33
4H	hk	3.263	50
24R	hkkkkhkk	2.72	25
8H	hkkk	2.8	25
21R	hkkhkkk	2.86	29
15R	hkhkk	2.986	40
33R	hkkhkkhkkhk	3.01	36

designates the existence of one unique hexagonal site and two distinct cubic atom locations. Similarly, from TABLE II-1, 15R-SiC is seen to be characterized by two symmetrically inequivalent hexagonal and three different cubic sites in a 15 layer structure. In addition to being a necessary crystallographic peculiarity for polytypic substances with long stacking orders, these inequivalent lattice sites manifest themselves in the electronic and optical activity of the SiC semiconductors. The feature by which we are able to observe the effects of site inequivalencies is related to the behavior of substitutional impurity atoms. If we consider a concentration of foreign atoms, which are introduced into the SiC lattice during growth, by diffusion, or energetic implantation of ionized species, we can assume to a first approximation that these impurities will randomly occupy the various SiC lattice sites. We say approximately because this requires the assumption that the free energies are equal for substutional occupation at the various hexagonal and cubic sites in the lattice. The ratio of impurities located at the various inequivalent sites will therefore conform to the physical abundance of these sites in the crystal.

The 2H-SiC polytype has the hexagonal crystal structure, and the point group of this crystal is C_{6V}. However, the point group of a substitutional impurity is of a lower symmetry, C_{3V}. The Brillouin zone of this structure is also hexagonal, and is shown in Figure II-3 with a number of points of high symmetry indicated and labeled in the conventional manner. The polytypes of interest to this dissertation, 6H and 4H, also have hexagonal symmetry, and possess the same crystal space group, C_{6V}. However as previously discussed, the key difference lies in the long unit cell, resulting from the

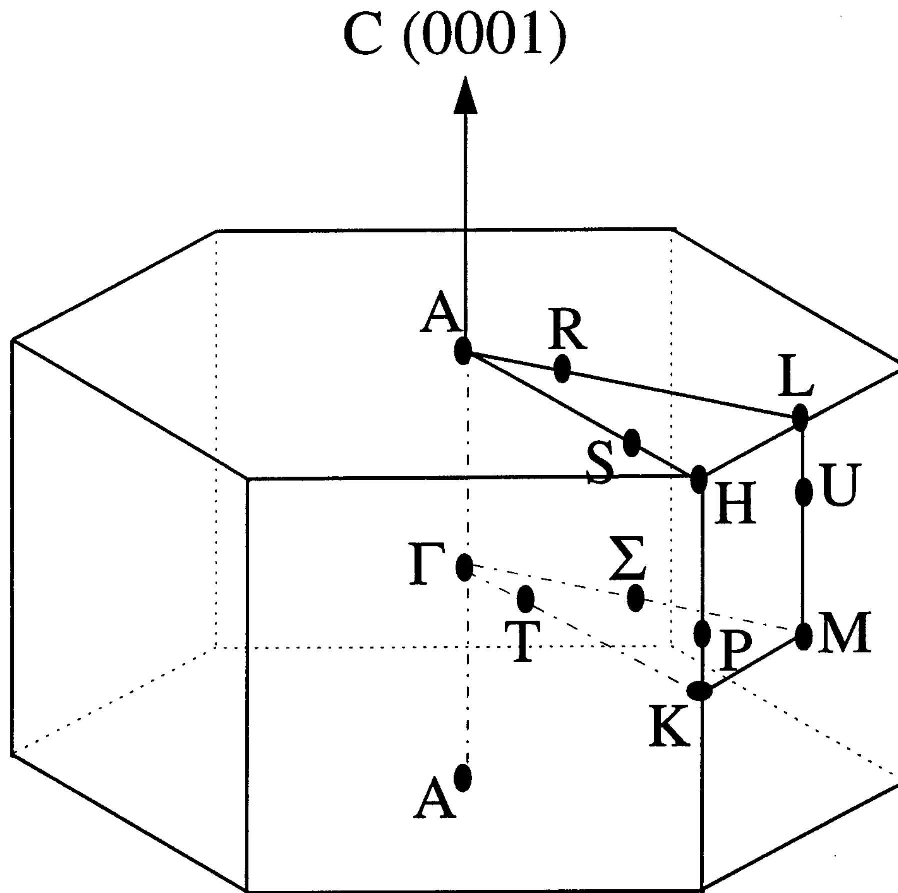

Figure II-3. Brillouin zone of a crystal with the wurtzite structure. Illustrated are some of the points of high symmetry. A point not at an intersection of two or more lines is meant to represent a general point along the line. C_{6V} is associated with Γ, and C_{3V} with the point labeled H.

stacking order requiring 4 and 6 layers to complete the 4H and 6H unit cells, respectively.

Wurtzite (2H) SiC is characterized by planes of identical layers, which stack in a manner such that the local symmetry of all lattice points is C_{3V}. As a result, the Hamiltonian characterizing a substitutional donor atom will be the same for every lattice point. In the cases where the substutional site symmetry varies between lattice points, there will necessarily exist a distinct Hamiltonian characterizing each unique location due to the slightly differing potential at the various lattice locations. The result is the

realization of differing eigenvalues (energies) and eigenvectors associated with the bound state wavefunctions at the impurity atom. These will in turn lead to ionization energies associated with the transitions between bonding and anti-bonding states which will differ between the various sites in a crystal.

The ionization energy differences attributed to these inequivalent lattice sites have been observed in both electrical and optical measurements on numerous SiC polytypes. In every case, the number of detected levels was found to correspond to the predicted number of inequivalent sites for the specific polytype. The connection to inequivalent lattice sites was first made by Choyke and Patrick [1962:1878], [1962:1868] in attempting to explain anomalous radiative transitions in their low temperature (4K) photoluminescence (PL) data from 6H-SiC. They observed three zero-phonon transitions (ZPL) which they attributed to recombination of excitons bound to unionized nitrogen donor impurities. After analysis of the temperature dependence, relative intensities, and associated phonon replicated spectrum, they assigned the three ZPL transitions to substutional nitrogen occupying the single hexagonal and two cubic inequivalent lattice sites in the 6H polytype.

It should be noted that the magnitude of the acceptor ionization energy splitting is not as great as that for the donor sites. This has been reported to be due to the sphericity and $\Gamma=0$ location of the valence band maxima, which translates simply to a dependence of the inequivalent site ionization potentials on the local dielectric constant [Hagen *et al.*, 1973:18]. The greater donor ionization energy differences may be attributed to the number of equivalent conduction band minima, 6, which have differing effective masses

[Pensl and Choyke 1993:264]. This conclusion is supported by the fact that mobility and effective mass in 6H-SiC have been shown to be very directionally dependent in **k**-space. However, the 4H polytype is characterized by 6 conduction band minima but very isotropic mobility and effective mass characteristics, nevertheless it possesses a significant donor ionization energy difference (50 meV).

SiC has been shown to possess several unique properties, stemming from its large cohesive energy; large bandgap, radiation resistance, thermal stability, physical hardness, and resistance to chemical attack. These along with its closely related superior electronic device properties position SiC to emerge as the next generation semiconducting material to satisfy existing deficiencies in the high temperature, high power, and high frequency markets. However, this can occur only after a thorough understanding of the device related electronic transport and performance degradation mechanisms are achieved. Attainment of this knowledge is complicated by the existence of multiple impurity ionization or energy levels arising from the presence of inequivalent atomic planes in the 1-D polytypic stacking order of SiC. Site inequivalencies coupled with non-ideal intentional doping levels, having larger than desired energy levels, complicate the analysis of device behavior in ways which are many times specific to a particular function. For example dynamic switching failures of large current and/or bias levels in p/n rectifiers have been tentatively attributed to the incomplete donor and acceptor ionization condition at temperatures as high as 500 K [Neudeck and Fazi, 1996].

III. Defect Induced Bandgap States

III-I. Impurities and Deep Level Defects

Since Bloch's discovery that it was deviations from periodic perfection in a crystal which scattered or perturbed the quasi-free plane wave states describing electronic motion, significant effort has been expended to explain and understand the electronic implications of crystalline flaws. The majority of research has been focused on the explanation of phenomena associated with foreign atoms substitutionally occupying lattice sites in a semiconductor crystal. Because unlike a metal, the physical properties of semiconductors can be radically changed by introducing small concentrations of foreign atoms, these impurities are technologically significant. Most studies have emphasized those atomic species which generate discrete energy levels in the semiconductor bandgap, close to a band of allowed states either of greater (CB) or lesser (VB) energy. These shallow energy impurity centers are technologically important because of the small thermal energy (kT) required to cause electron exchange between impurity-ion bound orbits and the nearest band of allowed energies. In this manner, the conductivity of a semiconductor can be increased over a 10^7 Ω^{-1} range by "doping" it with up to 10^{17} cm^{-3} of a suitable foreign atom that generates these shallow energy levels. Thus, conductivity level and type can be precisely controlled enabling electronic device functionality. It should be noted that impurity substitution of this magnitude does not affect the bandgap or other intrinsic material properties.

III-I-1. SiC Shallow Level Impurities. Due to its slightly polar (12% ionic) character, very nonspherical CB minima, and large measured donor ionization energies, SiC was a doubtful candidate for an application of the effective mass approximation. However, Suttrop *et al.* [1992:129] and Gotz *et al.* [1992:3332] showed that in spite of these deviations, the *excited state* donor levels in 6H- and 4H-SiC, respectively, are well described by an effective mass approximation provided the anisotropy of the effective mass is included. The ground state (1s) energy was found to deviate significantly from the hydrogenic approximation (40 meV), and in fact is split into two levels due to strong coupling between states in the six indirect conduction band minima. This valley-orbit-splitting of the hydrogenic ground state is common for multi-valley semiconductors [Colwell and Klein, 1972:498], and occurs even in Si [Dean *et al.*, 1969:837] although with much smaller magnitudes. Figure III-1 illustrates the infrared (IR) absorption transitions leading to the model for nitrogen donors in 6H-SiC as determined by Suttrop *et al.* [1992:129]. In both 6H- and 4H-SiC, the hexagonal site ground state valley-orbit-splitting was observed and measured to be 13.0 and 7.6 meV, respectively, from temperature dependent IR absorption analysis. This IR absorption characterization of the split ground state is enabled by the fact that the 1s(E) ground state level is empty during the low temperature (7 K) measurement, and is only populated as the temperature increases to 80 K. Cubic site 1s splitting was not observed during the 6H-SiC IR study due to their 60 and 62 meV magnitude which precludes thermal population at 80 K. The arrows shown from the ground states to the dashed lines in Figure III-1 are additional IR absorption transitions observed only when the electric field was polarized parallel to the

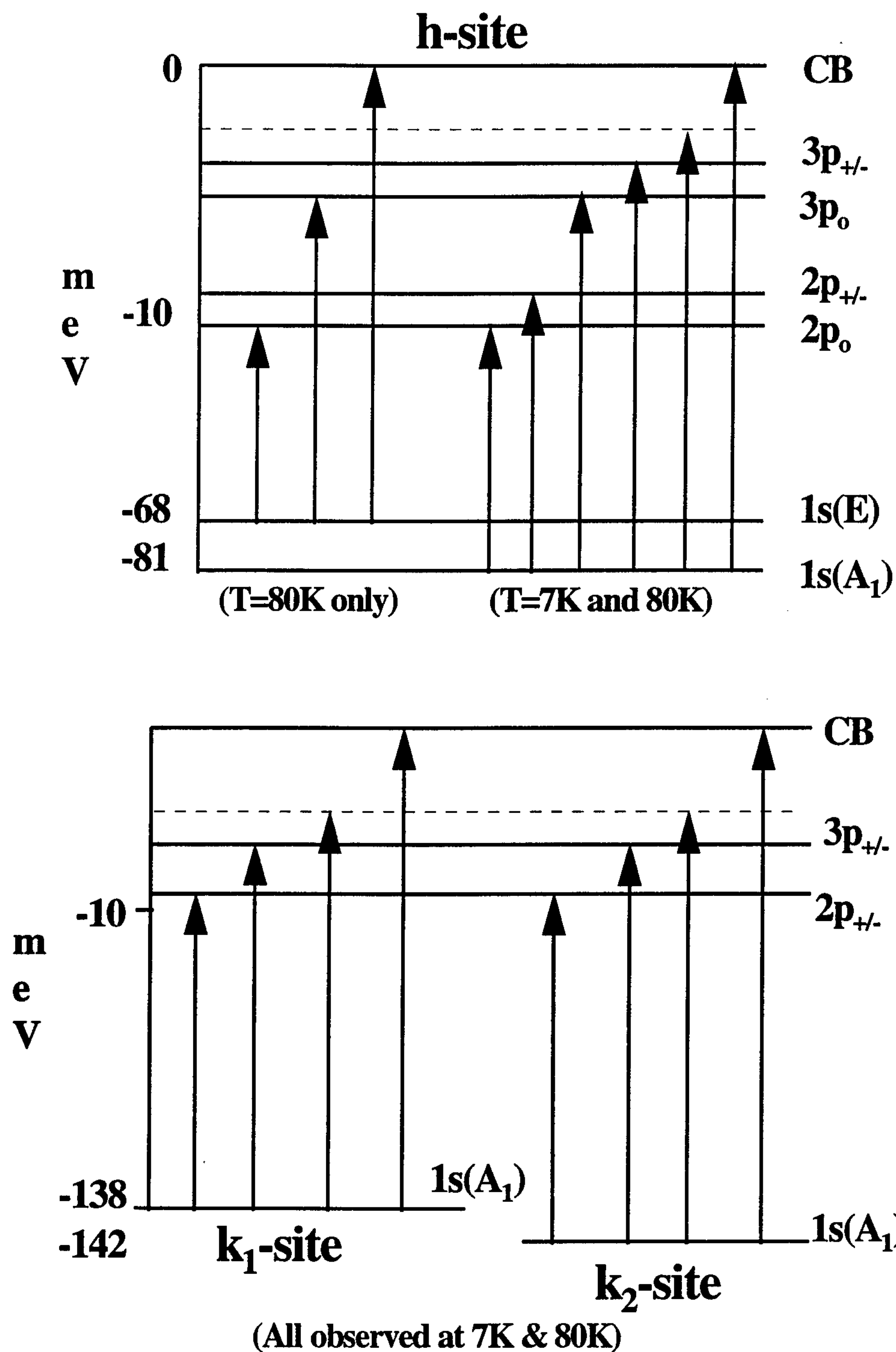

Figure III-1. 6H-SiC nitrogen donor model of Suttrop *et al.* which was concluded from analysis of observed IR absorption transitions shown by the arrows. The 13 meV valley-orbit splitting of the 1s ground state was observed only for the hexagonal sites due to their large (60 and 63 meV) magnitude for cubic (k_1, k_2) sites precluding population at 80 K.

c-axis, and was unexplained by the authors. The subscripted p-state indicators in the figure designate the three p-orbitals arising from the $\ell = 1$ angular momentum projection quantum number ($m = 0, \pm \frac{1}{2}$). Analogous results were obtained from an IR absorption study on the 4H-SiC polytype for the hexagonal and single cubic lattice site, [Gotz *et al.*, 1992:3332].

III-I-2. Unintentional Impurities and Deep Levels. No less important but analytically less tractable is the consideration of lattice deviations resulting from structural flaws, interstitial atoms, and complexes involving various combinations of impurity and structural defects in either a localized or extended geometry. Of particular interest is impurities or defects that produce bound states in the forbidden gap of a semiconductor, which lie at a considerable distance from either band of allowed states called deep levels. Deep states may be generally classified as those that are energetically positioned a greater distance from the resonant band than the hydrogenic shallow states. This definition includes acceptor levels which are located close to the conduction band and donor levels positioned near the valence band. Clarification of this last point will become important when we discuss the capture and emission kinetics of deep level traps in subsequent sections and chapters. The large ionization energy of these states implies a strong potential, which acts to localize the bound carrier wavefunction near the defect site. This localization is in contrast to the diffuse nature of the shallow level states in which the binding energy is screened by the square of the semiconductor dielectric constant, ε_r. If we restrict our considerations to substitutional atomic impurities, there are two primary consequences of wavefunction localization near the defect site. First, the

validity of the hydrogenic, effective mass theory becomes tenuous and strongly dependent upon the ionization energy magnitude of the ground state and the charge state of the impurity center when occupied. This consequence, along with a description of techniques used to overcome this difficulty, will be discussed in the balance of this section. The second consequence, which relates to the effect of particle localization on electronic transport and recombination will be the subject of a later section in this chapter.

If we consider that the radius of the ground state wavefunction scales with the depth of the impurity level, then there will be a range of defect energies over which a modified hydrogenic model may be valid. This range of energy will define a critical orbital radius, r_c, beyond which a hydrogenic treatment may be appropriate. Theoretical treatments of deep level wavefunctions have proceeded along these lines by computing the critical radius that defines the range over which the potential may be replaced by its asymptotic Coulombic form [Milnes, 1973:Ch. 1]. These calculations showed that r_c roughly equal to the nearest neighbor distance defines the boundary between the inner core and outer Coulombic regions. The problem then becomes one of determining a quantum-defect ground state wavefunction appropriate for the core region, where the ion cannot be represented by a point charge. Bound state wavefunctions describing all space are then calculated by requiring continuity between the solutions for the two regions delineated by the critical radius. Prediction of deep level impurity ionization energies in this manner has met with very limited success, and are typically limited to relatively shallow impurities [Tansley and Egan, 1992:10942]. On the other hand, several approaches involving semiempirical solutions have been developed. In the most widely

used approximation, it is initially assumed that the potential is Coulombic over all space. The influence of the core potential is then accounted for by scaling the calculated wavefunctions by adjusting the effective Bohr radius, a*, using the experimentally determined energy and the expression $E_{obs} = -(\hbar^2/2m^*)(1/a^*)^2$ [Milnes, 1973:Ch 6]. This procedure has been partially successful for shallow to intermediate level defects but is physically objectionable due to the required scaling of parameters formally determined by the host lattice. All of these considerations have been forwarded in response to the condition of electrically attractive bound carriers and oppositely charged ion cores. There are, however, situations in which the defect core will be neutral when unoccupied. These so-called isoelectronic defects are still capable of generating bound states in the semiconductor bandgap, resulting from differences in electronegativity and size from the host atom thus creating deviations from perfect periodicity. Nitrogen occupying a P lattice site substitutionally (N_P) in GaP and Ti_{Si} in SiC are examples of deep level defects formed when impurity atoms possessing the same valency of the host lattice are introduced. In these cases, the binding potential may be generated as a result of mechanical deformations to the perfect crystal periodicity. For example, the normally repulsive Coulomb force between a free electron and the outer impurity electrons can be screened by the perturbed ion cores on nearest neighbor sites resulting in an attractive potential that is electrically neutral. In these cases, the approximation to a hydrogenic point charge can become extremely questionable.

As bound state wavefunctions become more localized in real space, a delocalization in momentum or **k**-space occurs. This is because a larger number of

Fourier components are required to describe the smaller orbit ($\psi(\mathbf{r}) \propto \Sigma e^{i\mathbf{k}\bullet\mathbf{r}}$). Since the heart of the effective mass approximation is that the bound state wavefunctions can be constructed from a small number of Bloch functions in a narrow region of **k**-space, the theory breaks down completely as the energy level increases. In these cases, the energies and wavefunctions associated with deep levels have been calculated using techniques similar to band structure calculations. These calculations have typically employed a modified semi-empirical tight-binding theory. In the tight-binding method, a Green's function technique is utilized to obtain the form of the impurity defect potential [Talwar and Feng, 1991:3191]. In this theory, it is assumed that in the vicinity of the lattice point, the full periodic crystal Hamiltonian ($\mathcal{H}$) can be approximated by the Hamiltonian of a single atom (H_{at}) located at that lattice point. It is also assumed that the bound states of the atomic Hamiltonian are well localized. Thus if ψ_n is a bound level of H_{at} for an atom, then it is required that $\psi_n(\mathbf{r})$ be negligible when $|\mathbf{r}|$ exceeds a distance of the order of a lattice spacing (the range of $\psi_n(\mathbf{r})$). The basic premise then, is that the wavefunction $\psi_n(\mathbf{r})$ will be an excellent approximation to a stationary state wavefunction for the full Hamiltonian in cases where $\mathcal{H}$ deviates from the atomic Hamiltonian only at distances from $|\mathbf{r}| = 0$ exceeding the range of $\psi_n(\mathbf{r})$. In this manner, the bound state wavefunctions in the crystal are expanded using the free atom eigenstates as the basis functions. The eigenvalue solutions to Schrödingers equation are then obtained from

$$\mathcal{H}\psi(\vec{r}) = (H_{at} + \Delta U)\psi(\vec{r}) = E(\vec{k})\psi(\vec{r}) \;, \qquad \text{[III-1]}$$

where ΔU is the correction to the atomic potential required to produce the full crystal periodic potential. If Equation III-1 is multiplied by the atomic wavefunction, and

integrated over all **r** for each atom, n, and state, i, we obtain the matrix elements $<\psi_{ni}|\mathcal{H}|\psi_{mj}>$. In general, the atomic orbitals of different atoms are not orthogonal, thus the matrix representation of $\mathcal{H}$ is not diagonal due to the existence of many non-zero overlap integrals ($<\psi_{ni}|\psi_{mj}>$) between various states and lattice sites. Tight-binding theory ignores these integrals by invoking the assumption of localized bound state atomic wavefunctions. In practice, tight-binding has been mainly used to reproduce known experimental data by adjusting the Hamiltonian matrix elements. This modified matrix is then used to predict other physical properties semiempirically.

Using a semiempirical Koster-Slater model with an orthogonalized tight binding atomic function basis, Hjalmarson has developed an algorithm to predict the major chemical trends of elemental impurities in covalently bonded, zinc-blende semiconductors [Hjalmarson *et al.*, 1980:810]. The Hjalmarson formalism predicts which atomic substitutional impurities are likely to generate A_1-symmetric states with energies deep within the bandgap. A_1 symmetry, sometimes notated Γ_1, is related to the 1-dimensional irreducible representation of the isomorphic tetrahedral or octahedral point groups which denotes the symmetry of a particular orbital (s-like ground states). The Koster-Slater methodology, most commonly used for impurity calculations, involves using a one electron approximation and expanding the wavefunction in a basis set derived from Wannier functions rather than Bloch functions [Koster and Slater, 1954:1167]. The coefficients of this expansion are then shown to be obtained by solving a set of nonlinear difference equations. Hjalmarson assumes that the long range portion of the defect potential is negligible, and only the central cell potential is required to bind a state. This

is done in order to exploit the quasiatomic nature of substitutional point defects in semiconductors. Using only empirical adjustments to the nearest neighbor matrix elements of the host Hamiltonian, Hjalmarson found that the bound state ionization energies are asymptotic to the crystal dangling bond or ideal vacancy energies. Thus, the bound state wavefunctions are predominantly hostlike rather than impurity like, which explains why impurities with energy differences of up to 10 eV produce defect energies differing by only a fraction of an electron volt. It was found that the energy level trends for periodic table groups IIB through VIIA in GaAs, GaP, $GaAs_{1-X}P_X$, and Si were predicted remarkably well using this theory.

The theory of deep level energy trends in semiconductors described above is very successful at predicting only trends for substitutional atomic impurities but is not adequate in its estimates of the absolute ionization energy magnitudes. It has been observed that uncertainties up to a tenth of an eV can result, clearly of experimental significance when attempting to determine the chemical identity of an observed defect [Tansley and Egan, 1992:10944]. These discrepancies are most likely due to the neglected interactions with higher order coordinations, deformations of the lattice due to the physical size of an impurity, and many electron effects arising from the initial single electron assumption. These higher order corrections have been attempted in various modified algorithms and theories, but in each case little success has been realized except in specific idealized cases [Hong *et al.*, 1988:12549], [Myles and Sankey, 1984:6810]. In practice, there are so many factors that contribute to the energy levels of deep level impurities that there is little hope of a unifying theory to accurately predict this

phenomenon. We must therefore rely almost exclusively upon experimental determination of the energetic positions and physico-chemical identification of the technologically important class of crystal flaws which generate deep levels in semiconductors.

Consideration of deep level defects in hexagonal polytypes of SiC is fraught with complications beyond those discussed above for zinc-blende compounds. Complex band structures, the possibility of significantly greater ionization energies (due to the large forbidden gap), and especially the unique condition of multiple lattice site symmetries, manifesting themselves as multiple energy levels for each impurity, create additional complications for theorists. As we have shown above, the hydrogenic effective mass approximation was seen to be valid only for the series of excited states for "shallow" nitrogen donor impurities in 4H- and 6H-SiC. Elements introducing levels with even larger ionization energies are very unlikely to exhibit hydrogenic or effective mass like properties, and will therefore not likely benefit from modified EMA theories. Band structure type calculations, which only consider first coordination interactions, will not yield the effects of lattice site inequivalencies since a minimum consideration of second and third nearest neighbor environments are required to discriminate site differences. Thus, SiC defect wavefunction calculations will be extremely restrictive computationally since they will involve contributions from a much larger number of bands in **k**-space. Single band theories such as Hjalmarson's will not be able to accurately predict deep level activity in these SiC polytypes. The need for thorough, accurate, experimental deep level defect data is thus even more imperative for SiC technology. Knowledge of the

electrical, optical, and mechanical effects of deep impurity levels, and especially their causes or sources, is fundamental to the successful development of a viable device technology based on any material system. This knowledge base is very extensive for the more mature Si, Ge, and GaAs based material systems with up to forty years of effort having been focused in this area. Conversely, the extent of the knowledge regarding deep impurity levels in SiC is severely lacking. Research aimed at improving this situation has only recently begun, and thus is in its infancy. Although little previous work exists from which to build or extend, the foundation is currently being formed upon which the framework of knowledge will be available for crystal growers and device manufacturers to use in order to improve the quality of their SiC material and devices.

III-II. Defect Classification: Traps and Recombination Centers

The numerous descriptions and names which can be associated with deep defect states in semiconductors can be very confusing. These states are referred to as traps, recombination centers, generation centers, deep levels, deep impurities, and so on. These terms often have precise meanings but the situation is complicated by the fact that a defect may be both a trap and a recombination center. Delineation will depend upon the impurity, temperature, and on the doping conditions for intentional shallow donors or acceptors.

In general, a deep level defect is considered to be a trap if the capture rate for one carrier dominates over the rate associated with the other. Figure III-2 (a) illustrates the situation for an electron trap in neutral unbiased material illustrating the greater thermal electron capture rate, c^T_n, by the larger arrow. In Figure III-2 (b) the situation in which the capture rate for electrons and holes are both large is illustrated. This condition satisfies the general definition of a deep level defect acting as a recombination center. Even with the definitions just given, defect classification is still often dependent upon the doping and thermal conditions existing in the semiconductor. For example, in wide

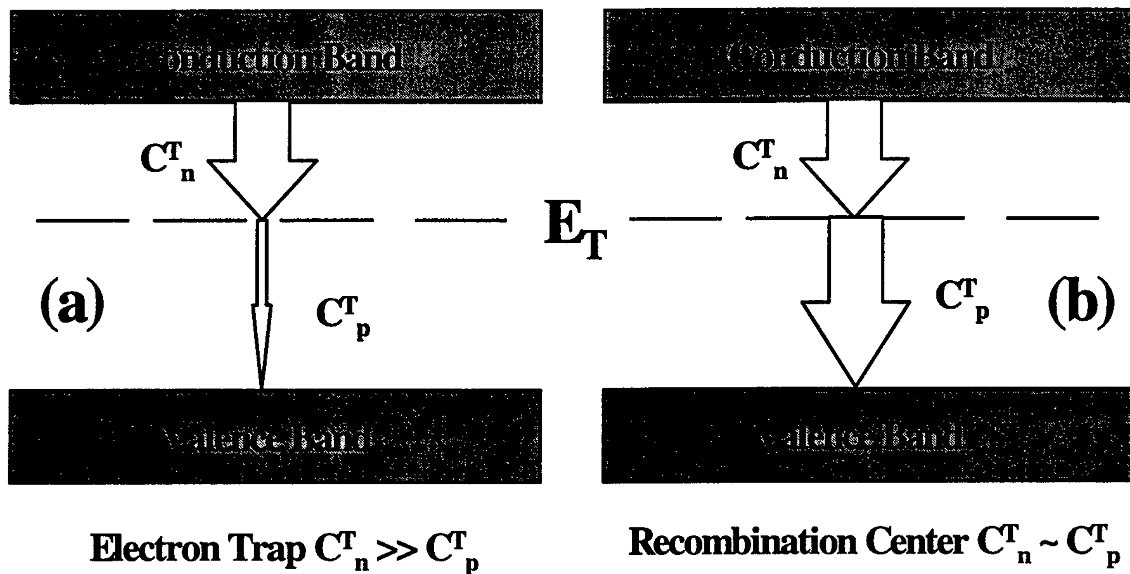

Figure III-2. Graphical representation of the differences between (a) traps and (b) recombination centers as related to a deep level bandgap state designated by the dashed line and label E_T. The arrow directions denote the loss of electron energy as trapping and recombination occurs. The arrow size relates to the magnitude of the capture rate.

bandgap semiconductors such as SiC, a recombination center in n-type bulk material may act only as a trap-like defect due to the absence of any free holes with which to complete the recombination process. This being due to the lack of an appreciable intrinsic carrier concentration over a wide temperature range as highlighted in Equation I-1 and Figure I-4. As a result, free holes in the valence band are not available for capture subsequent to electron acquisition. In order to fully appreciate the previous definitions, we should review the analytic expressions which define the capture rates used to describe traps and recombination centers.

III-II-1. Energy Conservation and Relative Recombination Probabilities. To this point we have not dealt with the issue of conservation of crystal momentum, which dictates the relative probabilities for competing transition or recombination paths. Specifically, the capture or recombination of free carriers will require the dissipation of up to several electron volts of kinetic and/or potential energy. This can occur through one of three primary energy release mechanisms. The carrier(s) may give up its (their) energy through collisions, the emission of optical photons, or by coupling to the available normal modes associated with thermal lattice vibrations. The relative probabilities of each of these mechanisms determines a specific lifetime or transition rate associated with the trapping or recombination of electrons and holes. The most probable process being that which translates to the shortest lifetime or largest transition rate.

Radiative capture, while always present to some extent, is unlikely to dominate the recombination of carriers at defect centers. In most semiconductors, the dominant recombination or capture processes are non-radiative. The choice for a dominant process

must lie between phonon and collisional recombination. As an example of the dominance of non-radiative processes, consider the calculated radiative lifetime for free carriers in germanium of one second [Pankove, 1971:Ch. 6]. The measured lifetimes are, however, only on the order of a millisecond, and often less than a microsecond. Thus, non-radiative processes in germanium are at a minimum one thousand times more probable than the radiative transition. In some instances, experimental data has indicated that for induced transitions to defect levels, only 1 in 10^9 are radiative [Blakemore 1987:243]. Dominance of the non-radiative transition probability is the motivation behind the tremendous efforts to control and eliminate deep level defects in optoelectronic device material, since they are the primary recombination paths, and thus seriously corrupt the detection or emission efficiency of such devices.

Conceptually, non-radiative processes may couple any occupied upper electronic state with all empty lower levels. The question of just how a particular transition will proceed, and what physical mechanism will account for the vertical transition energy conservation, as well as any momentum conservation required for initial and final states with differing **k**-values, has been the subject of much study and controversy. This is because non-radiative recombination presents a conceptual difficulty. In contrast to radiative recombination, it is indefinite, vaguely indicating any process which does not emit a photon. The experimental study of non-radiative processes is extremely difficult because the mechanism manifests itself only by the absence of an expected by-product, photons. The only measurable parameters are emission efficiency, carrier lifetime, and kinetics of the recombination or capture process in response to increased temperature or

carrier concentration. In the final analysis, conclusions are drawn on the basis of circumstantial evidence rather than definitive proof. In spite of these difficulties, non-radiative transitions are much studied, and can be classified into two energy conservation categories; 1) collisional or Auger and 2) thermal phonon emission.

The Auger effect is characterized by the transfer of a recombining particles energy to another particle which is excited to a higher energy state. A collisional mechanism is used to describe the kinetics of these transitions, and thus it is the complementary process to impact ionization. Figure III-3 graphically illustrates several possible Auger transitions involving interband free carrier recombination (a, b) and free carrier interaction with a defect level lying in the semiconductor bandgap (c-h). In the figure, upward arrows are associated with the particle receiving the collisional energy. The transitions shown are meant to be illustrative but are by no means an exhaustive list of possible carrier Auger interactions. As expected for a process totally dependent upon the interaction of free particles, the Auger transition rate is a strong function of the concentration of available carriers. If we consider band-to-band Auger recombination in an n-type semiconductor, which is non-degenerate ($|E_F - E_C| > kT$), the rate of recombination is proportional to n^2p times the equilibrium generation rate, G_{ee}. G_{ee} is a complex function involving the carrier effective masses, overlap integrals between conduction and valence band states, bandgap magnitude, and the sample temperature. The rate of Auger capture by a donor type defect level (positively charged when empty) in n-type material is obtained by replacing the free hole concentration, p, with the concentration of available empty donor states, N_d^+. This would correspond to transition (f) in Figure III-3.

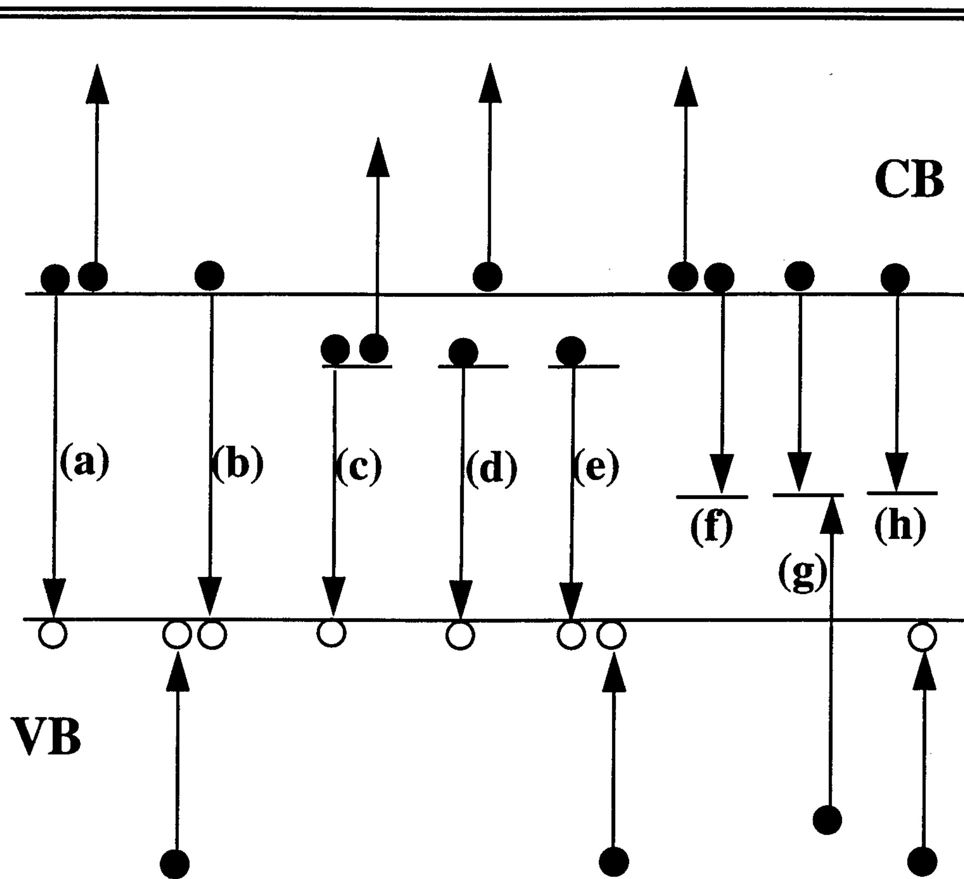

Figure III-3. Pictorial representation of several possible Auger recombination paths. (a) and (b) illustrate expected band-to-band transitions in n- and p-type material, respectively. The remaining three body recombinations (c) through (h) are illustrative possibilities but not exhaustive, for Auger particle exchange between the bands and forbidden gap defect states. Electrons are indicated by solid and holes by open circles.

Empirical data on a number of donor impurities in Si and Ge has shown that Auger capture of free carriers by flaw levels occurs with an extremely low probability, except for certain situations involving multivalent impurities which possess a repulsive Coulombic charge for the carrier being captured [Blakemore, 1987:244]. In these cases, the capture cross section for radiative and phonon transitions will be very small, and the relative probability of Auger capture is increased. Band-to-band Auger recombination

can, however, be a dominant process controlling the free carrier lifetime in some materials. However, the temperature and energy gap dependence of the Auger electron-hole pair lifetime, τ_A, follows the proportion

$$\tau_A \propto (\frac{E_G}{kT})^{3/2}[\exp(\frac{1+2M}{1+M}\cdot\frac{E_G}{kT})], \qquad \text{[III-2]}$$

where M is the ratio of the electron to hole effective masses. From Equation III-2 we can see that Auger dominated carrier lifetime in a semiconductor will strongly depend upon the intrinsic bandgap of the material and the temperature range being considered. A rough figure-of-merit of $E_G \geq 20kT$ ($\geq$0.5 eV @ 300K) is used to qualitatively determine the range of dominance for defect related transitions over band-to-band Auger or radiative recombination [Blakemore, 1987:195]. In practice, when radiative transitions are important, there will always be an Auger component as well, and this process must predominate at some sufficiently high temperature. Using the rough figure-of-merit defined above, interband Auger recombination in SiC should not be considerable until the temperature range exceeds the decomposition temperature of the compound ($T \approx 2750$ K). This is consistent with the absence of any reported Auger activity in SiC materials. Furthermore, the presence of Auger recombination is strongly dependent upon material of high purity (which SiC has yet to consistently achieve), to minimize phonon mediated and radiative transitions. Non-radiative capture and recombination via the emission of optical and acoustic phonons has been empirically shown to be the dominant process in the majority of situations, especially for wide bandgap materials with significant impurity related bandgap states such as SiC.

When the recombination energy of an electron captured at a defect level is released as one or more phonons, the capture rate has the same functional form as for radiative capture. This is true because in both cases the capture rate depends upon the non-equilibrium carrier concentration, n, and the excitation rate depends upon the density of occupied donor states for n-type material. The capture and emission rates used in these discussions are obtained from first order differential equations describing the temporal and spatial variation of the free carrier concentration in response to recombinative and generative processes and carrier drift and diffusion. These processes, which alter the steady state concentration of free carriers include those arising both from external stimulation and thermal equilibrium conditions. Consider the density of conduction band electrons, n(x,y,z,t). The term "generative processes" includes all the mechanisms by which electrons may be excited to the conduction band from the valence band and from impurity states. In addition to generation and recombination, the presence of an electric current will also change the local electron density. It has been shown analytically that the capture coefficient for trapping, via energy conserving phonon emission, can be written numerically in terms of G_p for typical semiconductor parameters as [Milnes, 1971:Ch 5]

$$< c_P > = \frac{G_P}{n_0 (n_0 + N_A)} \approx 6 \text{x} 10^{-8} T^{-1/2} \ \text{cm}^3 \sec^{-1} , \qquad \text{[III-3]}$$

where G_P is an integral expression involving the capture probability and density of levels in the valence or conduction bands, N_A is the concentration of all compensating levels, and n_0 is the free carrier concentration. An analytically similar capture coefficient can be written for radiative and Auger capture by defect levels in a semiconductor yielding an

analogous numerical form. If the conduction band is non-degenerate, the probability function is of the Boltzmann type, the defect is donor like, and the effective mass approximation is invoked, then the radiative capture coefficient can be calculated to be [Blakemore, 1987:Ch. 5]

$$< c_R >= \frac{G_R}{n_0(n_0 + N_a)} = \frac{1.2\text{x}10^{-12}\,\varepsilon^{1/2} E_D}{T^{1/2}}\left(\frac{m_0}{m_C}\right)^{5/2}, \qquad \text{[III-4]}$$

where ε is the dielectric constant of the semiconductor, E_D is the defect energy level, m_0 is the free electron mass, and m_C is the conduction band density of states effective mass. Using similar defect level and conduction band assumptions, the analogous approximate capture coefficient quantity for Auger capture is calculated to be

$$\frac{< c_A >}{n_0} = \frac{G_A}{n_0^{\,2}(n_0 + N_A)} \approx \frac{2\text{x}10^{-20}}{T^2 E_D}\left(\frac{m_0}{m_C}\right)^2 . \qquad \text{[III-5]}$$

Although calculated for simplified, analytically tractable, physical conditions, Equations III-3, III-4, and III-5 demonstrate the dominance of phonon mediated capture of free carriers at a defect level, and validate the abundance of experimental data supporting phonon mediation as the dominant mechanism.

III-II-2. Electronic Lattice Coupling. Various models have been developed to describe the excitation and capture of electrons involving the absorption and emission of phonons. A crucial feature is the manner in which they allow for transitions involving multi-phonon processes, since in most cases the energy to be conserved is much greater than available in a single phonon. This is especially true for energy levels in the bandgap located far from the band with which it exchanges carriers. Intuitively one might reason

that as the bound electron wavefunction becomes more localized (larger binding energy) and the associated energy conservation requirements more restrictive, the probability of free carrier capture by emission of low energy phonons would decrease relative to photon or Auger mechanisms. This was in fact the widely held belief prior to understanding the complex interactions between free carriers and lattice vibrations. Following this heuristic argument, it was assumed that the cross section for carrier capture, mediated by the emission of large numbers of phonons, would be on the order of 10^{-22} cm^2 or smaller [Milnes, 1971:95]. It was subsequently observed that cross sections on the order of 10^{-12} cm^2 were common for non-radiative transitions not involving Auger collisions. It is the localized nature of deep level defect bound states which enhances this coupling, due to the large extent of the wavefunction in momentum space. This requires that the wavefunction be described by a larger number of Fourier components but, it also allows the coupling to a larger number of the available normal modes in the crystal. This is the second consequence of wavefunction localization at deep levels, and it is the primary reason for the dominance of non-radiative transitions involving these states.

There have been two primary theories in which the accounting of free carrier capture and recombination energy is described by the emission of large numbers of phonons. They are the cascade capture model of Lax [1960:1502], and the lattice relaxation, multi-phonon emission theory of Henry and Lang [1975:989].

The theory developed by Lax proposes that the extremely large cross sections observed for non-radiative capture of free carriers is enabled by initial capture into excited states characterized by very large orbital radii. The large energy loss required to

transition to the ground state is accomplished by the emission of one or two phonons, at each step ΔE, as the carrier plummets down through the excited states. The model is thus primarily restricted to relatively shallow levels which are Coulombically attractive to the free carrier. Defect levels satisfying these criteria will have a large series of closely spaced, hydrogenic, excited states available for this process to occur. These excited states of large radius explain the huge observed cross sections of some defect centers. Figure III-4 graphically illustrates the mechanism of cascade capture for a level of energy E_T, showing the single phonon emissions ($\hbar\omega_n$) associated with transitions between excited coulombic states. In actuality, only those states whose binding energy is greater than kT will be capable of capturing an electron or hole. Thus, qualitatively we would expect that the capture cross section of this process would have an inverse temperature dependence, since excited states with increasing radii would be allowed to participate in capture events as the temperature is decreased. In practice, this is exactly what has been observed at low temperatures for shallow donors and acceptors in germanium and silicon [Milnes, 1971:98] with a cross sectional temperature dependence of between T^{-1} to T^{-2}. The calculated capture cross section for an attractive coulombic center in the cascade model is

$$\sigma(T) = \frac{\pi^2}{8}\frac{W}{l_C}\frac{Zq^2}{\varepsilon kT}(\frac{Zq^2}{\varepsilon \hbar\omega})\frac{\lambda}{1-\exp(-\lambda)}C(\lambda) \ , \qquad \text{[III-6]}$$

where Z is the charge of the defect, l_c is the mean free path for phonon collision, W is the

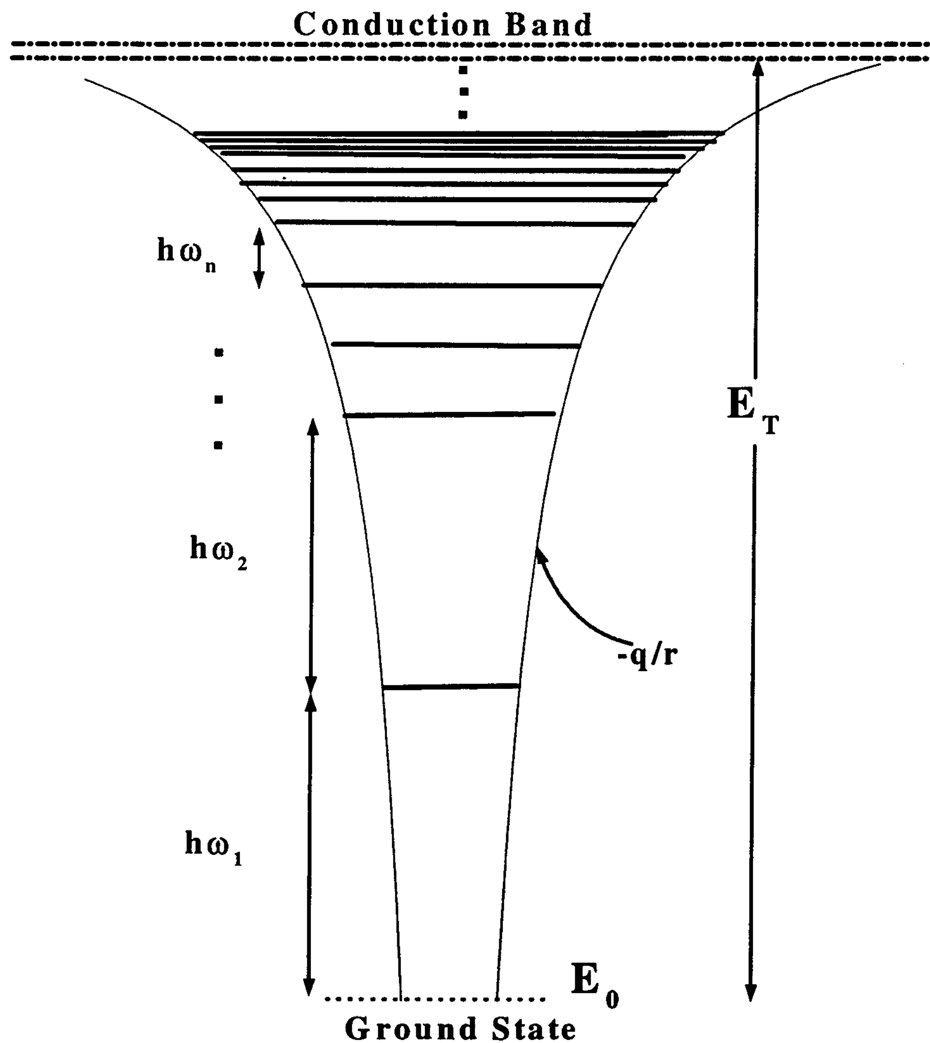

Figure III-4. Graphic representation of Lax's cascade capture mechanism for a Coulombically attractive (+) defect potential with a ground state ionization energy of E_T. The $\hbar\omega_i$ are single or double phonon energies excited by the electron as it descends through the series of excited states.

ratio of the matrix elements for acoustic and optical phonon scattering with the carrier wavefunction, and is obtained from the temperature dependence of the mobility through Hall effect measurements, and $\hbar\omega$ is the phonon energy. $C(\lambda)$ is defined as

$$C(\lambda) = \int_0^\lambda P(\lambda - x)e^{-x}(1-\frac{x}{\lambda})^{-5/2}dx \cdot [1+y-y\frac{x}{\lambda}]^{1/2} \quad , \qquad \text{[III-7]}$$

with

$$P(y) \approx 1-(1+y+\frac{1}{2}y^2)\exp(-y) \qquad \text{[III-8]}$$

being the probability of carrier capture into the ground state after initial capture in a high level excited state rather than being re-emitted to the resonant band. The parameters λ and y are dimensionless quantities defined as U/kT and $\hbar\omega$/kT, respectively. Additionally, U is the binding energy of the highest excited state which can capture a free carrier (i.e. $U \geq kT$).

Trapping occurs when a carrier within the capture cross section of a trap emits a phonon due to lattice scattering and loses energy. If the energy loss (E - $\hbar\omega$) due to this phonon emission is great enough to reduce the energy of the electron below the minimum free carrier energy then the particle will be trapped, and cascade down through the series of Coulombic levels to the ground state. Using reasonable silicon material parameters and assuming capture proceeds via emission of optical phonons, Lax estimated the cross section for electron capture by a singly charged impurity level to be roughly 10^{-14} cm^2 at room temperature. This was found to be in reasonable agreement with the electron capture cross section of the Au^+ impurity in silicon, which was measured to be approximately $5\text{x}10^{-15}$ cm^2 [Milnes 1971:99].

Unique cross sectional temperature dependencies of the various carrier capture processes provide a basis for which carefully obtained experimental results may be compared to the various models. The determination of a capture mechanism, for the numerous deep level defects observed in the SiC polytypes studied during this project, was a primary focus of the work outlined in this dissertation. This being motivated by the complete absence of this information in the literature, which is a result of the infancy of defect studies in these materials. It was determined that several of the frequently occurring deep level defects in both the 6H- and 4H-SiC polytypes were characterized by non-radiative electron and hole capture kinetics which were strongly energy dependent. However, contrary to the Auger and cascade phonon emission dependencies upon free carrier concentration and inverse temperature, respectively, the capture cross section of these defects were found to have a strongly positive temperature coefficient, and appeared concentration independent. The capture kinetics of SiC deep levels with ionization energies from 0.2 to almost 1.0 eV were compared to several theoretical models. It was finally determined that the mechanism of energy conservation describing trapping at these centers was best represented by the lattice-relaxation, multi-phonon emission (MPE) model developed by Henry and Lang. The following paragraphs will outline the particulars of MPE theory while the detailed analysis of experimental results will be presented in Chapter V.

A graphical representation of a trap, used to describe the kinetics of carrier capture, is given by the one-dimensional configuration coordinate diagram of Figure III-5. In this figure, the total elastic plus electronic energy is plotted versus a single, direct-

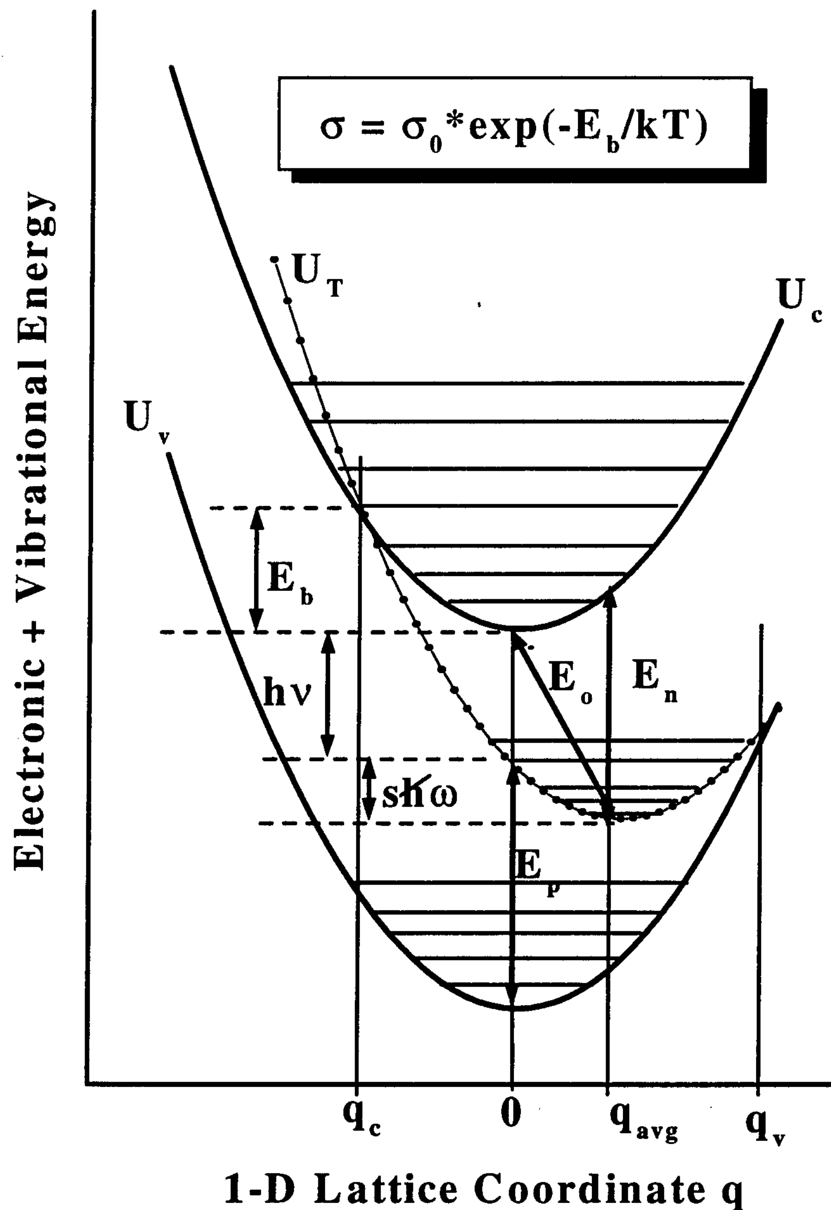

Figure III-5. Configuration coordinate diagram for a deep trapping level illustrating the origin of the exponentially varying capture cross section σ(T). Included are the optical excitation threshold before (E_P) and after (E_n) relaxation, total binding energy (E_0), lattice relaxation increase in binding energy ($s\hbar\omega$) after relaxation, and the thermal capture barrier (E_b). The average trap coordinate position (q_{av}) and the peak vibrational positions when the trap level crosses into the conduction (q_c) and valence (q_v) bands are also indicated.

space lattice coordinate, q. U_C, U_V, and U_T are the potential wells for an electron in the conduction band, valence band, and bound to the trap, respectively. The various energies of transition shown in Figure III-5 are detailed in the caption, and the exponential dependence of the cross section for carrier capture heads the figure.

For an electron in one of these states (i = c, t, v), the potential well for the lattice $U_i(q)$ is dependent upon the positions of the atoms making up the defect and its nearest neighbors (chemical bond energies), and is given by

$$U_i(q) = E_i(q) + \frac{1}{2} M\omega^2 q^2, \qquad \text{[III-9]}$$

where M is the reduced mass, ω is the frequency of harmonic oscillations, q is the lattice displacement position, and E_i are the eigen-energies associated with the eigenfunctions for a free state at the bottom of the conduction band, $|c\rangle$, trapped electron, $|t\rangle$, and a free state at the top of the valence band, $|v\rangle$. Non-radiative capture takes place as a result of strong coupling between the defect and the lattice. Effectively what occurs in the MPE model of carrier capture is that the defect level moves up and down in the energy gap as the lattice vibrates. At high enough temperatures the vibrational amplitudes can become great enough to cause the level to cross into the conduction band and capture an electron, or into the valence band and capture a hole. Considering only electron capture from the conduction band, when a free carrier is trapped the defect relaxes (physically relocates its equilibrium position to q_{avg}) in such a way as to lower the equilibrium location of the energy level in the bandgap. This results in an increase in the binding energy of the level as shown in Figure III-5, where the trap potential well is

illustrated in a relaxed state in which the optical ionization energy has increased from $h\nu$ to ($h\nu + S\hbar\omega$) subsequent to electron capture. The increase in trap binding energy is equal to the energy of the lattice phonons, which damped the large amplitude vibrations, $S\hbar\omega$. This energy shift is exactly analogous to an optical Stokes shift of energy and coordinate position, and is also sometimes referred to in the literature as a Frank-Condon shift [Pankove, 1971:113]. This process is accomplished through a rapid damping of the large amplitude vibrations of the defect, which initially facilitated the CB crossing and electron capture, with the localized energy being propagated away by several normal mode lattice phonons. If significant numbers of phonons are not rapidly emitted, then the oscillating defect energy level will subsequently experience several crossings into the conduction band, increasing the probability of re-emitting the electron before capture into the ground state can be completed.

The free and bound-state electronic wavefunctions $|c\rangle$, $|v\rangle$, and $|t\rangle$ are obtained by solving the eigen-equation for the system Hamiltonian. If we consider the capture of an electron by a neutral impurity, the non-adiabatic Hamiltonian for a quantized lattice (phonons) is given by

$$\begin{aligned} H &= H_E + H_{EL} + H_L \\ &= [\frac{p^2}{2m^*} + V(r)] + BqV(r) + [\frac{P^2}{2M} + \tfrac{1}{2}M\omega^2 q^2] \ , \end{aligned} \qquad \text{[III-10]}$$

where H_E is the adiabatic electronic Hamiltonian with $q=0$, H_{EL} describes the change in the potential well depth with the lattice displacement q, and H_L is the Hamiltonian of a harmonic oscillator vibrating about $q=0$. It was assumed that the potential is spherical

with a radius, *b*, equal to the nearest neighbor distance and a potential depth V_0. If we let $|c\rangle = \varphi_{CB}(\mathbf{r})$, $|v\rangle = \varphi_{VB}(\mathbf{r})$, and $|t\rangle = \varphi_T(\mathbf{r})$ correspond to the adiabatic states at q = 0, then the electronic energies of these states are given by the matrix elements

$$E_i(q) = \langle i | \frac{p^2}{2m^*} + V(r) + BqV(r) | i \rangle, \qquad \text{[III-11]}$$

where i = c, v, or t, and all other terms have been previously defined. For a free carrier, the eigenvalues are independent of the values of the lattice coordinate, q, since the probability of being in the well is negligible (delocalized), and thus $Bq\langle c|V(r)|c\rangle \approx 0$, and similarly for the VB states. However, the matrix element involving the trapped state eigenfunction and the lattice vibration, $Bq\langle t|V(r)|t\rangle$, may be large, and this term describes the crossing into the conduction band by the bound state to at $q = q_C$ and into the valence band at $q = q_V$ as shown in Figure III-5. The harmonic oscillator states $|n_c\rangle$, $|n_t\rangle$, and $|n_v\rangle$, also illustrated in Figure III-5, must be included to form a direct-product space with electronic wavefunctions $|\varphi_i\rangle$ to accurately describe the complete wavefunctions; $|n_i\rangle|\varphi_i\rangle$. These wavefunctions are still not exact since the BqV(r) term mixes the $|c\rangle$, $|v\rangle$, and $|t\rangle$ states. Of course, it is just this coupling which allows capture transitions to occur. It has been analytically shown that this coupling is very weak, and can be readily dealt with by first-order, time-dependent perturbation methods [Engleman and Jortner, 1969:145].

To a good approximation, the MPE capture cross section for conduction band electron capture is proportional to the product of three probabilities

$\sigma \propto P_{vib}P_{ct}P_{tt}$.

P_{vib} is the probability that sufficiently strong lattice vibrations will occur so that the energy level of the bound state |t> will cross an occupied conduction band state |c> during each oscillatory period. P_{ct} is the probability that during the crossing, a capture transition occurs. P_{tt} is the probability that subsequent to capture the electron will not be re-emitted into another conduction band level before the defect relaxes to its occupied equilibrium configuration q_{avg}. It is convenient to write the capture cross section proportionality given above as

$$\sigma = \sigma_c P_{tt},$$

where now σ_c is the cross section for initial capture and P_{tt} is the probability that the electron will not be re-emitted. Detailed calculations by Henry and Lang showed that P_{tt} was roughly of order 1/2 and independent of the semiconductor or impurity, thus the quantity of interest is σ_c. The cross section for initial capture was also shown to be equal to the nonradiative transition rate, W, times the crystal volume to average thermal velocity ratio, $\Omega/\langle v \rangle$. The transition rate (probability per unit time that an electron will be captured) is given by the matrix elements of the nonadiabatic Hamiltonian, Equation III-10, and is given by

$$W = \frac{2\pi}{\hbar} \mathrm{ave}_{n_c} \sum_{n_t} \left| \langle n_t t | H | n_c c \rangle \right|^2 \delta(E_C - E_T). \qquad \text{[III-12]}$$

In Equation III-12, $E_C = n_c\hbar\omega$, $E_T = n_t\hbar\omega - E_0$, ave_{nc} indicates an average over the initial state vibrational occupation numbers , and the electronic and vibrational states $|n_i\rangle$, $|c\rangle$, and $|t\rangle$ have previously been defined. The summation in Equation III-12 is over the

range of localized defect vibrational frequencies, and thus W represents an average over this range of phonon energies. In order to evaluate Equation III-12, the usual approach is to use the Condon approximation, which asserts that the electronic, |c> |t>, and vibrational, $|n_i\rangle$, states are separable because <c | H | t> is independent of q. In this case, we can write the average probability as

$$\overline{W} = \frac{2\pi}{\hbar^2\omega}\left|\langle t|H|c\rangle\right|^2 \mathrm{ave}_{n_c}\left|\langle n_t|H|n_c\rangle\right|^2 = \frac{2\pi}{\hbar^2\omega}\left|\langle t|H|c\rangle\right|^2 w_p, \qquad \text{[III-13]}$$

where we have taken the range of the phonon energy averaging summation to be $\Delta E = \hbar\omega$, and have compacted the harmonic oscillator state overlap integral as w_p. For SiC polytypes of interest (6H and 4H), the typical values for $\hbar\omega$ are on the order of 100 meV. Thus, for trap levels observed during the course of this research with $h\nu + s\hbar\omega$ (see Fig. III-5) between 0.2 and 1.0 eV, there will roughly be a range of phonons numbers, p, from 2 to 10 required for energy conservation such that $p\hbar\omega = h\nu + s\hbar\omega$ in these cases. With such small numbers, a low temperature approximation for w_p will be valid over a wide range. The general condition which must be satisfied for this to be true is

$$\frac{S^2}{p}\overline{n}(\overline{n}+1) << 1, \qquad \text{[III-14]}$$

where S is illustrated in Figure III-5 and $\overline{n}$ is simply the Bose-Einstein occupation factor

$$\overline{n} = [e^{\hbar\omega/kT} - 1]^{-1}. \qquad \text{[III-15]}$$

Assuming that $\overline{n}$ is smaller than one (1), it is easily seen that the constraint of Equation III-14 is satisfied for

$$\frac{\hbar\omega}{kT} >> \text{Ln}\left|1+\frac{S^2}{p}\right|. \qquad \text{[III-16]}$$

S will be a maximum for a given trap potential when U_T intersects U_C at $dU_C/dq = 0$, as can also be seen in Figure III-5, and in this case S=p. If $S^2/p \sim 1$ then the low temperature regime is defined for T << 1600 K. For an optical transition with S ~ 1, then T for the low temperature range is predicted to be << 10,000 K, assuming that S^2/p is between 0.1 and 0.5 for traps in SiC. These intervals predict that the low temperature range will be valid for the majority of experimental techniques used to characterize defect levels in SiC, especially DLTS. Similarly large transition temperatures between the low and high temperature regimes have been predicted for deep levels in GaAs (600 K and 3000 K) [Borgoin and Lannoo, 1983:191], but have been found to be grossly overestimated when compared to experiment [Henry and Lang, 989:1977].

In the low temperature limit, the capture cross section can be written as

$$\sigma = W\frac{\Omega}{<v>} = \sigma_0(\bar{n}+1)^p \frac{S^p}{p!}\exp[-2S(\bar{n}+\tfrac{1}{2})] \qquad \text{[III-17]}$$

with

$$\sigma_0 = \frac{2\pi}{\hbar^2\omega}\frac{\Omega}{<v>}\left|\langle c|H|t\rangle\right|^2. \qquad \text{[III-18]}$$

We can similarly define the high temperature region by the condition p >> 1, and if

$$\frac{4S}{p}\sqrt{\bar{n}(\bar{n}+1)} >> 1, \qquad \text{[III-19]}$$

which we can simplify to a form similar to Equation III-16

$$\frac{\hbar\omega}{kT} << \text{Ln}(1 + \frac{4S}{p}). \qquad \text{[III-20]}$$

Using the same SiC estimates (p ~ 2-10, $\hbar\omega$~0.1 eV, and S ~ 1-2 but dependent upon lattice relaxation magnitude), then the constraint of Equation III-20 is satisfied for T much larger that 720 K. In this case the capture cross section is given by

$$\sigma \approx \sigma_0 \sqrt{\frac{\hbar\omega}{4\pi kTS}} \exp[-\frac{(p-S)^2 \hbar\omega}{4kTS}]. \qquad \text{[III-21]}$$

In the parabolic approximations used for $U_C(q)$ and $U_T(q)$, the exponential argument of Equation III-21 is equal to the thermal capture barrier, E_b, over kT as shown in Figure III-5, and yields the observed temperature dependence. Thus, σ is seen to explicitly increase with temperature in this regime when capture is conducted via MPE kinetics, in contrast to the temperature independent cross section predicted for the low temperature region. As previously mentioned, the estimate for delineation between the low and high temperature regions is overestimated, and several deep levels in a variety of semiconductors have been observed to possess capture cross sections which obey Equation III-21.

It has been assumed that the physical mechanism by which MPE capture is enabled is mechanical motion of the defect in a crystal lattice, although the cause may be entirely electronic in origin. Consideration of the exact nature of the forces which conspire to create a favorable environment for this process to occur will undoubtedly create complications to the model.

The exact mechanism by which carrier capture will occur will depend entirely upon the form of the defect potential. This will in turn depend upon the geometry of the defect, atomic species involved, and the lattice in which it is created. Determination of the first two factors is extremely difficult for non-radiative traps and recombination centers, and a consensus is usually not reached until numerous studies, using several experimental techniques, have all consistently supported a given model. This again highlights the need for detailed studies of the physical characteristics of semiconductor defect centers in order to control or eliminate these electronic device dominating entities. Figure III-6 graphically illustrates the three possible point defect potential forms which

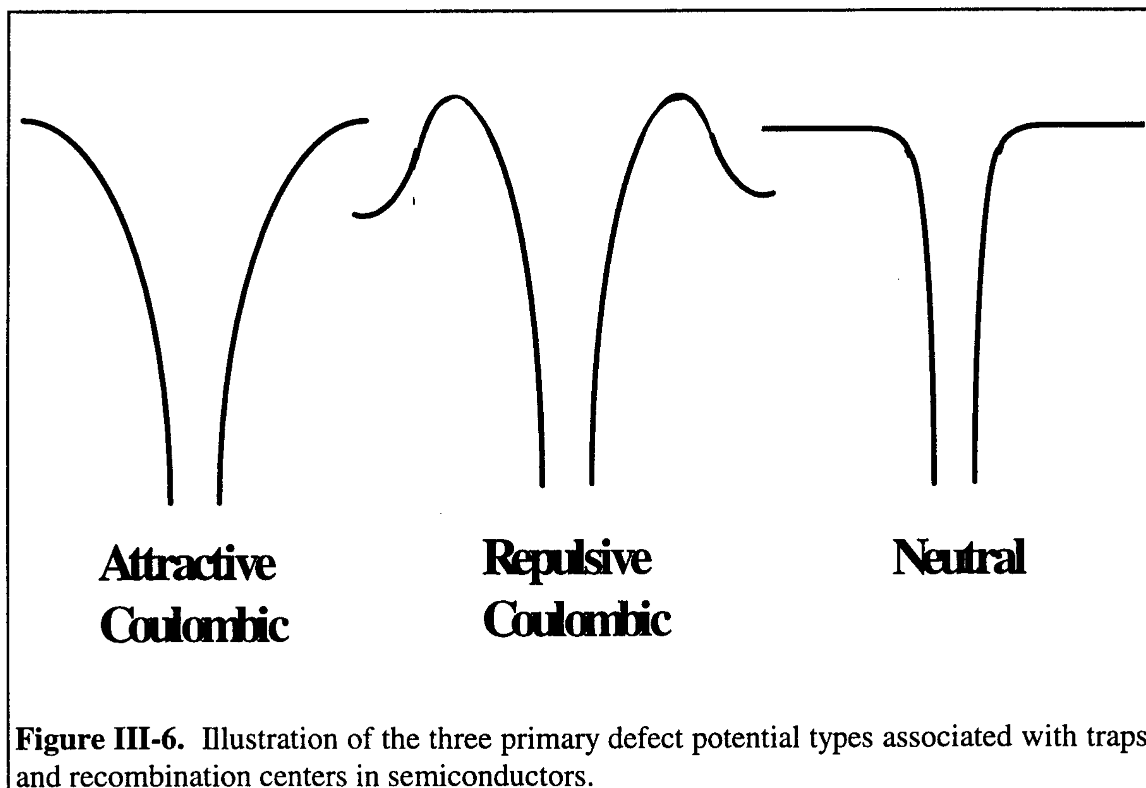

Figure III-6. Illustration of the three primary defect potential types associated with traps and recombination centers in semiconductors.

correspond to the previous discussions. Illustrated are the analytic spatial variations of the potentials for an attractive Coulombic, electrically neutral, and a short range repulsive potential modulating a longer range attractive potential which is the model typically used to represent the thermal capture barrier of MPE kinetics. As has been outlined, the determination of a trap potential and the capture kinetics associated with a given defect center requires the careful analysis of experimental data and comparison to the various models as functions of temperature and carrier concentration.

IV. SiC Defect Characterization

IV-I. Deep Level Transient Spectroscopy

As was discussed in the previous chapter, it is wavefunction localization in coordinate space which results in the tendency for crystalline defects with large ionization energies to act as nonradiative traps and recombination centers. Recall that, this is due to the associated delocalization in reciprocal (**k**) or momentum space requiring large numbers of Fourier components to describe the bound state wavefunction. Thus, coupling to a significantly larger number of normal mode lattice vibrations (phonons) results, and the probability of phonons acting as the energy conservation mechanism for electronic transitions is increased tremendously. For this reason, experimental methods which record the optical recombination energy of transitions to deep levels are not of much value for the study of these centers.

IV-I-1. Principles and Physics of DLTS Measurement. One of the most useful methods employed for the characterization of deep level ionization energies, defect concentrations, and the nature of capture and emission kinetics is deep level transient spectroscopy (DLTS). The DLTS technique was originally developed by Lang [1974:3023], and subsequently has been an important tool for the characterization of semiconductor defects. In short, the DLTS method involves monitoring the emission rate of trapped carriers as a function of temperature. Information obtained includes the trap thermal ionization energy, defect concentration, and capture cross section parameters.

The DLTS principles utilized during this research are identical to the original formalism outlined by Lang, however, the methods of data acquisition and subsequent analysis are radically different. For example, the original procedure was an analog technique with ionization energies obtained using a Gaussian type spectral peak analysis, whereas the system implemented and employed during this project utilizes digital data acquisition and digital signal processing data analysis methods. These systemic differences allow a more detailed investigation of the capture and emission kinetics of deep level defects, reduce system complexity, and provide greater flexibility in fitting experimental data with various analytic models.

DLTS requires the use of p-n junction, metal-insulator-semiconductor (MIS), or Schottky barrier device structures. These structures all have the common feature of possessing a volume or region of semiconductor in which the concentration of free carriers can be varied from near zero to a maximum value dictated by the electric current carrying capability of the device. The primary condition of interest for DLTS measurements is that of free carrier depletion $n \approx 0$, $p \approx 0$. Additionally, the volume of this depletion region may be modulated, in response to an externally applied voltage bias, resulting in a variation of one of the spatial dimensions, designated as the depletion width. These features of the simple devices mentioned above yield two important properties which are the crux of the DLTS technique. First, traps in the depletion region may be filled (capture) and emptied (emission) sequentially in response to applied voltage bias conditions defined by the experimenter. Secondly, the formalism leading to the equations governing DLTS data analysis is predicated upon linearization of the first-order

differential rate equation alluded to in Chapter III, Equation III-16. This can be seen by considering the rate equation describing the temporal dependence of the concentrations of electrons (n_T) and holes (p_T) occupying a deep level bandgap state of concentration $N_T = n_T + p_T$,

$$\frac{dn_T}{dt} = -(<c_n> n + e_n + <c_p> p + e_p)n_T + (<c_n> n + e_p)N_T. \qquad [IV-1]$$

In Equation IV-1, n and p are the free carrier concentrations and $<c_i>$ and e_i are the capture coefficients and emission rates, respectively, for electrons (i = n) and holes (i = p). In its most general form, Equation IV-1 is written using explicit definitions for the capture coefficients and emission rates, which are given by

$$\begin{aligned} <c_n> &= <c_n{}^T> + <c_n{}^O> + <c_n{}^n n> + <c_n{}^p p> \\ <c_p> &= <c_p{}^T> + <c_p{}^O> + <c_p{}^p p> + <c_p{}^n n> \\ e_n &= e_n{}^T + e_n{}^O + e_n{}^n n + e_n{}^p p \\ e_p &= e_p{}^T + e_p{}^O + e_p{}^p p + e_p{}^n n. \end{aligned} \qquad [IV-2]$$

In each of the capture coefficient and emission rate definitions of Equation IV-2, the first terms are non-radiative phonon mediated processes, as denoted by the T (thermal) superscript, the second terms are the rates associated with radiative transitions (O = optical), and the third and fourth terms describe the rates associated with Auger processes, as indicated by the association with free carrier concentrations n, and p. Thus, we can see that linearization of the rate equation will be achieved if the electron and hole concentrations are zero or constant, and the use of a depleted semiconductor region is

ideal for this purpose. The primary benefit of this linearization is that any perturbation applied to the system will decay exponentially with time. The reciprocal of the decay time constant will be equal to the sum of all the emission and capture rates, as indicated by the two equations above, and independent of the defect concentration, N_T. An additional simplification is obtained by performing measurements in the dark, resulting in the optical emission terms dropping from the expressions. Thus, experimental conditions can be realized in which the rates defined by Equation IV-2 are dominated by thermal (phonon) processes.

Thermal emission rates for carriers trapped on deep level defect sites are proportional to a Boltzmann factor, $\exp(-E_T/kT)$, with E_T being the ionization energy of the ground state trap level. If we consider only electron emission to the conduction band, this rate is given by

$$e_n = B_n \exp(-\frac{E_T}{kT}), \qquad \text{[IV-3]}$$

where we have dropped the T superscript since we are now only considering thermal processes. The principle of detailed balance is used to evaluate the coefficient B_n. This postulate is a statistical concept, and states that the rates of a process and its inverse are equal and balance in detail under conditions of thermal equilibrium. With this assumption we can write

$$e_n P = c_n (1 - P), \qquad \text{[IV-4]}$$

where P is the probability that a deep level will contain a trapped electron and c_n is the capture rate. Using the cross sectional definition of the average capture coefficient given

in Chapter III ($\langle c_n \rangle = \sigma \langle v \rangle$), which has units of volume/sec, the capture rate (sec^{-1}) which will be used for the balance of this dissertation is defined as

$$c_n = \langle c_n \rangle n = \sigma \langle v \rangle n = \sigma \langle v \rangle N_C \exp(\frac{E_f - E_C}{kT}), \qquad [IV-5]$$

where the non-degenerate CB simplification has been made for the free electron concentration, n (See Equation [III-11]). Recall that N_C is the effective density of states in the conduction band, which is given by

$$N_C = 2M_C(\frac{2\pi m^* kT}{h^2})^{3/2}, \qquad [IV-6]$$

where M_C is the number of equivalent conduction band minima and all other terms have previously been defined. With these definitions, the trapped electron emission rate to the conduction band is seen to be

$$e_n = \frac{\sigma \langle v \rangle N_C}{g} \exp(\frac{-E_T}{kT}), \qquad [IV-7]$$

with the factor g included to account for any degeneracy of the defect level. As always, a completely parallel development yields the emission rate for trapped holes.

The DLTS method of trap characterization involves monitoring the exponential decay of device capacitance, associated with the depletion region width W, following a pulsed bias-voltage perturbation. This bias event disturbs the thermal equilibrium occupation of trapped carriers, and when the disturbance is removed the system exponentially relaxes back to equilibrium at a rate given by Equation IV-7. This process is shown graphically by Figure IV-1 for an n-type Schottky barrier junction device. Illustrated in the figure is a typical voltage waveform used to sequence the diode through the DLTS measurement cycle indicating forward (V+), reverse (V-), and zero bias levels.

During the forward bias event (II in Figure IV-1), the empty traps in the depletion region, W - λ, are filled at the characteristic capture rate by flooding this region with free carriers, n. After a predefined temporal period (pulse width), the bias voltage is returned to a reverse condition and the free carriers are rapidly swept out of the expanding depletion region by the strong electric field. Under these conditions, trapped carriers energetically higher than the Fermi level (E_f) will be emitted to the conduction band at the rate defined by Equation IV-7, as the system exponentially relaxes back toward equilibrium.

The original DLTS methodology involved monitoring the decaying depletion-capacitance signal at two well defined sampling times, t_1 and t_2, as a function of temperature. The quantity of interest is the change in capacitance, ΔC, between times t_1 and t_2, which define the so-called rate window. This ΔC will be directly dependent upon the defect emission rate since the rate of capacitance decay toward equilibrium conditions is strongly temperature dependent. The analog DLTS signal is thus given by

$$S(T,t) = C(t=\infty)[\exp(-e_n t_1) - \exp(-e_n t_2)], \qquad \text{[IV-8]}$$

where $C(t=\infty)$ is the relaxed, steady-state junction capacitance. The capacitance signal defined by sample times t_1 and t_2 is monitored using boxcar integrators with the data record plotted against temperature. For a single deep defect-level in the semiconductor bandgap, S(T) will result in a Gaussian type DLTS spectral characteristic having a peak position corresponding to equality between the defect emission rate and the rate window defined as

$$e_{RW} = \frac{\mathrm{Ln}(\frac{t_2}{t_1})}{t_2 - t_1}, \qquad \text{[IV-9]}$$

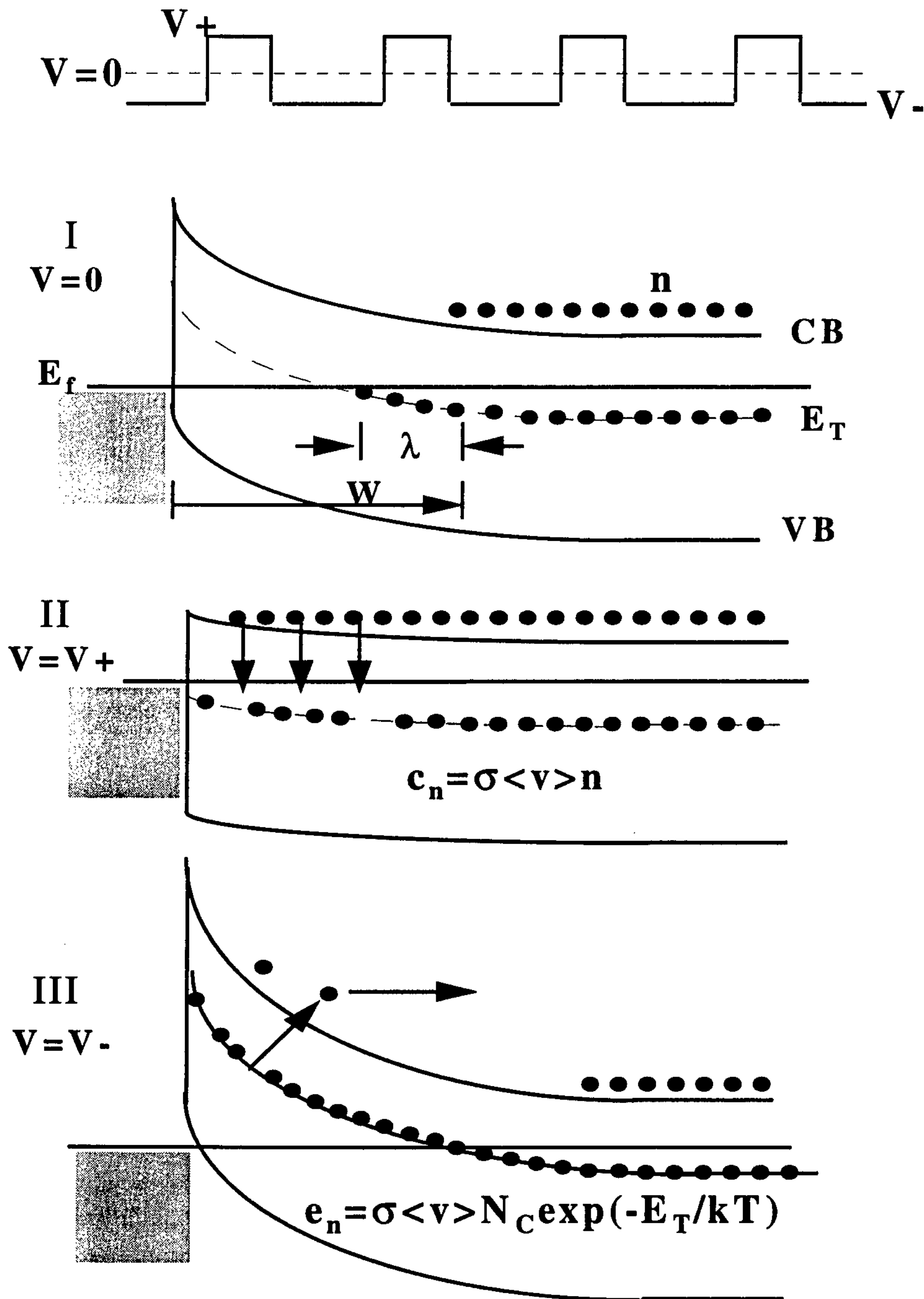

Figure IV-1. Simplified band diagram of an n-type Schottky barrier diode with a single deep level (E_T) present under conditions of I) quiescent zero bias, II) forward bias flat-band trap filling period, and III) reverse bias at $t=0^+$, the initial stages of transient decay . Illustrated at the top of the figure is a typical voltage waveform used to sequence the diode through these states during the DLTS measurement cycle.

which is obtained by simply evaluating the S(T) expression for analytic minima and maxima (dS(T,t)/dT = 0). This peak is then used to fix the emission rate at the peak temperature. If the rate window times t_1 and t_2 are subsequently reset to different values, and the thermal scan is accomplished again, a spectral characteristic with a different peak position (T) occurs as determined by the rate window Equation IV-9. Repeating this procedure several times results in several e_n and T pairs of data which can be analyzed using a standard Arrhenius plot of $Ln(e_{RW}/T^2)$ versus $1/kT$ to yield the thermal ionization energy using Equation IV-7. The ordinate contains the factor T^2 to account for the density of states ($T^{3/2}$) thermal velocity ($T^{1/2}$) prefactor product. The log plot of the data pairs yields the activation energy from the linear slope, and the y-intercept provides information regarding high temperature limit of the capture cross section. The density of defects (N_T) in the material is related to the magnitude of the ΔC signal at the peak temperature, and for $\Delta C << C(t=\infty)$ can be shown to be equal to

$$N_T \cong 2(N_D - N_A)\frac{\Delta C}{C} \qquad \text{[IV-10]}$$

for an n-type material with donor concentration N_D and N_A compensating acceptor impurities per cubic centimeter. Figure IV-2 illustrates the previous discussions regarding the analog DLTS method. The figure specifically highlights the rate window definition in a) for a series of 35 millisecond capacitance transients showing the temperature evolution of the defect emission rate with increasing temperature. Three t_2 (t_2, t_2', t_2'') values are explicitly labeled, from which ΔC is measured, and three rate windows are defined per Equation IV-9. Also shown in Figure IV-2 a) is the specific

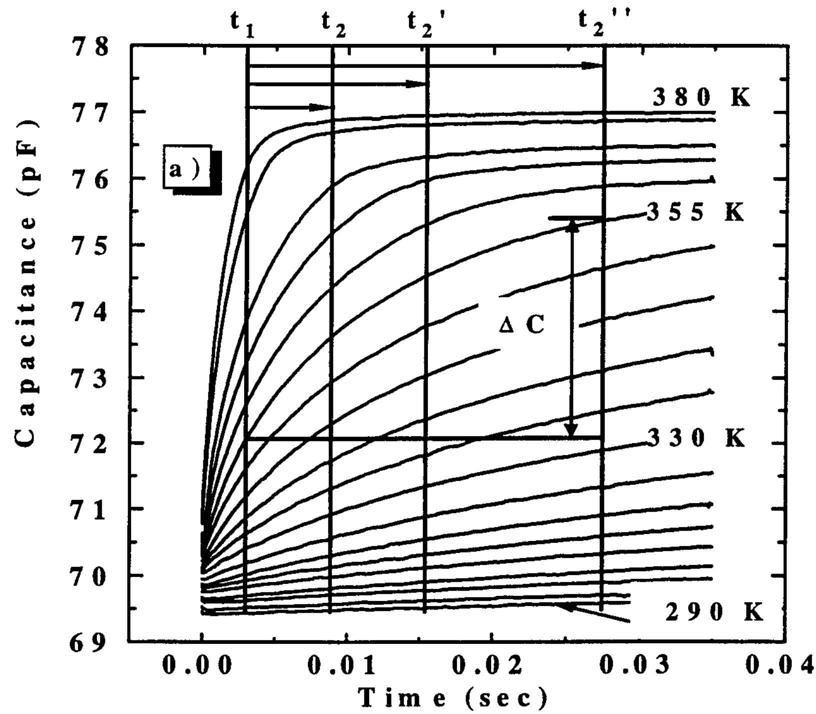

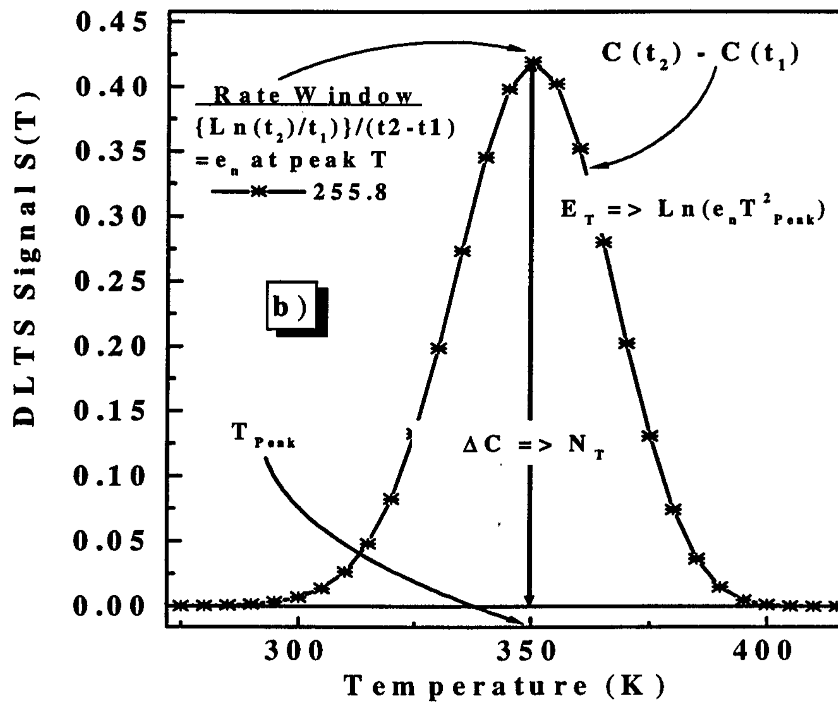

Figure IV-2. a) Capacitance-transient thermal evolution showing ΔC and three rate window definitions and b) resulting rate window spectral peak for one rate window ($255.8\ s^{-1}$).

value of ΔC for the capacitance decay at 355 K for the (t_1, t_2'') rate window interval. Part b) of the figure illustrates the spectral characteristic, S(T), resulting from a single rate window plot (255.8 s^{-1}) from which the peak positions and magnitudes will yield estimates for E_T, N_T, and σ, from Arrhenius analysis. Included in the figure is identification of the S(T) peak at approximately 350 K, which is the point at which the rate window being plotted is equal to the defect emission rate. The data plotted in Figure IV-2 was obtained from a numerically simulated data set which utilizes specific SiC material parameters in a model which was developed and used during this dissertation project to both predict and fit empirical DLTS results. This was accomplished to assist in determining the effects of several SiC peculiarities, which result in unique deep level phenomenon not observed in other materials. The specifics of these computations and the models used will be detailed in Chapter VI.

Since the presence of a junction capacitance is dependent upon the existence of a region depleted of free carriers, which itself is an equilibrating response to the imbalance of oppositely charged particles, then any perturbation to that charge balance will increase or decrease the junction capacitance. This perturbation can be a change in the applied bias to the diode since $C = dQ/dV$. However, the DLTS measurement cycle is specifically designed to monitor the effects due to changes in the total junction charge Q. This is simply due to the fact that as a deep level defect captures and emits carriers, single units of charge ($\pm q$) are added and subtracted from the total Q. So, the capacitance change we are interested in monitoring is due entirely to the exchange of carriers between trap levels and the resonant bands. The depletion region of a rectifying junction provides

a convenient vehicle for this process to be monitored. Thus, $\Delta C \propto \Delta Q$ since the applied voltage is constant during the data collection cycle. This is because all measurements are made when V-applied is at the reverse-bias value.

The ability to discriminate between hole and electron traps and the band to which they are being emitted is enabled by the dynamics of capacitance change described in the previous paragraph. The nomenclature used for DLTS or other capacitance spectroscopy methods is that a defect center is either a majority or a minority carrier trap. A majority carrier trap is defined as a defect where the thermal emission rate for majority carriers is greater than the thermal emission rate for minority carriers ($e_{maj} >> e_{min}$) . A minority carrier trap has the opposite definition. Thus, an electron trap is a majority carrier trap in n-type material and a minority carrier trap in p-type material. The reason for this definition is so that a single descriptor will unambiguously define a defect level for DLTS purposes. The bipolar nature of the non-equilibrium capacitance decay enables the determination of majority or minority carrier trap type. This is due to the manner in which the reverse-bias junction capacitance changes in response to the addition and removal of charges to the trap sites in the depletion region volume. The result is that for majority carrier traps, the capacitance is lower when the traps are full than when empty. Thus, the transient relaxation corresponding to carrier emission is in the direction of increasing capacitance. The opposite is true for minority carrier traps. This can be seen explicitly by considering the expression for the capacitance per unit area of an n-type Schottky diode

$$C(T,t) = \frac{\varepsilon}{W(T,t)} = \sqrt{\frac{q\varepsilon(N_D{}^+ \pm N_T(T,t))}{2(V_{bi} + V_R)}}. \qquad \text{[IV-11]}$$

What is immediately seen is that the change in capacitance is due to a change in the depletion width, W(T,t), which changes in response to carrier exchange with a density of trap sites, N_T(T,t), in order to maintain charge neutrality for the crystal. In Equation IV-11, the dependence upon the junction potential, V_{bi}, and applied bias, V_R, are shown but are constant during the measurement cycle, as is the temperature, T. The quantum unit of charge, q, is a positive quantity in all cases, and N_D^+ is the concentration of ionized (positive) shallow dopants impurities. Thus, in response to the addition or removal of a density of unit charges, the depletion width varies in a quadratic manner as does C(T,t) since $C = \varepsilon A/W$. If the concentration of trapped charges in the depleted region is zero (traps empty), then the capacitance has its reverse-bias, steady-state value, C(T,t = ∞). The ± sign preceding N_T(T,t) in Equation IV-11 is determined on the basis of whether the polarity of trapped carriers is the same as (+) or opposite to (-) the ionized dopant charge state, which is positive in this case (N_D^+). It is now easily seen to correspond with minority carrier (+) and majority carrier (-) trapping, is independent of the carrier type, and only dependent upon the base material conductivity. It is also straightforward to now see the increasing or decreasing nature of the non-equilibrium capacitance decay for majority or minority carriers respectively.

IV-I-2. Specific System Hardware and Implementation. The experimental characterization of SiC deep level defects performed during this research effort is a significant modification to the analog or rate window formalism described in the previous

subsection. The modifications implemented extend the capabilities of DLTS defect characterization by improving the resolution of multiple trap levels with comparable emission rates, enhanced ability to ascertain capture kinetics, reduced data acquisition time, and an increased flexibility to tailor experimental conditions while reducing system complexity. First, the method in which data is collected is digital rather than analog. Using digital acquisition, the entire capacitance decay transient is sampled and recorded at fixed isothermal intervals, typically between 2 and 5 K. Thus, rather than monitoring the capacitance at only two discrete points, while ramping the temperature several times at a well defined rate, the entire transient is recorded for subsequent analysis at fixed temperatures and only a single temperature sweep is required. This is accomplished by using an AT&T 386 personal computer for experiment control. A National Instruments high resolution 16-bit data acquisition hardware board (NIDAQ) was installed in the PC, allowing data collection and instrument control to be orchestrated by software written in the Lab Windows™ programming environment. The entire DLTS system is built around a SULA Corp. Deep Level Spectrometer, which contains the high speed (10 μs) capacitance meter required for accurate measurement of fast transients, and also performs the modulation of the D.C. bias-voltage waveforms with a 1 MHz A.C. signal required for capacitance measurement. Pulse waveform generation is accomplished using a Lecroy 9210 pulse generator, and a Lecroy 9410, 500 MHz oscilloscope is used to monitor the capacitance decay. Temperature control of the device under test (DUT) is performed in an RMC Corp. LTS22HT, closed-cycle, refrigerated He cryostat using Lakeshore 330 temperature controller electronics and a resistance heated test platen. This

enables thermal scans from 30 to 750 K, representing a significant extension of the upper temperature range limit for typical DLTS systems. This extended capability was implemented in order to characterize the potentially large ionization-energy traps in wide bandgap materials such as SiC and GaN. The necessity of a high temperature measurement capability can be seen by considering the temperature dependence of trap emission rates given in Equation IV-7 as they relate to the thermal ionization energy E_T. Additional system instrumentation include the Keithley 590 capacitance-voltage (C-V) meter and a Keithley 236 source-measure-unit (SMU), which allow additional device-under-test (DUT) characterization such as current-voltage (I-V) and C-V analysis including temperature dependencies, simply by executing software programs developed for the specific test. Figure IV-3 illustrates a detailed diagram of the experimental DLTS hardware configuration developed and used during this dissertation.

Signal-to-noise (SNR) is improved by averaging a significant number of transients at each isothermal step. The number required varies between samples and depends upon signal strength, but typically from 150 to 1000 transients are averaged. This averaging allows us to assume that the noise in our signals is zero-mean Gaussian, through the Central Limit Theorem. This point will become important when the discussion regarding transient fitting and parameter extraction are covered in the next chapter. Finally, if desired, the signal can be passed through a simple low-pass filter which was fabricated using operational amplifier circuitry and which has a cutoff of slightly greater than 1 MHz. With these SNR enhancements, the system sensitivity was determined to be in the mid-10^{-5} range.

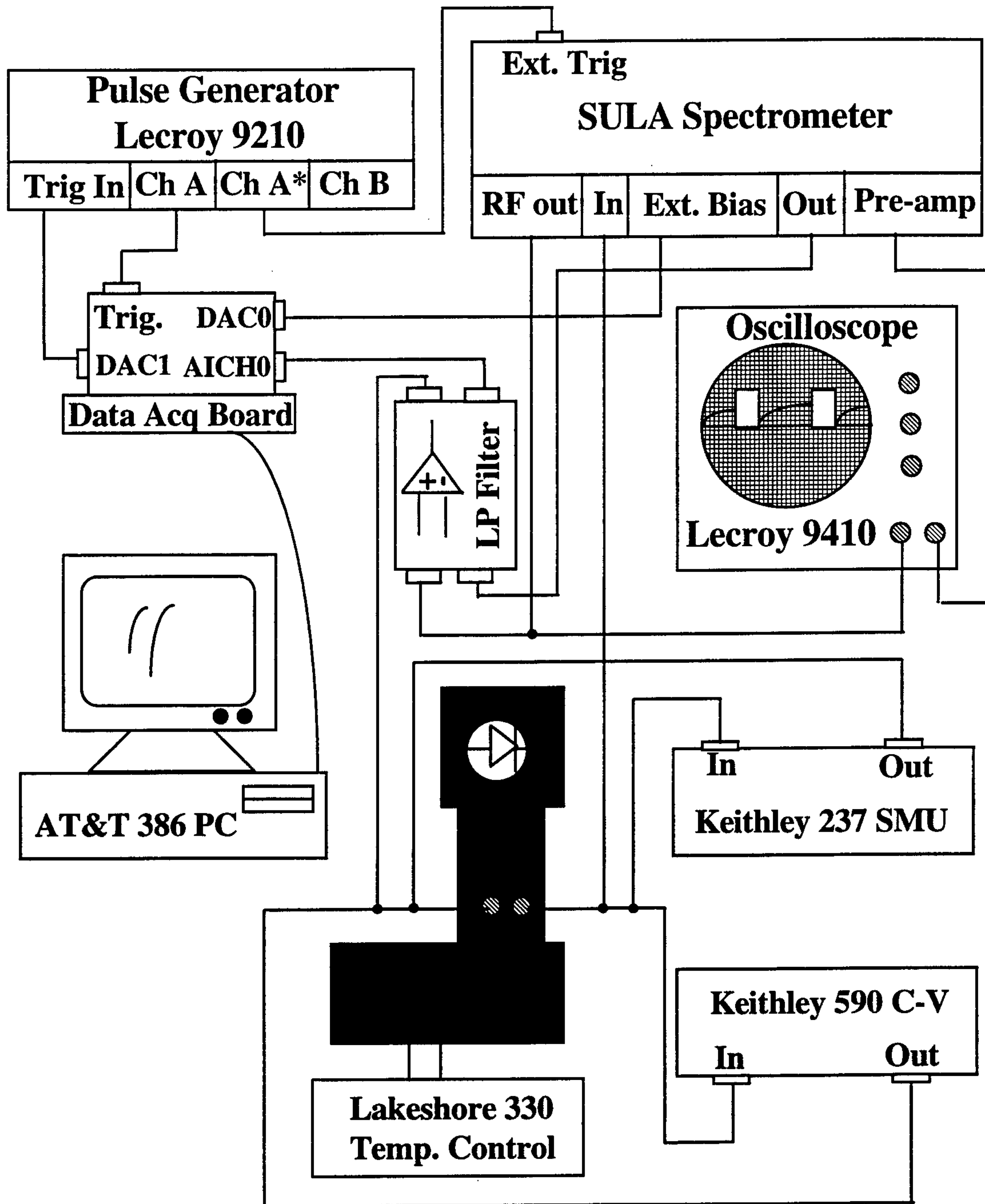

Figure IV-3. Schematic diagram of the DLTS system implemented and used to perform the characterization of SiC deep level defects. System is fully automated and the inclusion of a source-measure-unit (SMU) and capacitance-voltage (C-V) meter allow additional characterization such as I-V and C-V measurements including temperature dependencies.

This means that defect concentrations as low as 5×10^{-5} of the shallow dopant concentration are able to be detected. Thus, if the doping density were 10^{15} cm^{-3}, then trap concentrations of 5×10^{10} cm^{-3} or greater can be detected with this system.

Transient data records are determined by the sampling interval, number of data points or samples taken, the temperature range, and temperature interval (ΔT) step size. The sampling interval can vary from between 1 ms to 40 μs, and at this defined rate there are typically from 100 to 500 points recorded to comprise a digital record of the capacitance decay. Each of these isothermal transients is averaged the requisite number of times to improve SNR as mentioned above, and the temperature range over which the emission rate is favorable for measurement is typically around 100 K. Thus, recorded transient periods can vary from 0.5 seconds to several milliseconds at each isotherm with upwards of 50 transient records over a 100 K range available for subsequent analysis. The details of the transient fitting algorithms used to analyze the empirical data will be discussed in the following section.

Since the validity and accuracy of DLTS analysis depends upon the precision with which the time evolution of a trap emission rate is recorded, the need to maintain a high degree of control and accuracy on the sample temperature is acute. As a necessity, calibration of the DLTS hardware is periodically accomplished using a well established deep level standard. The procedure involves performing routine DLTS data acquisition scans on GaAs samples containing the EL2 level. The EL2 level is an anti-site defect in which an arsenic atom occupies a gallium lattice site As_{Ga}, resulting in a deep donor type defect level. The EL2 level has been well characterized using a variety of techniques

[Buchwald and Johnson, 1988:958], and the thermal ionization energy and capture cross section are established with a high degree of certainty. The accepted activation energy and capture cross section of the EL2 level are 0.810 ± 0.02 eV below the conduction band edge and (4.0±2.0) x10^{-15} cm^2, respectively. Consistent agreement with the reported EL2 trap parameters supports the high degree of confidence in the accuracy of DLTS results reported in this work.. The relatively large uncertainty (~50%) in the EL2 cross section assignment is typical of the imprecision with which this quantity is reported when estimated using DLTS techniques. This is due in part to the inherently large uncertainty associated with generating Arrhenius plots using only three or four points obtained from analog rate window spectral peaks. Since the original rate window method is still pervasive, the scatter in reported data is large due to this inefficiency. However, the primary factor causing the large σ uncertainty is the nominal assumption that the capture cross section is temperature or energy independent. In practice this is rarely the case, however, this assumption is consistently invoked in the literature when DLTS data is reported. In this regard, it would actually be much more appropriate to report defect data in terms of the capture and emission rates, however, the accepted formalism involves reporting defect parameters rather than rates. Representative DLTS calibration data for the GaAs EL2 level will be presented in the following chapter when we discuss its use as a standard to verify the functionality of a newly developed transient fitting algorithm

Other calibration detractors, which are systemic in nature, involve the parasitic capacitance due to leads and coaxial cabling, which can induce unphysical artifacts in the data records by altering the RC time constant of the sample plus hardware. These effects

are minimized by utilizing coaxial cabling of minimum length and ensuring good electrical contact at all interconnections. Finally, the individual instruments have on-board calibration routines which are periodically executed to ensure accurate operation, and DLTS biasing waveforms are monitored with an oscilloscope to verify compliance with run parameters.

V. DLTS Transient Analysis

V-I. Transient Data Fitting:Modulating Functions and Generalized Least Squares

The extraction of trap parameters from the digitized and recorded DLTS capacitance signals is accomplished using two digital signal processing techniques. The first method involves utilizing a correlation-like integral to fit exponential decay amplitude and time constant quantities to the empirical capacitance data. The method has been termed Modulating Functions (MF), and was originally developed to determine the dynamic properties of industrial factories, i.e., the differential or functional equations which describe their behavior [Loeb and Cahen, 1965:359]. In other words, to determine the equivalent of a linear system transfer function for complex non-linear industrial systems. The MF formalism was adapted to DLTS data analysis by Ransom *et al.* [1986:337], and was shown to be superior to Fourier transform, least squares, and the Method of Moments algorithms, which had previously been applied to the DLTS transient analysis problem. A second technique for data analysis was developed during this dissertation project, and resulted from a collaboration with Maj. Edward Ingham, Ph.D., of the Electrical Engineering Department at AFIT. The algorithm, which will be explained in detail below, is a novel parameter estimation methodology based on the Linear Prediction (LP) formalism. As will be shown, the algorithm was demonstrated to be superior to a previous linear prediction technique used for DLTS [Shapiro, Senturia, and Adler, 1984:3453], as was verified on synthesized as well as challenging actual DLTS signals.

V-I-1. Modulating Functions. The problem of parameter estimation for DLTS involves analyzing each isothermal capacitance transient, which has been sampled and recorded. The task becomes one of determining the baseline constant A_0, amplitude coefficients A_i, and time constants τ_i associated with a decaying capacitance signal. Under carefully constructed experimental conditions and with trap concentrations not violating the constraint leading to Equation IV-10 (i.e., avoiding conditions leading to non-exponential capacitance decay), the temporal, isothermal capacitance transient signal, g(t), may be modeled by

$$g(t) = A_0 + \sum_{i=1}^{N} A_i \exp(-t/\tau_i), \qquad \text{[V-1]}$$

where the summation is over the number N of distinguishable defects contributing to the signal, and is identified as the model order. In all cases of interest, the model order for DLTS decay transients is $N \leq 3$.

Determination of signal parameters A_0, A_i, and τ_i in the MF formalism proceeds by writing a relationship which eliminates the baseline constant A_0 as shown by

$$\frac{dg}{dt} + \alpha_1 \frac{d^2 g}{dt^2} + \ldots + \alpha_N \frac{d^{N+1} g}{dt^{N+1}} = 0 \qquad \text{[V-2]}$$

in which the α_i satisfy

$$\tau^N - \alpha_1 \tau^{(N-1)} + \ldots + (-1)^N \alpha_N = 0. \qquad \text{[V-3]}$$

The roots of τ in Equation V-3 are the τ_i in Equation V-1. Equations V-2 and V-3 must be solved for the α_i, which is accomplished by multiplying Equation V-2 by an

appropriate function and integrating over the length of the transient record. The function which multiplies Equation V-2 must satisfy the conditions given by

$$\left(\frac{d^m\theta}{dt^m}\right)\Big|_{t=t_{start}} = \left(\frac{d^m\theta}{dt^m}\right)\Big|_{t=t_{end}} = 0, \quad \text{where } m = 0,1,\ldots,N. \qquad \text{[V-4]}$$

The quantities t_{start} and t_{end} are the times where valid data starts and data collection terminates, respectively, and θ is the so-called *modulating function*. The resulting integro-differential equation, after integrating by parts N+1 times to transfer the g(t) derivatives of Equation V-2 to the modulating function, is

$$\int_{t_{start}}^{t_{end}} g\,\dot{\theta}\,dt - \alpha_1 \int_{t_{start}}^{t_{end}} g\,\ddot{\theta}\,dt + \ldots + \alpha_n \int_{t_{start}}^{t_{end}} g\,\overset{N+1}{\theta}\,dt = 0. \qquad \text{[V-5]}$$

For a desired model order, N, the α_i can now be obtained from the system of equations generated by using N different θ in Equation V-5. The α_i solutions can then be used to determine the τ_i from Equation V-3.

The amplitude coefficients are similarly found, once the time constants have been determined, using the relationship

$$\dot{g} = -\sum_{i=1}^{N} \frac{A_i}{\tau_i} e^{-\frac{t}{\tau_i}}. \qquad \text{[V-6]}$$

Then, as was done for the τ_i, Equation V-6 is multiplied by the same N weighting functions θ, and integrated by parts to obtain a system of equations from which the A_i are obtained. These equations have the form

$$\int_{t_{start}}^{t_{end}} g\,\dot{\theta}\,dt = -\sum_{i=1}^{N} \frac{A_i}{\tau_i} \int_{t_{start}}^{t_{end}} e^{-\frac{t}{\tau_i}}\,\dot{\theta}\,dt, \qquad \text{[V-7]}$$

and are easily solved for the amplitudes, A_i. The amplitude factors could actually be calculated using least squares or other algorithms, but using the MF formalism provides a more self-consistent solution.

To a great extent, the adequacy of the MF solutions to provide accurate parameter estimates is dependent upon the weighting or modulating functions selected. It is in this sense that the MF algorithm is often characterized as a "smoke and mirrors" technique, especially when also considering the entirely heuristic nature of the theoretical development. Thus, the choice of weighting functions is a rather nebulus task which borders on being classified as an art form. It has recently been determined that to maximize the energy resolving capability of the MF technique, weighting functions should be used which are sharply peaked, but not so sharp as to introduce errors in the numerical integration of Equation V-5 [Doolittle and Rohatgi, 1994:4560]. The functions implemented in the MF algorithm for fitting our DLTS experimental data are Lagrange type polynomial multipliers modulated by a sinusoidal function. The weighting functions commonly used to maximize the energy resolving power and which also satisfy the conditions of Equation V-4, are given by [Ransom *et al.*, 1984]

$$\theta_A(t) = (t - t_{start})^K (t_{end} - t)^K \sin\left(2\pi \frac{(t - t_{start})}{(t_{end} - t_{start})}\right), \qquad \text{[V-8]}$$

where K is greater than or equal to the model order number, N. To obtain N different modulating functions required to solve the N equations in N unknowns generated from

Equation V-5, we simply use various values of $K \geq N$ in Equation V-8 ($K = N, N+1,...,2N-1$).

In the actual analysis of experimental data records, the model order is an unknown, and must therefore become a parametric solution to the transient fitting problem. The determination of the number of exponential components in a signal plus noise is the most difficult parameter to accurately estimate. The methodology used to determine the model order and therefore, the correct exponential rates ($1/\tau_i$) is to sequentially fit the data using fixed values of N (1, 2, 3), and then compare the numerical results to the actual transient in a least squares sense. The fit which minimizes the least squares error quantity is then compared to results obtained using the determined model order, but now using entirely different modulating functions. If the solutions obtained using substantially different modulating functions agree closely, then the decay data is accurately described as this sum of exponentials. Once this processing has been completed, the model order and time constants are then utilized to compute the transient amplitude factors, A_i, using Equation V-7.

The MF algorithm has been demonstrated to have several advantages over analog rate window and other digital signal processing formalisms for obtaining accurate parameter estimates on challenging DLTS transient signals. Energy resolution of closely spaced emission rates, insensitivity to truncation error introduced due to finite measurement times, and excellent performance under low SNR conditions have all been demonstrated for the MF algorithm. An additional advantage which is afforded by using

the MF method is that of calculation speed, since it is not an iterative algorithm, making it attractive for implementation on personal computers.

Although the MF technique has significant merit as a credible approach to the parameter estimation problem presented by DLTS signals, the determination of an optimal set of weighting functions has no analytic basis, can depend upon the specific signal properties, and is therefore an undesirable aspect of accurate solution determination. In order to overcome these uncertainties, and provide a more straightforward process for the determination of signal parameters, a novel algorithm was developed and demonstrated during this dissertation project. The new methodology provides a solid analytic basis, and although iterative in nature, it is easily implemented as a MATLAB procedure, and executes in a time period comparable to the existing MF FORTRAN-77 software. As mentioned at the beginning of the chapter, this accomplishment was realized through a collaborative effort. Maj. Edward A. Ingham, Ph.D. of the Electrical Engineering Department, working under the tutelage of Dr. Meir Pachter, was responsible for the theoretical and software developments leading to an improved data analysis algorithm. The author was responsible for the original problem definition, demonstration and verification experiments, and computations and analysis of DLTS results. The algorithm, which resulted from these efforts, is based on a linear prediction formalism from signal processing theory, and was shown to be superior to previous linear prediction based algorithms [Ingham, Scofield, and Pachter, 1996:2805]. Additionally, initial comparisons between MF and the newly developed generalized least squares (GLS) algorithms indicate that GLS may be superior to MF in the poor SNR

regime. A thorough, comparative study of the relative strengths of these two methods has been planned as a near-term future project. The background summary of the algorithm and performance verification on simulated and real data is presented below.

V-I-2. Linear Prediction and Generalized Least Squares. The linear prediction (LP) parameter estimation method was originally proposed as an analysis tool for DLTS in 1984 by Shapiro *et al.* [1984:3453]. Since then, it has gained recognition as a credible approach to the challenging parameter estimation problem posed by transient DLTS signals [Doolittle and Rohatgi, 1994:4560, 1994:4570]. Based on advancements realized in the signal processing communities, the following paragraphs outline the improved linear prediction estimation approach developed for DLTS transient analysis. First, the original LP formalism is developed using a time domain approach rather than the transfer function paradigm previously used. Secondly, algorithms are developed for capacitance signals both with and without a baseline constant. The improved algorithm results primarily from the manner in which the effects of additive noise are dealt with. The enhanced performance of the improved LP estimator will be shown by comparison to synthesized transient data, which also serves to carefully calibrate the estimator. Finally, the ability of the novel parameter estimator will be applied to actual DLTS signals obtained on several defects in GaAs and SiC semiconductors.

Rewriting Equation V-1 with slightly different notation, we can write the discrete time isothermal capacitance transient signal as

$$g[m] = a_0 + \sum_{i=1}^{N} a_i (\lambda_i)^m + w[m], \quad \text{with } m = 0,1,\ldots,M-1 \; , \qquad \text{[V-9]}$$

where a_0 is the baseline constant, N is the number of modes or model order, λ_i are the decay exponentials ($\lambda_i = \exp[\Delta/\tau_i]$, where Δ is the sample period, and τ_i is the time constant), a_i are the amplitude coefficients for each exponential, M is the number of sample points, and w[m] are the additive noise contributions. The assignment of a statistical distribution to the noise will be deferred until later.

Shapiro *et al.* [1984:3453] recognized that the presence of an additive baseline constant with a magnitude much larger than the exponential amplitude factors seriously degraded the performance of their LP estimator. Their solution involved differencing successive points of the discrete signal prior to implementation of the fitting routine. This provided some improvements to their trap parameter estimates. Others have introduced hardware to estimate and remove the baseline constant directly from the capacitance signal [Doolittle and Rohatgi, 1992:5733]. The following derivations will sequentially include;

a) original LP estimator assuming a baseline free signal,

b) improved LP algorithm for signals without a baseline,

c) improved LP algorithm for signals with baseline constant a_0.

The resulting algorithms a) and b) are compared on simulated transient data in addition to a) and b) being compared to c). Finally, verification of the improvements afforded by the new algorithms on actual DLTS data is presented.

When a_0 is estimated and removed with system hardware, the signal model of Equation V-1, written in vector notation is given by

$$\vec{g} = \mathbf{V}\vec{a} + \vec{w} \ , \qquad \text{[V-10]}$$

where

$$\vec{g} = \{g[0]\ g[1]\ \ldots\ g[M-1]\}^T,$$
$$\mathbf{V} = \{\vec{v}(\lambda_1)\ \vec{v}(\lambda_2)\ \ldots\ \vec{v}(\lambda_N)\},$$
$$\vec{v}(\lambda_i) = \{1\ \lambda_i\ \lambda_i^2\ \ldots\ \lambda_i^{M-1}\}^T,$$
$$\vec{a} = \{a_1\ a_2\ \ldots\ a_N\}^T,$$
$$\vec{w} = \{w[0]\ w[1]\ \ldots\ w[M-1]\}^T.$$

As seen from the above definition, the matrix **V** is MxN dimensional, and has Vandermonde structure, which implies invertibility if the following conditions are satisfied: for $M > N$ (always satisfied for real DLTS data sets) and $\lambda_{i1} \neq \lambda_{i2}$, **V** will have full column rank N.

In a least squares analysis, we desire the parameters a_i and λ_i which minimize the quantity

$$\begin{aligned} J(a_i, \lambda_i) &= \sum_{m=0}^{M-1} \left(g[m] - \sum_{i=1}^{N} a_i \lambda_i^m \right)^2 \\ &= (\vec{g} - \mathbf{V}\vec{a})^T (\vec{g} - \mathbf{V}\vec{a}) \\ &= \vec{g}^T \vec{g} - 2\vec{g}^T \mathbf{V}\vec{a} + \vec{a}^T \mathbf{V}^T \mathbf{V}\vec{a} \, . \end{aligned} \qquad \text{[V-11]}$$

Assuming that the λ_i in V can be accurately estimated, the amplitude coefficients vector $\vec{a}$ can be estimated from Equation V-11 using the pseudo-inverse estimator

$$\vec{a} = (\mathbf{V}^T \mathbf{V})^{-1} \mathbf{V}^T \vec{g} \ , \qquad \text{[V-12]}$$

which is obtained by setting the gradient of J with respect to $\vec{a}$ in Equation V-11 equal to zero. Thus, we see that the estimation problem is reduced to that of accurately determining the λ_i in **V**.

Previously, in order to obtain analytic expressions for the estimation of λ_i, the procedure has been to apply the discrete z-transform, and take the transfer function approach. Alternatively, the derivation here adheres to a time domain approach following from differential equation theory [Lanczos, 1956]. If we notate the noiseless signal minus baseline constant, A_0, as s[m], then g[m] = s[m] + w[m] from Equation V-9. We know that a linear combination of exponentials is the solution to an ordinary differential equation with constant coefficients. The same is true, in discrete time, for a difference equation with constant coefficients. We can then claim that the noiseless signal

$$s[m] = a_1\lambda_1^{\ m} + a_2\lambda_2^{\ m} + \ldots + a_N\lambda_N^{\ m} \qquad \text{[V-13]}$$

satisfies the difference equation

$$s[m] + b_1 s[m-1] + \ldots + b_N s[m-N] = 0. \qquad \text{[V-14]}$$

Furthermore, the characteristic polynomial formed from the coefficients of the linear difference equation [V-14]

$$z^N + b_1 z^{N-1} + \ldots + b_N = 0 \qquad \text{[V-15]}$$

can be rooted to yield the soluble exponential transient factors λ_i.

If 2N noiseless data points of s[m] are available, the difference equation [V-14] can be written as N-equations in N-unknowns. From this system of equations, the constant coefficients b_i can be solved, and the exponentials, λ_i, can be rooted for the desired solution.

Note that the estimator just developed is based on a noiseless signal model. If s[m] is replaced by the actual observed signal, g[m], the estimators performance will be seriously degraded even at relatively high SNRs. Nevertheless, Equation V-14 has been applied to real signals by including an error expression, e[m], to form the linear prediction equation for real signals with noise

$$g[m] = -b_1 g[m-1] \ldots - b_N g[m-N] + e[m]. \qquad \text{[V-16]}$$

The error term, e[m], is referenced as the LP error. Again, if more than 2N data points are available, Equation V-16 can be written as a system of equations, but which in this case are overdetermined. The result is

$$\vec{g}_0 = -\mathbf{G}\vec{b} + \vec{e}\ , \qquad \text{[V-17]}$$

where we now have

$$\begin{aligned}
\vec{g}_0 &= \{g[N]\, g[N+1] \ldots\, g[M-1]\}^T,\\
\mathbf{G} &= \{\vec{g}_1\, \vec{g}_2 \cdots \vec{g}_N\},\\
\vec{g}_i &= \{g[N-i]\, g[N+1-i] \ldots\, g[M-1-i]\}^T,\\
\vec{b} &= \{b_1\, b_2 \ldots\, b_N\}^T,\\
\vec{e} &= \{e[N\}\, e[N+1] \ldots\, e[M-1]\}^T.
\end{aligned}$$

The matrix **G** is an (M-N) x N dimensional data matrix. In a least squares sense, b_i can be estimated by finding the $\vec{b}$-vector that minimizes the quantity

$$J(b_i) = (\vec{g}_0 + \mathbf{G}\vec{b})^T (\vec{g}_0 + \mathbf{G}\vec{b}). \qquad \text{[V-18]}$$

Following the same procedure leading to Equation V-12 yields the pseudo-inverse estimator for the $\vec{b}$-vector defined below as

$$\vec{b} = -(\mathbf{G}^T\mathbf{G})^{-1}\mathbf{G}^T\vec{g}_0. \qquad \text{[V-19]}$$

In practice, this widely used least squares estimator of the b_i, which upon rooting leads to the λ_i estimates, performs poorly even at relatively high SNRs [Kay, 1988]. The poor performance will be explained when a statistical distribution is assigned to the noise component, w[m], and the improved LP estimator is derived and compared to the least squares estimator given above.

In practice, estimates of λ_i are achieved by initially assuming a model order L, assumed to be much greater than N, then estimating L linear prediction coefficients, b_i, and finally eliminating the L-N extraneous solutions using some discrimination criteria. It is heuristically argued that the L-N extraneous modes actually model the noise components while the N remaining modes accurately model the desired signal component of the recorded data. This commonly used procedure is called overmodeling, and L has been termed the prediction order.

The overmodeled least squares estimator developed to this point is exactly the algorithm that Shapiro *et al.* applied to DLTS signal analysis [1984:3453]. This algorithm will henceforth be referenced as overmodeled least squares (OLS). The discrimination criteria that they applied to identify the L-N undesired modes was based on the postulate that all extraneous exponentials are complex. Thus, actual mode acceptance and model order were determined entirely on the basis of this complex number sort. During our comparison of OLS performance with the improved estimator, it

was determined that the complex criteria was insufficient for complete mode identification, and an additional criteria was included, which is known as an energy sort.

Heuristic in nature also, but appealing, the energy sort has been successfully applied to radar signals [Sacchini *et al.*, 1994:91]. It is based on the calculation of the amplitude coefficients with the pseudo-inverse estimator, Equation V-12, which is rewritten here for convenience

$$\vec{a} = \left(V^T V\right)^{-1} V^T \vec{g}.$$

When applied to the OLS algorithm, the coefficient estimator above will require the signal vector, $\vec{g}$, and the overmodeled exponential matrix $\mathbf{V}_{\mathbf{over}}$ to yield overmodeled amplitude coefficients, a_i, in a vector $\vec{a}_{over}$. The heuristic argument used to validate the energy sort criteria is as follows: when an exponential, λ_i, is unphysical or extraneous to the observed data, g, its corresponding amplitude coefficient, A_i, is typically small. A simple, but intuitively pleasing argument. The energy sort is applied subsequent to OLS estimation of the overmodeled λ_i, and A_i extraneous modes are sorted and separated as described below. The energy of a single mode is defined as

$$
\begin{aligned}
E_i &= \sum_{m=0}^{M-1} \left| a_i (\lambda_i)^m \right|^2 \\
&= \left| a_i \right|^2 \sum_{m=0}^{M-1} \left| \lambda_i \right|^{2m} \qquad\qquad . \qquad\qquad \text{[V-20]} \\
&= \begin{cases} \left| a_i \right|^2 \left(\dfrac{1 - \left| \lambda_i \right|^{2M}}{1 - \left| \lambda_i \right|^2} \right) & \text{if } \left| \lambda_i \right| \neq 1 \\ \left| a_i \right|^2 M & \text{for } \left| \lambda_i \right| = 1 \end{cases}
\end{aligned}
$$

Using the energy sort criterion, the N *real* modes with the highest energy, E_i, are considered to be the actual decay modes of the DLTS signal. Although it was not the objective, and was not pursued, the energy sort procedure should have model order selection applications as well. In practice, the model order is assumed, and we execute the algorithm sequentially for N = 1, 2, and 3, and in each instance the solution mode with the largest energy value is retained as the estimated decay mode. Intuitive analysis of the resulting Arrhenius data is required to match physical reality with the estimates to arrive at a final determination of the decay model order.

Despite the improved performance, overmodeling presents several drawbacks. First, the prediction order, L, introduces another unknown, which is critical to the performance of the estimator. Shapiro *et al.* suggested that values from between 20 and 50 should be tested to determine the best transient fit. Secondly, the larger model order creates the necessity to root a higher degree polynomial. Unfortunately, rooting is an inherently ill-conditioned numerical procedure, and errors are significantly exacerbated by increasing the polynomial's degree.

Fortunately, as will be demonstrated shortly, improved LP performance without overmodeling can be achieved by properly incorporating the effects of additive noise, w[m]. In order to accomplish the desired improvements, a statistical assumption must be made regarding the noise component. Specifically, it was assumed that the w[m] for each measurement point, g[m], are Gaussian random variables, which are uncorrelated across all M data points of each isothermal transient, and are identically distributed with zero mean and variance σ^2. The justification for this assumption is based on the large number of signal averages executed for each transient record and the Central Limit Theorem [Papoulis, 1991].

Before the improved estimator is developed, a few definitions are required to demonstrate the implications of our statistical noise assumptions, and will be required in the subsequent derivation. Consider the overdetermined set of equations in vector notation

$$L\vec{u} = \vec{f}, \qquad \text{[V-21]}$$

where the vector $\vec{u}$ is unknown. Following the previous developments, we desire the $\vec{u}$-vector that minimizes the following quantity in a least squares sense

$$\left(L\vec{u} - \vec{f}\right)^T\left(L\vec{u} - \vec{f}\right) = \vec{r}^T\vec{r}. \qquad \text{[V-22]}$$

Now, when the residual $\vec{r}$-vector in Equation V-22 is distributed Gaussian, mean vector zero with covariance matrix $\sigma^2 I$ (I is the identity matrix), then the pseudo-inverse estimator

$$\vec{u} = \left(L^T L\right)^{-1} L^T \vec{f} \qquad \text{[V-23]}$$

is a minimum variance unbiased (MVU) estimator of the $\vec{u}$-vector [Kay, 1993]. Therefore, with our noise distribution assumption, the amplitude coefficient estimator given by Equation V-12 is an MVU estimator.

The outline of the improved linear prediction fitting algorithm can now proceed by recalling that the signal model including noise is given by g[m] = s[m] + w[m]. If we insert this expression into the noiseless difference equation previously introduced as Equation V-14, we will obtain the same linear prediction Equation V-16 with the exception that the LP error term is now given by

$$e[m] = w[m] + b_1 w[m-1] + \ \dots \ + b_N w[m-N] \qquad \text{[V-24]}$$

where as before, m ranges from zero to the total number of sampled data points (M-1). The LP error given by Equation V-24 now has known structure. It is the sum of Gaussian random variables, and although each w[m] is uncorrelated over all m, each e[m] is correlated with the ±N adjoining elements e[m].

We can now write the overdetermined set of equations consistent with Equation V-17 as

$$\vec{g}_0 + \mathbf{G}\vec{b} = \vec{e}. \qquad \text{[V-25]}$$

We know the distributional structure of the LP error vector, $\vec{e}$, which is that each w[m] in e[m] has zero mean, thus the mean of $\vec{e}$ is the zero vector. We can define the LP error covariance matrix, $\sigma^2 R$, of $\vec{e}$ as

$$\sigma^2 R = \begin{bmatrix} E\{e[N]e[N]\} & E\{e[N]e[N+1]\} & \cdots & E\{e[N]e[M-1]\} \\ E\{e[N+1]e[N]\} & E\{e[N+1]e[N+1]\} & \cdots & E\{e[N+1]e[M-1]\} \\ \vdots & \vdots & \ddots & \vdots \\ E\{e[M-1]e[N]\} & E\{e[M-1]e[N+1]\} & \cdots & E\{e[M-1]e[M-1]\} \end{bmatrix}_{(M-N)x(M-N)},$$

[V-26]

where the matrix entries are obtained from Equation V-24 as shown explicitly below

$$E\{e[m_1]e[m_2]\} = E\left\{\left(w[m_1]+\sum_{i=1}^{N} b_i w[m_1-i]\right)\left(w[m_2]+\sum_{i=1}^{N} b_i w[m_2-i]\right)\right\} \quad \text{[V-27]}$$

with $m_1 = N, N+1, \ldots, M-1$, and $m_2 = N, N+1, \ldots, M-1$,

and E{*} represents the expectation value operator.

When the matrix elements, $\sigma^2 R_{ij}$, are calculated using Equation V-27 and the uncorrelated noise assumption, $E\{w[m_1]w[m_2]\} = 0$ for m_1 m_2, is invoked for the cross terms, we can write

$$R_{ij} = \begin{cases} 1+\sum_{n=1}^{N} b_n^{\,2} & \text{for} \quad i=j \\ b_{|i-j|} + \sum_{n=1}^{N-|i-j|} b_n b_{n+|i-j|} & \text{for} \quad |i-j|<N \\ b_{|i-j|} & \text{for} \quad |i-j|=N \\ 0 & \text{for} \quad |i-j|>N \end{cases} \quad \text{[V-28]}$$

Observing the resulting matrix structure, it is discovered that we could alternatively write

$$R = BB^T, \quad \text{[V-29]}$$

where **B** is an (M-N) x M Toeplitz matrix

$$\mathbf{B} = \begin{bmatrix} 1 & b_1 & \dots & b_N & 0 & \cdots & 0 \\ 0 & 1 & b_1 & \cdots & b_N & \ddots & \vdots \\ \vdots & \ddots & \ddots & \ddots & \ddots & \ddots & 0 \\ 0 & \cdots & 0 & 1 & b_1 & \cdots & b_N \end{bmatrix} . \quad [V-30]$$

The matrix B has full row rank M-N. Therefore R has full rank M-N and is positive definite. A Cholesky decomposition of R will provide a nonsingular lower triangular matrix R_l such that

$$R = R_l R_l^T \ . \quad [V-31]$$

If R was known, then R_l^{-1} could be used to linearly transform the LP error vector, $\vec{e}$. The vector $R_l^{-1}\vec{e}$ would still have a mean vector zero, but would possess a covariance matrix $\sigma^2 R_l^{-1} R (R_l^{-1})^T$ [Scharf, 1990]. Because $R = R_l R_l^T$ from Equation V-31, we can write

$$R_l^{-1} R = R_l^T \ , \ \text{thus} \Rightarrow \ R_l^{-1} R (R_l^{-1})^T = I.$$

Therefore, $R_l^{-1}\vec{e}$ would have a covariance matrix $\sigma^2\mathbf{I}$. Applying this result to Equation V-18 gives the minimization expression

$$R_l^{-1}\vec{e} = R_l^{-1}\vec{g}_0 + R_l^{-1}\mathbf{G}\vec{b}, \quad [V-32]$$

and thus the pseudo-inverse estimator Equation V-19 can now be written as

$$\begin{aligned} \vec{b} &= -\left((R_l^{-1}G)^T (R_l^{-1}G)\right)^{-1} (R_l^{-1}G)^T \vec{g}_0 \\ &= -\left(G^T (R_l R_l^T)^{-1} G\right)^{-1} G^T (R_l R_l^T)^{-1} \vec{g}_0 \\ &= -(G^T R^{-1} G)^{-1} G^T R^{-1} \vec{g}_0 \end{aligned} \quad [V-33]$$

which is an MVU estimator of $\vec{b}$, and is the improved, generalized least squares (GLS) estimator.

In practice, **R** is unknown because $\vec{b}$ is unknown. This difficulty is circumvented by resorting to an iterative generalized least squares (IGLS) approach. With the IGLS algorithm, previous estimates of $\vec{b}$ are utilized to create R for re-estimation of $\vec{b}$ using Equation V-33. Our initial $\vec{b}$ is obtained from a least squares solution, and convolution routines are implemented to efficiently create **R** [Ingham, 1996].

Our first comparison of the IGLS and OLS estimators was on simulated DLTS transient data. Artificial decay records of 100 sampled points were generated with the inclusion of randomly generated Gaussian noise. A model order of 2 was selected for resolution comparison with the following amplitude and exponential decay signal parameters: $a_1 = -1$, $a_2 = -0.5$, $\lambda_1 = 0.8$, and $\lambda_2 = 0.9$. The τ_2/τ_1 time constant ratio was 2.12, and the a_0 baseline constant was assumed to have been estimated and removed with hardware. The SNR was varied and determined, in dB, using the formula

$$\sigma^2 = \frac{|a_1|^2}{10^{SNR/10}} .$$

For each realization, 10 iterations were performed with the IGLS algorithm and three separate runs of the OLS routine were executed with prediction orders L = 20, 30, and 40. The energy sort described previously was used for the OLS algorithm.

Figures V-1 and V-2 graphically illustrate the performance comparisons of IGLS versus OLS for λ_1 and λ_2 estimates, respectively. The data is represented in a format in which 10Log_{10} of the inverse mean squared error (MSE) is plotted against SNR for each of the decay exponential fit results. The MSE is calculated after 200 Monte-Carlo

simulations for each SNR point. The use of the 10Log_{10} and 1/MSE plot as a comparative figure-of-merit is justified by the linear relation to the Cramer Rao Bound (CRB), which is also plotted in both of the figures. For each parameter, the CRB identifies a log-linear bound for the variance of all unbiased estimators [Kay, 1993]. Additionally, the CRB is

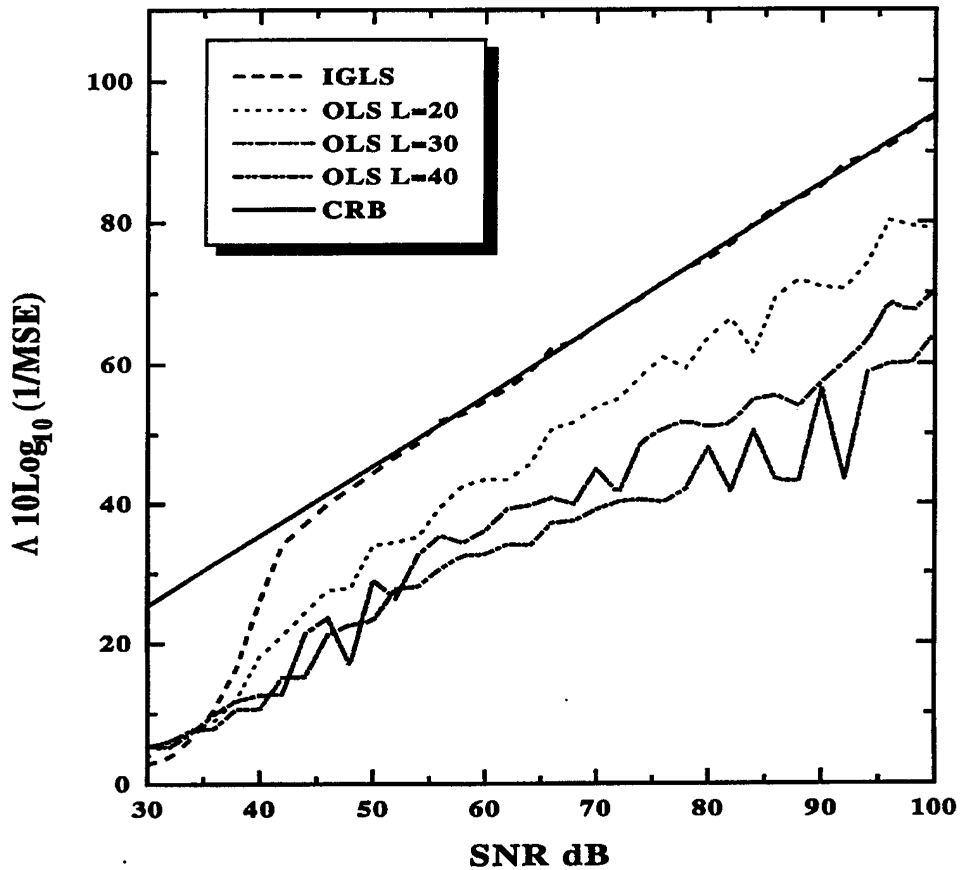

Figure V-1. Inverse mean square error versus SNR plot for the IGLS and OLS estimates of exponential component $\lambda_1 = \exp(-\Delta/\tau_1)$. Illustrated are the performance comparisons between results of the two fitting algorithms on 2-mode (λ_1,λ_2) simulated decay signals without a baseline constant, as related to the Cramer Rao Bound (CRB) metric. The OLS prediction order was varied between L = 20 , 30, and 40 as notated in the inset. The simulated signal parameters are described in the text.

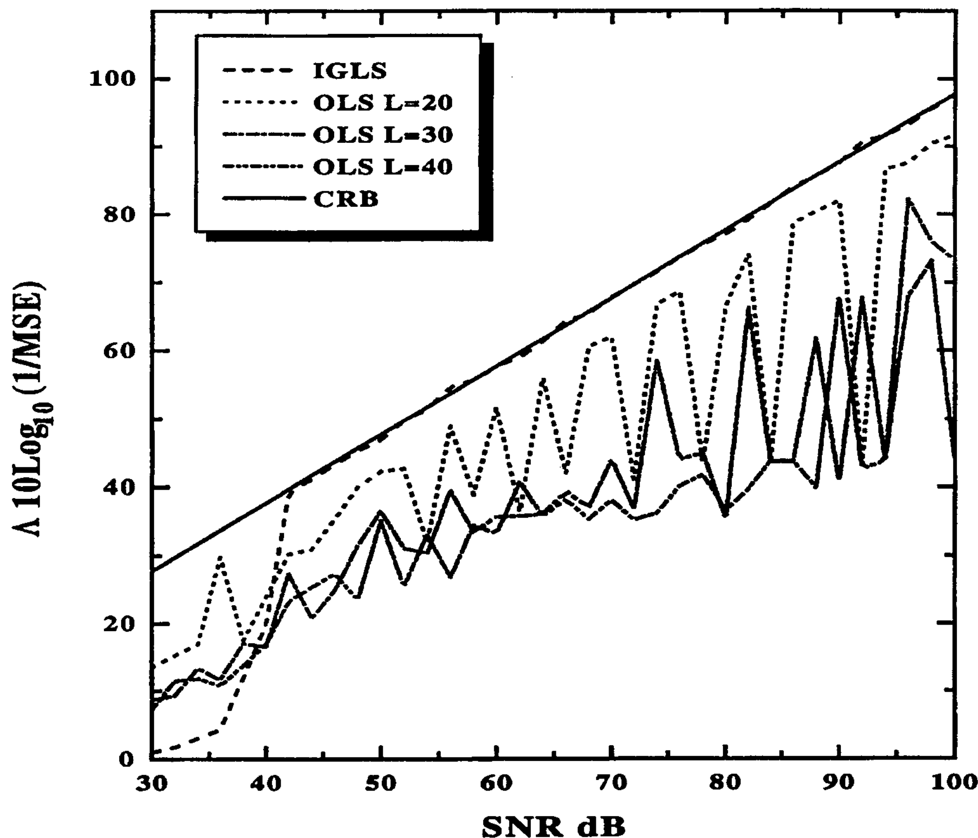

Figure V-2. Inverse mean square error versus SNR plot for the IGLS and OLS estimates of exponential component $\lambda_2 = \exp(-\Delta/\tau_2)$. Illustrated are the performance comparisons between the two fitting algorithms on the same 2-mode (λ_1,λ_2) simulated decay signals without a baseline constant used for the data of Figure V-1. The Cramer Rao Bound (CRB) metric is illustrated again as the solid curve, and the OLS prediction orders are consistent with the previous figure.

dependent only upon the signal parameters, and is therefore an excellent benchmark for the comparison of all competing estimators.

As seen in Figures V-1 and V-2, the IGLS results consistently yield lower variance estimates than OLS, regardless of prediction order L over a usable range of SNRs. It is also significant to note that IGLS attains the CRB above an approximately 44 dB threshold, as seen in the figures. The OLS performance is seen to decrease as SNR

increases because overmodeling becomes inappropriate as the noise becomes less significant.

Performance verification of the IGLS algorithm on actual DLTS signals with unknown model order and arbitrary SNR is critical to the claim of improved parameter estimation capabilities. Our experiments to verify these results did not employ hardware for the estimation and removal of the baseline constant, a_0. Consequently, the results of IGLS performance comparisons on empirical data will be deferred until the following necessary derivation is presented, in which the procedure is modified to handle signals with baselines a_0.

Consistent with the approach taken by Shapiro *et al.* [1984:3453], we utilize the differencing approach to remove the baseline constant, a_0, prior to implementing IGLS estimation. In the case of LS or OLS, differencing compounds the problems related to their inadequate noise analysis, causing performance to degrade significantly as SNR decreases. Using the methodology leading to the GLS estimator, Equation V-33, a differenced IGLS algorithm was developed, which completely accounts for the inclusion of random noise fluctuations. As will be shown, simulations confirm that the accuracy of parameter estimates on signals with baseline offsets are similar to that which was achieved using IGLS on signals without a baseline constant a_0.

We begin by writing the signal model originally defined in Equation V-9 with the explicit consideration of differencing adjacent data points to eliminate the baseline constant a_0. The model under consideration now is given as

$$g_d[m] = g[m] - g[m+1]$$
$$= s_d[m] + w[m] - w[m+1], \qquad m = 0,1,\ldots,M-2 \ , \qquad \text{[V-34]}$$

where recalling that g[m] = s[m] + w[m] (signal plus noise). We see that the differenced noiseless signal, $s_d[m]$, is defined as

$$s_d[m] = \sum_{i=1}^{N} (1-\lambda_i) a_n \lambda_i^{\ m} . \qquad \text{[V-35]}$$

As was the case for Equation V-13, the noiseless signal $s_d[m]$ is also a solution to a difference equation with constant coefficients consistent with Equation V-14. Therefore, if we let

$$s_d[m] = g_d[m] - w[m] + w[m+1] \ , \qquad \text{[V-36]}$$

we can write a linear prediction equation comparable to Equation V-16 for the differenced signal plus noise as

$$g_d[m] = -b_1 g_d[m-1] \cdots \ - b_N g_d[m-N] + e_d[m], \qquad \text{[V-37]}$$

where we now have

$$e_d[m] = w[m] + b_1 w[m-1] \cdots \ + b_N w[m-N]$$
$$- w[m+1] - b_1 w[m] \cdots \ - b_N w[m-N+1] \ . \qquad \text{[V-38]}$$

The differenced LP error expression has a greater number of elements than the previous e[m], but is still composed entirely of weighted Gaussian random variables. Following the previous derivations, we can define an overdetermined system of equations

$$\vec{g}_{d0} + \mathbf{G_d}\vec{b} = \vec{e}_d \,, \qquad \text{[V-39]}$$

where as before, the LP error vector $\vec{e}_d$ is distributed with mean vector zero and covariance matrix $\sigma^2\mathbf{R_d}$. If we now define the (M-N) x (M-1) Toeplitz matrices, which as before, are obtained by performing the expectation operator products in the error covariance matrix $\sigma^2\mathbf{R_d}$

$$\mathbf{B_1} = \begin{bmatrix} \mathbf{1} & \mathbf{b_1} & \cdots & \mathbf{b_N} & \mathbf{0} & \cdots & \mathbf{0} \\ \mathbf{0} & \mathbf{1} & \mathbf{b_1} & \cdots & \mathbf{b_N} & \ddots & \vdots \\ \vdots & \ddots & \ddots & \ddots & \ddots & \ddots & \mathbf{0} \\ \mathbf{0} & \cdots & \mathbf{0} & \mathbf{1} & \mathbf{b_1} & \cdots & \mathbf{b_N} \end{bmatrix} \qquad \text{[V-40]}$$

and

$$\mathbf{B_2} = \begin{bmatrix} 0 & 1 & b_1 & \cdots & b_{N+1} & b_N & 0 & \cdots & 0 \\ 0 & 0 & 1 & b_1 & \cdots & b_{N+1} & b_N & \ddots & \vdots \\ \vdots & \vdots & \ddots & \ddots & \ddots & \ddots & \ddots & \ddots & 0 \\ \vdots & \vdots & & \ddots & \ddots & \ddots & \ddots & \ddots & b_N \\ 0 & 0 & \cdots & \cdots & 0 & 1 & b_1 & \cdots & b_{N+1} \end{bmatrix} . \qquad \text{[V-41]}$$

Then the differenced LP error covariance matrix, $\mathbf{R_d}$, is obtained using

$$R_d = 2B_1B_1^T - B_1B_2^T - B_2B_1^T \,, \qquad \text{[V-42]}$$

and finally, the GLS pseudo-inverse estimator becomes

$$\vec{b} = -(G_d{}^T R_d{}^{-1} G_d)^{-1} G_d{}^T R_d{}^{-1} \vec{g}_{d0} \,. \qquad \text{[V-43]}$$

As before, an iterative process is required to finally obtain the coefficients, $\vec{b}$, of the linear difference equation. Recall that the roots of the characteristic polynomial

(Equation V-15) formed from these difference equation coefficients, $\vec{b}$, will yield the desired exponentials λ_i. Finally, as was defined in Equation V-12, the signal amplitude coefficients a_i can be estimated from an expanded pseudo-inverse estimator

$$\begin{bmatrix} a_0 \\ \vec{a} \end{bmatrix} = (V_{co}^T V_{co})^{-1} V_{co}^T \vec{g} \ , \qquad [V-44]$$

where the matrix $\mathbf{V}_{co}$ consists of an M-dimensional column of ones (1's) appended in front of **V** (to account for the constant a_0).

Comparison experiments were conducted using the differenced, iterative, generalized least squares (DIGLS) estimator on the same simulated 2-mode decay signals, but this time including a baseline constant, a_0, with a value of 50. Performance was measured against the differenced, overmodeled, least squares (DOLS) algorithm, which utilized the same energy sort as the OLS algorithm in the previous baseline free experiments. The experiment was conducted under identical conditions as the IGLS and OLS comparison, including the prediction order selection of L = 20, 30, and 40. Figures V-3 and V-4 graphically illustrate the results of the DIGLS versus DOLS performance comparison for the λ_1 and λ_2 estimates, respectively. Similar to the results of the previous comparison, the DIGLS is seen to consistently outperform DOLS over a usable range of SNRs, and also attains the CRB at a comparable SNR. Figure V-5 represents a comparison between IGLS and DIGLS results for estimates of exponential signal component λ_1. Immediately apparent from the Figure V-5 data is that addition of the a_0 constant does not significantly affect the accuracy of the improved estimators.

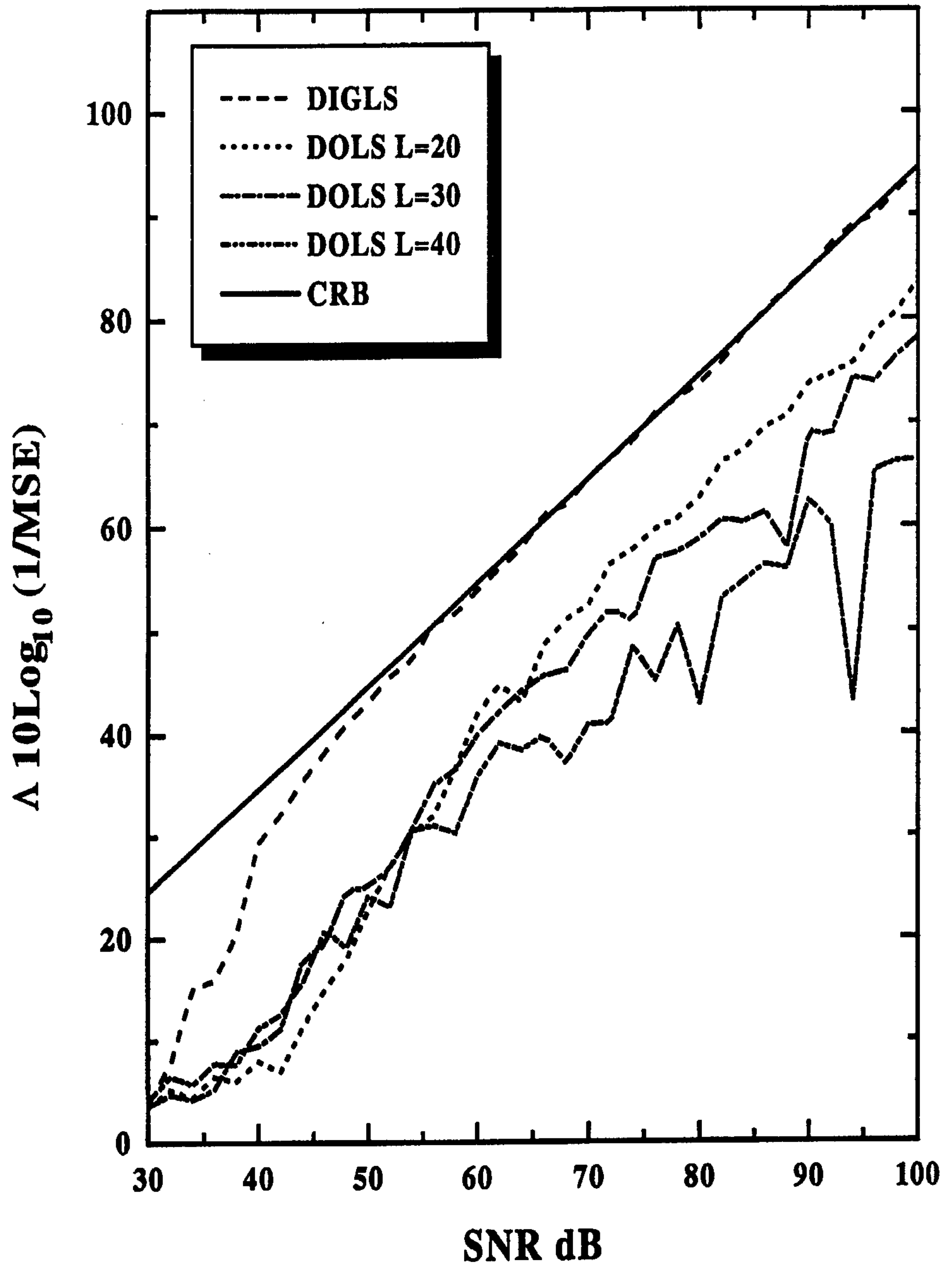

Figure V-3. Inverse MSE versus SNR plot for the DIGLS and DOLS estimates of exponential component $\lambda_1 = \exp(-\Delta/\tau_1)$. Performance comparisons between results of the two fitting algorithms on 2-mode (λ_1,λ_2) simulated decay signals with a baseline constant, as related to the CRB metric, are illustrated. The DOLS prediction order was again varied between L = 20 , 30, and 40. The simulated signal parameters are described in the text, and were unchanged from the previous IGLS and OLS comparisons except with the addition of a baseline constant value of 50.

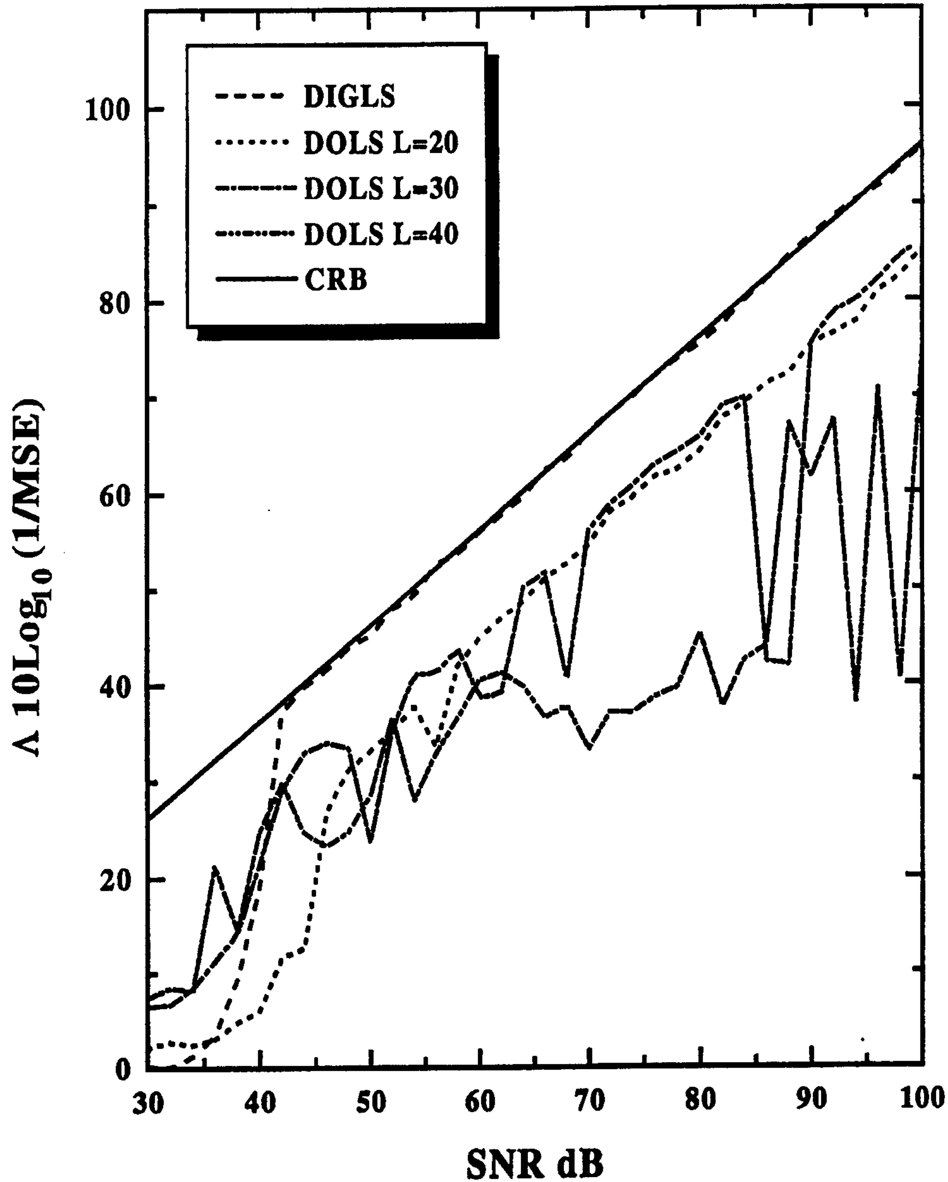

Figure V-4. Inverse MSE versus SNR plot for the DIGLS and DOLS estimates of exponential component $\lambda_2 = \exp(-\Delta/\tau_2)$. Performance comparisons between results of the two fitting algorithms on 2-mode (λ_1,λ_2) simulated decay signals with a baseline constant, as related to the CRB metric, are illustrated. The DOLS prediction order was varied between L = 20 , 30, and 40. The simulated signal parameters are described in the text, and were unchanged from the previous IGLS and OLS comparisons except with the addition of a baseline constant value of 50.

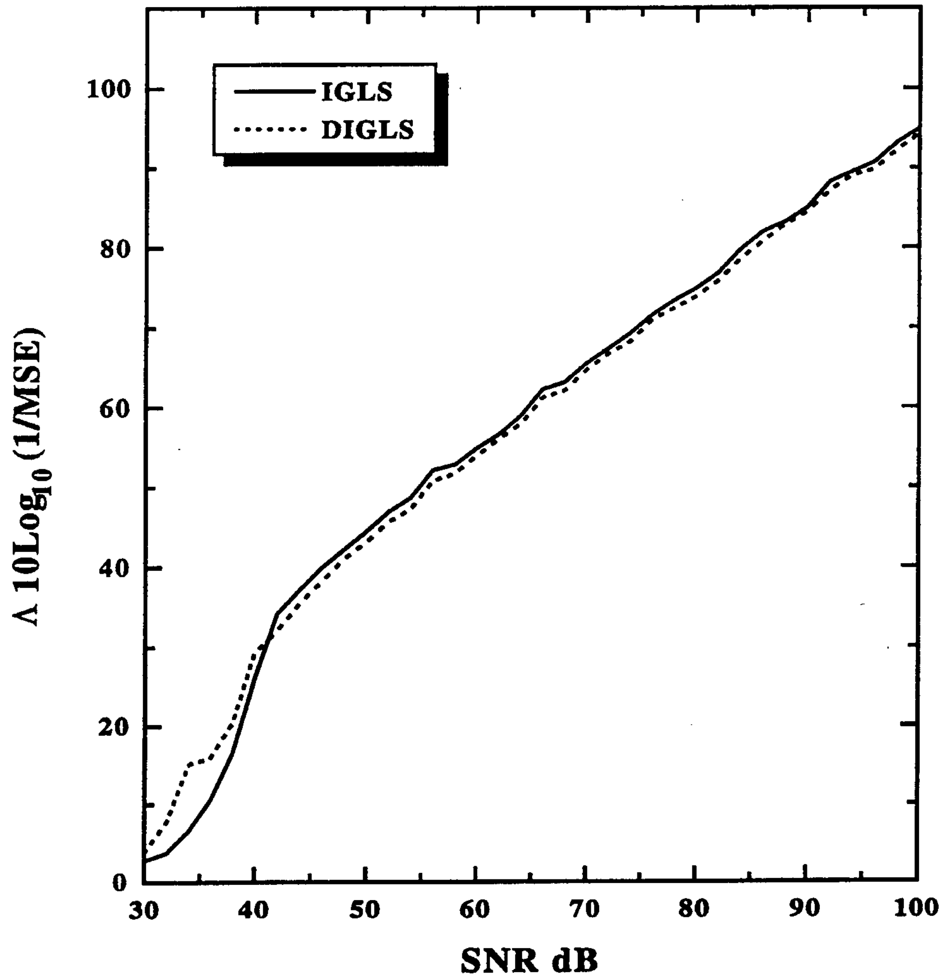

Figure V-5. Comparison of the IGLS and DIGLS estimates of λ_1 in a plot of inverse MSE versus SNR. Estimator performance is compared on simulated data fits of 2-mode decay transients with and without a baseline constant. Data illustrates that the generalized least squares algorithm is not seriously affected by the inclusion of a constant offset value.

Conversely, the overmodeled algorithms indicate a performance degradation resulting from the baseline addition, as can be seen by comparing the OLS (Figures V-1 and V-2) results with the DOLS performance (Figures V-3 and V-4).

The improvements over previous linear prediction algorithms, which have been applied to DLTS signals, are seen to be satisfactorily verified and demonstrated on

artificially realized data. The ultimate verification of performance gains necessitates a comparative demonstration on challenging DLTS signals originating from actual deep level defects. This was accomplished initially on the GaAs deep level, EL2, because of its well documented parameters. Subsequently, more challenging SiC deep level DLTS data, with potential multi-mode character was selected for DIGLS exercise. The results of these experiments are summarized in the following subsection.

V-I-3. Improved Linear Prediction Applied to Empirical DLTS Signals. In order to make a comparison to empirical data of the Linear Prediction algorithms developed in the previous sections, we have applied the DIGLS and DOLS estimation techniques to deep trapping levels in two different material systems. First, we consider the well-known arsenic anti-site defect, As_{Ga}, in GaAs, namely the EL2 level. The compensating EL2 deep donor (D^0/D^+) level was selected for initial verification of the improved Linear Prediction estimator because its trapping kinetics and deep level parameters have been well characterized using DLTS techniques [Lagowski *et al.*, 1982], [Vincent *et al.*, 1979]. Thus, direct comparison of the estimated trap emission rates from digitized capacitance transients may be made between the iterated generalized and overmodeled Least Squares algorithms with a degree of knowledge as to the expected outcome. This will allow us to compare the validity of our noise assumption and simulated results with physical reality using a well-known trapping center. The EL2 transient capacitance data was first recorded in a maximum SNR scenario, and subsequently for DOLS and DIGLS comparisons as SNR was artificially degraded.

DLTS transients of the EL2 samples were digitized and recorded at isothermal increments of 4 K using conventional constant-voltage (CVDLTS) biasing of Ti/Pt/Au Schottky diodes formed on low-temperature grown, Si-doped, GaAs substrate material. Degraded signal-to-noise comparisons of estimator performance were accomplished using the double correlated mode of DLTS operation (DDLTS) to control and reduce the volume of space charge from which emission occurs. The DDLTS mode involves recording the difference signal obtained when the emission transients resulting from two different forward bias filling pulse levels V_{f1} and V_{f2} are subtracted $\{C(t) = C(t,V_{f1}) - C(t,V_{f2})\}$. Figure V-6 graphically illustrates the changing depletion widths of an n-type Schottky barrier diode resulting from unequal trap filling pulse magnitudes. The decay signal obtained in this manner can be restricted to a specific region of the space charge volume, defined by the depletion widths W_1 and W_2 associated with bias voltages V_{f1} and V_{f2}, respectively. The resulting region of recorded emission is shown in Figure V-6 as the shaded area defined by $W-W_1$ and $W-W_2$, where W is the constant reverse bias depletion width occurring during the measurement portion of the temporal cycle. The reader is referred back to Figure IV-1 and its associated discussion for a review of the complete DLTS biasing sequence and the resulting depletion width dependence upon voltage levels and polarity. This differencing is accomplished at each isotherm over the entire scan, with all other run parameters remaining constant, to obtain a complete data record of the thermal emission evolution from this reduced semiconductor volume. It is this well defined reduction to the transient signal source volume which enables SNR variations, since the decay signal magnitude, a_i, is dependent upon the total number of

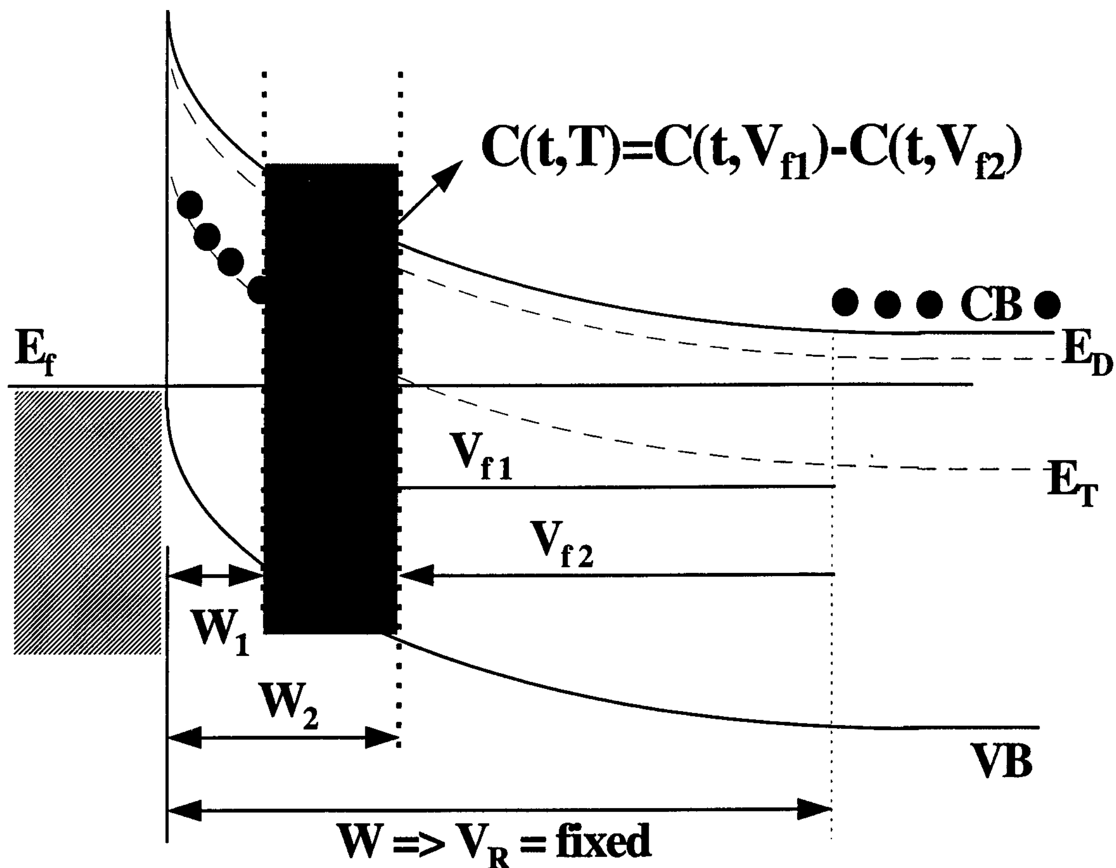

Figure V-6. Flatband idealization of an n-type Schottky barrier illustrating the positional dependencies of the depletion layer edge, W_i, as a function of the filling pulse applied bias voltages (V_{f1}, V_{f2}) utilized for DDLTS mode transient measurement. The shaded region illustrates the well defined volume from which the resulting transient signal originates. As shown by the included C(t) expression, this signal is obtained as a result of the differencing of consecutive transients generated by the two different filling pulses.

carriers being emitted, n = (N_{conc})(Volume). Because the concentration of defects, N_{conc}, is fixed, the signal magnitude is easily reduced by restricting the volume which comprises the signal source. This is accomplished by utilizing values of V_{f1} and V_{f2} such that $| V_{f1} - V_{f2} |$ is decreased until the desired SNR is achieved.

In both SNR cases, a large CVDLTS reverse bias voltage of -5.0 was utilized to maximize the measurement bias (V_R) depletion width, W, and minimize non-exponential effects due to the free carrier tail at the edge of the space charge region [Grimmeiss, 1980:307]. A bias voltage of this magnitude should not effect the expected thermal activation energy, since EL2 has been shown to be unaffected by large junction electric fields which normally result in Poole-Frenkel type barrier lowering for attractively charged centers [Buchwald, Johnson 1988].

Forward bias filling pulse heights and pulse durations used to completely saturate the traps were 1.5 volts and 10 ms, respectively, for the maximal SNR runs. The resulting capacitance transients were sampled at 100 μs intervals (Δ from Equation V-9) with 500 sample points (M) recorded to yield a 50 ms digitized transient period. The noise averaging at each isothermal step is nominally high to ensure validity of the zero-mean Gaussian assumption, and was 200 transients in this case. As previously noted, the offset capacitance, C_0, is not nulled using hardware or external circuitry.

The Arrhenius plot shown in Figure V-7 illustrates the comparison between the DOLS and DIGLS results for the GaAs EL2 deep defect center. It should be noted that in all cases involving experimental data, overmodeled least squares estimation was accomplished using L=30 as the prediction order, and DIGLS was implemented with 10 iterations. The energy sort criteria was also utilized for the DOLS estimates. The data shown in the figure correspond to the solutions for a single mode analysis (N = 1) using the DOLS and DIGLS estimators on data which was collected under maximum SNR conditions. Immediately apparent from the Arrhenius plots is the very significant

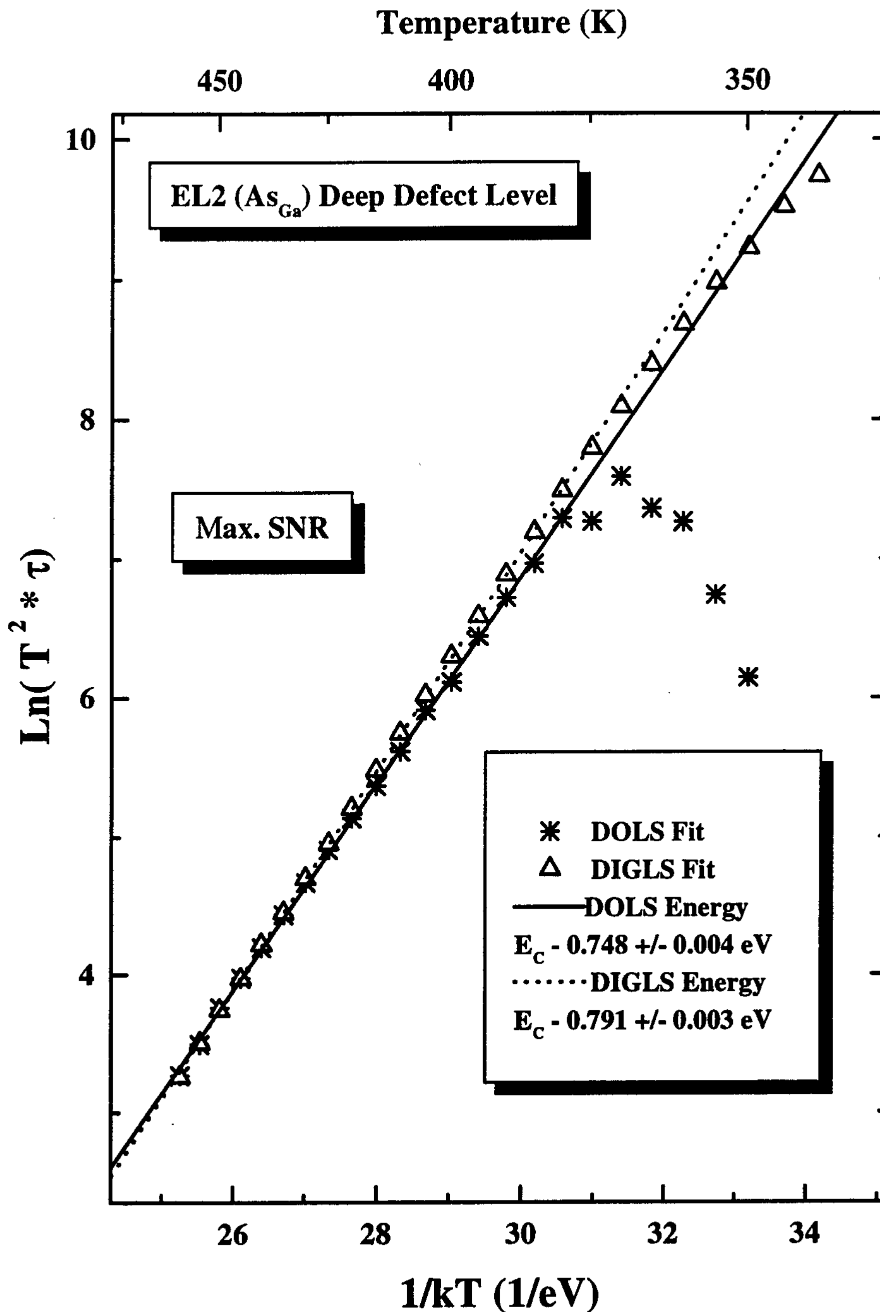

Figure V-7. Arrhenius plot comparison of the GaAs EL2 deep level emission rate estimates using the DOLS and DIGLS algorithms under maximal SNR conditions. DOLS was implemented with a prediction order of L=30 and DIGLS was performed using 10 iterations. The resulting DIGLS estimates of the thermal ionization energy (0.791 eV) were found to be in much better agreement with accepted literature values for the antisite defect than the DOLS results (0.748 eV). Additionally, the DIGLS estimator

extension of the range of linear emission rate data in the case of DIGLS estimation. In other words, the DIGLS algorithm is seen from the figure to be much more robust over the lower temperature range where the capacitance transient is significantly truncated, or equivalently, is characterized by slower emission rates. A more important point to make regarding the data shown in the figure is that the activation energy of E_T=791 meV obtained from the resulting linear slope to the DIGLS emission rate estimates is in much better agreement with accepted deep level transient spectroscopy energy range of 800±15 meV than the DOLS fit yields. The best fit to the linear region data obtained from the DOLS algorithm yields an ionization energy of E_T=748 meV, which underestimates even the low end activation energies obtained using Hall effect measurements [Look, 1983].

Figure V-8 illustrates more concisely the superiority of the improved DIGLS linear prediction algorithm. The data represents the iterative and overmodeled emission rate fits of the EL2 transients with degraded SNR. As can be observed from the data of Figure V-8, the improved linear prediction estimator underestimates the EL2 energy level 10% in this degraded SNR case. However, in comparison, the DOLS utilizing the energy sort algorithm is seen to be completely ineffective in its ability to accurately estimate the transient decay modes in this noisy situation. The extent of signal degradation and significance of the improvements afforded by the DIGLS estimator can be fully appreciated by observing the rate window plots of the maximized and degraded SNR cases illustrated in Figure V-9 and Figure V-10, respectively. An effective defect concentration in this situation can be estimated by dividing ΔC in the degraded SNR case

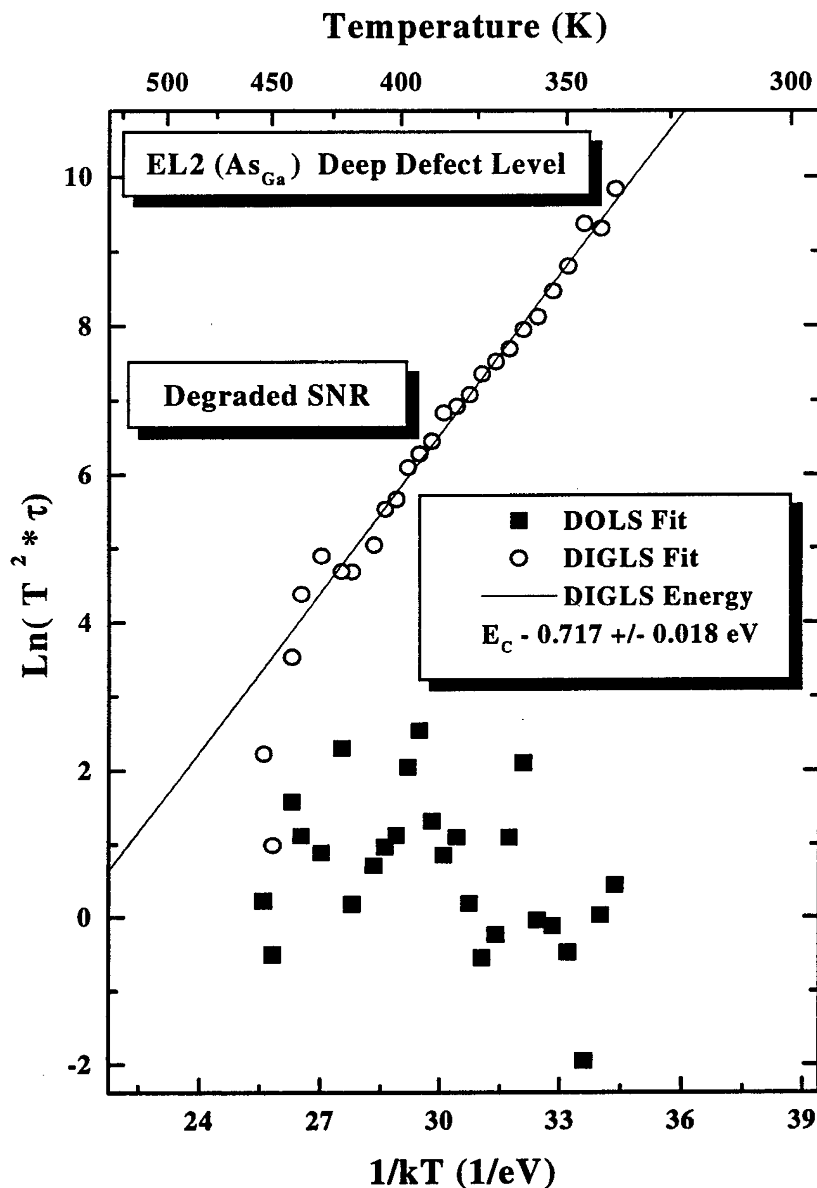

Figure V-8. DDLTS results of the GaAs EL2 deep level emission rate estimates when SNR was severely degraded. The Arrhenius plot comparison shows DIGLS algorithm superiority over DOLS estimates. Although DIGLS underestimates the thermal ionization energy by roughly 10% (0.717 eV), the DOLS algorithm was incapable of providing emission rate estimates in this degraded signal case. An artificial trap concentration is estimated from $\Delta C/C$, and found to be $N_T/N_D \geq 10^{-4}$ for this data, indicating a superiority over previously published SNR data in terms of detection sensitivity. As before, DOLS was implemented with a prediction order of L=30 and DIGLS was executed using 10 iterations.

by the full reverse biased junction capacitance C_{MAX} to yield an effective, normalized, defect-concentration detection-limit for the DIGLS estimator determined to be $N_{TT}/N_D \geq 10^{-4}$. This is in comparison to previous linear prediction sensitivity-limit estimations of

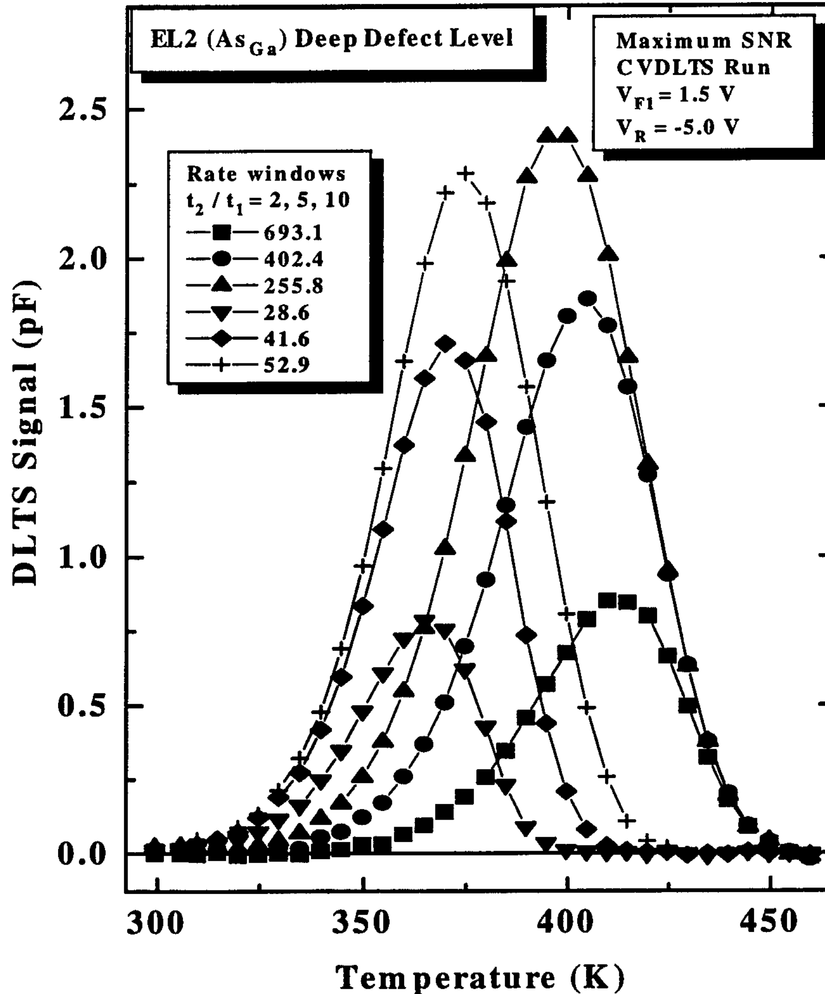

Figure V-9. Rate window plot of the EL2 emission rate thermal evolution under the maximal SNR scenario used for DIGLS and DOLS comparison experiments. Rate windows utilized are shown in the inset, and are obtained by generating six values using t_2/t_1 = 2, 5, and 10 for two different t_1 values.

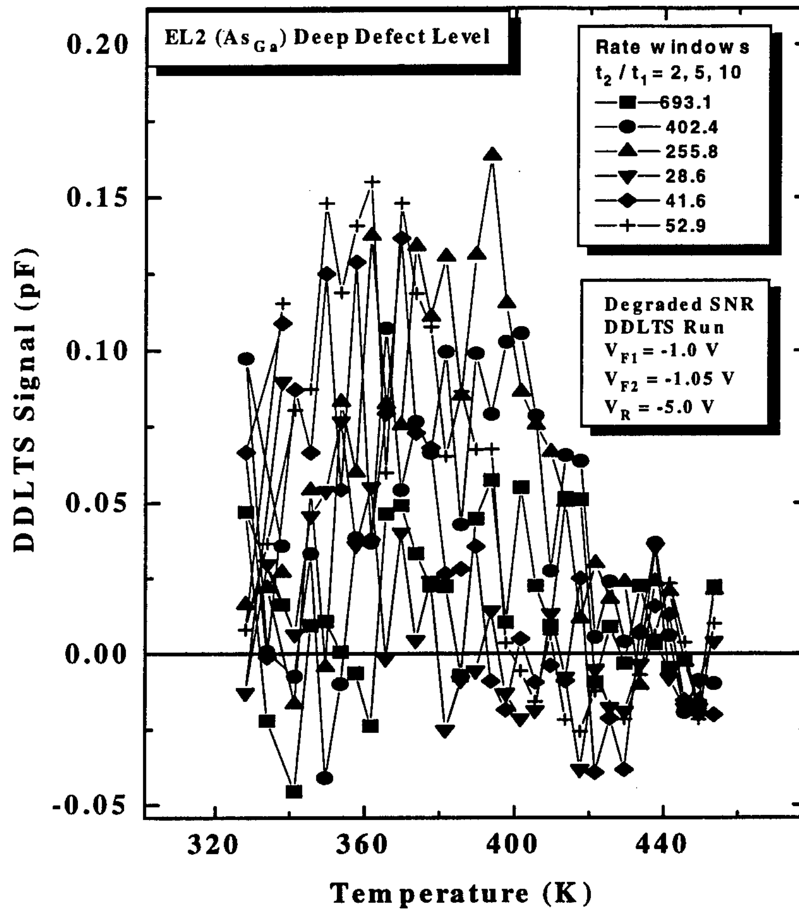

Figure V-10. EL2 rate window plot with artificially degraded SNR used for DIGLS and DOLS comparison experiments. DDLTS filling pulse bias was adjusted to yield an effective trap concentration $\propto \Delta C/C$ of $N_T \sim 10^{-4}$. Filling bias values and rate windows utilized are shown in the insets.

only 10^{-3}, which were associated with an approximately ± 20% error in the emission rate estimates [Doolittle, Rohatgi 1993]. Thus, even with a 10% underestimation of the EL2 activation energy in the present situation, the DIGLS estimator clearly shows a significant improvement over previous linear prediction algorithms utilizing overmodeling.

With the improvements clearly demonstrated by the DIGLS estimator in simulated and controlled DLTS experimental conditions, we applied the algorithm to a more general problem potentially involving multi-mode transient decay. Decay transients from two deep defects in the 6H polytypic modification of the SiC material system were analyzed. There are postulated to be as many as three ionization energy levels, or equivalently three decay modes associated with each point defect in the 6H-SiC material system. As was detailed in Chapter II, these energetic triplets are assumed to result from differences in the local symmetry of various lattice sites. Using thermal generative methods, resolution of the two quasi-cubic levels is not expected due to their close energetic spacing, which has been measured for nitrogen donors to be ~4 meV using photoluminescence characterization of the bound-exciton recombination at nitrogen donors [Choyke, Patrick 1962]. Therefore, we anticipate a DLTS signal with only two resolvable activation energies for substitutional impurities. Additionally, empirical evidence of deep level energetic pairs or triplets in SiC have yet to be demonstrated using DLTS methods. Only heuristic arguments and the postulation that other experimental data, yielding closely spaced deep energy levels, are due to these site inequivalencies [Evwaraye *et al.*, 1995]. Thus, hexagonal SiC provides us with an estimation application on DLTS data with an unknown model order, but likely to be greater than one, and has been included as experimental verification of the iterative estimators performance on problems of increasing difficulty.

Figure V-11 shows the rate window spectral DLTS characteristic associated with a deep electron trap in n-6H-SiC bulk substrate material, which was observed to be a

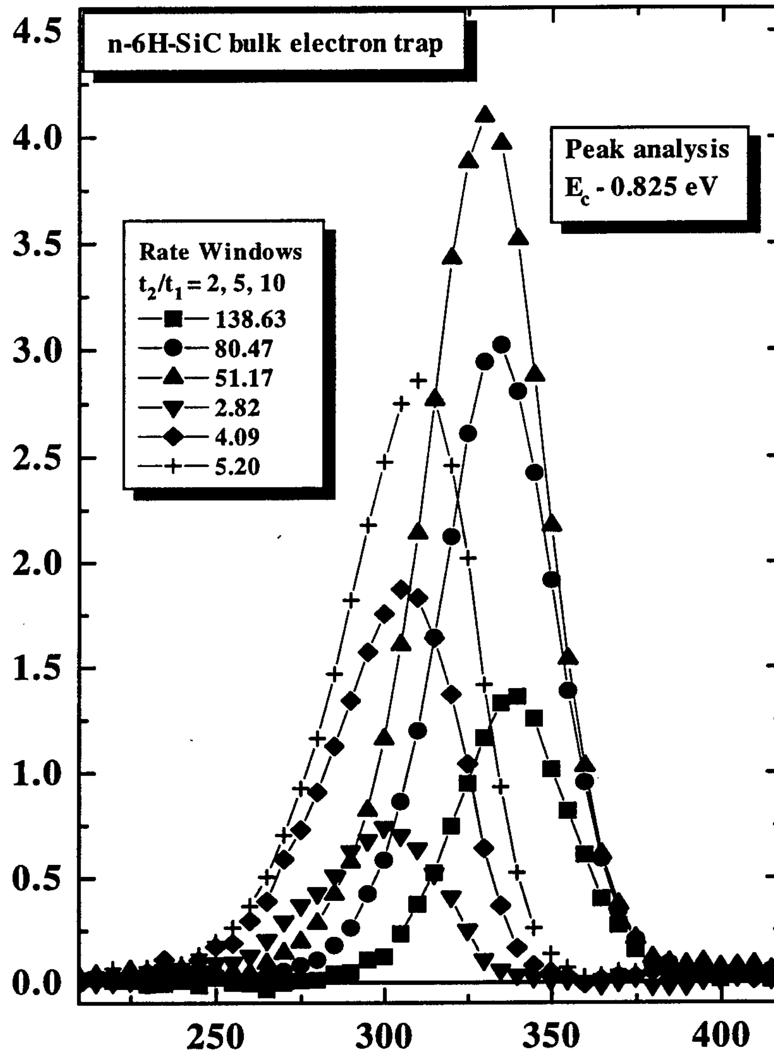

Figure V-11. Rate window spectral characteristic of an electron trapping center in n-type, 6H-SiC, bulk, substrate material. Peak features do not indicate the presence of more than a single decay mode (single energy level) as evidenced by the apparent lack of more than one peak structure. Classical peak analysis yields a thermal ionization energy for electron emission to the conduction band (E_C) of 0.825 eV.

commonly occurring defect in a large number of samples. The rate windows applied to the transient decays are listed in the inset, and as can be seen, the spectral features exhibited do not appear to reflect the existence overlapping peaks associated with multi-mode decay. Using a classical rate window peak analysis the energy level of the electron trap was found to be at E_C-0.825 eV, which is in close agreement with a reported deep level attributed to vanadium impurity [Evwaraye *et al.*, 1994]. However, careful inspection of the capacitance transient data with the DIGLS estimator revealed strong evidence for the presence of two exponential decay modes. Figure V-12 illustrates the resulting Arrhenius analysis of the fitted decay time constants showing convincing evidence for a two mode transient decay. The activation energies of 509 and 543 meV obtained from the linear slope are seen to deviate significantly from the value of 825 meV obtained by the peak analysis method. This should not be surprising when remembering that the classical peak analysis method is invalid if more than a single decay mode exists [Lang 1976].

Additionally, we see that the energetic separation obtained from the Arrhenius analysis illustrated in Figure V-12 is roughly the order of shallow nitrogen donor h-k level separation. This information alone can not be assumed to be anything more than coincidence, since the unknown defect-potential will be the dominant factor in determining absolute energy level and separation magnitudes. However, a connection to inequivalent lattice sites for these energy levels is supported by additional data which was collected from several samples containing this deep level center. A strong correlation between capture cross sections and defect densities for the two levels of Figure V-12 will

be presented in the following chapter, which enables a strong argument for the assignment of inequivalent lattice sites for the same defect. In other words, this result may well be the first explicit DLTS data supporting the existence of SiC deep level energetic pairs for an apparent spectral feature indicating only single mode decay. At the

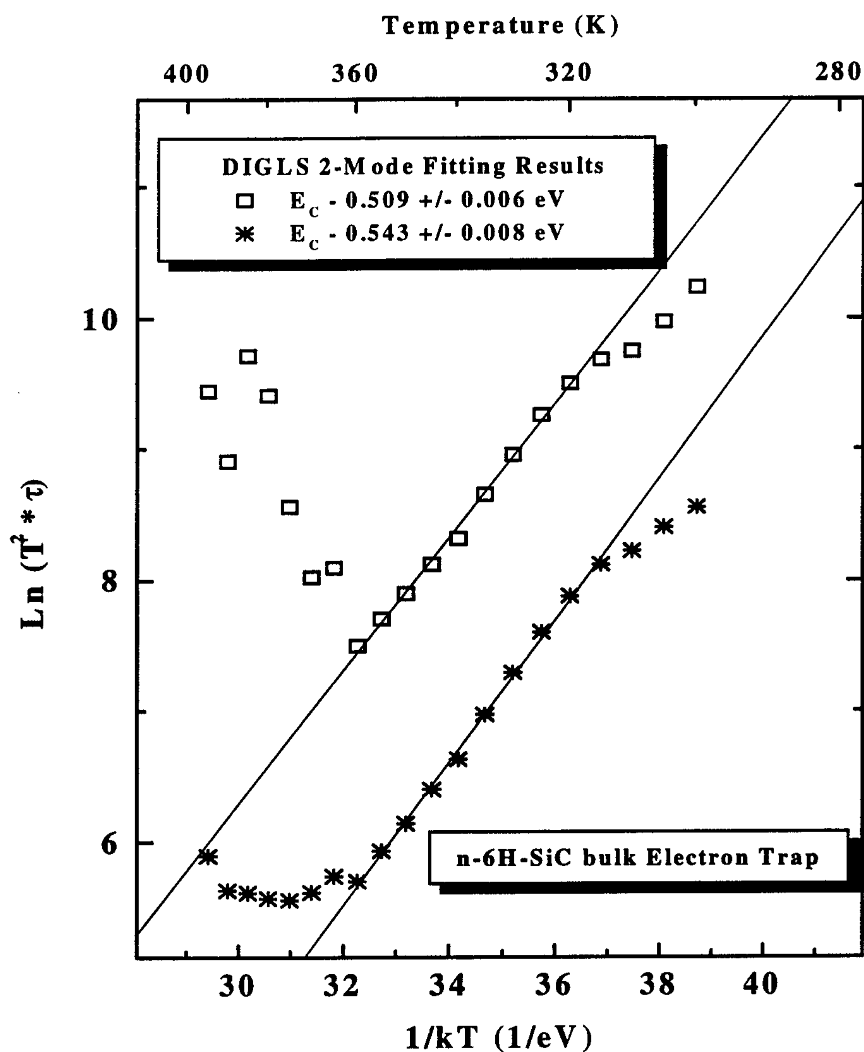

Figure V-12. Arrhenius plots of the DIGLS fitting results showing convincing evidence for the presence of two exponential components in the capacitance decay transients. The fitted emission rate fits obtained from the DOLS estimates did not resolve this feature.

very least, this result indicates the resolving power of the improved linear prediction algorithm in deconvolving closely spaced energy levels as shown in Figure V-12

The apparent success obtained in identifying two closely spaced levels of the electron trapping center in n-6H-SiC led us to apply the DIGLS estimator to a hole trap commonly observed in p-type 6H-SiC. This defect center has been observed by us to be present in most substrate wafer material, and is readily formed upon ion-implantation into epitaxial material [Scofield *et al.*, 1995]. We thought this to be an intrinsic defect in this material which could to be related to vacancies or a vacancy-complex type structure. This data will also be elaborated upon in a subsequent chapter. In this instance, both the DIGLS and DOLS algorithms applied to the CVDLTS transients definitively indicate the presence of only a single exponential decay component. One and two mode DIGLS numerical fitting attempts yielded nearly identical time constants, with the resulting Arrhenius energy of E_V+0.861 eV in close agreement between the two results. Figure V-13 illustrates the Arrhenius plot of fitted data for this defect along with the results obtained using the DOLS routine. The ionization energies obtained between the two methods are in much closer agreement than was the case for the EL2 defect, but the striking feature is the extension of useful transient data by almost 50 degrees or 10 transient emission rate data points on the low temperature side. Although further evidence for the presence of deep level pairs was not obtained for this SiC deep level, the connection of this defect to lattice imperfections may indicate a relationship to an extended type structure which is insensitive to lattice site inequivalencies. Additionally, shallow acceptor levels which are coupled to the valence band have been shown to be

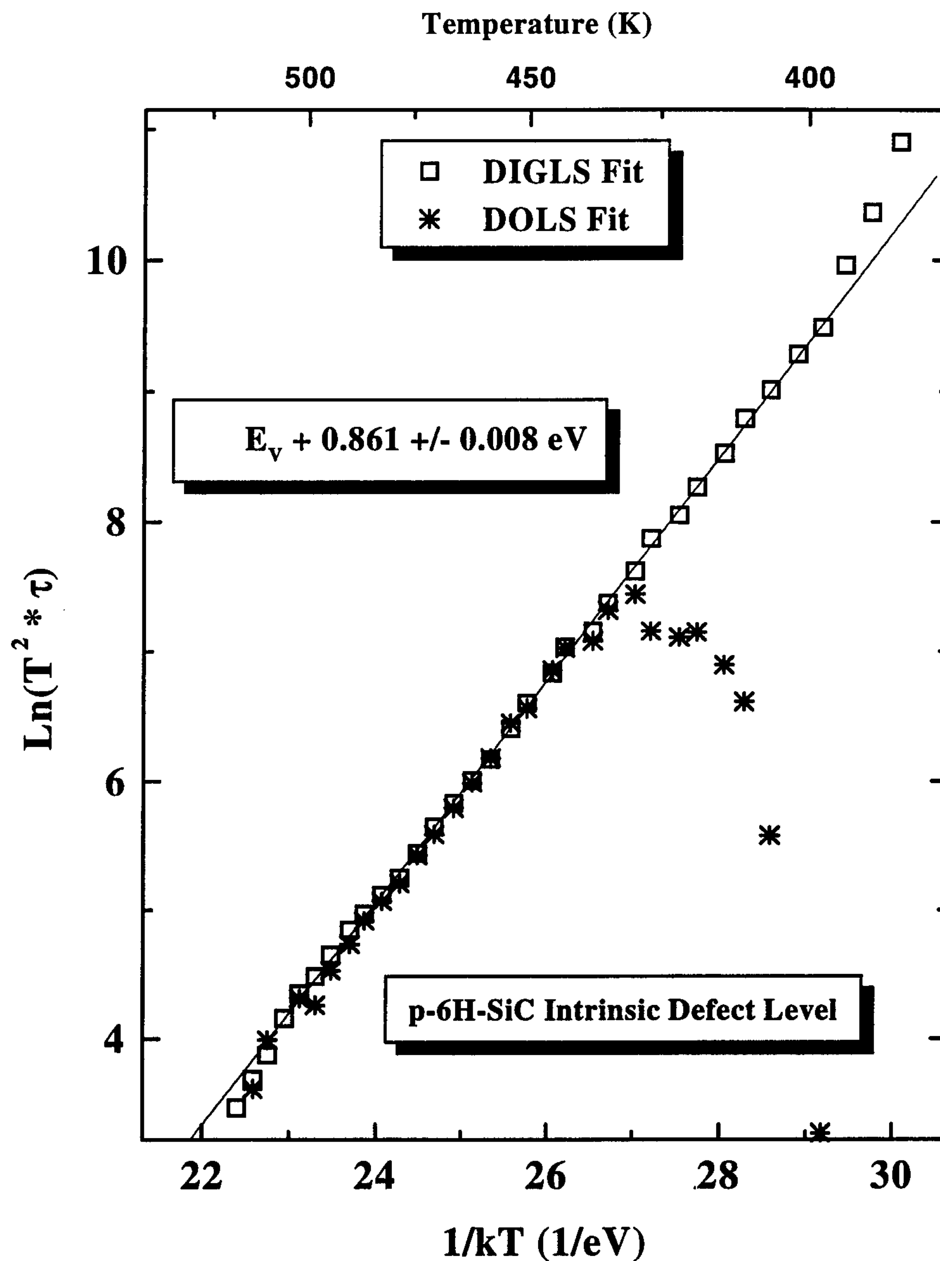

Figure V-13. Arrhenius plot comparison of the DIGLS and DOLS fitting results on a vacancy or crystalline damage related hole trap in p-type 6H-SiC. The superiority of DIGLS fitting is shown by the extension of useful emission rate estimates in the low temperature regime of transient decay.

much less affected by the symmetric inequivalencies of hexagonal or cubic lattice sites. Therefore, a one mode postulation for this deep level is acceptable.

A final comparison was accomplished on the EL2 defect data between the newly developed DIGLS fitting algorithm and the existing modulating functions routine. Doolittle and Rohatgi [1994:4560] concluded that when SNR is large, the OLS and MF algorithms were equivalent and superior to other methods in their ability to resolve closely spaced decay rates, but when SNR was degraded, their OLS implementation was slightly superior to MF. However, in terms of detection sensitivity (minimum detectable trap concentration), we have concluded that MF is superior to the overmodeled least squares algorithm. Therefore, we performed initial SNR sensitivity experiments on the EL2 data presented earlier in this section in order to compare our existing MF DLTS analysis tool with the new DIGLS algorithm.

Figure V-14 illustrates the Arrhenius plots resulting from the two fitting algorithm estimates of the EL2 emission rate under the maximal SNR conditions corresponding to the data from Figure V-9. As shown in the figure, the exponential time constant estimates are effectively coincident for the two algorithms. This supports the conclusions of Doolittle and Rohatgi regarding the ability of the MF formalism under large SNR conditions. However, for single mode decay under optimal noise conditions, the majority of mode estimators will perform flawlessly. The true benchmark of comparison is under nonideal or fringe conditions. Thus, the estimators were tasked to perform under several SNR conditions with the noise component artificially varied as before. MF and DIGLS

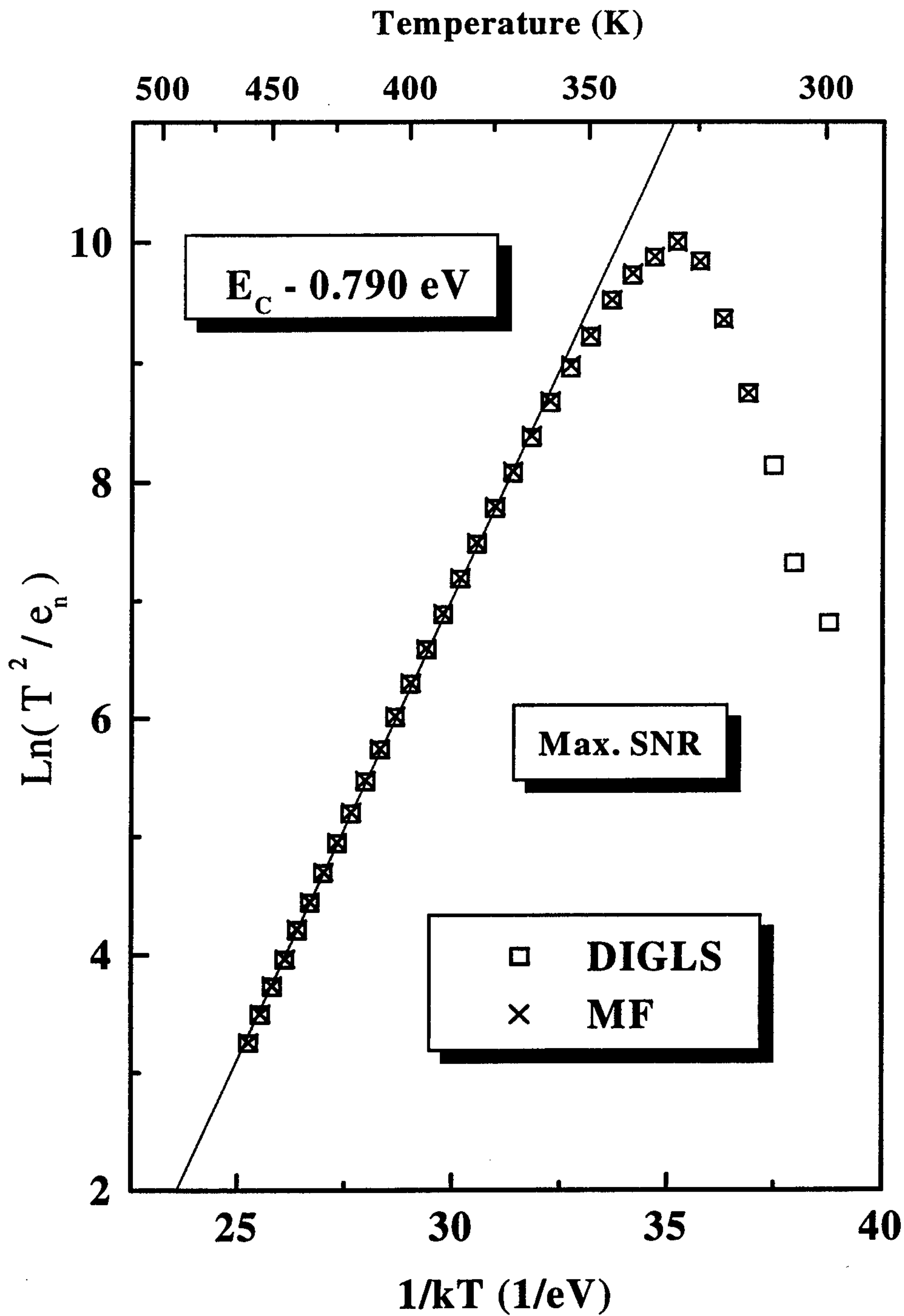

Figure V-14. Arrhenius plot of the EL2 data under maximal SNR conditions showing both the MF and DIGLS results. Under this large SNR scenario, the two algorithms result in coincident estimates of the transient decay emission rate.

performance was found to be comparable until the normalized effective trap density (N_{TT}/N_D) was decreased to approximately 10^{-3}. It was observed that in each of the degraded signal cases, MF underestimated the accepted thermal ionization energy to a greater extent than did the DIGLS fits. Additionally, as SNR was further decreased, the DIGLS algorithm was observed to extend the linear Arrhenius data over a wider temperature range, consistent with a lower sensitivity to truncation error. Figure V-15 illustrates the comparative Arrhenius results for the 10^{-4} concentration data used to compare DOLS and DIGLS in Figure V-8. As shown by the Arrhenius data, the MF routine has the ability to reasonably estimate decay rates in this limiting case. This illustrates the superiority of MF over the DOLS predictions which were previously shown to be completely ineffective in this range of SNR. However, as described above, the DIGLS results are extended over a wider temperature range, and the energy estimate is better representative of physical reality than values obtained using MF. Thus, we have concluded that the DIGLS algorithm is, additionally, superior to MF parameter estimation as applied to DLTS trap emission signatures.

The DIGLS and IGLS algorithms have been shown to be superior to both overmodeled LS and modulating functions for estimating deep level trap parameters. Improved sensitivity to low defect concentrations and excellent resolving power were demonstrated with the extended linear prediction theory. The theoretical contributions of Drs Ingham and Pachter are extremely relevant to all DLTS researchers interested in extending data analysis capabilities and improving their trap parameter estimates. The collaboration between the author and theoreticians was especially fruitful. It provided a

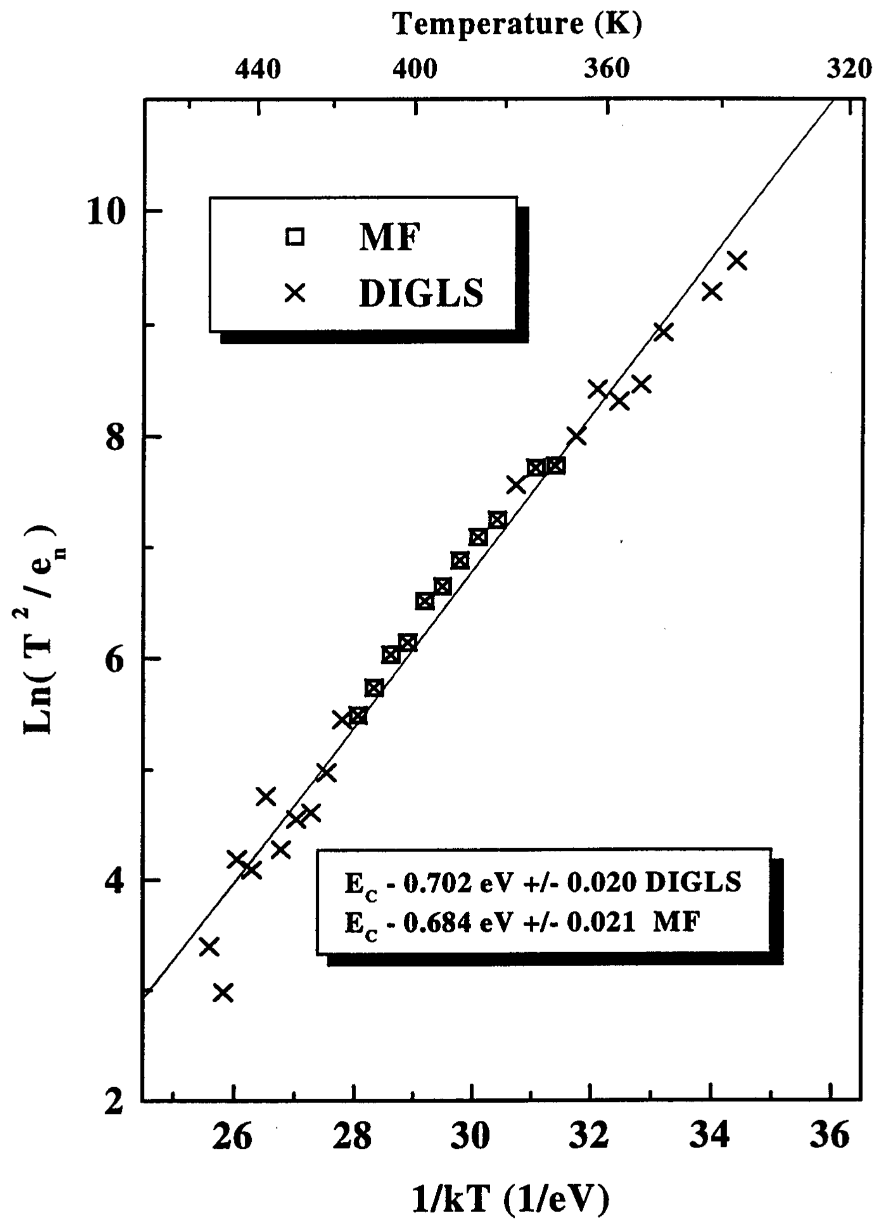

Figure V-15. Arrhenius plot of the artificially degraded SNR data for the GaAs EL2 deep donor level. Both the MF and DIGLS fitting results are plotted for comparison. The SNR conditions correspond to a normalized trap density of approximately 10^{-4}. DIGLS results, while underestimating E_T as before, are seen to be superior to MF results in both energy estimates and sensitivity over a wider temperature range.

much needed application for the basic tenets of the abstract theoretical realizations, and resulted in a well defined project which culminated in the demonstration of a superior parameter estimation algorithm for DLTS data analysis. The detailed derivations outlined earlier in this section will provide future students, and any DLTS researcher referencing this document, with the ability to easily understand and implement this formalism in their studies of deep level defects.

VI. Simulation and Model Analysis

In this chapter, we shall discuss the relevant specifics of performing DLTS characterization of deep defect levels and especially analysis of experimental results on hexagonal SiC polytypes. One of the primary contributions of this research project was identification of the mechanism controlling carrier trapping in the SiC crystals. This mechanism was observed to control the capture kinetics for a majority of the deep defect centers studied. A careful analysis of trap occupation densities as a function of temperature, subsequent to DLTS filling pulse events, revealed the presence of significant thermal impediments or barriers to the capture of free carriers. These barriers were identified with specific, well-defined energies, E_b, which parametrically describe free particle capture via multi-phonon emission (MPE). Numerical fitting of the temperature-dependent captured carrier-concentration profiles, $N_T(T,t_p)$, for these defects revealed a correlation with the MPE theory of Henry and Lang [1975:989] outlined in Chapter III. The observation of this trapping mechanism in SiC polytypes is consistent with previous reports of persistent photo-conductivity (PPC) observations in 6H-SiC [Son, 1994:2687]. PPC is identified with the presence of an appreciable barrier to the capture of photo-induced free carrier concentrations, resulting in an increased conductivity with a characteristically long lifetime. This occurs at low temperatures because the kinetic energy of induced free carriers is insufficient to overcome the energetic barrier associated with the dominant trap or recombination center controlling carrier lifetimes. As a result, the relaxation back to thermal equilibrium conditions can be on the order of hours or even

days, depending upon the barrier magnitude, E_b, and sample temperature. This duration is in contrast to typical non-radiative relaxation times on the order of 10^{-6} to 10^{-3} seconds for situations in which the dominant recombination centers do not possess a thermal barrier impeding carrier capture.

Deep level energetic pairs associated with homotype defects occupying inequivalent SiC lattice sites were found to be difficult to identify and correlate. However, as shown in the previous chapter, there were two distinct electron traps in 6H-SiC which might be identified as possessing energy levels associated with hexagonal and cubic lattice sites. The data to be presented represents the first convincing evidence of this phenomenon obtained using DLTS techniques. An apparent lack of compliance with the physical constraints of SiC lattice symmetries was observed for most deep levels studied. In other words, the majority of traps were not observed to occur in pairs. This is possibly related to bound state wavefunction localization and/or variations in the exact form of a particular defect's binding potential. The latter explanation would suggest that energetic splittings do occur, but that their magnitudes will vary, possibly over a wide range, in response to the specific atomic potential, $V(\mathbf{r})$. In this case, the resulting energy level pairs might be identified as distinct and unrelated due to large ionization differences. The former explanation is based on the idea that bound state wavefunctions must have a significant extent in coordinate space in order to experience the potential energy inequivalency resulting from the slightly altered arrangement of atoms surrounding the two different lattice sites. Thus, more tightly bound particles would tend to have a decreasing influence from lattice symmetric inequivalencies, and would not

exhibit energetic differences for wavefunction radii less than a few atomic spacings (~3-10 Å). Determination of the exact mechanism controlling this phenomenon requires extensive solutions to the quantum problem, which as yet has not been attempted.

An additional area of consideration during this research project has been the modeling of deep level capture and emission kinetics using SiC material specifics and incorporating various theoretical models. The primary purposes for this task were to provide a basis for empirical expectations, fit experimental data, and generate a degree of self-consistency for conclusions made on the basis of data analysis. One of the most important lessons learned from this exercise was that significant errors in estimated deep level trap parameters will result if consideration for the incomplete ionization of shallow doping impurities (N, Al) is not included. Due to the large activation energies for dopant impurities in SiC, the temperatures at which the N and Al atoms are fully ionized approach 600 and 800 K, respectively, for the 6H polytype. The result is a free carrier concentration that rapidly changes with temperature over ranges of experimental interest. When considering other semiconductors such as Si and GaAs, whose doping impurities are effectively ionized at temperatures below 100 K, we find that this situation is unique to the SiC wide-bandgap material system. Under certain circumstances, this condition will be shown to significantly alter capture and emission processes for deep levels in this material.

This chapter will outline the simulations performed to model expected SiC deep level behavior, with inclusion of the effects associated with the unionized dopant condition. The routines developed were ultimately used to fit experimental data and estimate MPE

capture parameters for traps exhibiting this behavior, and to verify the existence of deep levels associated with inequivalent lattice sites. The application of these models to experimental data will be the subject of the following chapter.

VI-I. Modeling of Capture and Emission Processes in SiC

Mathematica® and Mathcad® algorithms were developed to simulate capacitance transients based on; 1) SiC material considerations, and 2) routines incorporating models of deep level capture and emission kinetics. Simulated transient data were recorded over a specified temperature range with digital data points corresponding to realizable DLTS experimental parameters, such as pulse heights (volts), durations (sec), and frequency (sample rates). The artificially generated transient records are subsequently handled in the same manner as experimental data records, and are fitted for emission rate and amplitude parameters using MF or DIGLS routines. The resulting fitted data is then subjected to rate window and Arrhenius analysis to yield projections of typical SiC DLTS results. Alternatively, these routines were used to provide self-consistency with experimental results by utilizing empirically obtained trap parameters as inputs to the software algorithms and comparing the simulated results with the original data. Differences between the experimental and simulated results were considered to be inadequacies of the simple models. Modifications were then made in order to identify the dominant mechanisms dictating capture and emission kinetics. This would be accomplished iteratively until self-consistency was achieved. Finally, in the case of $N_T(T,t)$ analysis, these "soft-math" routines were used to fit experimental data. Routines

of this nature could have been more efficiently developed in a structured programming environment, however, modeling was not a primary emphasis of this dissertation, and these mathematical packages enable quick implementation. The draw backs are extremely slow execution times and time consuming manual iterations for fitting and self-consistency exercises.

The implementation of a numerical routine to simulate the transient capacitance decay associated with carrier emission from bound defect states requires an analytic expression for the temporal trap occupation density, $N_T(T,t)$. This concentration is obtained from the solutions to Equation IV-1. Invoking the depletion approximation (n=p=0), valid for reverse biased p/n junctions, Schottky barriers, or metal-oxide-semiconductor (MOS) capacitors, rate equation IV-1 is linearized. Using this simplification, the trap concentration solution is easily obtained for the case of defect emission. However, this is the solution to an initial value problem, and requires an expression for the capture event occurring immediately prior to emission in order to obtain the particular result from a general solution. As described in Chapter IV, the capture event portion of a DLTS temporal cycle occurs in neutral material. Thus, the depletion approximation will not be valid. A general solution to Equation IV-1 without linearization is extremely prohibitive. We, therefore, make the linearizing assumptions that Auger processes are negligible, and that measurements will be performed in the dark. This eliminates terms involving n and p, and the optically induced coefficients and rates indicated by the superscript O in Equation IV-2. As was detailed in Chapter III, the Auger assumption is very reasonable for wide bandgap semiconductors, and the

realization of non-illuminated experimental conditions is easily accomplished. Thus, the boundary value problem to be solved for the rate of change of electron occupation on a donor-like trap of total density N_{TT} in neutral material is now given by

$$\frac{dN_T^{\ 0}}{dt} = (\text{capture} - \text{emission}) = c_n N_T^{\ +} - e_n N_T^{\ 0}, \qquad \text{[VI-1]}$$

where N_T^0 is the concentration of filled (occupied) traps, N_T^+ is the density of empty traps, and $N_T^0 + N_T^+ = N_{TT}$ is the totality condition. Recall that e_n and c_n are characteristic electron emission and capture rates, respectively, defined by Equations IV-3 and IV-5. Note also that the notation has been altered slightly from Equation IV-1 with $N_T^0 = n_T$ and $N_T^+ = p_T$. Applying the boundary conditions $N_T^0(T,t{=}0) = 0$ and $N_T^0(T,t{=}\infty) = N_{TT}$ to the general solution of Equation VI-1, we obtain the expression for the captured carrier concentration during the filling pulse event as shown by

$$N_T^{\ 0c}(T,t) = N_{TT}\frac{A}{A+B}\left[1-\exp(-A-B)t\right],$$

$$\text{where} \quad \begin{cases} A = c_n + e_p \\ B = e_n + c_p \end{cases} . \qquad \text{[VI-2]}$$

The additional superscript, c, is now included to discriminate the capture from emission event solutions. The temperature dependence of Equation VI-2 is contained in the capture and emission rates comprising A and B, which were given in the first subsection of Chapter IV. The desired initial value condition for the emission solution is now defined. It is obtained by evaluating Equation VI-2 at the end of a filling pulse of

duration $t=t_p$. The particular solution describing the temporal and temperature dependent trap occupation density during the DLTS emission event can now be given as

$$N_T^{0e}(T,t) = N_T^{0c}(T,t_p)\left[\frac{A'}{A'+B'} + \frac{B'}{A'+B'}e^{(-A'-B')t}\right],$$
$$\text{where} \quad \begin{cases} A' = e_p \\ B' = e_n \end{cases}, \qquad \text{[VI-3]}$$

and A' and B' are defined by assuming validity of the depletion approximation during the emission event. Furthermore, it is typically assumed that the capture rates, c_i, are much greater than the emission rates, e_i, and that either electron (i=n) or hole (i=p) processes are dominant in order to further simplify these solutions. For modeling purposes, the solutions were implemented in their more general forms. The modeled statistics and physical mechanisms controlling thermal equilibrium conditions and trapping kinetics, respectively, determine the relative rate magnitudes and dominant capture/emission processes in a more physical manner than simply ignoring their contribution completely. Inserting the most general capture and emission rate expressions from Chapter IV into the two solutions above and using Equation IV-11, the desired transient capacitance expression for an n-type Schottky diode is obtained. Rewriting Equation IV-11 for convenience and using Equation VI-3 gives the DLTS emission transient expression as

$$C(T,t) = \sqrt{\frac{q\varepsilon\left(N_D^+ \pm N_T^{0c}(T,t_p)\left[\frac{A'}{A'+B'} + \frac{B'}{A'+B'}\exp(-(A'+B')t)\right]\right.}{2(V_{bi}+V_R)}} \quad . \qquad \text{[VI-4]}$$

The kinetics of various capture processes are considered by inserting the appropriate rate expressions for A and B when computing $N_T^{0c}(T,t_p)$. Recall that in general the capture rate is given by

$$c_i = \sigma < v > i, \quad \text{where } i = n \text{ or } i = p \qquad \text{[VI-5]}$$

represent the free carrier electron and hole concentrations, respectively. Capture mechanisms are considered by utilizing the appropriate capture cross-section expressions, for example, using the theories and equations outlined in Chapter III.

It is in the implementation of Equation VI-4 and Equation VI-5 that the consideration of non-constant carrier concentrations must be included. Since n(T) and especially p(T) can be significantly less than their respective doping concentrations, the typical assumption of complete ionization with $n=N_D$ or $p=N_A$ in Equation VI-5 will result in capture rate overestimates covering a wide temperature range. Significant errors associated with estimating trap parameters from experimental data are ultimately the result. Thus, an expression for the free carrier concentration as a function of temperature must be derived, and included in the DLTS transient model. A simple Fermi-Dirac probability factor appropriate for single energy level impurities, is not valid for the hexagonal SiC polytypes. Free carrier statistics must include contributions from 2 or 3 impurity levels. In general, if we have M species of monovalent donor impurities, in which the jth class is of density N_{Dj}, and binding energy E_{Dj}, the number of ionized impurities, N_{Dj}^+, in this class is given by

$$N_{Dj}^{+} = \frac{N_{Dj}}{1 + \frac{1}{\beta_j}\exp(\eta + \varepsilon_{Dj})} , \qquad \text{[VI-6]}$$

where β_j is the quantum level degeneracy factor, $\varepsilon_{Dj} = (E_f - E_{Dj})/kT$, and recall that $\eta = (E_f - E_C)/kT$ defines the Fermi level position. The requirement of electrical neutrality for the crystal necessitates that the total positive charge equals the total negative charge. Thus, the concentration of all ionized donors, N_{Dj}^{+}, is equal to the density of conduction band free electrons, n, plus all electrons in compensating acceptor levels, N_A. Written explicitly for M donor levels in n-type material, we have

$$[N_A + n] = [N_A + N_C \mathcal{F}_{1/2}(\eta)] = \sum_{j=1}^{M} \frac{N_{Dj}}{1 + \beta^{-1}\exp[\eta + \varepsilon_{Dj}]} , \qquad \text{[VI-7]}$$

where the free electron concentration has been replaced by the Fermi-Dirac integral of order 1/2, which was first introduced in Chapter III. If we assume non-degenerate conditions, then $\mathcal{F}_{1/2}(\eta)$ can be replaced by a Boltzmann factor $\exp(\eta)$. This condition is easily realized by avoiding excessive doping levels and extremely low temperatures. If these conditions are satisfied, the Fermi level will be positioned several kT below the conduction band edge, E_C, and non-degenerate conditions will prevail. When this substitution is made, Equation VI-7 becomes an algebraic equation of order (M+1) in either n or $\exp(\eta)$. Thus, for SiC with M=2 or 3, it becomes necessary to root a cubic or quartic equation. Using the polynomial rooting functions in Mathematica® and Mathcad®, Equation VI-7 is solved for roots corresponding to $\exp(\eta)$. The temperature dependent free carrier concentration is then easily computed using $n = N_C \mathcal{F}_{1/2}(\eta) =$

$N_C\exp(\eta)$. Table VI-1 summarizes the ionization energies used for nitrogen donors and aluminum acceptors when calculating carrier concentration for 6H- and 4H-SiC. The notation used in the table relates subscripts as identifying hexagonal (h) and cubic (k1, k2) lattice sites. The energetic values listed have been obtained from the literature, and represent average values of those reported [Pensl and Choyke, 1993:264], [Suttrop *et al.*, 1992:129], [Ikeda Matsunami and Tanaka, 1979:11], [Choyke and Patrick, 1962:1868]. The Al acceptor levels have been shown to be relatively independent of the particular host polytype [Pensl and Choyke, 1993:264], and thus consistent values have been used in all computations of p(T).

Figure VI-1 illustrates the calculated conduction band electron (n) and valence band hole (p) densities as a function of temperature for both SiC polytypes using Equation VI-7. Included in the figure are data corresponding to an experimental determination of the free carrier concentration obtained from temperature dependent Hall effect

Table VI-1. Ionization energies for 6H- and 4H-SiC nitrogen donor and aluminum acceptor impurities and relative concentration distributions on each lattice site.

Polytype	E_{h1}	CONC	E_{k1}	CONC	E_{k2}	CONC
n-6H	85 meV	$0.33N_D$	135 meV	$0.33N_D$	150 meV	$0.33N_D$
n-4H	47 meV	$0.5N_D$	102 meV	$0.5N_D$	n/a	n/a
p-6H	225 meV	$0.33N_A$	240 meV	$0.66N_A$	n/a	n/a
p-4H	225 meV	$0.5N_A$	240 meV	$0.5N_A$	n/a	n/a

measurements on an n-type 6H-SiC crystal. The total nitrogen doping concentration in these samples was determined to be 2.86×10^{17} cm^{-3} from Hall effect data. This value was additionally corroborated by conventional capacitance-voltage (C-V) [Sze, 1981] measurements taken at 290 K. The experimentally determined total doping concentration along with the ionization energies in Table VI-1 were used as inputs to the numerical algorithm in order to compute the simulated temperature dependent carrier densities illustrated by the open symbol data in the figure. The individual concentrations, N_{Dj}, for the hexagonal:cubic site ratio was taken to be 1:2 and 1:1 for the 6H- and 4H-SiC polytypes, respectively, in accordance with the natural abundance of sites in each of the crystals. Finally, a nominal value of $N_A = 5 \times 10^{14}$ cm^{-3} was used in all computations as a low-level compensation density. This value was selected as typical of reported compensation densities for 6H-SiC obtained from Hall effect data [Pensl and Choyke, 1993:264], [Suttrop *et al.*, 1992:129]. As a minimum, this analysis provides us with an excellent estimate of the low temperature bound of DLTS measurement validity. In other words, for a given trap concentration, over what temperature range will there exist sufficient free carriers for trap filling without causing nonexponential transient behavior. This occurs when the density of available free carriers becomes less than an order of magnitude greater than the trap concentration. For example, with the doping concentration of 2.86×10^{17} cm^{-3} used for the figure calculations and assuming a trap concentration of 1×10^{15} cm^{-3}, the standard DLTS analysis will be of marginal validity for temperatures below 75 K and 170 K for 6H-SiC n- and p-type material, respectively.

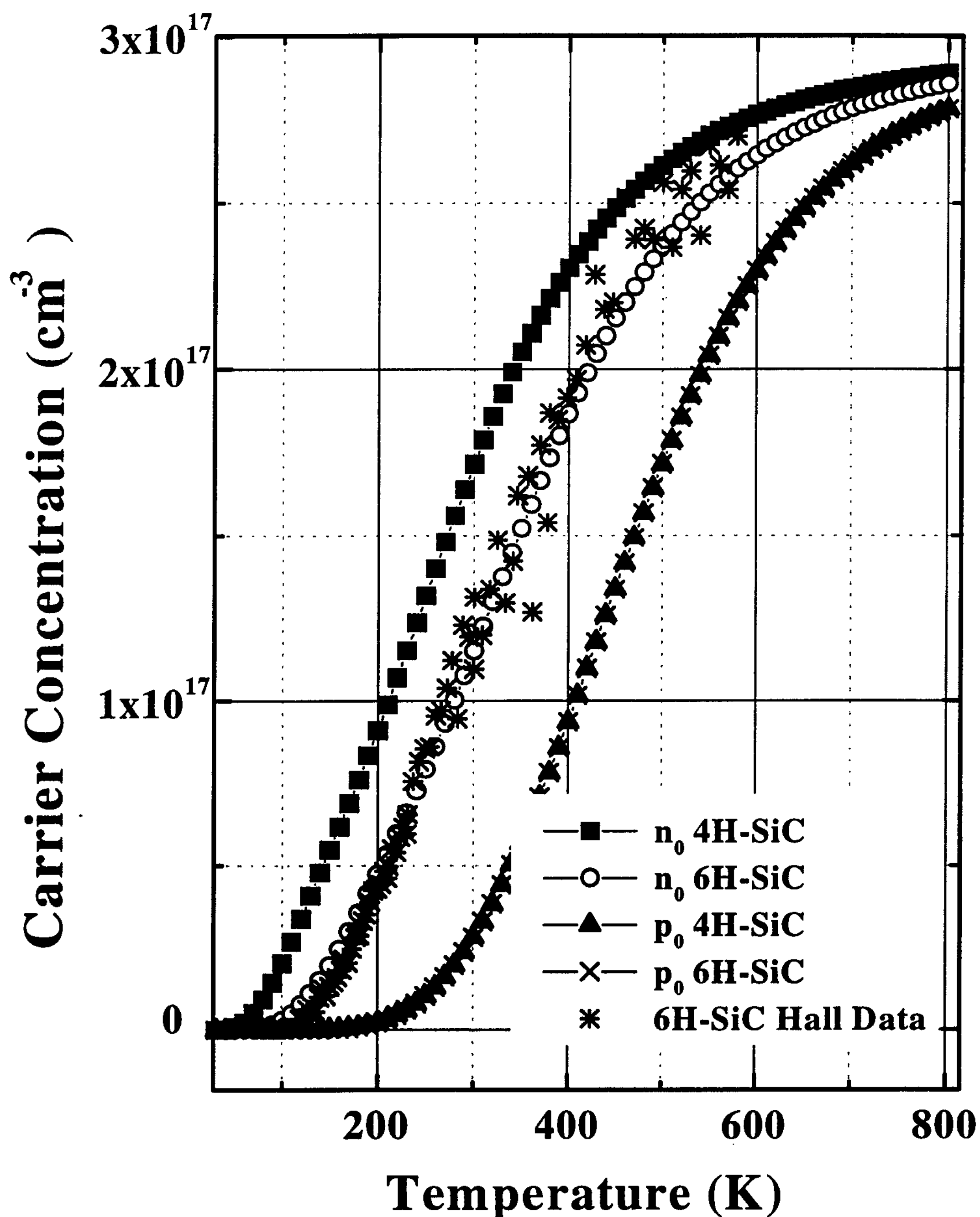

Figure VI-1. Calculated free carrier concentration as a function of temperature for n- and p-type 4H- and 6H-SiC. Computations were performed using Equation VI-7 and the ionization energies of Table VI-1. Illustrated by the symbol, *, are the experimentally determined carrier concentration of a 6H-SiC sample obtained from Hall effect measurements. The data shows reasonably good agreement between computed and experimental n(T) data. Compensation density, N_A, was estimated to be 5×10^{14} cm^{-3}.

Figure VI-2 shows the Fermi level temperature variation for a) n-type SiC and b) p-type SiC with horizontal lines representing donor and acceptor ionization energy levels for both polytypes. Correct physical behavior is observed for the temperature variation of the calculated quantity. At T=0, the Fermi level locks onto the shallow donor or acceptor level, which is predicted for any semiconductor with non-zero compensation [Blakemore, 1987: Ch.3]. This is true no matter how small the fractional compensation, since if there are any compensating impurities at all, the principal donors are not 100% occupied at T=0. As temperature is increased from zero, the rising (n-type) or lowering (p-type) behavior of E_f is due to the fact that $(N_D-N_A)/N_A$ is greater than unity in accordance with theory [Blakemore, 1987:138].

With confidence in the carrier concentration computations, Equation VI-7, Equation, and IV-7 were inserted into Equation VI-4, and simulations of deep level capacitance transients were realized for 4H- and 6H-SiC crystals. Transient data records are generated at simulated isothermal increments (2-5 K), which correspond to typical DLTS data collection run parameters. As described above, simulated transient data records are placed in the appropriate format, and analyzed using the fitting algorithms detailed in Chapter V. From the fitted time constants and amplitude coefficients, standard DLTS rate window and Arrhenius analysis are performed. Figure VI-3 illustrates simulated DLTS rate window (a) and Arrhenius (b) plots realized for a 470 meV electron trap in n-type 6H-SiC. The trap characteristics define a constant capture cross section and

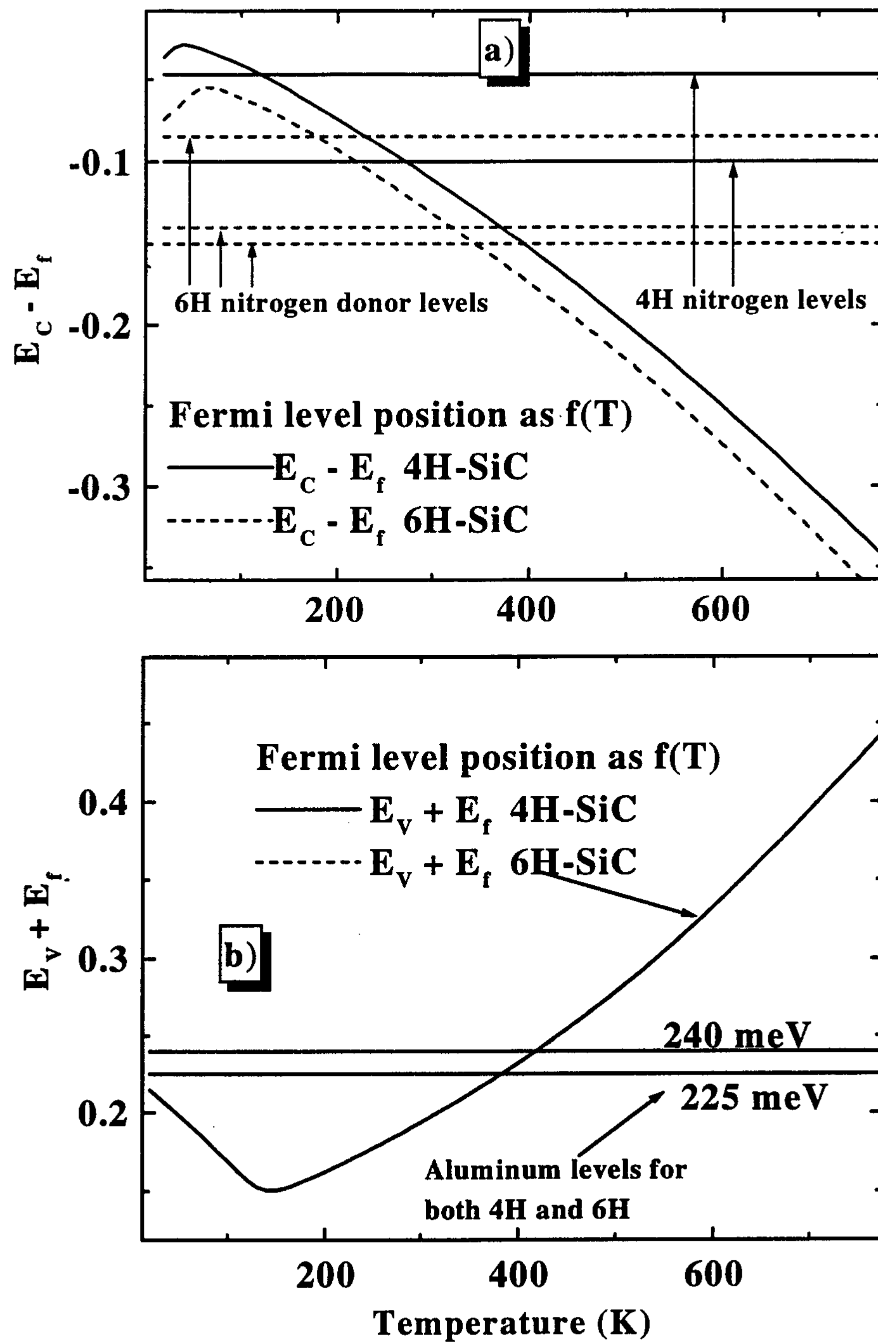

Figure VI-2. Data illustrates the calculated Fermi level position for a) n- type and b) p-type 6H and 4H-SiC with donor and acceptor levels indicated by the horizontal constant energy lines. The Fermi level is obtained from the exponential argument exp(η), which is solved for by rooting the polynomial given by Equation VI-7.

defect density of 1×10^{-17} cm^2 and 1×10^{15} cm^{-3}, respectively. A simulated filling pulse period of 0.1 ms was used to completely fill the deep level defect, and an SNR of 70 was selected. Capacitance was computed assuming depletion of an ideal Schottky barrier diode of 500μm diameter on material with a donor density of 2.5×10^{17} cm^{-3}. Figure VI-3 a) shows the standard rate window plot utilized for all DLTS trap data. Six rate windows are generated as described in Chapter IV, and applied to the transient data to obtain the curves shown. As illustrated by the Arrhenius data of Figure VI-3 b), an excellent agreement between the fitted results and programmed trap parameters was consistently observed, and verified the accuracy of simulation routines. The data shown in these figures are computed with consideration for incomplete ionization of three nitrogen donor levels.

In addition to the carrier capture mechanisms of Chapter III, there was also included an option to account for the effects of a strong electric field on the emission rate of carriers trapped at deep level defect sites. The large electric fields (10^6-10^7 V/cm) typically present in the depleted region of a reverse biased junction necessitate this consideration. The situation in which the electric field invokes an appreciable effect on the defect emission rate is when there exists a strong Coulombic attraction between the defect and trapped carrier of opposite charge. Under these conditions, it has been shown that an electric field lowering of the binding energy barrier is realized due to an increase in the dipole charge separation [Frenkel, 1938:657]. This so-called Poole-Frenkel barrier lowering has been well quantified for a number of defects in various material systems

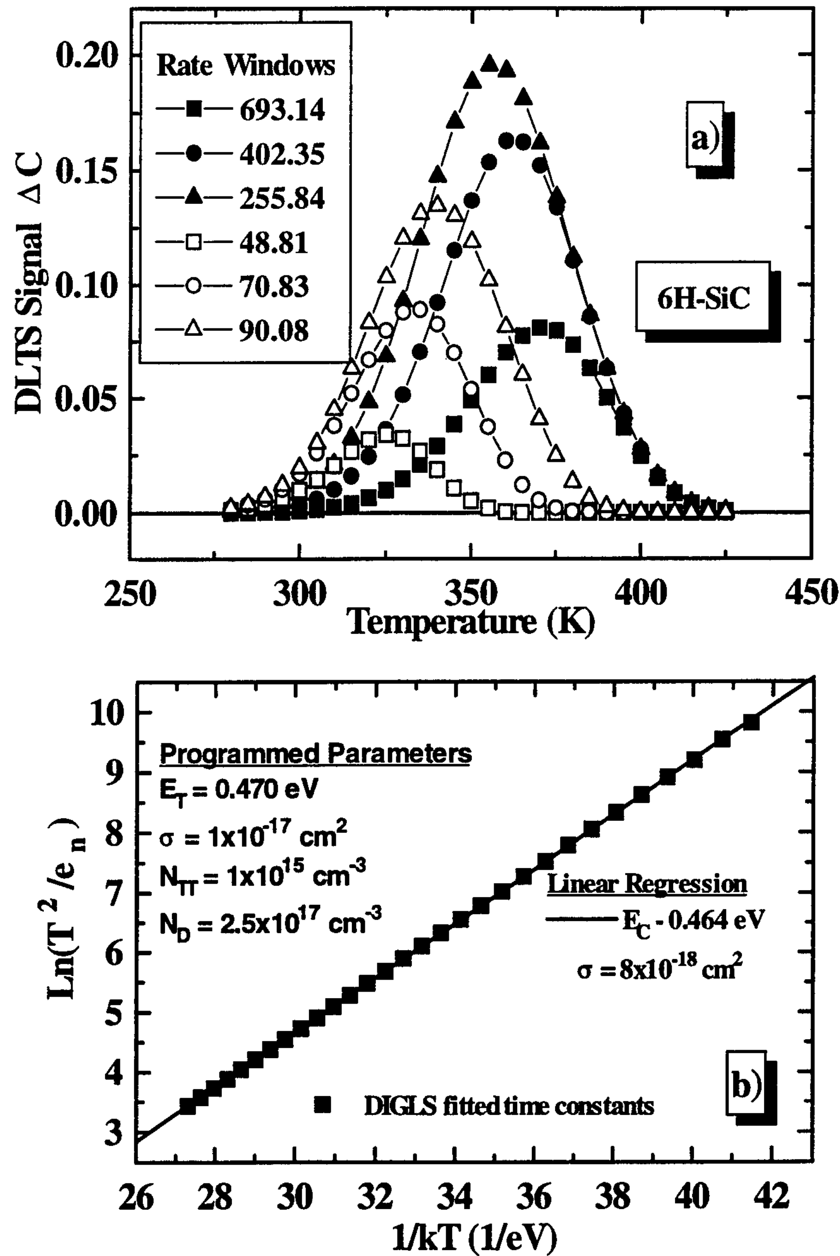

Figure VI-3. Rate window a) and Arrhenius b) representation of DIGLS fitted and reduced simulation data for a single deep level defect in n-type 6H-SiC material doped to $1x10^{-17}$ cm^{-3}. As illustrated in b), the programmed and transient analyzed ionization energies and capture cross sections are in close agreement. Data and figure represent typical comparison and analysis used to verify the accuracy of defect capture and emission simulations for various carrier exchange kinetics with n(T) condition included.

[Vincent, Chanter, and Bois, 1979:5484], [Rosencher *et al.*, 1985:2823]. Figure VI-4 graphically illustrates the effect of barrier lowering on a single Coulombic trap potential in the depleted region of a reverse biased diode. Shown in the figure is the electric field barrier-lowering for realizations of four different field values, F = 0, $5\text{x}10^4$, $1\text{x}10^5$, and $2\text{x}10^5$ volts/cm. Also shown is the significant reduction (ΔU) of the ground state ionization energy, E_T, which can result when this mechanism is present. The total electric field is the sum of the defect potential and that resulting from the applied bias, and is given by

$$U(x) = \frac{-\gamma q^2}{\varepsilon x} - qFx \,, \qquad \text{[VI-8]}$$

where F is the junction field intensity, q the electronic charge, ε the semiconductor permitivitty, and γ is the charge on the trap subsequent to carrier emission [Hartke, 1968:4871]. Differentiating Equation VI-8 with respect to x and solving for the potential maximum (zero slope) yields the minimum potential barrier position, x_{min}, which is seen to be approximately 0.14 μm for the F = $2\text{x}10^5$ V/cm field in Figure VI-4. Inserting this minimum expression into Equation VI-8 allows calculation of the Poole-Frenkel barrier reduction as a function of the electric field intensity. Performing this substitution yields

$$\Delta U = U(x_{min}) = 2q\left(\frac{\gamma qF}{\varepsilon}\right)^{1/2} . \qquad \text{[VI-9]}$$

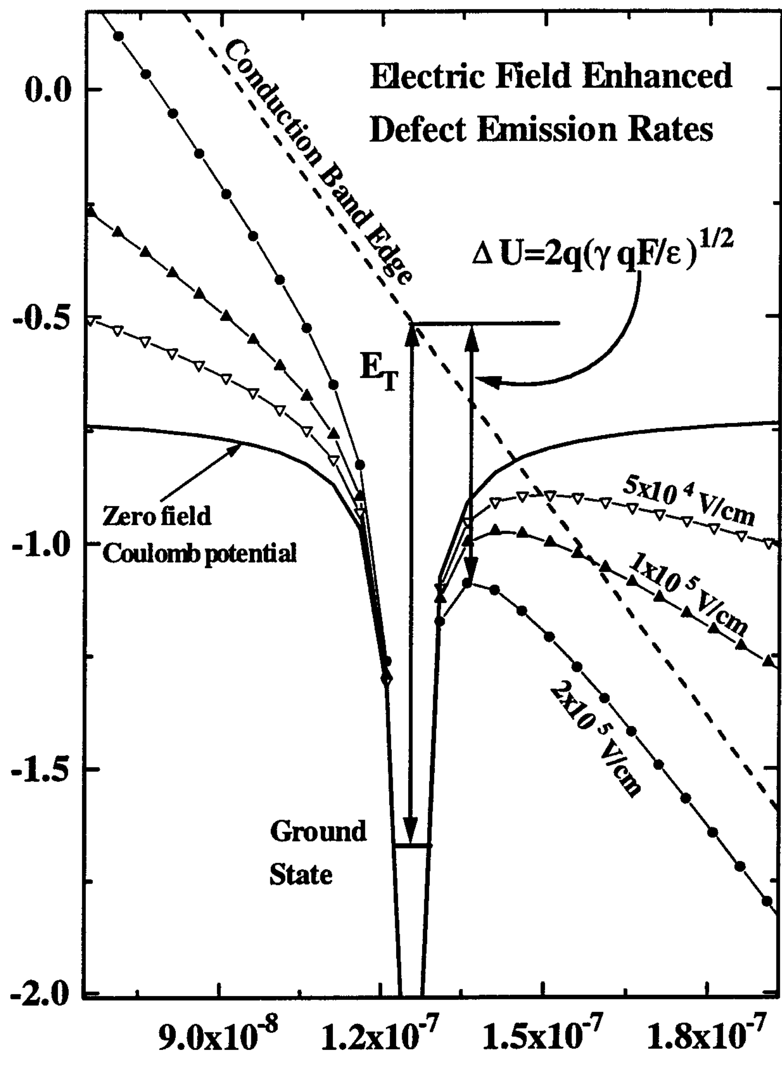

Figure VI-4. Illustration of the electric field barrier lowering of an attractive Coulombic defect potential. Shown are the progressive barrier reductions for increasing electric fields of 0, 5×10^4, 1×10^5, and 2×10^5 volts/cm. Explicitly indicated is the magnitude of the Poole-Frenkel barrier reduction, ΔU, and the conduction band edge for $F=2\times10^5$ volt/cm along with the zero field ionization energy E_T. These field-reduced barriers result in enhanced trap emission rates.

Barrier lowering translates directly into an enhancement of the trapped carrier emission rate. Since DLTS measurements are performed in the high field region of a reverse-biased diode, consideration of this mechanism is crucial to accurate estimates of defect parameters. We can represent the rate enhancement for electrons by rewritting Equation IV-7 to include a ΔU reduction in the trap binding energy

$$e_n = \frac{\sigma < v > N_C}{g} \exp\left(\frac{-E_T + \Delta U}{kT}\right) = e_{n0} \exp\left(\frac{\Delta U}{kT}\right), \qquad \text{[VI-10]}$$

where e_{n0} is the zero field emission rate. Thus, implementation of this physical process in simulations is accomplished in a simple, straightforward manner.

Double pulsed DLTS procedures described in Chapter IV are slightly modified to experimentally identify the electric field enhancement of defect emission rates. In order to accurately measure the emission rate as a function of electric field, DDLTS is used to define a narrow spatial window from which trap emission is exclusively recorded. Recall that Figure V-6 illustrates the DDLTS biasing sequence, and identifies the specific region which defines the emission window. Because the electric field varies linearly with position, x, it becomes necessary to limit the transient signal to a narrow portion of the reverse-biased depletion region in order to correlate a well-defined electric field to the measured emission rate. In this procedure, a fixed temperature is maintained, which corresponds to a strong transient signal for the trap under consideration. Then, with defined filling pulse heights V_{f1} and V_{f2}, the transient decay signal is recorded at intervals corresponding to increased reverse bias values. In this manner, the electric field is varied as the square root of the measurement bias, $E \propto V^{1/2}$. Estimated emission rates are

obtained in the usual manner, and when used in conjunction with Equation VI-10, Equation VI-9 can be used to determine the charge states of a defect.

As a final consideration, the simulation algorithms were applied to determine the maximum detectable trap depth in the wide bandgap SiC materials. When considering the large bandgap of the SiC polytypes, it is apparent that even with thermal scan capabilities in excess of 700 or 800 K, trap energies larger than a specified fraction of the bandgap will not have a significant emission rate. Thus, detection of trap emission for levels over an appreciable range of energies will not be possible using only thermal excitation for reasonable DLTS run parameters. Calculations using a range of trap energies and capture cross sections ($\sigma=10^{-21}$ to 10^{-12} cm^2) led to the conclusion that for reasonable transient periods ($\tau \leq 1.0$ sec.) and sampling rates (≤ 0.1 Mhz), the maximum trap depth detectable was below midgap (~1.2 eV) for temperatures up to 800 K in 6H-SiC. This is due simply to the negligible emission rates in this temperature range for defects with larger ionization energies. The presence of defect potentials exhibiting thermally activated capture cross sections and electric-field barrier-lowering effects would serve to lower and raise this maximum detectable energy limit, respectively.

Subsequent to implementing the capture and emission kinetics outlined above into the simulation algorithms, numerous realizations were accomplished in order to verify accuracy of the modeled kinetics. When these tasks were completed, the algorithms were applied to experimental data fitting and self-consistency validation of conclusions based on initial data analysis. The results of these implementations are central to the results and discussions of the following two subsections.

VI-II. Dominant SiC Carrier Capture Mechanism

In contrast to the wealth of information available regarding the rich radiative recombination spectra in the hexagonal SiC polytypes, studies of the electrical activity of deep level defects in SiC has only recently advanced beyond a few initial efforts to characterize the nonradiative recombination at deep traps in these materials [Suttrop *et al.,* 1990:231,1992:129], [Uddin *et al.,* 1994:908], [Evwaraye *et al.,* 1993:5269;1994:2691], [Anikin *et al.,* 1985:1357]. Several excellent review articles and research efforts in the study of SiC deep level impurities have been recently accomplished, including the results of electron spin- and paramagnetic-resonance methods applied to chemically identify Ti, V, and Cr as omnipresent substitutional impurities in 6H-SiC [Baranov *et al.,* 1994:1340], [Maijer *et al.,* 1992:27], [Schneider *et al.,* 1990:1184], [Vainer *et al.,* 1986:201], but subsequent reports of efforts in this area have not been forthcoming. As a result of the very limited and preliminary studies regarding the characteristics of non-radiative recombination and trapping in SiC, there was a need for continued progress in the study of these mechanisms in order to support the ever increasing device development activities in this emerging material system. Until now there have been no reports of the non-radiative carrier capture mechanisms for deep defect levels in hexagonal SiC.

Data presented in the following chapter demonstrates for the first time that the carrier capture kinetics of several electron and hole deep level trapping centers in 6H- and 4H-SiC are dominated by capture cross-sections which are strongly temperature dependent. Evidence is presented in these instances which indicates that the mechanism

of carrier trapping is accurately described by the lattice-relaxation, multi-phonon emission (MPE) theory of non-radiative deep level capture, with a temperature dependent capture cross section accurately described by $\sigma(T) = \sigma_\infty \exp(-E_b/kT)$. Additionally, the magnitude of the capture barrier, E_b, has been measured for several centers to be on the order of the de-trapping thermal emission energy, E_T, which characterizes the DLTS carrier emission rate, $1/\tau = N_{c,v}\sigma\langle v_{th}\rangle \exp(-E_T/kT)$. The measured barrier energies fall in a range of 100 to 850 meV for deep level traps with ionization energies in the range of 300 to 1040 meV, and high temperature cross section, σ_∞, values of between 10^{-11} to 10^{-21} cm^2.

Carrier recombination in the hexagonal SiC polytypes of interest requires the dissipation of larger amounts of energy (2.9-3.2 eV) than in most previously studied semiconductors. Accordingly, non-radiative carrier trapping at deep levels in these wide bandgap semiconductors requires similarly large lattice-energy or collisional-energy dissipation mechanisms in order to conserve crystal momentum. Deep traps, with large capture cross sections associated with fast capture rates, must necessarily be increasingly efficient in the dissipation of this energy as the magnitude of the trap depth or the bandgap increases. Recall from Chapter III that Auger and multiple lattice phonon emission (MPE) are the most likely mechanisms with which such large energies may be conserved nonradiatively. A third process, the cascade capture mechanism of Lax [1960:1502] was shown to be valid only for the coulombic (charged) series of shallow hydrogenic excited states located near the bandedge. Henry and Lang [1974:3023, 1975:989, 1976:47] theoretically and experimentally showed in a series of articles that

large (>1 eV) amounts of energy could be efficiently dissipated in a rapid, nonradiative capture process. This was shown to be possible due to strong electronic-lattice coupling associated with lattice-relaxation defect motion subsequent to carrier trapping. Using calculations of the free-to-bound transitions (Equation III-13) and comparing the semiclassical limit at high temperatures to experiment, they showed that capture by multi-phonon emission (MPE) was accurately described by the exponentially-activated, temperature dependent capture cross section of Equation III-21. This was then shown to corroborate experimental results yielding very large capture cross sections in GaP and GaAs (10^{-13}-10^{-15} cm^2) for fast non-radiative capture, despite the requirement to dissipate up to 1.3 eV of energy. As shown in Chapter III, the Auger effect in large bandgap materials is relatively temperature independent, with the carrier lifetime being proportional to the inverse square of the free carrier concentration, and can thus not be confused with thermally activated capture cross sections associated with MPE or cascade processes. Gibb *et al.* [1977:1021] have also presented a theory to describe the capture kinetics of a 0.75 eV hole trap in GaP. In their two-step model, it is proposed that carrier capture into the ground state of a deep, *charged* trap is preceded by capture into a shallow coulombic excited level within an effective Rydberg of the bandedge. For the SiC defect centers studied during this effort, the temperature dependencies of capture cross sections were not observed to exhibit the predicted trends of this two-step capture mechanism.

In this portion of the SiC defect study, deep level trap parameters and capture kinetics were measured on various 4H- and 6H-SiC junctions using deep level transient spectroscopy (DLTS) techniques, with careful attention to biasing and filling pulse

dependencies. Capture rates were determined from reverse biased, pulse-width dependent measurements, and when possible from unbiased neutral material. The capture cross sectional dependence upon temperature was subsequently compared to theoretical models by considering the computer simulated transient-capacitance results using both experimental and contrived deep level trap parameters. Deep level trap concentration versus temperature profiles, obtained from judiciously selected DLTS arrhenius data for various t_p settings, were also fit to the MPE capture model using the commercial curve fitting software package Origin™, which utilizes Levinberg-Marquardt least squares algorithms.

VI-III. Modeled Capture Cross Section Trends from Deep Level Emissions.

If trap filling pulses used during the capture event described by Equation VI-2 are of a short enough temporal duration, t_p, then over some finite temperature range, T_R, the deep level center will be incompletely filled after t_p seconds ($N_T^{0c}(T,t_p) < N_{TT}$). The T_R of interest for the analysis that follows is that over which the defect center has an appreciable reverse bias emission rate. In other words, T_R is roughly the temperature range over which the DLTS spectral peaks occur. As the temperature increases, the capture rate becomes larger, increasing the density of trapped carriers for a fixed t_p. The result is a temperature dependent trap occupation profile, uniquely determined by the characteristic defect capture kinetics. This trap occupation profile is in fact given by the rate-ratio prefactor, A/(A+B), and exponential product for $N_T^{0c}(T,t_p)$ defined by Equation VI-2. In other words, this product, which has a maximum value of 1, can be loosely

considered as the trap distribution function or occupation probability, parametrically dependent upon the fixed filling pulse width, t_p. Figure VI-5 (c) shows this distribution function along with the prefactor and exponential product terms plotted separately in Figure VI-5 (a) and (b), respectively. Equation VI-2 was modeled using MPE capture mechanisms, and the plots reflect the capture barrier, E_b, effect on the resulting distribution function. This will shortly be seen to be a crucial aspect of this analysis. The plotted data reflects results for a simulated 748 meV electron trap in 6H-SiC with a filling pulse width of 1 ms and σ_∞=5x10^{-15} cm^2. It was determined that the important physical parameter describing the behavior reflected in Figure VI-5 was not simply the capture barrier magnitude but rather the ratio to the thermal ionization energy of the trap, E_T. This is because both capture and emission processes are considered in these experiments and analysis.

Temperature dependent DLTS emission transient data can be used in conjunction with this distribution function information to obtain a profile proportional to the trap occupation density. This is accomplished by using the capacitance emission transient amplitude ΔC, which is proportional to the trap concentration data at each isothermal step. The proportionality factor is simply the captured carrier concentration normalized to the ionized shallow doping concentration ($N_T^{0c}(T,t_p)/N_S$), which can be seen by rewriting Equation VI-4 in the following form

$$C^2(T,t) = C^2(T,t=\infty)\left\{1 - \frac{N_T^{0c}(T,t_p)}{N_S}[\exp(-e_n t)]\right\}, \qquad \text{[VI-11]}$$

where for simplicity we have assumed electron trapping in n-type material (N_s=N_D^+) and

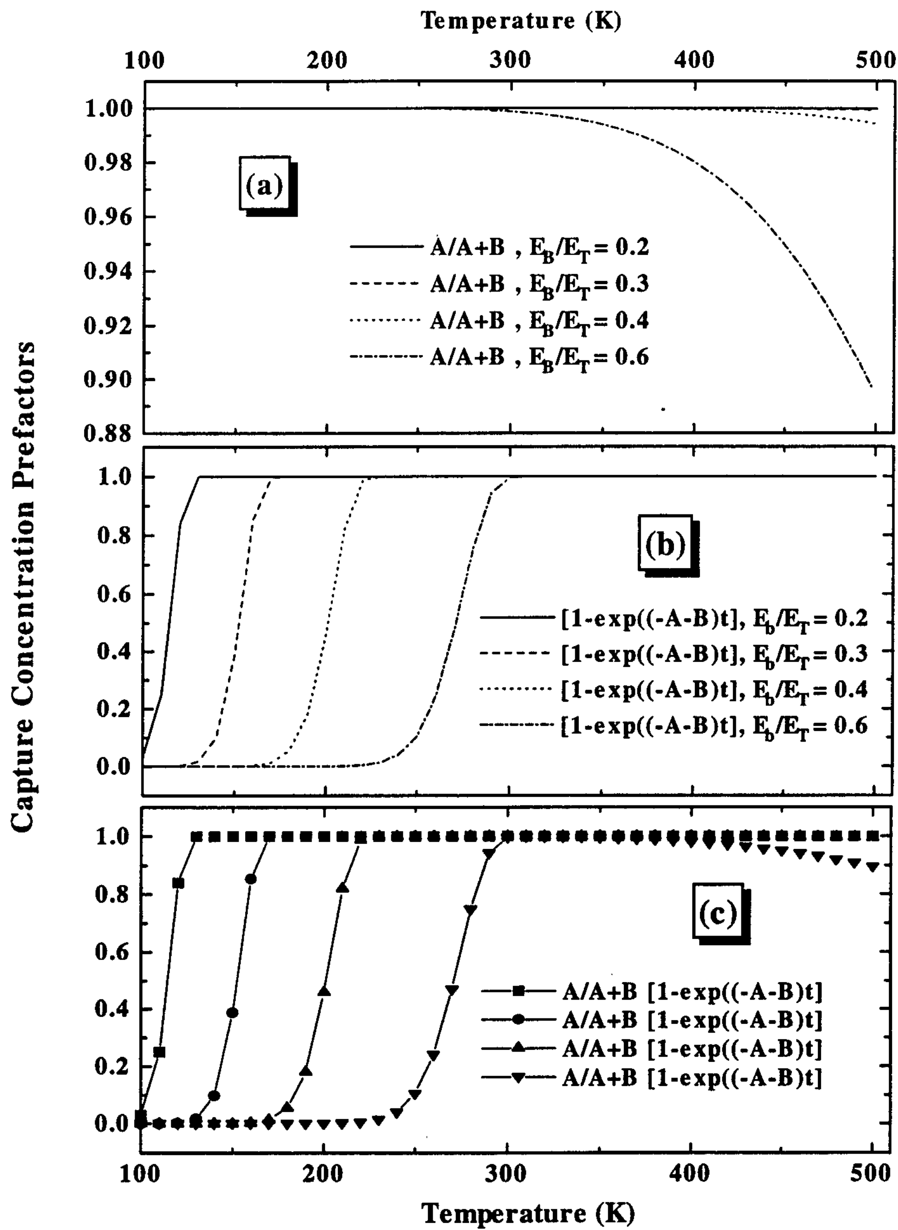

Figure VI-5. Simulated data plots of the prefactor (a), exponential factor (b), and the resulting product (c) associated with the captured carrier concentration Equation VI-2. The temperature variations are illustrated for a fixed trap emission energy, E_T=748 meV, and four different E_b values. A simulated filling pulse of 1 ms was used in the computations. This analysis led to the development of a novel MPE barrier estimation technique which is realized by comparing transient amplitude data with Equation IV-2.

that $e_n >> c_n$. Emission rates are obtained from MF or DIGLS fits to the isothermal capacitance transients, and are subsequently used to obtain amplitude factors. The amplitude factors are then used to plot trap concentration information $N_C^{0c}(T,t_p)/N_S$ using Equation VI-11. If this information is plotted versus T or 1/kT, and an appropriate incompletely saturating filling pulse was utilized, the desired distribution function profile will be realized. Figure VI-6 illustrates this filling pulse dependent trap occupation profile for a numerically simulated, 450 meV majority-carrier, electron trap in 6H-SiC of density 1×10^{15} cm^{-3}. MPE capture kinetics were also included in this computation with a thermal capture barrier of 190 meV. The lower curves in the figure are DLTS spectral characteristics associated with carrier emission for the two rate windows listed on the plot. The trap distribution profile or filling factor from Equation VI-2 for several filling pulse periods are reflected in the upper set of curves. The programmed trap parameters are listed as insets in the figure. Experimentally obtained transient amplitude profiles will be dependent upon the filling pulse used as seen in the upper set of curves. Using DLTS methods, the trap emission rate is measurable only over the temperature range indicated by the rate window peaks and the shaded region. Therefore, the occupation profile obtained from transient amplitude factors will be uniquely determined by the particular filling pulse used. It will correspond to the portions of the N_T^{0c} curves intersecting the shaded region.

Two points are in order when considering the transient amplitude factors in this manner. First, it is always true that for short enough filling pulse durations, the trap will never be saturated at any temperature as indicated in the figure for pulses shorter than 0.3

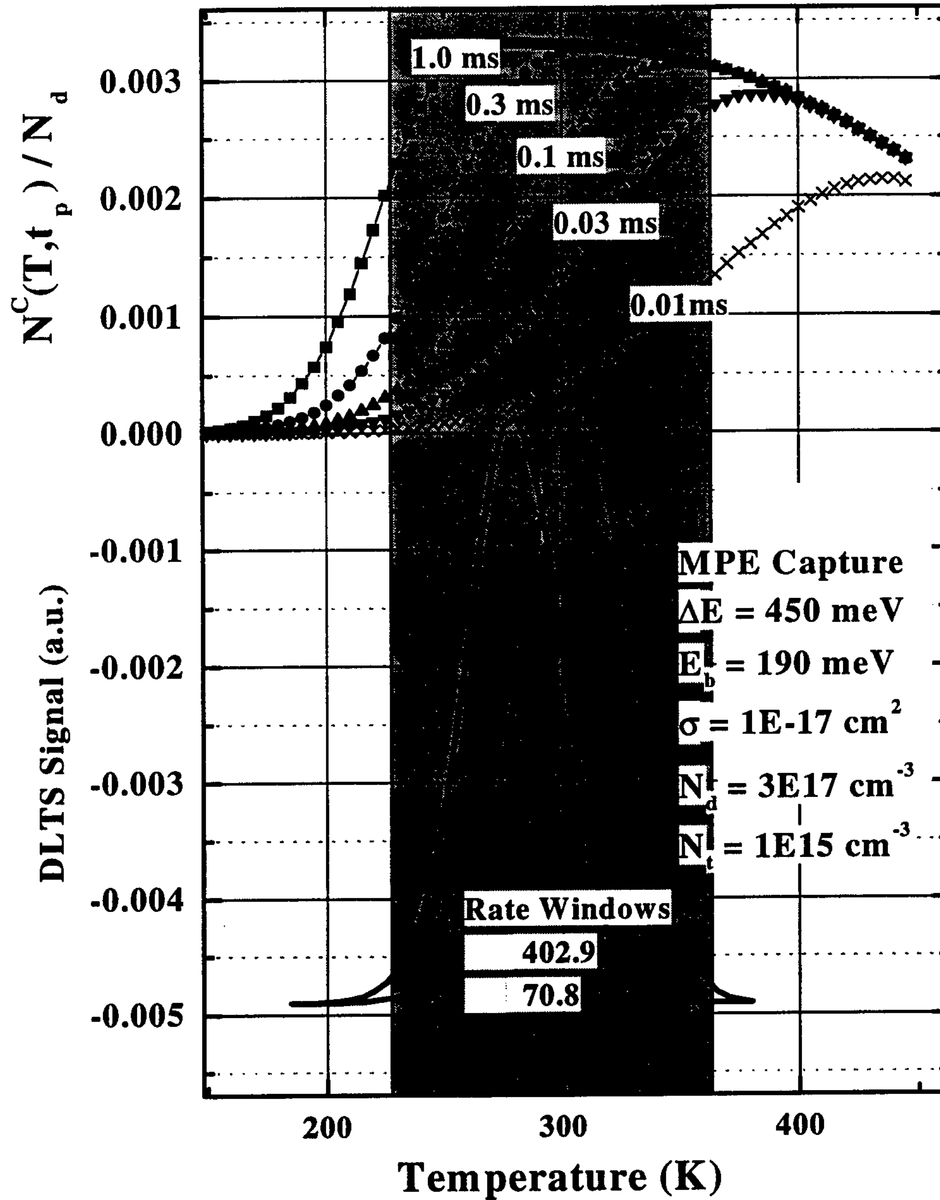

Figure VI-6. Normalized trap occupation prefactor illustrated by the upper family of curves simulated with MPE capture kinetics for electron capture in n-type 6H-SiC. Each member corresponds to filling pulse durations varied over the range of 0.01ms $< t_p$ $<$1.0ms. The lower pair of characteristic DLTS rate window spectral peaks represent the simulated defect emission transient data for the same trap center, programmed with the parameters listed beside the plots. The shaded area represents the temperature range over which the capacitance transient data is detectable using DLTS methods.

ms for this particular set of defect parameters. This is due to the exponential term of Equation VI-2 being always less than unity until a specified high temperature limit is realized. However, the condition $c_n >> e_n$ will no longer be valid in the high temperature range, where the capture rate would be large enough to completely fill the traps during the narrow filling pulse. Thus, the trap is never saturated since A/(A+B) is always less than one in this range, and dominates the high temperature behavior as shown in Figure VI-5. Thus, experimentally observed peak transient amplitudes will underestimate the actual defect concentration if the apparent saturation plateau is interpreted absolutely. The temperature range and pulse width at which this will become significant are predominantly dependent upon the magnitude of the capture barrier energy, or more correctly, the ratio of the barrier to thermal emission energies (E_b/E_T). A more explicit illustration of these pulse width and E_b/E_T ratio effects on N_T^{0c} are shown in Figures VI-7, VI-8, and VI-9 for MPE barrier to trap ionization energy ratios of 0.2, 0.43, and 0.65, respectively. The curves in each figure correspond to filling pulse widths of 1 ns to 1 ms for Figure VI-7, and 30 ns to 1 ms for Figure VI-8 and Figure VI-9. The simulated data in these figures are associated with the emission transient amplitude factors for a 750 meV electron trapping center in n-type 6H-SiC. Values of $N_{TT}=1x10^{16}$ cm^{-3} and $\sigma_\infty=5x10^{-14}$ cm^2 were used in the calculations. As the barrier increases, a shift toward higher temperatures is explicitly observed for the concentration profiles due to the greater kinetic energy required to surmount the capture barrier. As this occurs, the pulse width required to maximize the profile within the DLTS measurement range, indicated by the shaded regions, increases from roughly 3 ns to 0.1 ms. Also included in these figures is

the comparison between N_T^{0c} calculations utilizing the n(T) condition, illustrated by the line-plus-symbol plots, and N_T^{0c} computations assuming complete donor ionization ($n=N_D^+=N_D$). Immediately apparent in these figures, especially Figure VI-9, is that the condition of incomplete saturation is exascerbated by large E_b/E_T ratios. This is due to the dominance of the exponential prefactor term at lower temperatures for large E_b values. The need to consider n(T) arising from incomplete dopant ionization is now clearly illustrated by the significant temperature shift and amplitude variability between the two cases. The errors introduced when fitting experimentally obtained profiles like those shown in these three figures is significant, as will be shown on real SiC DLTS data in the following subsection.

The second point to be made is in regard to the selection of trap filling pulse periods, and was alluded to in the previous paragraph. In order to accurately estimate defect capture parameters, pulse widths must be chosen to maximize the important features of the captured concentration profile which are occurring over the temperature range of DLTS measurements. This is accomplished by selection of a filling pulse which will maximize the information carrying portion of the distribution function that is measured during the DLTS thermal scan. Critical features of the profile are the peak position and the rate at which the N_T^{0c} changes as a function of temperature on the low energy (kT) side of the peak. Referring back to the previous three figures, this corresponds to pulse periods of roughly 10 ns, 3 μs, and 0.5 ms for Figures VI-7, VI-8, and VI-9, respectively, for this particular set of simulated trap parameters.

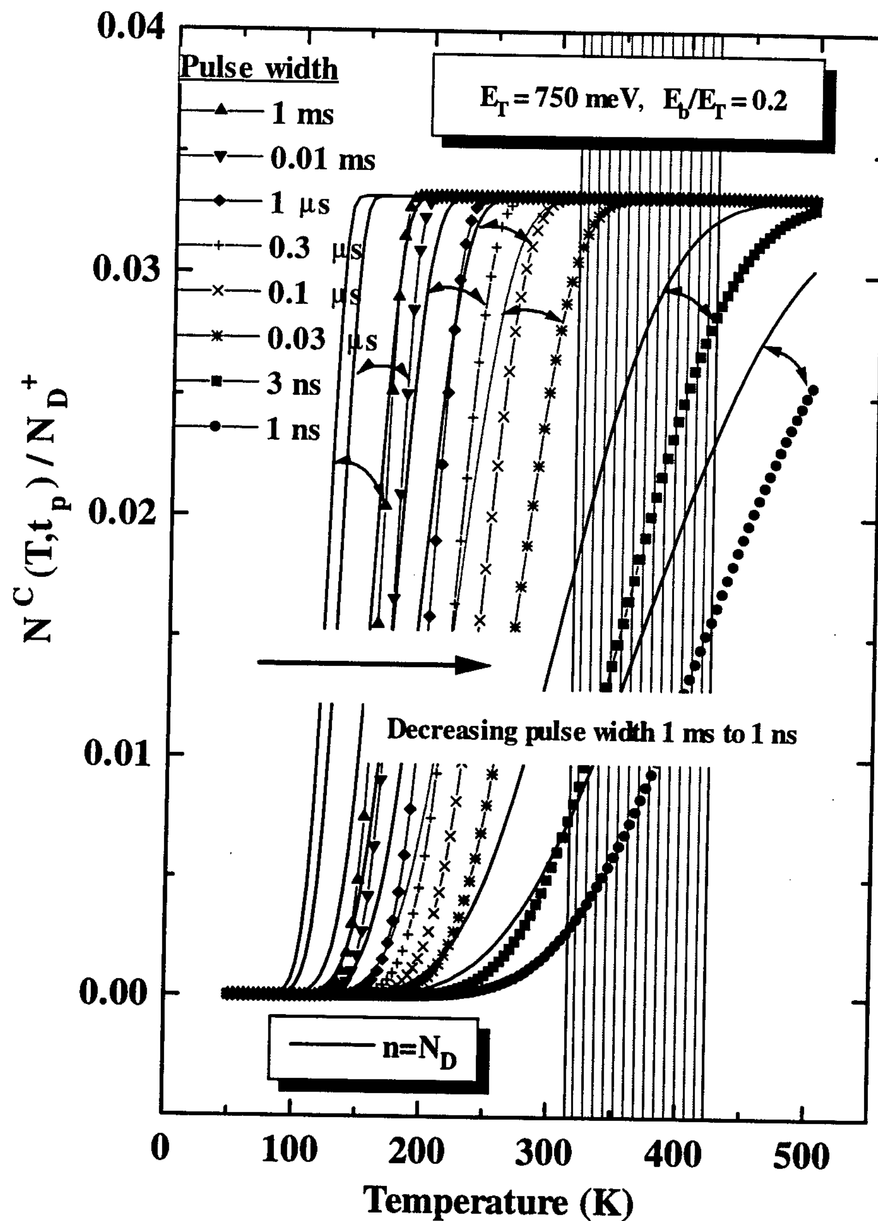

Figure VI-7. Normalized, MPE, captured carrier concentration in 6H-SiC as a function of filling pulse duration for a fixed E_b/E_T ratio of 0.2, where E_T=750 meV. Included as solid line curves are the same calculations assuming complete ionization of the shallow donor impurities $n(T)=N_D$. The shaded region corresponds to the range of temperatures over which DLTS data is collected, and thus this figure illustrates the expected amplitude profiles for the various pulse widths listed in the figure.

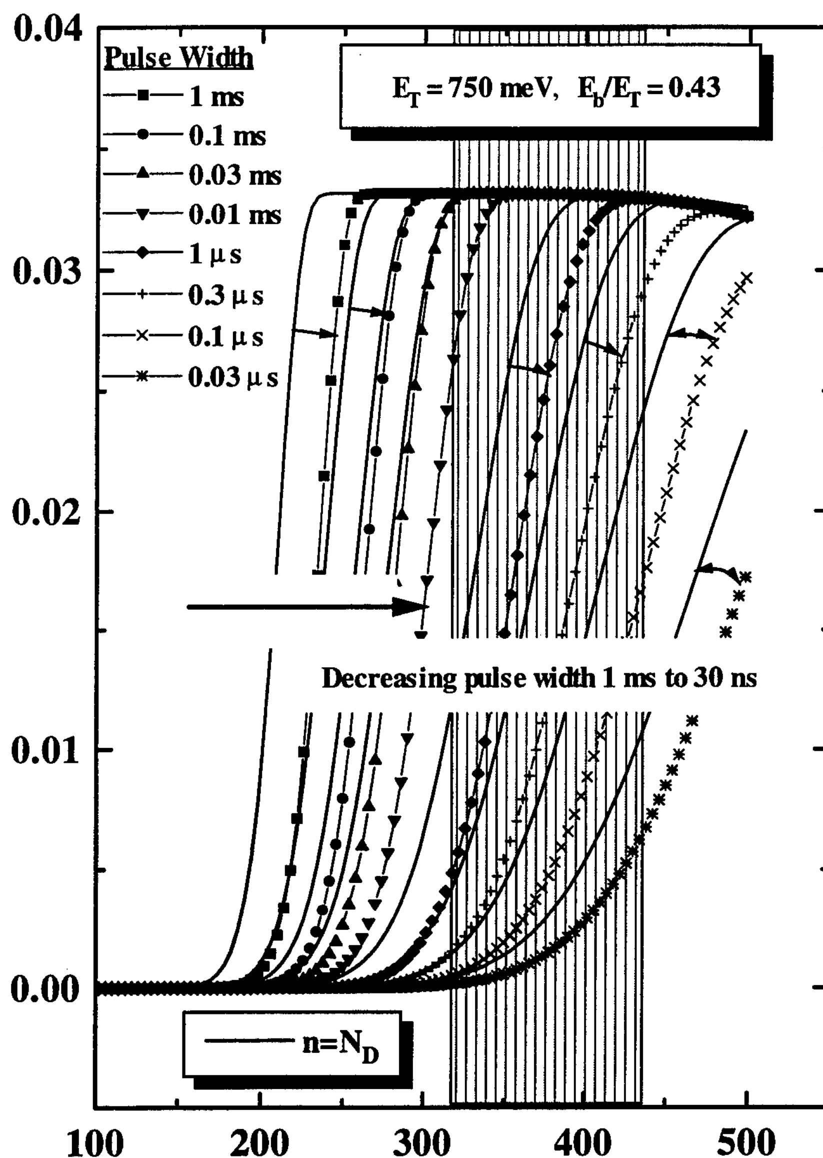

Figure VI-8. Normalized, MPE, captured carrier concentration in 6H-SiC as a function of filling pulse duration. Calculations are identical to Figure VI-7 with the exception of increasing the fixed E_b/E_T ratio to 0.43. In comparison to Figure VI-7, the increased capture barrier shifts the profiles to higher temperatures for the same filling pulse duration.

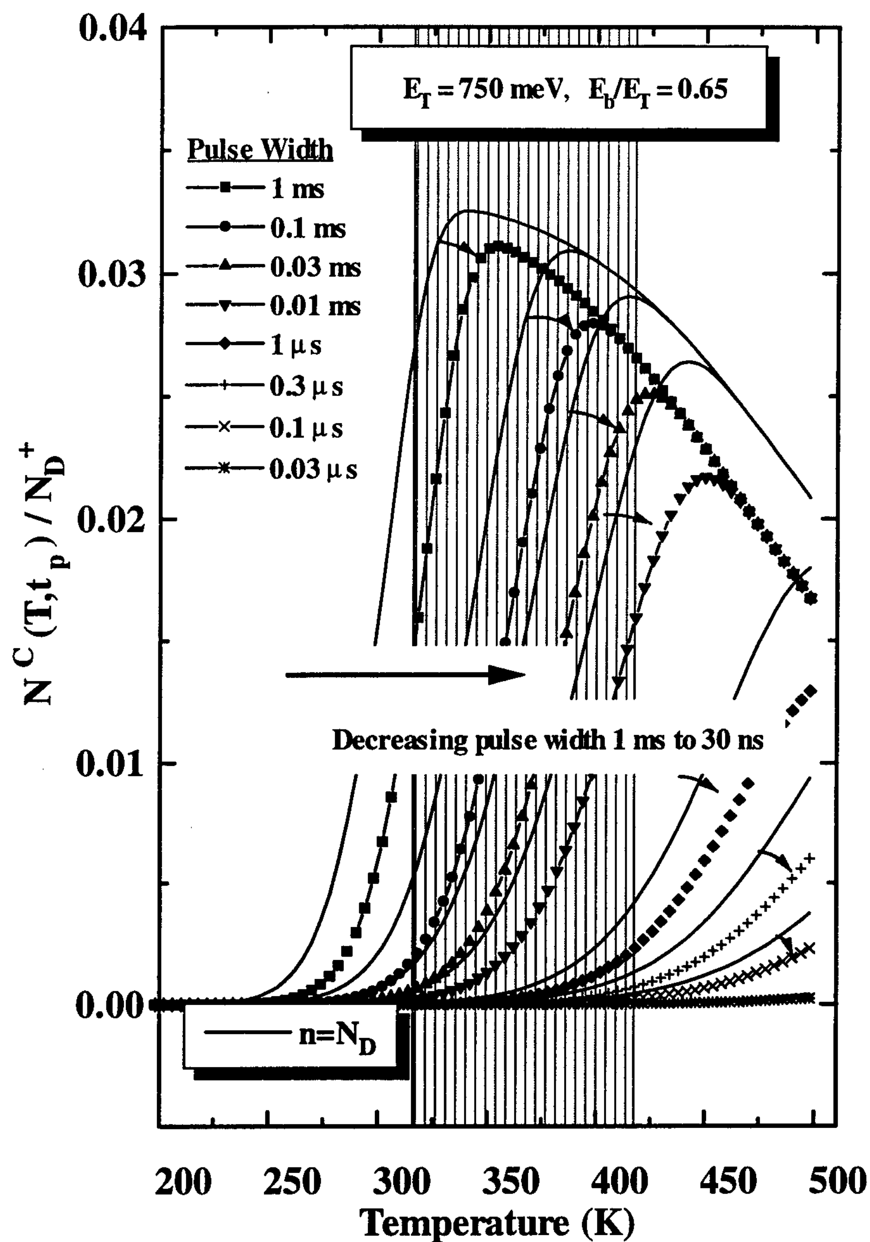

Figure VI-9. Normalized, MPE, captured carrier concentration in 6H-SiC as a function of filling pulse duration. Calculations are identical to Figure VI-7 and Figure **VI-8** except that the fixed E_b/E_T ratio is now increased to 0.65. In this range of E_b/E_T, the traps are now seen to be incompletely saturated for all values of the filling pulse durations used. This is due to the dominance of the A/(A+B) prefactor in the expression describing the trap occupation density (Equation VI-2).

For very small E_b/E_T ratios, there will be a practical hardware limit to the pulse width period, which will result in incomplete trap saturation, and for our system it is in the 10 μs range. But more importantly, small E_b/E_T ratios require very narrow filling pulses to effectively stretch the distribution profile up to the temperature range of significant trap emission. This results in a much reduced fraction of the temperature dependent trap occupation function being represented by the emission data. This can be inferred from the 1 and 3 ns profiles shown in Figure VI-7, and for smaller E_b/E_T ratios, the effect will be greater. Thus, it becomes apparent that MPE capture analysis of the emission transient amplitude factors will be increasingly difficult as the E_b/E_T ratio decreases. Fortuitously, the SiC deep levels exhibiting this capture mechanism were found to be characterized by large barrier to trap energy ratios.

Recognition of the potential pitfalls associated with extremely narrow filling pulses required for small E_b/E_T ratios and the information of temperature dependent free carrier concentration are necessary to accurately interpret deep trap emission data and to extract capture information. We utilize two techniques with which the obtained data may be reduced to yield capture barrier E_b, trap concentration N_{TT}, and high temperature cross section σ_∞ values. The first is easily implemented using an Arrhenius type analysis, but it can result in a large degree of uncertainty for a non-negligible range of E_b/E_T ratios, and is used primarily to obtain quick estimates of E_b magnitudes. The other involves using the previously described software model to iterate to a complete solution with much less uncertainty in the returned parameters.

Combining the expressions of Equations VI-2, VI-4, and V-1 and recalling that the capacitance transient amplitude is proportional to the captured carrier concentration (Equation VI-11), we can derive the following expression, which will be used to analyze the DLTS emission transient amplitude data for MPE capture of free carriers, as

$$\frac{N_T^{0C}(T,t_p)}{N_s} = FNT \cdot \{1-\alpha \cdot \exp[(F_\sigma/(kT)^2) \cdot \exp(-E_b/kT)]\}, \qquad \text{[VI-12]}$$

where $$FNT = \frac{\Delta C}{C(t=\infty)}, \quad F_\sigma = N_{c,v} \cdot \langle v \rangle \cdot t_p \cdot \sigma_\infty, \quad \text{and } \alpha = \frac{A}{A+B}.$$

For clarity of presentation purposes, a single exponential decay is assumed. Thus, N_T^{0c} is the amplitude coefficient A_1 of Equation V-1, and N_s is the ionized doping fraction. ΔC is the amplitude of the capacitance transient assuming saturation of traps during the filling pulse event and complete evacuation during the emission period. $C(t{=}\infty)$ is the steady-state relaxed capacitance equal to coefficient A_0 of Equation V-1. Therefore, FNT defines the saturated or maximum normalized captured carrier concentration ratio. $N_{C,V}$ is meant to express inclusion of either the conduction or valence band density of states in the general expressions for majority carrier transitions in n- or p-type material, respectively. All other terms have been previously defined.

Implementation of Equation VI-12 is accomplished by performing a Levenberg-Marquardt, non-linear, least-squares fit of the empirical N_T^{0c}/N_s data, obtained from MF or DIGLS fitting of the decay transients. For this purpose, we utilize a commercial plotting and fitting software package to numerically fit the empirical distribution function profile. The iterative curve fitting routine returns parametric values for FNT, F_σ, α, and

the capture barrier E_b. Physically we know that over the temperature range of detected DLTS emission data, the condition that $c_n >> e_n$ must be satisfied so that $\alpha = 1$ and constant, otherwise $\alpha = \alpha(T)$, and the above analysis will become invalidated with respect to the curve fitting algorithm. This translates, of course, to a requirement that E_b/E_T be less than some upper bound, which will depend upon the carrier type, effective mass, free carrier concentration during trap filling, and high temperature cross section limit, σ_∞. Thus, the returned value of the α parameter is used as an indicator to the validity of the above fitting model for a given data set. Additionally, the extraction of σ_∞ values from the F_σ parameter has associated with it the inherent imprecision involved with calculating a small number from a large quantity. F_σ values are typically in the range of 10^{10} to 10^{14} for effective mass values of SiC and filling pulse durations in the 10^{-3} to 10^{-5} second range. Therefore, the estimation of σ_∞ from this quantity, which is typically in the range of 10^{-12} to 10^{-20} cm^2, results in a large uncertainty. This difficulty can be eliminated by noting that when the emission rate prefactor method is used to compute the capture cross section from the y-intercept of an Arrhenius plot, the measured quantity is actually the cross section extrapolated to $T=\infty$. Therefore the insertion of σ_∞, which is obtained from Arrhenius data activation energy plots, as a fixed parameter into the curve fitting data set removes a degree of freedom, and results in minimized χ^2 and improved energy estimates, E_b. In practice, using computer simulated trap capture and emission transients, we have observed that use of the emission prefactor cross section as a fixed fitting parameter is a necessary condition to the attainment of accurate results using this method.

Figure VI-10 shows a $N_T^{0c}(T,t_p)/N_D$ profile obtained from simulated and DIGLS fitted capacitance transients for a deep level majority-carrier electron trap in n-type 6H-SiC. The simulation included MPE capture kinetics for a single deep level ionization energy of 450 meV. The donor and defect concentrations were given values of $1x10^{17}$ and $1x10^{15}$ cm^{-3}, respectively. The filling pulse used for this simulation was 100 μs, and the transients were sampled at 14.3 kHz. The E_b/E_T ratio was selected to be 0.58. Shown in the inset is the Arrhenius emission data from which the transient amplitude for each emission rate data point is used to obtain the N_T^{0c}/N_D profile. Shown also is the resulting fit using Equation VI-12 and the commercial fitting package, yielding a value of E_b=270±20 meV. This value is in fairly good agreement with the modeled 260 meV thermal barrier value.

This data illustrates the difficulties associated with MPE capture parameter estimation method using Equation VI-12. First, the $0.01N_D$ defect concentration for this large E_b/E_T ratio is underestimated by 25% as seen by the peak value of -0.0075. This is due to the large energy ratio and the incomplete ionization of the SiC donors as can be seen by referring back to Figure VI-9. Secondly, the validity of Equation VI-12 to only ~325 K due to violation of the c_n>>e_n condition leaves a significant portion of the information carrying data unused. As a result of these shortcomings, this technique was determined to be useful only for quick estimates of the thermal capture barrier energy, which can be easily accomplished while analyzing Arrhenius data.

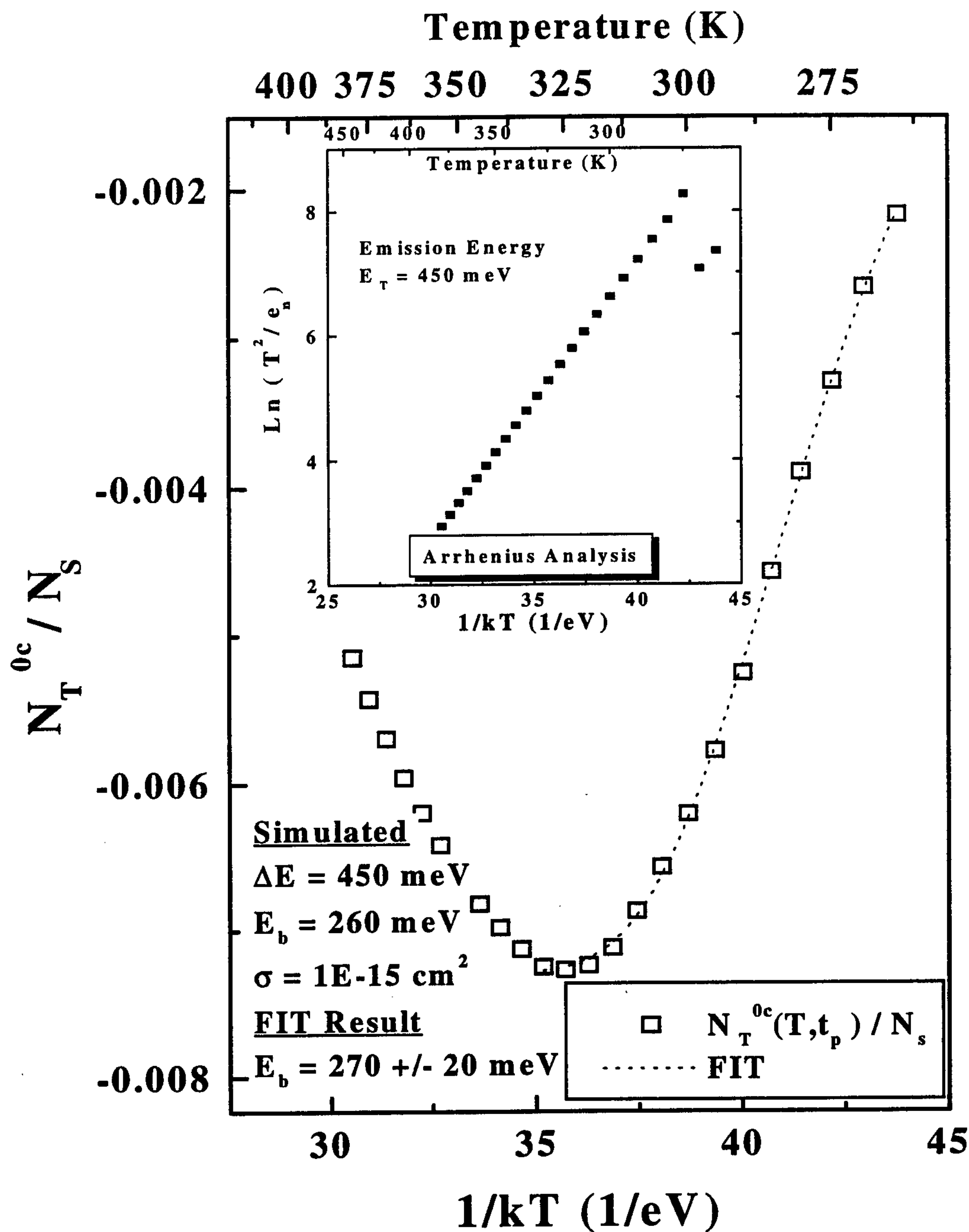

Figure VI-10. Capacitance transient amplitude data plotted as a function of 1/kT. Data was obtained from simulated and DIGLS fitted transients, which were generated with the inclusion of MPE capture kinetics. The programmed trap parameters are shown in the lower portion of the figure. The N_T^{0c} data represents the quasi-distribution function for the defect center. The dotted line represents the fit obtained using Equation VI-12. The inset plot reflects the emission rate Arrhenius analysis from which the σ_∞ estimate used for N_T^{0c}/N_s fitting was obtained.

A more complete and accurate method to obtaining the capture parameters from emission data is to utilize the full expressions given by Equations VI-2 and VI-4, numerical iteration to a solution based on the empirical emission data, and initial guesses at the desired parametric quantities. Application of the routines described earlier in this chapter, which incorporate these general expressions, to experimental data obtained from DLTS isothermal scans of 6H- and 4H-SiC junctions will be presented in the following chapter.

VII. Nonradiative Capture in SiC

VII-I. Evidence for Capture by Multi-Phonon Emission in SiC

As previously outlined, the efficient dissipation of large amounts of energy in a fast non-radiative capture process must be facilitated by one of the physical processes described in Chapter III or some as yet undefined mechanism. In this section we present empirical DLTS data which implicates the MPE capture process in several deep trapping centers in 4H- and 6H-SiC.

The SiC samples used were (0001) 6H-polytype n- and p-conductivity bulk material grown by the vapor transport process, and doped with nitrogen and aluminum, respectively, to a concentration range of $1x10^{17}$ and $7x10^{18}$ cm^{-3}. MOCVD grown 6H and 4H (0001) epitaxy with shallow impurity doping levels of $1x10^{16}$ to $2x10^{17}$ cm^{-3} were also obtained and characterized. Schottky contacts of 500 μm diameter and ohmic contacts were formed following the recipes and processes described in Appendix C. Due to the large diode area, the higher doped n-type samples required an initial sputter deposition of a thin (50 nm) Ti layer prior to Ni coverage in order to eliminate leakage currents in the reverse biased devices. 4H-SiC p+/n epitaxial grown diodes with N_A=$1x10^{19}$ Al/cm^{-3} and N_D=$5.7x10^{15}$ N/cm^{-3} were also obtained from a commercial vendor, and included in the matrix of samples investigated during this portion of the completed research. MOS capacitors on epitaxial SiC layers were obtained by a single rf-sputtered deposition of Mo, 300 nm thick, to form the 500 μm contact areas on thermally grown SiO_2 layers.

As already demonstrated, the large ionization energies associated with shallow dopants in the SiC hexagonal polytypes result in free carrier concentrations that are strong functions of temperature. In fact, at 300 K the fraction of ionized shallow impurities in 6H-SiC is only ~40% and 10% for nitrogen and aluminum, respectively. Thus, deep level parameters as determined from DLTS capture and emission data will have an additional temperature dependency beyond that included in conventional DLTS analysis. Obviously, effects will be more or less serious depending upon the temperature range of the measurements and the conductivity type of the material. The most seriously affected quantity will be the carrier capture rate, which is directly dependent upon the concentration of free carriers in bias free neutral material. As a result of using reverse biased junctions for emission transient measurements, the depletion (n=p=0) approximation eradicates this difficulty in the emission rate analysis for the most part, provided the reverse bias quasi-Fermi level is several kT below the trap level. However, depending upon trap energy level, dopant and defect concentrations, bias levels, and temperature range of interest, the consideration of detailed balance may require re-evaluation in order to accurately represent the deep level emission rate. In neutral material, for the general case of electron trapping in an n-type semiconductor, this is given by Equation IV-4 rewritten for convenience as

$$e_n \cdot \mathcal{P} = c_n \cdot (1 - \mathcal{P}) \;\; \Rightarrow \;\; e_n = N_C \cdot \mathcal{F}_{1/2}(\eta) \cdot \langle v \rangle \cdot \sigma(T) \cdot \frac{1 - \mathcal{P}}{\mathcal{P}} \, , \qquad \text{[IV-4]}$$

with $\mathcal{P}$ being the probability of electron occupation at the impurity level, and all other terms have been previously defined. If $\mathcal{P}$ is accurately represented by Fermi-Dirac statistics and non-degeneracy conditions exist, then the well known DLTS expression is

obtained. However, it has been previously demonstrated that the application of detailed balance between capture rates in neutral material and emission rates in the space charge region of a reverse biased junction is of questionable validity under some conditions, and may have to be considered separately [Sah, 1976:975], [Miller *et al.*, 1977:377]. This is a concept which is frequently overlooked in the literature, and when considering the additional complications presented by the n(T) condition in SiC, it may be even more relevant especially at lower temperatures. The most direct way to determine the extent of these complications on DLTS data is to compare measured capture rate parameters with emission rate prefactor quantities obtained under reverse bias conditions, and using simulated data with enough physics built into the model. Both approaches have been taken in attempting to evaluate these issues.

Figure VII-1 represents the results obtained from DLTS emission experiments on a deep hole trapping center in p-6H-SiC bulk wafer samples. This level was observed in most bulk Schottky diodes investigated. There are no previous reports of this defect being observed in 6H-SiC, and its source is unknown. In fact, the availability of DLTS related publications documenting deep level activity in p-type SiC of any polytype is effectively nonexistent. Illustrated on the plot are the DIGLS estimated transient amplitude factors shown by the "+" symbols. Curves corresponding to the commercial curve fitting package using Equation VI-12 and the computer modeled solution using Equations VI-2 and VI-4 are shown as dotted and solid lines, respectively. The modeled fit to the data utilized the thermal ionization energy of E_T = 1.04 eV obtained from the emission rate Arrhenius

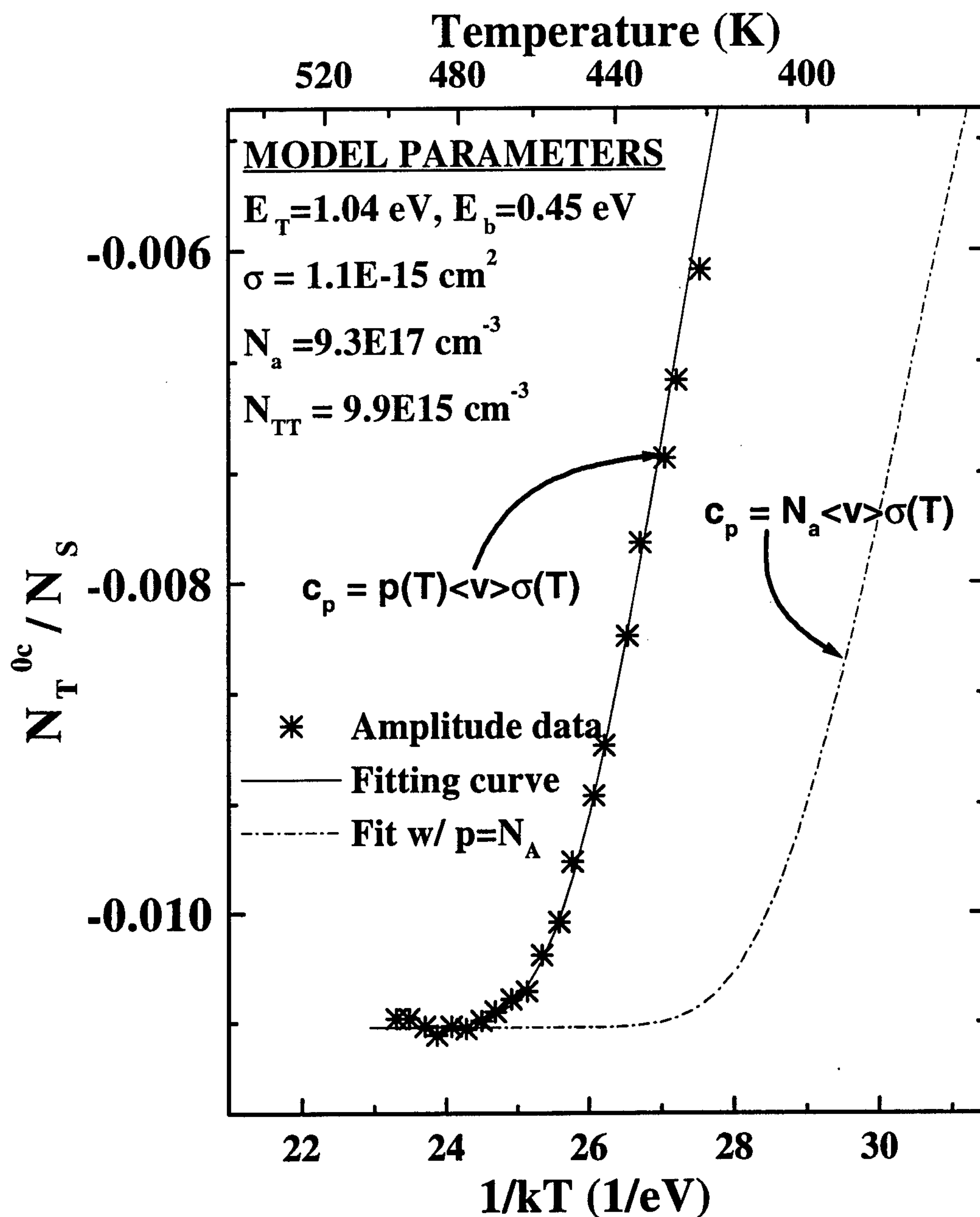

Figure VII-1. Empirical transient amplitude data plotted as the "+" symbols associated with a 1.04 eV hole trap in p-6H-SiC substrate material. The dotted line represents a fit to the data using Equation VI-12, which in this case is seen to agree closely with the more general fit using Equations VI-2 and VI-4 represented by the solid line curve. The dot-dash curve illustrates the error introduced by inconsideration of the ionized shallow acceptor fraction. This curve was generated using the correct trap parameters, but defining the capture rate as $c_p=N_A<v>\sigma(T)$ as illustrated in the figure.

analysis, and the extrapolated cross section $\sigma_\infty = 1.1\text{x}10^{-15}$ cm^2 at T = ∞ from the emission rate prefactor. The doping concentration was obtained from capacitance-voltage measurements, and agreed with the manufacturers quoted value. DLTS run conditions consisted of an 80 μs filling pulse with a 2.0 volt magnitude, 100 μs sampling by 500 collection points yielding a 50 ms digitized isothermal capacitance transient, and an 180 K scan range in 4 K steps. The data are seen in the figure to be very accurately represented by the MPE capture model, and in this case, the data are reasonably well fit using both Equation VI-12, and Equations VI-2 and VI-4. The thermal capture barrier and trap concentration values were determined to be 452 meV and $9.95\text{x}10^{15}$ cm^{-3}. The good agreement between the two fitting methods is due primarily to the fact that for the given pulse width and E_b/E_T value, the approximation that α = 1 in Equation VI-12 remained valid. Therefore, the saturated peak concentration exhibited by the data mirrors the true trap density. Included in the curves of Figure VII-1 is another representation of the error introduced by ignoring the changing free carrier concentration p(T). The dot-dash curve of Figure VII-1 corresponds to this situation. This curve is generated by utilizing the correct trap parameters obtained from emission rate Arrhenius analysis, and the fits accurately represent the experimental data points. The difference is obtained simply by letting p(T) = N_A rather than the correct thermal variation. The modeled data in the figure corresponding to the assumption of complete ionization (p_0=N_A), if forced to fit the experimental data, would result in values of E_b = 585 meV and $\sigma_\infty = 7.5\text{x}10^{-15}$ cm^2. Furthermore, a fit with χ^2 comparable to those of the solid and dotted lines could be

obtained only if the filling pulse width were assumed to be 105 μs due to the uniqueness of the distribution profile for given t_p, E_b, and σ_∞ values.

A second hole trap frequently observed in the bulk p-6H-SiC was also found to exhibit MPE capture behavior as determined from the captured carrier concentration data. This level was also found to be easily formed in epitaxial material subjected to ion implantation and subsequently annealed at T>1000 °C, and is the same defect illustrated in the Arrhenius data of Figure V-13. Since the formation of this defect was found to be independent of the implanted species, it was postulated that it is closely related to lattice vacancies or a vacancy-complex structure. Figure VII-2 shows the DLTS transient amplitude data, represented by the open squares, along with the computer simulated curves for three pre-convergent solutions and the best fit. These simulations are illustrated by the curves closely clustered around the experimental data and labeled with the hole capture rate expression involving p(T). On the other hand, we also have included curves corresponding to identical simulation conditions, but using $p=N_A$ when computing the hole capture rate. These data are shown with labels indicating the capture barrier magnitude (meV) used for each of the calculations. This comparison is included to again emphasize the absolute necessity to include a consideration for the incomplete ionization of shallow impurities in SiC when evaluating carrier transport and recombination events.

The deep level binding energy for this center was measured to be E_V+ 861 meV with σ_∞= 2.2x10^{-15} cm^2. DLTS data was collected using a filling pulse bias and duration of -1.0 V and 1 ms, respectively, and a reverse measurement bias of 5.0 V. 500 points

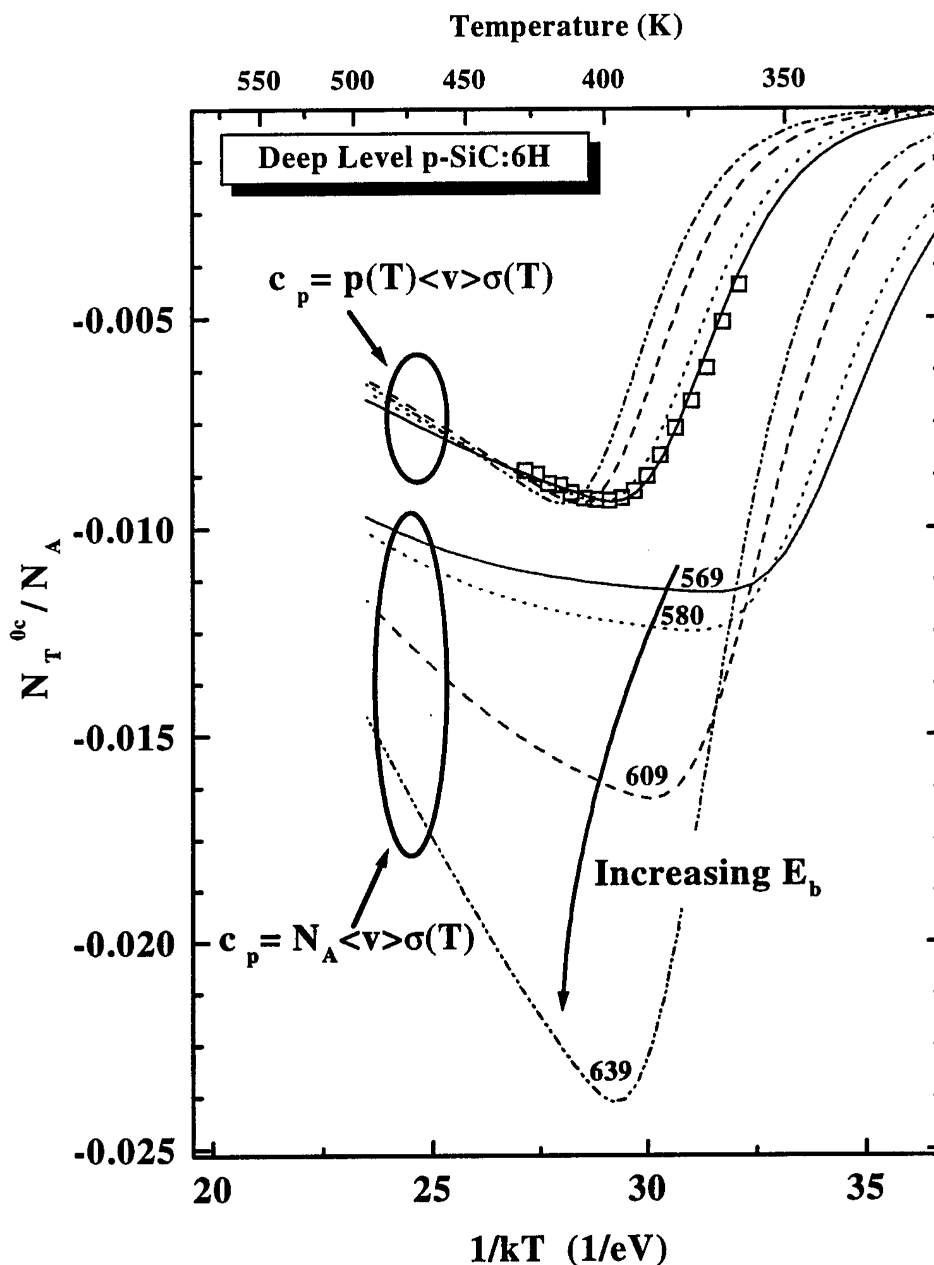

Figure VII-2. Transient amplitude data indicated by the hollow squares and associated fits using Equations VI-2 and VI-4 for various pre-convergent E_b values for an 861 meV hole trap in p-SiC. As shown in the lower set of curves, the p(T) effect is exacerbated by an increasing thermal capture barrier(E_b/E_T ratio) indicated by the lower set of curves. E_b values in meV indicated on the four curves associated with $c_p=f(N_A)$. Both capture rate calculations are identical for the same line type. In other words, both solid lines are calculations with E_b=569 meV with the only difference being $p=N_A$ or $p=p(T)$.

were collected at 14.3 kHz at each 4 K isothermal increment. For this center, the capture barrier was determined to be 569 meV, and the defect concentration obtained from the best data fit was 1.4×10^{16} cm^{-3}.

Owing to the large E_b/E_T ratio for this SiC hole trap, the data fit using Equation VI-12 and the simpler Origin™ fitting method yielded E_b=473 meV. Additionally, using this method, the trap concentration was underestimated by approximately 21% with respect to the 1.4×10^{16} cm^{-3} value returned by the more complete model using Equations VI-2 and VI-4.

Two electron traps in n-6H-SiC, one in bulk material and the other in MOCVD grown epitaxial layers, were also observed to exhibit capture trends indicating MPE kinetics. Figure VII-3 illustrates the DLTS rate window spectra plots in a) and the resulting N_T^{0c}/N_S profiles obtained from the transient amplitude data in part b). The thermal emission energies were measured to be E_C-612 meV and E_C-745 meV for the epitaxial and bulk related peaks, respectively. The emission-prefactor extrapolated capture cross sections at $T=\infty$ were 7.0×10^{-16} and 2.1×10^{-15} cm^2 for the 612 and 745 meV levels, respectively, as estimated from an Arrhenius analysis of the fitted emission rates. Using these values, the fit parameters yielded thermal emission barriers of E_b = 517 meV and E_b = 332 meV for the bulk defect and the epitaxial 612 meV level, respectively.

The incidence of apparent MPE dominated capture kinetics in the hexagonal SiC polytypes investigated during this study were pervasive throughout all the materials and junction structures considered. The symbol data of Figure VII-4 and Figure VII-5 also illustrates several trapped carrier concentration profiles fitted well by the MPE capture

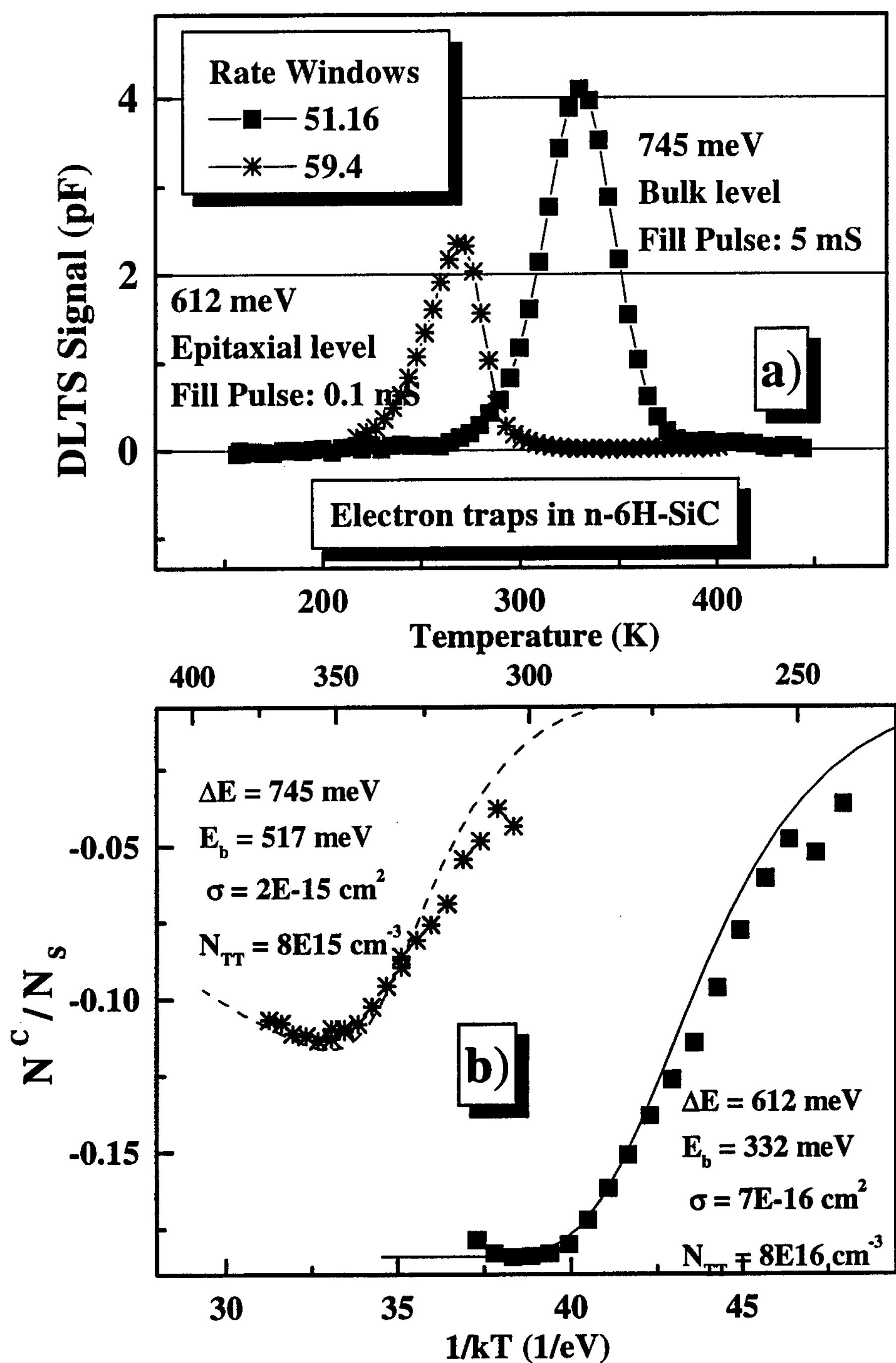

Figure VII-3. a) DLTS rate window spectral plots for two electron trapping centers in bulk and epitaxial n-type 6H-SiC. b) These levels were characterized by MPE capture kinetics as revealed by fits to the transient amplitude factors. Large E_b/E_T ratios of 0.69 and 0.54 were observed for the bulk and epitaxial defects, respectively.

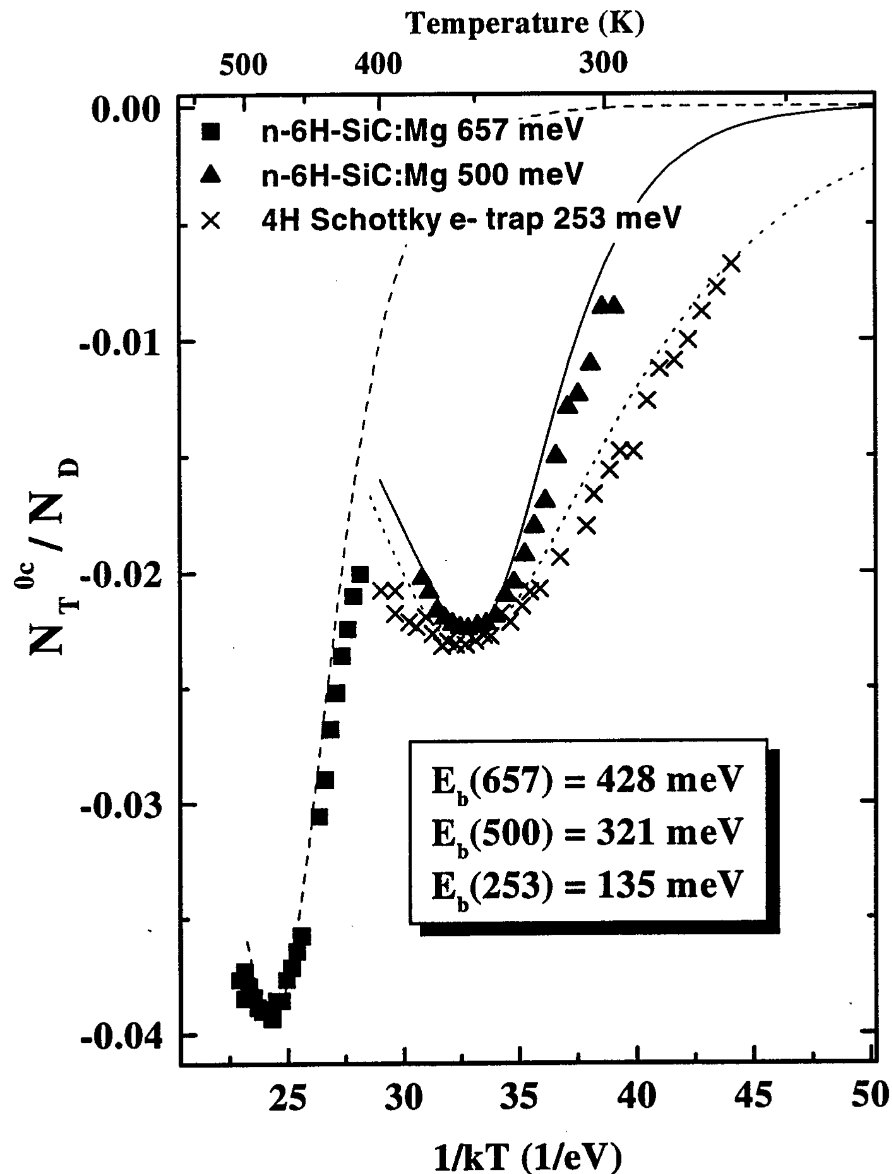

Figure VII-4. Plots illustrating the agreement of experimental data, illustrated by symbols, with the MPE capture mechanism for three additional majority carrier traps in bulk and epitaxial 6H-SiC. The 657 and 500 meV trap levels are associated with radiation damage induced by ion implantation. These particular data sets were obtained from samples implanted with Mg at an energy and dose of 150 keV and 1×10^{13} cm^{-2}, respectively, and subsequently annealed at 1000 °C for 180 minutes. The remaining profile was observed in Pt:Schottky diodes fabricated on 4H-SiC material. The thermal capture barriers listed on the plot are identified with their corresponding emission energy and are consistent with the large E_b/E_T ratios observed for most of the SiC defects.

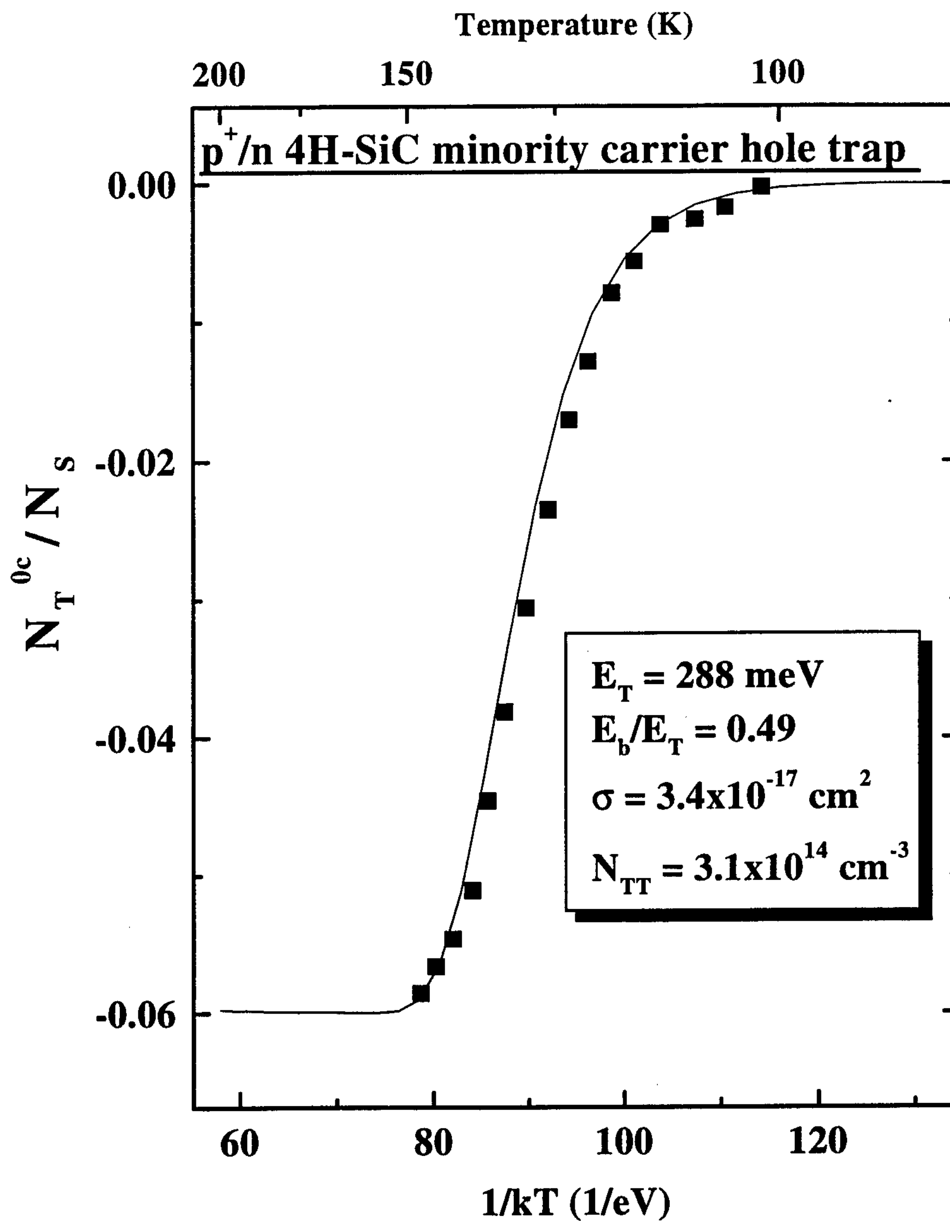

Figure VII-5. Trap occupation distribution of a minority carrier hole trap found in asymmetrically doped epitaxially formed p^+/n diodes. The barrier to emission energy ratio of 0.49 for this defect yielded good agreement between the fits using Equation VI-12 and Equations VI-2 and VI-4. This is possible since over the temperature range of data collection, $\alpha=1$ for this value of E_b/E_T. Measured and fitted trap parameters are illustrated in the lower portion of the figure. These rectifying devices were also obtained from a commercial source.

model. These profiles include two crystal damage related levels occurring in n-type 6H-SiC, ion-implanted with Mg, Cr, and Ar. The profiles shown in Figure VII-4 were measured on n-type, bulk, 6H-SiC, which was implanted with Mg at an energy and dose of 150 keV and $1x10^{13}$ cm^{-2}, respectively, and subsequently annealed at 1000 ^0C for 180 minutes. The deep level electron trap found at E_C-657 meV is possibly the same previously reported irradiation damage center [Pensl and Choyke, 1993:185] seen in n-type 6H-SiC. In that report, the defect pair was correlated to lattice site inequivalencies and named Z_1/Z_2. Our DIGLS analysis of this emission spectra did not, however, reveal the presence of two closely spaced energy levels as reported, but 657 meV is close to their 640 and 620 meV level pair. Additionally, our value of σ_∞=$5x10^{-18}$ cm^2 is only slightly less than their reported values. It should be noted that their analysis was based on fitting closely spaced Gaussian peaks to an asymmetric feature of an analog rate window spectrum. As mentioned previously, this technique suffers from non-uniqueness difficulties for the resulting solutions. Thus, analog methods are inappropriate for the analysis of multi-mode transient decay when the peaks are not distinct and resolvable. In the following section, we present more conclusive data to support the claim of deep levels due to inequivalent lattice site pairs using digital methods.

The remaining data set in Figure VII-4 was obtained from DLTS scans on n-type epitaxial 4H-SiC, Pt:Schottky diodes, which were obtained from a commercial vendor. In all three cases, the data are seen to be accurately fit by the exponentially activated MPE capture model, illustrated by the solid lines coinciding with each data set.

Figure VII-5 illustrates evidence for this capture mechanism for a minority carrier hole trap, detected in the n-region of asymmetrically doped p^+/n 4H-SiC diodes. The smaller barrier to emission energy ratio of 0.49 for this defect resulted in good agreement between the two fitting techniques, using first Equation VI-12 and subsequently Equations VI-2 and VI-4. This is possible because the fitting parameter α is a constant and equal to unity over the temperature range of data collection for this value of E_b/E_T. Measured and fitted trap parameters for this 4H-SiC hole trap are illustrated in the lower portion of the figure. These rectifying bipolar junction devices were also obtained from a commercial source.

Table VII-1 organizes and summarizes the 6H- and 4H-SiC deep level parameters for the electron and hole trapping centers found to possess capture cross sections which obey the MPE model of Equation III-21. The capture related barrier energy, E_b, defect density, N_{TT}, high temperature limiting cross section values, σ_∞, and the capture to emission energy ratio, E_b/E_T, are all listed in Table VII-1. Several points are immediately apparent when considering the cross section and barrier data of Table VII-1. The first important thing one should notice is that for several traps characterized, the high temperature limit of the capture cross section appears to uniformly be approaching a narrow range of values ($\sim 10^{-15}$ to 10^{-16} cm^2). This is in agreement with the theoretical predictions of Henry and Lang [1975:989]. They calculated the capture cross section in terms of the radiative lineshape $f(h\nu)$ with $h\nu=0$, and assumed the temperature dependence of $f(0)$ to be determined by lattice relaxation. In the semiclassical high temperature limit, they estimated that for MPE capture in GaAs and GaP, the limiting

Table VII-1. Deep level trap parameters and multi-phonon emission capture barrier, cross section, and defect concentrations obtained by fitting the temperature dependent, SiC DLTS trap emission, transient amplitude profiles.

Material	Junction	E_T meV	Maj/Min	E_b meV	σ_∞ (cm^2)	N_{TT} (cm^{-3})	E_b /E_T
p-6H Bulk	Schottky	1040	Majority	452	$1.1x10^{-15}$	$9.9x10^{15}$	0.43
p-6H Bulk	Schottky	861	Majority	569	$2.2x10^{-15}$	$1.4x10^{16}$	0.69
n-6H Bulk	Schottky	745	Majority	517	$2.3x10^{-15}$	$8.0x10^{15}$	0.69
n-6H Epi	p^+/n	612	Majority	332	$7.3x10^{-16}$	$2.3x10^{15}$	0.54
n-6H:Mg	Schottky	500	Majority	321	$1.3x10^{-17}$	$1.3x10^{16}$	0.64
n-6H:Mg	Schottky	657	Majority	428	$4.1x10^{-18}$	$3.6x10^{16}$	0.65
n-4H:Epi	Schottky	253	Majority	135	$2.5x10^{-21}$	$5.3x10^{14}$	0.53
n-4H:Epi	p^+/n	288	Minority	142	$3.4x10^{-17}$	$3.1x10^{14}$	0.49

cross sectional values should converge to approximately $\sigma_\infty \approx 10^{-15}cm^2$. They found this to be in good agreement with experimental data for several deep levels in these materials. However, the calculations of Henry and Lang were accomplished for a neutral type impurity as shown in Figure III-5, where both the free carrier and bound state wavefunctions were describable in a one-band effective mass approximation (EMA). Thus, we should expect significant deviations from this benchmark for attractive and repulsive defect potentials, and especially for deep levels in SiC which are likely not to satisfy the EMA.

In light of these remarks, the deviation of σ_∞ from this limit, in the case of the 657 and 500 meV n-6H-SiC:Mg levels and the 288 and 253 meV n-4H-SiC:Epi levels listed in Table VII-1, is not considered to be a violation of the theory. The key point, is that the temperature dependence is quantified in each case to coincide with theoretical predictions, and these deviations are only indicative of non-neutral potentials or complex defect structures. This latter possibility is likely to account for the σ_∞ deviations for the ion implanted samples, which contain significant structural lattice damage, resulting in the probability for extended defects and complex geometries. Additionally, Kukimoto *et al.* [1973:2486] reportedly observed a similar deviation, from predicted MPE behavior, for the electron capture cross section of the oxygen trap level in GaP. In that study, the cross section for the capture of an electron was seen to have a limiting value over two orders of magnitude below other MPE activated GaP traps they investigated.

The second point to make regarding the data of Table VII-1 is that in each case, the MPE capture barrier energy is an appreciable fraction of the DLTS emission energy estimated from Arrhenius analysis (E_b/E_T large). Large capture barriers with similarly large magnitudes have been observed for lattice relaxation, MPE, capture at deep traps in GaAs and GaP [Lang and Kimmerling, 1974:1863]. However, as was the case in these previous studies, we did not observe traps with small thermal barriers or E_b/E_T ratios. This does not exclude their existence, but rather illustrates a practical limitation to the pulse generation duty-cycle capabilities of our experimental setup.

Additional evidence for the MPE mechanism in SiC is found in the data of Yu *et al.* [1995:475], where they have reported large discrepancies between the optical and

thermal ionization potentials of a boron related defect center in 6H-SiC. Recall from Chapter III that these ionization differences are directly attributable to the presence of an MPE thermal capture barrier. In their analysis of optical absorption data it was estimated that the lattice relaxation energy was on the order of twice the thermal ionization energy of 400 meV. Barriers of this magnitude cannot be observed using DLTS methods due to the extremely high temperature ranges required to thermally fill such defects. However, the data of Yu *et al.* supports the presence of large magnitude capture barriers associated with defects in the SiC crystal, and illustrates that energies in the range of those reported in Table VII-1 are by no means unreasonable or anomalous.

Finally, the narrow range of E_b/E_T values listed in Table VII-1, for a wide range of deep level energies, E_T, may be indicative of some phenomenon specific to the hexagonal SiC lattice or band structure. For example, a common deep electron trapping center in n-type $Al_xGa_{1-x}As$, known as the DX-center, is postulated to be related to impurity levels that are coupled to the Γ–X indirect conduction band minimum [Mooney, 1983:208]. When the Al mole fraction is less than 45% ($x<0.45$), the bandgap is characterized by direct Γ-Γ transitions, and the DX center possesses a significant capture barrier. This barrier is equal to the thermal energy required to populate the indirect X-minimum. When the X-minima is populated with electrons, the DX center can participate in capture and emission events. Thus, $E_b(DX) \approx E(\Gamma)-E(X)$, and varies with Al composition as the bandgap moves from direct ($x<0.45$) to indirect ($x>0.45$). Although the band structure of SiC is dictated by a fixed binary composition, there are several conduction band minima in both the Γ-K and Γ-M directions, which could potentially function in a similar fashion.

The final point to make regarding the data of Table VII-1 is related to the defect concentration estimates obtained by fitting the DLTS transient amplitude profiles. These densities are significantly underestimated if the incomplete dopant ionization condition is not considered, and conventional DLTS analysis is utilized, as highlighted by Figure VII-1 and Figure VII-2. This is due to the fact that although the trap filling factor or distribution function exhibits a peak value, the trap is in reality not achieving saturation due to the invalidation of the condition $c_n >> e_n$ ($\alpha<1$) for large E_b/E_T ratios. These large ratios coupled with a rapidly changing free carrier concentration will also seriously affect DLTS rate window spectral representations of SiC deep levels. Peak position will shift in temperature and peak heights will be lowered resulting in erroneously large ionization energy estimates and under estimates of trap concentration and capture cross section when analog analysis is applied. Since the majority of DLTS researchers still utilize analog methods, the result will be large discrepancies between reported values for the same defect center. Thus, confusion and misinterpretation could result, leading to an obscuration of defect identification and complicating the ultimate correlation with chemical or structural sources. The identification of these SiC specific phenomenon realized during this effort are therefore seen as crucial to the accuracy of DLTS results and crucial to the consistency of data reported in the literature.

The method developed to estimate MPE capture barriers and defect concentrations from DLTS emission transient amplitudes has been successfully demonstrated on both simulated decay signal realizations and on several 6H- and 4H-SiC deep trapping centers. By using the full capture and emission rate expressions and Equations [VI-2] and [VI-4],

greater accuracy was shown to be achieved than when the simpler Equation VI-12 was used. This is especially true for the large E_b/E_T ratios found to characterize the SiC defects exhibiting MPE capture mechanisms, since the α=1 requirement for Equation VI-12 was invalidated. Additionally, the absolute necessity to consider the SiC ionized shallow impurity fraction was demonstrated, and the significant error which would otherwise result has been highlighted.

In order to provide further verification for the correlation of MPE capture kinetics with the SiC deep levels identified in this subsection, an additional series of experiments was accomplished. The following section deals with calculating the capture rate directly from trap filling experiments, and subsequently computing the capture cross sectional temperature dependence more directly.

VII-II. SiC Capture Events In Neutral Material.

The previous analysis of DLTS emission transient data is amenable to any system capable of isothermal transient digitization and subsequent signal processing. However, there are inherent difficulties associated with obtaining capture parameters from emission data. Firstly, the application of detailed balance to semiconductor defect levels in neutral material, as is done in deriving the classical DLTS emission rate expression, is often not valid in the space charge region of a reverse biased junction where large electric fields exist. The conclusion is that detailed balance must be considered for each region separately. However, without knowledge of the cross sectional field dependencies, difficulty in obtaining exact expressions for the carrier transition rates is encountered

[Miller *et al.*, 1977:377]. The alternative is to measure the carrier capture rate directly in neutral material during a filling pulse event. Data collection under the conditions characterizing neutral material is complicated by several factors. When considering trap filling kinetics, the capture rate is directly dependent upon the free carrier concentration n(T) or p(T). Additionally, unlike the reverse bias emission measurements, the complimentary carrier transition process is not excluded. This is especially true for the large E_b/E_T ratios characterizing the centers listed in Table VII-1, which results in the capture and emission rates being of comparable magnitude over the measurement temperatures. Therefore, signal analysis may be severely complicated due to the need to discriminate the capture rate from emission processes. Finally, the majority of material investigated was characterized by the presence of numerous deep level trapping centers. Thus, competing processes from other trap sites will further obscure the resulting analysis. Due to these complications, only the 612 meV and the 253 meV electron traps in 6H- and 4H-SiC, respectively, yielded conclusive data supporting the MPE capture mechanism assignment. This is most likely due to the smaller E_b/E_T values for these traps, which simply means that there exists a reasonable measurement temperature range dominated by the capture process. Measurements on samples containing the remaining defects yielded severely non-exponential transients, which could unfortunately not be analyzed to provide useful information.

Because the MPE capture cross section is characterized by a thermally activated capture barrier, the capacitance decay during a DLTS filling pulse event will exponentially evolve. This means that the filling pulse transients recorded during

standard DLTS thermal scans will yield results similar to those of the complimentary emission decay signals. Rate window spectral characteristics will be realized, and a modified Arrhenius analysis can be applied to obtain E_b estimates.

In the case of capacitance decay during a filling pulse bias event, subsequent to a trap clearing reverse bias pulse, the signal will be given by a modified Equation VI-4

$$C(T,t) = \sqrt{\frac{q\varepsilon(N_D{}^{+} \mp N_T{}^{0c}(T,t))}{2(V_{bi} + V_R)}} \,, \qquad \text{[VII-1]}$$

where we again assume n-type material. The temporal trap occupation term is now the captured carrier concentration expression previously defined in Equation VI-2. The direction of capacitance decay, characterizing minority (+) or majority (-) carrier capture, will be opposite to that for the emission transient case. With the relaxation toward equilibrium occurring exponentially, capacitance transients can be fitted for decay time constants using the DIGLS algorithm. The estimated time constants may then be utilized to determine the thermally activated capture barrier. This is accomplished by utilizing a modified Arrhenius analysis, which is easily seen by rewriting the MPE capture rate expression given by

$$c_n = n\langle v\rangle\sigma_\infty \exp\left(\frac{-E_b}{kT}\right) . \qquad \text{[VII-2]}$$

Taking the natural logarithm of this expression and rearranging yields the capture rate Arrhenius evaluation, which for electron capture in n-type material is given as

$$\mathrm{Ln}\left(\frac{T^{1/2}n}{c_n}\right) = -\mathrm{Ln}\left(\sigma_\infty\sqrt{\frac{8k}{\pi\, m^*}}\right) + \frac{E_b}{kT} \ . \qquad \text{[VII-3]}$$

Since the temperature dependence of the free carrier concentration, n, cannot be separated, the resulting plotted quantity differs from the complimentary emission quantity, $Ln(T^2/e_n)$. For the majority of semiconductors, n may be replaced by the doping density, N_D, with minimal error, provided the temperature is not prohibitively low. However, as we have shown for SiC, this is not the case. Thus, computations of the carrier density at temperatures corresponding to the c_n estimates must be included in the Arrhenius analysis. When this is accomplished, and the quantity on the left of the equality in Equation VII-3 is plotted versus 1/kT, the resulting linear slope will yield the MPE capture barrier estimate.

Figure VII-6 illustrates this analysis applied to the DIGLS estimated capture rates, obtained from DLTS capture transient runs, for the 612 and 253 meV electron traps listed in Table VII-1. As mentioned at the beginning of this subsection, these two centers were the only traps which consistently yielded exponential capture transients. This being due to the lower E_b/E_T ratio compared to the other deep levels listed in Table VII-1, validating the $c_n >> e_n$ condition. Both experiments involved recording the capacitance transients realized subsequent to a trap emptying, 100 ms, reverse-bias pulse. Reverse bias voltage levels of -1.0 and -2.0 V were utilized for the 253 and 612 meV levels, respectively, and data were recorded during forward bias levels of 1.0 volt.

The values of E_b estimated from the Arrhenius capture analysis were 319 and 184 meV for the 6H- and 4H-SiC deep levels, respectively. These values are listed on Figure VII-6 and are seen to correspond favorably with the previously estimated quantities of 332 and 135 meV, which are shown in Table VII-1. Free carrier concentrations were

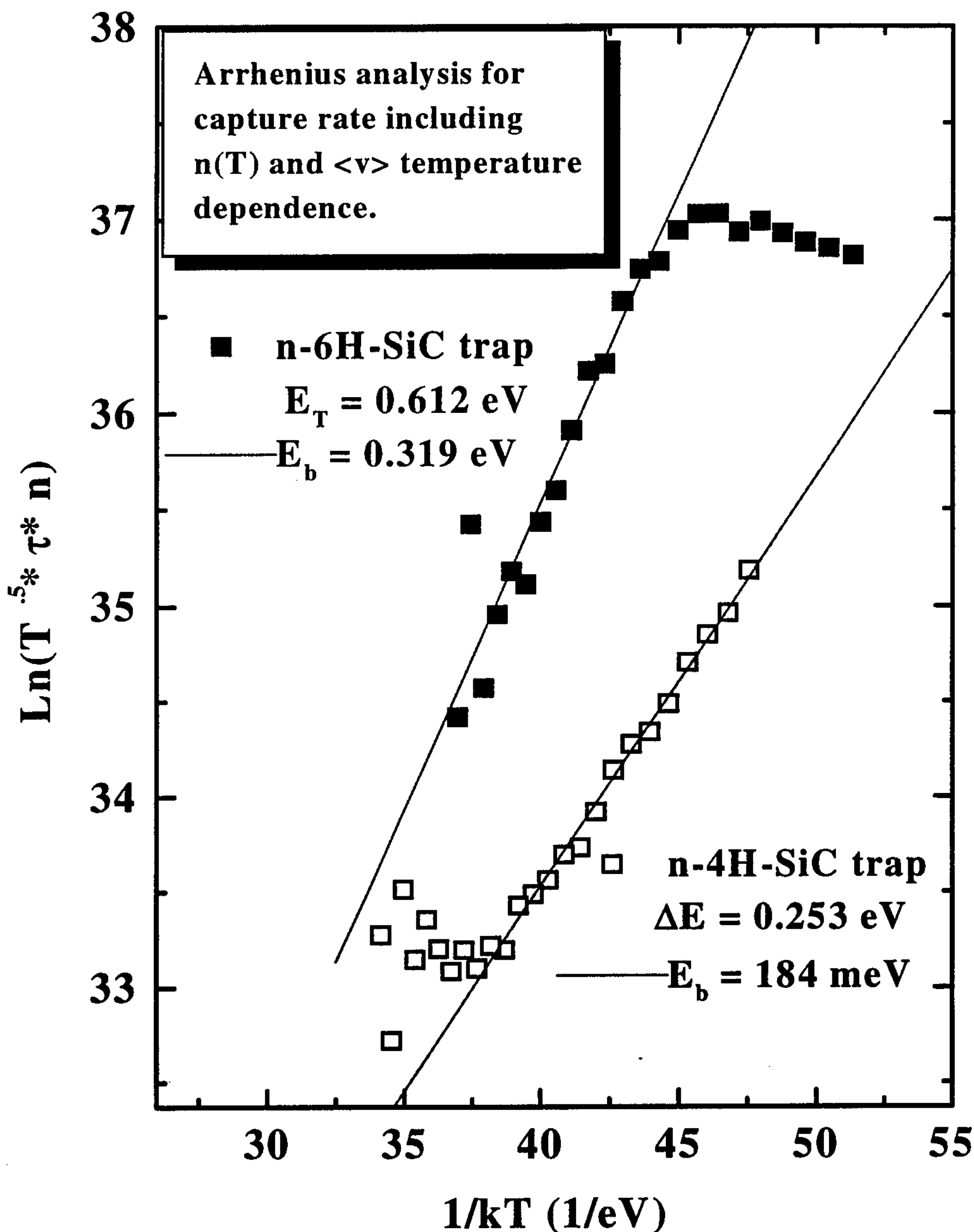

Figure VII-6. Arrhenius analysis of the capture rate estimates for the 253 and 612 meV electron traps observed in epitaxial 6H- and 4H-SiC. As shown by the quantity plotted on the ordinate, the Arrhenius analysis is appropriately modified to account for the capture rate expression and the incomplete donor ionization condition. The energy levels estimated from the linear region slopes agree reasonably well with the values obtained from previous analysis of the temperature dependent emission transient amplitude profiles.

computed using Equation VI-7 and incorporated into the analysis. High temperature limits for the capture cross sections were computed using the capture rate data and Equation VII-2. Values obtained from this analysis were 4.0×10^{-17} and 2.3×10^{-20} cm^2 for the 612 and 253 meV deep levels, respectively. These quantities are both roughly one order of magnitude smaller than the corresponding quantities calculated from the emission rate prefactor method. This is not alarming when considering that this behavior has previously been predicted [Miller *et al.*, 1977:404]. Miller *et al.* predicted that due to the strong temperature dependence of the MPE capture cross section, values calculated from emission rate Arrhenius analysis would be typically an order of magnitude greater than those calculated directly from capture transients and extrapolated to $T=\infty$. They demonstrated this phenomenon for several defect centers in GaAs and GaP. Thus, we see again that our data is in excellent agreement with the predictions of MPE capture kinetics.

Figure VII-7 and Figure VII-8 illustrate the rate window spectral features of the DLTS capture scans for the 612 meV 6H-SiC and 253 meV 4H-SiC deep levels, respectively. These data sets were recorded using the run parameters outlined above and listed in the figure insets and using our standard rate window temporal ratios (t_2/t_1 = 2, 5, 10, 1/2, 1/5, and 1/10 where t1 is the fourth data point). For these two deep electron trapping centers the spectral plots in Figure VII-6 correspond to the modified Arrhenius data representations, and were found to be very repeatable between diodes. The fact that rate window plots can be generated from trap filling transients is further verification that carrier capture at these deep centers proceeds via the MPE mechanism. This claim is validated by the fact that a realization of Gaussian-like DLTS spectra is possible only if

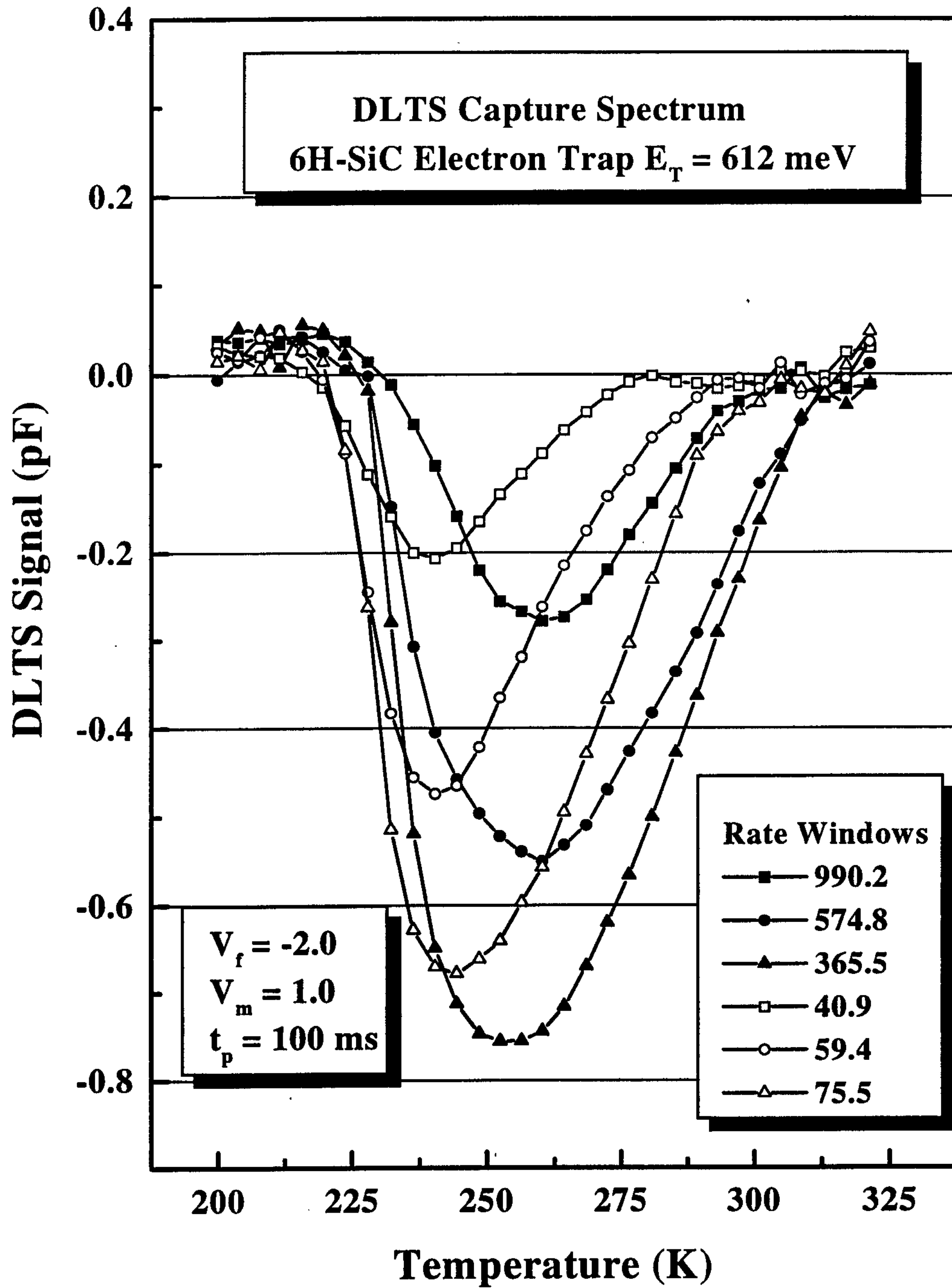

Figure VII-7. Rate window capture spectrum of the 612 meV electron trap frequently observed in n-type epitaxially grown 6H-SiC. Data were collected using the biasing levels indicated in the plot inset. Trap refilling rates were measured subsequent to 100 ms, trap emptying, reverse bias (V_f) pulses.

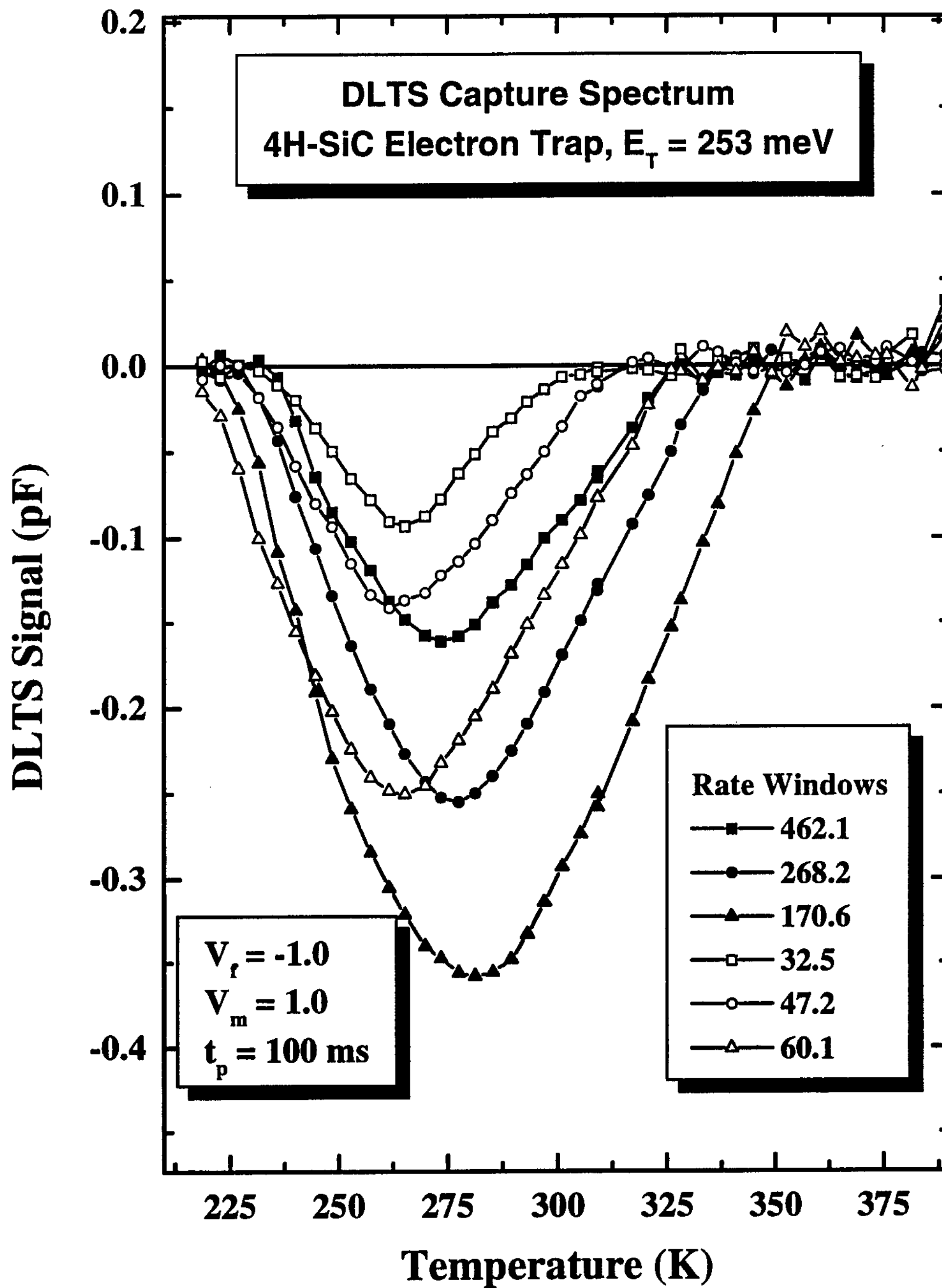

Figure VII-8. Capture spectrum for six rate window temporal ratios (t_2/t_1) of the 253 meV electron trap in n-type epitaxial grown 4H-SiC. Data were collected using the biasing levels indicated on the plot. Capture rates were measured subsequent to 100 ms, trap emptying, reverse bias (V_f) pulses. Data provide further support for the assignment of MPE capture kinetics to the SiC deep levels initially characterized using emission transient amplitudes.

transient evolution as a function of temperature is exponentially activated. Thus, capture rates characterized by temperature independent cross sections (n<v>σ) will not result in exponential capacitance relaxation. Under these circumstances this analysis is not valid, and DLTS spectra will not be realizable.

The preceding presentations have shown that carrier capture at deep level defects in 4H- and 6H-SiC is characterized by transitions in which energy conservation is achieved through lattice relaxation, multi-phonon emission. This behavior of the trapping kinetics was observed in both 6H and 4H polytypes and in epitaxial and bulk-substrate grown materials for several types of reverse biased junctions (MOS, p/n, Schottky). Vibrational amplitudes and Stokes-like shifts of the magnitudes observed were not expected for substitutional point defects in a lattice with such large cohesive energies and small lattice constant (~3Å). Therefore, it is proposed that the SiC MPE capture phenomenon must be related to interstitial defects or defect vacancy pairs. However, since the exact origin of this mechanism is not fully understood, the assignment to a particular defect geometry, complex, or location is extremely tenuous. Independent of whether the source of these temperature dependent capture cross sections is electronic, mechanical, or related to band structure, the frequent occurrence of this mechanism in hexagonal SiC has been demonstrated.

A new technique was developed to estimate the thermal capture barrier from DLTS emission transient amplitudes. The technique involves fitting the temperature dependent trap occupation profile with MPE theoretical predictions. This has been accomplished through an implementation of the theoretical expressions using

commercially available mathematical software products. Verification of this procedure was accomplished on computer simulations of deep level capacitance transient decay prior to the applications on real SiC DLTS data. Additional support for the assignment of MPE capture kinetics to several 4H- and 6H-SiC deep centers was realized by a direct measurement of the carrier capture rates. These experiments verified that deep level capture was an exponentially activated thermal process with a well defined activation energy. A modified Arrhenius analysis was defined, and thermal activation energies were found to be in close agreement with the capture barrier estimates obtained from prior transient amplitude analysis. Furthermore, capacitance transients obtained during trap refilling experiments were found to be amenable to rate window type analysis, leading to the DLTS spectra shown in Figure VII-7 and Figure VII-8. Unfortunately, only two of the originally identified defects were amenable to this direct capture analysis. This was due to the larger E_b/E_T ratios associated with these traps and signal interference from other defect centers. The resulting transients under these conditions were found to be severely non-exponential, eliminating the possibility of further analysis.

When estimating trap parameters in hexagonal SiC, the absolute necessity to consider the incomplete ionization of shallow dopant impurities was also clearly demonstrated in this presentation. Surprisingly, this consideration and analysis have not previously been accomplished and included with reported SiC DLTS results. The significant errors were highlighted, and corrective procedures were outlined and implemented. This involved computing the temperature dependent free carrier concentration for a semiconductor with two or three impurity levels.

VII-III. Deep Level Energetic Pairs Attributable to Inequivalent Lattice Sites

One of the questions which remains unanswered regarding the energetic positioning of deep level defects in hexagonal (α) SiC is that relating to symmetrically inequivalent lattice sites. This condition for SiC polytypes with stacking orders greater than two is well understood in relation to the shallow dopant impurity levels. For example, how are the levels associated with various charge states of a transition metal impurity positioned in the bandgap of SiC, and how do the magnitude of the "level splittings" relate to the trap depth. Transition metal and other impurities using paramagnetic and spin resonance techniques [Stallinga *et al.*,1992:32] [Maier *et al.*, 1992:27] have been detected and shown to reside on inequivalent lattice sites in hexagonal SiC. However, these techniques are unable to discern electrical activity or energetic bandgap location of the various charge states of the impurity. In a few cases, infra-red (IR) absorption spectroscopy has been used to quantify the free energy of deep level transition metal levels such as vanadium [Maier *et al.*, 1992:27], although the assignment of observed electronic transitions is sometimes misinterpreted [Jenny *et al.*, 1995:3160]. Additionally, the enthalpy measured using deep level transient spectroscopy (DLTS), or other techniques using thermally induced carrier transitions is seldom in agreement with the true free energy of optical transitions. As a result, much confusion and difficulty can result when attempting to correlate different measurement methods associated with the same electronic transitions. It is commonly assumed that the existence of multiple ionization energies and their relative energetic positions, which are observed for shallow SiC substitutional impurity atoms, will translate directly to energies

deeper in the forbidden gap. In terms of the local symmetry associated with lattice sites in α-SiC, this will be true. However, this information is obtained only from the eigenstate solutions to the crystal Hamiltonian, which includes the defect potential. Thus, qualitative assumptions such as this are totally lacking in any theoretical basis. Therefore, while the assumption of the existence of multiple energies for all point defects in hexagonal SiC polytypes may be valid, the notion that the associated level splittings will be spaced energetically close is physically unfounded, and will depend entirely upon the explicit form of the defect potential. As a result, solid empirical evidence and analysis are required before claims of inequivalent site association between measured energetic deep level pairs should be made, especially when using a thermally stimulated technique such as DLTS.

For the first time, electrical measurements yielding direct evidence of electrically active deep level energetic pairs associated with lattice site inequivalencies in hexagonal SiC are presented. While conclusive photoluminescence and other optical data have been reported for this phenomenon, there has been no solid evidence of this condition reported using DLTS or other electrical techniques. Using the modeling routines outlined in the earlier sections of this chapter to provide self-consistency, we have found that strong evidence for site inequivalence exists for two electron traps in 6H-SiC n-type material.

Multi-mode decay was not observed or resolvable for any trapping centers studied in p-SiC, indicating that deep level centers coupled to the valence band may be less affected by symmetric inequivalencies. This would be consistent with observations of the shallow acceptors in this material [Pensl and Choyke, 1993:264].

VII-III-1. N-type 6H-SiC Deep Electron Trap. The bulk n-6H-SiC deep electron traps, which have been shown in Chapter V to be comprised of two levels in the upper half of the bandgap at energies of 543 meV and 509 meV below the conduction band edge, have been determined to be related to hexagonal and cubic lattice sites. Similarity of the capture cross section data for the two levels, and especially the MPE defect concentration magnitudes and thermal profiles support the premise that these centers are related to the same defect. Simulated capture and emission kinetics of two-level systems, including thermally activated capture cross section mechanisms and incomplete shallow dopant level ionization, yielded results in direct agreement with experimental DLTS data, and provide self consistency with the fitted experimental results. Additionally, a Mg ion-implanted n-type 6H-SiC deep level was identified as possessing two distinct time constants. Subsequent to 1200 ^{0}C anneal for 120 minutes, this Mg and/or damage related electron trapping center in n-SiC was found to exhibit closely spaced deep energy levels associated with a single rate window spectral peak.

The samples studied were comprised of 6H bulk SiC crystals grown by the physical vapor transport process and epilayers grown by chemical vapor deposition (CVD). The conductivity was n-type resulting from intentional nitrogen incorporation to doping levels of between 1 x 10^{16} to the low 10^{18} cm^{-3} range. DLTS capacitance decays were measured on our standard 500 μm diameter Schottky junctions formed using the processes previously outlined in Appendix C. Magnesium was implanted into the n-type samples at an energy and dose of 195 keV and 10^{13} cm^{-2}, respectively.

The commonly applied technique of fitting multiple Gaussians to a single analog rate window spectral characteristic exhibiting apparent superimposed peaks is fundamentally flawed. This is because the system is underdetermined, and uniqueness of solution is not achieved. Accuracy can only be obtained by a consistent fitting of several different rate window spectra for a given set of estimated trap parameters. Even solutions obtained in this manner are subject to significant error, if the assumptions of thermally independent capture cross sections and complete trap filling are not satisfied. Additionally, electric field modifications to the thermal emission rates can serve to further corrupt the analog estimates of defect parameters when the capacitive decay model order is greater than one. Finally, in a situation such that an analog spectrum does not reveal a distinct demarcation of superimposed spectra, this method becomes extremely qualitative and of marginal utility.

Figure VII-9 illustrates the DLTS rate window spectrum and associated Arrhenius plot of the 6H-SiC deep level electron trap first presented in Chapter V. The data collected on these Schottky diodes were accomplished using a filling pulse height of 2.0 volts with a period of 10 ms, a reverse bias offset of -4.0 volts, the sample interval was 500μs, 1000 points per transient were recorded, and the temperature increment was 4.0 K over the range indicated in the figure. As can be clearly seen from Figure VII-9 a), the analog characteristic for this particular trapping center does not readily indicate the presence of multi-exponential capacitance decay. However, the Arrhenius plot shown in Figure VII-9 b), resulting from an application of the improved linear prediction estimator

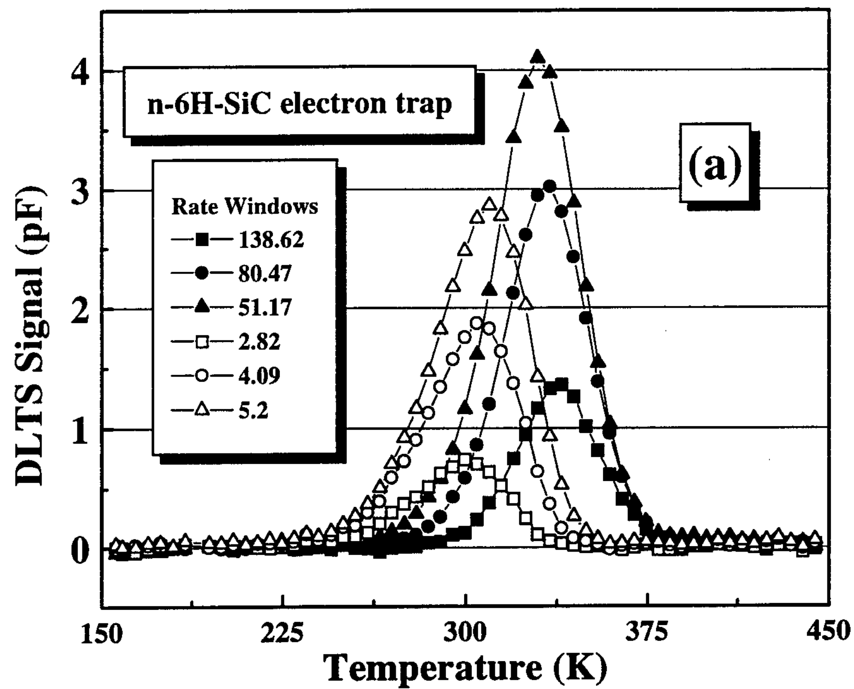

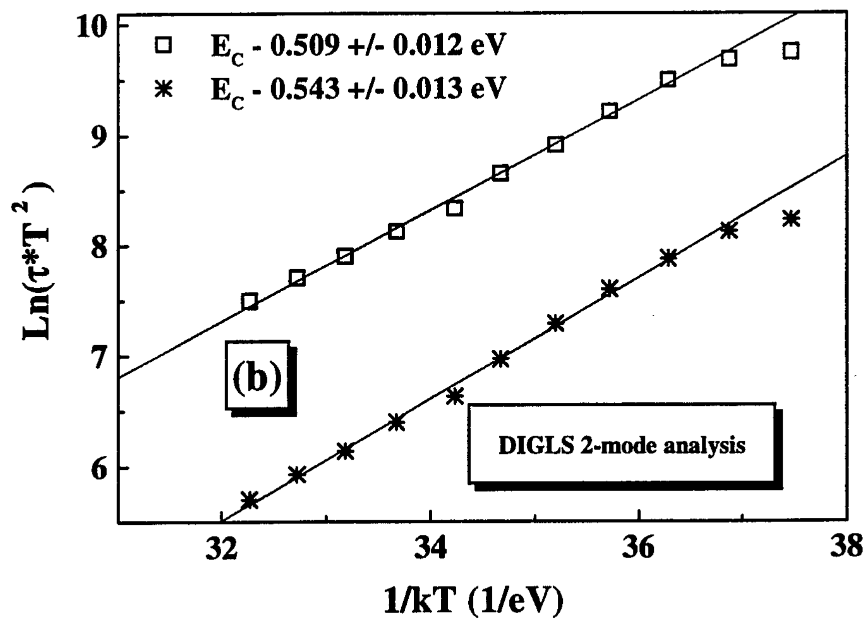

Figure VII-9. Rate window spectrum a) and Arrhenius plot b) for the deep level electron trap commonly found in 6H-SiC n-type bulk material. These data were first introduced in Chapter V when discussing DIGLS resolution of multi-mode decay. This center may be related to a substitutional vanadium impurity, which is a common impurity in these wafers. The asymmetry of the peak rate window spectral peaks between the solid and hollow symbol sets in a) is indicative of a large thermal capture barrier.

to the digitized capacitance transients, does provide convincing evidence for 2-mode decay.

If the spectral characteristic of Figure VII-9 a) were interpreted as being indicative of single mode exponential decay, and the data were analyzed for only a single deep energy level, an ionization energy of E_C-0.673 eV would be obtained. This single mode transient fit analysis is represented by the data illustrated in Figure VII-10. The ionization energy obtained in this manner is very close to the previously obtained DLTS values of 0.66 and 0.71 eV which were attributed to the acceptor level of vanadium (V^{4+}/V^{3+}, $(3d^1)/(3d^2)$) in bulk 6H-SiC [Jenny *et al.*, 1996:1963], or a level of unknown origin in epitaxial material [Uddin and Uemoto, 1993:1670], respectively. Regardless of whether this trap is the same as those reported, our results highlight the necessity to closely scrutinize all DLTS results obtained from SiC polytypes with stacking orders greater than three. This is especially true for results obtained using rate window or analog methods exclusively.

The capture cross section (σ) estimates for the two resolved levels, calculated from extrapolated y-intercept values of Arrhenius plots, were 6×10^{-18} and 1.75×10^{-16} cm^2 for the 509 and 543 meV levels, respectively. However, closer analysis revealed the capture cross section for this defect center to be strongly temperature dependent, thus the y-intercept estimates are assumed to be representative of σ_∞. Direct analysis of the trap concentration data led to the discovery that carrier capture at these centers were also consistent with MPE capture theory.

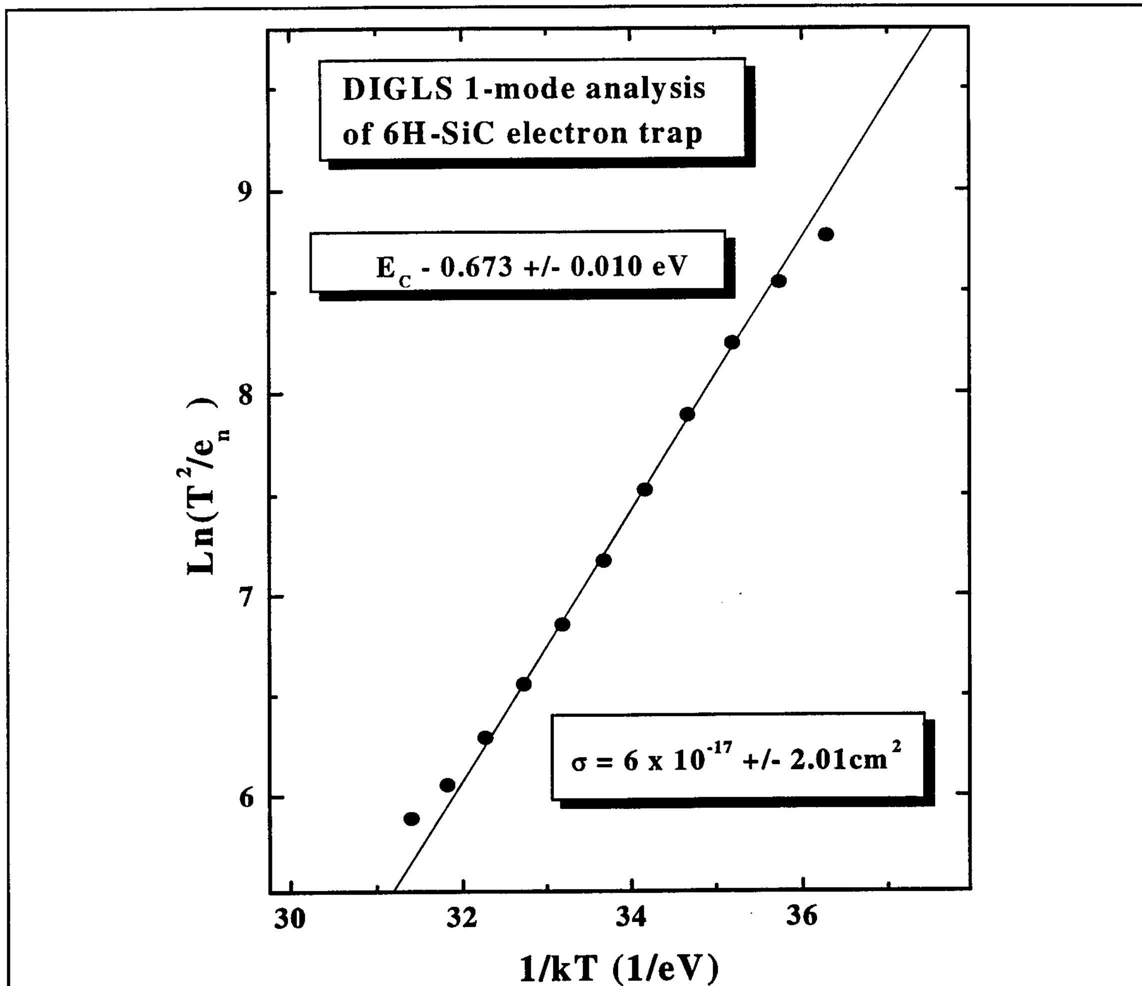

Figure VII-10. Arrhenius plot of the emission rate estimates obtained by considering only a single decay mode for the DLTS data associated with the electron trap in bulk n-6H-SiC illustrated in Figure VII-9. The listed energy and cross section obtained in this analysis agree well with values reported for vanadium levels.

The symbol data shown Figure VII-11 represents the estimated normalized DIGLS transient amplitudes for the two decay modes associated with the electron trapping center shown in Figure VII-9. Immediately apparent is the strong temperature dependence exhibited by the transient amplitude prefactors. Reflected also in Figure VII-11 are curves representing the computer modeling of N_T^{0c} (T,t_p), using the MPE cross sectional

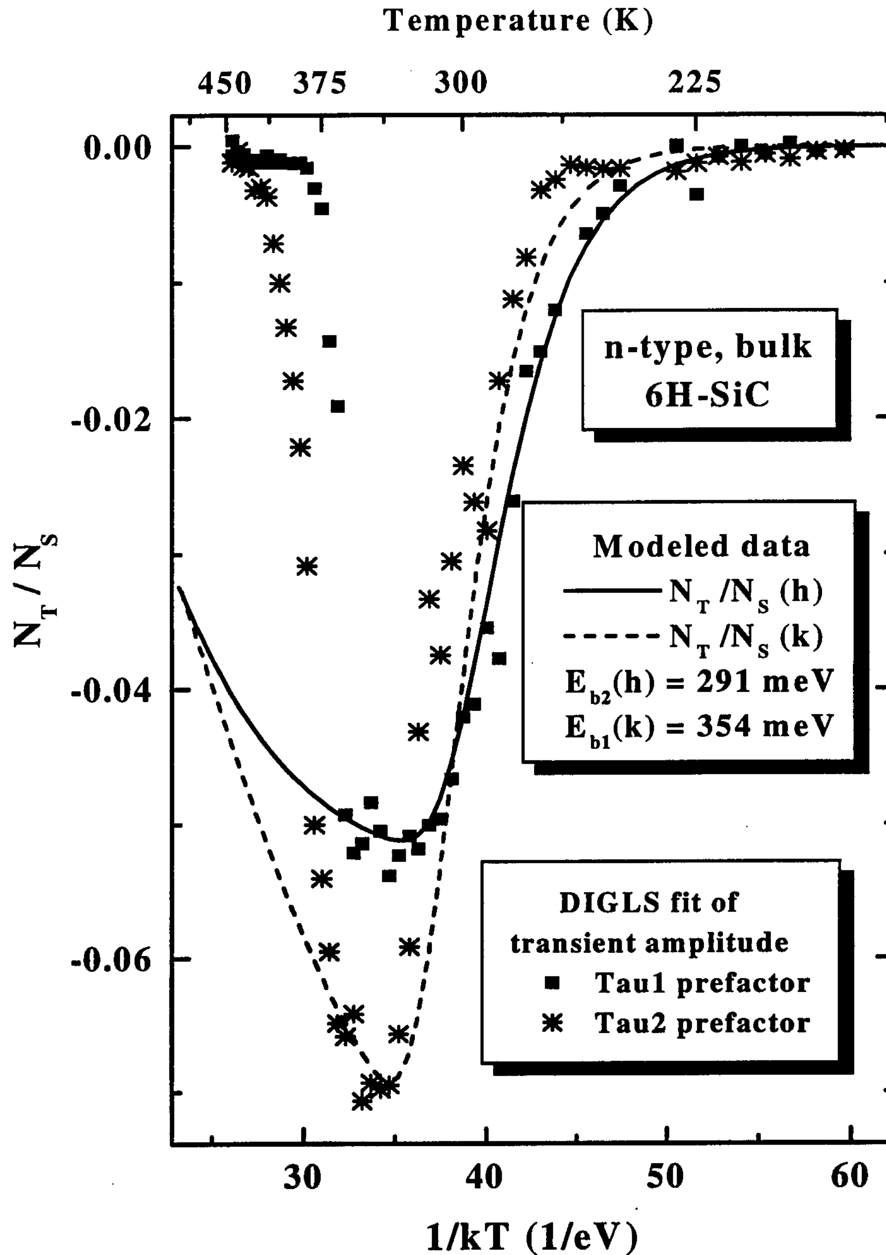

Figure VII-11. Emission transient amplitude profile, resulting from the DIGLS fits to the DLTS data for the electron trap in bulk n-6H-SiC illustrated in Figure VII-9. Experimental data is indicated by the symbol markers for the 543 (*) and 509 (■) meV levels and the computer simulated fit curves are illustrated by the solid and dashed lines. E_b estimates are listed on the figure. The deviation of experimental data from the fitted curves at high temperatures is due to increasing imprecision of the DIGLS fits as the emission rate becomes extremely large. This can be correlated to temperatures above the DLTS spectra shown in Figure VII-9.

expression, and are illustrated by the solid and dashed lines. Minimizing the error between the experimental and simulated data in a mean square sense we obtain estimates for the capture barrier, E_b. These values were determined to be 354 and 291 meV for the 553 and 509 meV levels, respectively, and are listed on Figure VII-11. These values yield E_b/E_T ratios of 0.57 and 0.64 for the shallow and deeper levels, respectively, which fall into the narrow range of values listed in Table VII-1 for the other deep levels exhibiting MPE behavior. Trap concentration values, N_{TT}, were determined from the N_T^{0c}/N_D fits to be 2.4×10^{16} and 4.5×10^{16} cm^{-3} for the shallower and deeper levels, respectively. The doping concentration of the substrate wafer was determined from C-V profiling to be a uniform value of 8.2×10^{17} cm^{-3}.

As seen by the data illustrated in Figure VII-11, data and theory agree closely for temperatures below approximately 375 K. The deviation from theory at higher temperatures is due to the large trapped-carrier emission rate in this range of temperatures. Thus, for the sampling interval of 500 μs and transient period of 0.5 s used to collect this data, transient decay is complete within a few sample intervals above this temperature. This is evidenced by the position of the high temperature edge of the spectral peak illustrated in Figure VII-9. Therefore, a very limited number of data points are recorded over the decaying portion of the transient, while the majority of points are taken over the flat offset portion of the signal. Thus, the data record does not portray a reasonable representation of the capacitance decay, and over this temperature range the time constant and amplitude estimates are becoming increasingly inaccurate.

Although the ratio is not exactly 2:1 (1.88:1), the fact that the deeper level is associated with the higher defect concentration hints association with lattice site inequivalencies. Additionally, both levels are seen to possess identical capture mechanisms. Similarity of the cross sectional behavior and the concentration ratio begin to provide compelling evidence that these levels are due to the same defect at hexagonal and cubic 6H-SiC lattice sites.

In order to provide more explicit evidence for deep levels associated with inequivalent SiC lattice sites, we numerically modeled junction capacitance transients for two level systems. Self-consistency with the empirical data is attempted through these simulations. Capacitive decay that is determined to be multi-modal is reduced to yield ionization energy levels, capture cross sections, and trap concentration information from Arrhenius and N_T^{0c}/N_S analysis on the DIGLS emission rate estimates. These experimental defect parameters are then used to generate simulated data records for comparison to the original data.

In this manner, we compare simulated rate window spectra and Arrhenius data to experimental results. This analysis serves two functions. First, if consistency is obtained we have a degree of confidence in our DIGLS multi-modal results. Secondly, we can assume that the material parameters and trapping kinetics we utilize to model N_T^{0c}/N_S are accurate.

Figure VII-12 illustrates the self consistency data comparison for the experimental data which yielded the rate window spectra of Figure VII-9. The solid line curves are the spectra obtained experimentally while the dotted lines are the simulated $\Delta C/C_0$ results

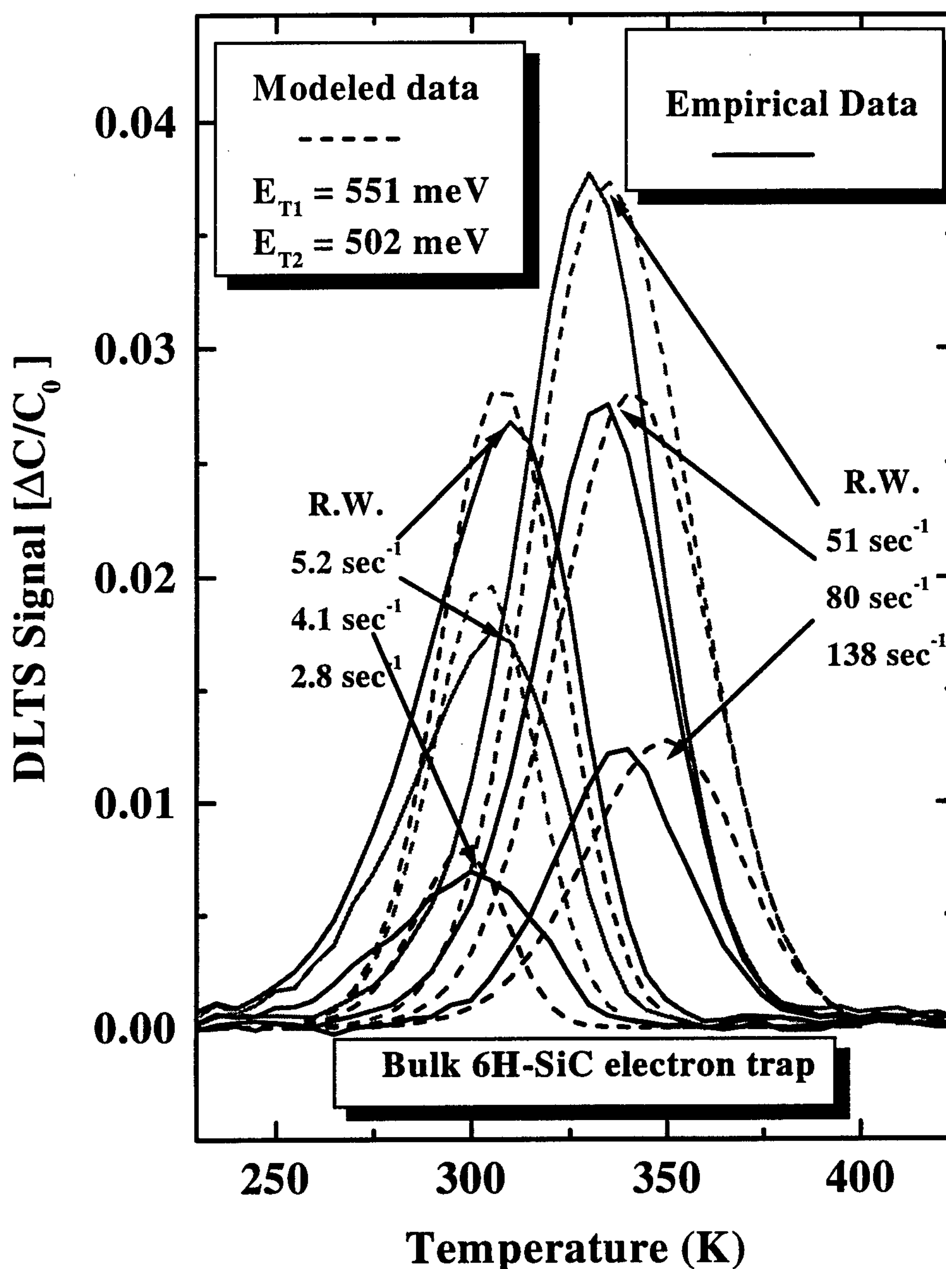

Figure VII-12. Rate window spectral plots illustrating the results of self-consistency experiments for the electron trapping center in n-type 6H-SiC bulk material. The simulated curves were generated using the empirically estimated trap parameters E_T, E_b, N_{TT}, and σ for the two levels. The numerical data (dashed lines) is seen to be in good agreement with the experimental spectra (solid lines), especially when considering the effective mass and number of conduction band minima uncertainties.

using the fitted parameters as inputs and the identical rate window values, which are shown in the figure. Simulated data is generated using the identical sampling, biasing, pulsing, and thermal sequences utilized experimentally. Transients with 0.5 s periods are numerically simulated using the junction capacitance expression with the appropriate rate equation solution as described earlier in this chapter. Rate windows are generated using the S(T) expression of Equation IV-8. For two level capacitance decay, which is normalized to the steady state value, the DLTS spectral equation is given as

$$S(T) = \sum_{k=1}^{2} (-1)^k \sqrt{\frac{q\varepsilon}{2(V_{bi} - V_R)} \sum_{i=1}^{2} N_{Ti}^{0c}(T, t_p)[\exp(-\frac{t_k}{\tau_i})]}, \quad \text{[VII-4]}$$

where the two values of t_k are associated with the rate window definition. Rate windows utilized are such that $t_2/t_1 = 2$, 5, and 10 with the value of t_1 being held constant and varying t_2 to satisfy the ratio. The six values are obtained by generating three ratios for two different t_1 values. First, t_1 is fixed as the 10th data point in all recorded transients. Subsequently, t_1 is given a value near the end of the transient, typically the end point minus 16 sample intervals and t_2 generated as factors of 1/2, 1/5, and 1/10 t_1. This procedure results in two sets of three rate windows, as illustrated in Figure VII-9. In this manner we are able to maximize both signal-to-noise (t_2/t_1=10) and energy resolution (t_2/t_1=2) for any given set of analog capacitance data. In Figure VII-12 we see that the six experimental rate window spectral peaks are reasonably well replicated by the simulation using empirical trap parameters as inputs to our computer model. The inability to reproduce closely the broadened spectra associated with the low-temperature 5.2, 4.1, and

2.8 sec^{-1} rate windows, and the slight (~5K) shift of the three higher temperature peaks are probably due to other processes or mechanisms occurring during the capture or emission events that are not considered in our model. On the other hand, the discrepancies may simply be resulting from our assumptions of an isotropic effective mass and an unquantified value of M_C=6 for the number of equivalent conduction band minima in the density of states, N_C, expression. In fact, a change in the M_C value from 6 to 2 will shift the spectral peaks by 15 K due to the proportional dependence of the emission rate on the density of states quantity. Additionally, the effective mass in 6H-SiC is actually best represented by a **k**-vector dependent tensor, and any discrepancy from physical reality this causes will also have a proportional effect on the carrier emission rate. Finally, the peak heights are very sensitive functions of the trap concentrations, doping level, and thermal capture barrier quantities used as inputs to the model. Thus, the results shown in Figure VII-12 indicate that the modeled trap kinetics and assumed material quantities are actually in good agreement. Therefore, a high degree of self-consistency is reflected, which supports our DIGLS two-mode decay predictions and our assignment of these levels to inequivalent 6H-SiC lattice sites.

An additional feature of the rate window data in Figure VII-9a) and the simulation results of Figure VII-12 is the asymmetric peak heights associated with the two sets of three rate windows. This was discovered to be due entirely to the presence of a large thermal barrier to the capture of free carriers. In the absence of this condition, the two sets of three rate window curves will possess identical peak heights between corresponding t_2/t_1 ratios. This difference in peak height for identical t_2/t_1 ratios was

found to occur for E_b/E_T ratios of approximately 0.5 and above. Simulated deep level transient emission data for a 525 meV electron trap in n-type 6H-SiC, is shown in Figure VII-13 and illustrates this effect. Five rate window data sets are plotted in the figure, each corresponding to a different MPE capture barrier magnitude. These values are listed next to each set of curves, and are seen to increase from the lower to upper data sets. The modeled trap parameters are also listed on the figure, including the trap filling pulse period of 1 ms and the transient sampling interval of 100 μs.

In Figure VII-13, we see that the capture barrier effect on rate window symmetry becomes discernible for the 0.47 ratio, and increases dramatically as $E_b/E_T>0.5$. This is easily understood in terms of the trap filling factor or "quasi-distribution function." If we refer back to the data of Figure VI-5, we see that as the barrier magnitude is increased, the temperature range over which the trap filling factor approaches unity increases. Thus, if the emission spectral characteristics are peaking over this same temperature range, then slight increases in temperature will result in significantly higher trap occupation. Since the DLTS rate window spectral height is directly proportional to the trap occupation density, this height will correspondingly reflect the changes in trap occuption. During the approximately 30 K between the two series of rate windows, the traps are filled to a significantly greater degree at the higher temperatures. This argument is supported by the digitized and fitted amplitude results of Figure VII-11, which show a rapidly increasing trap concentration over this same temperature range. In addition, our modeled results

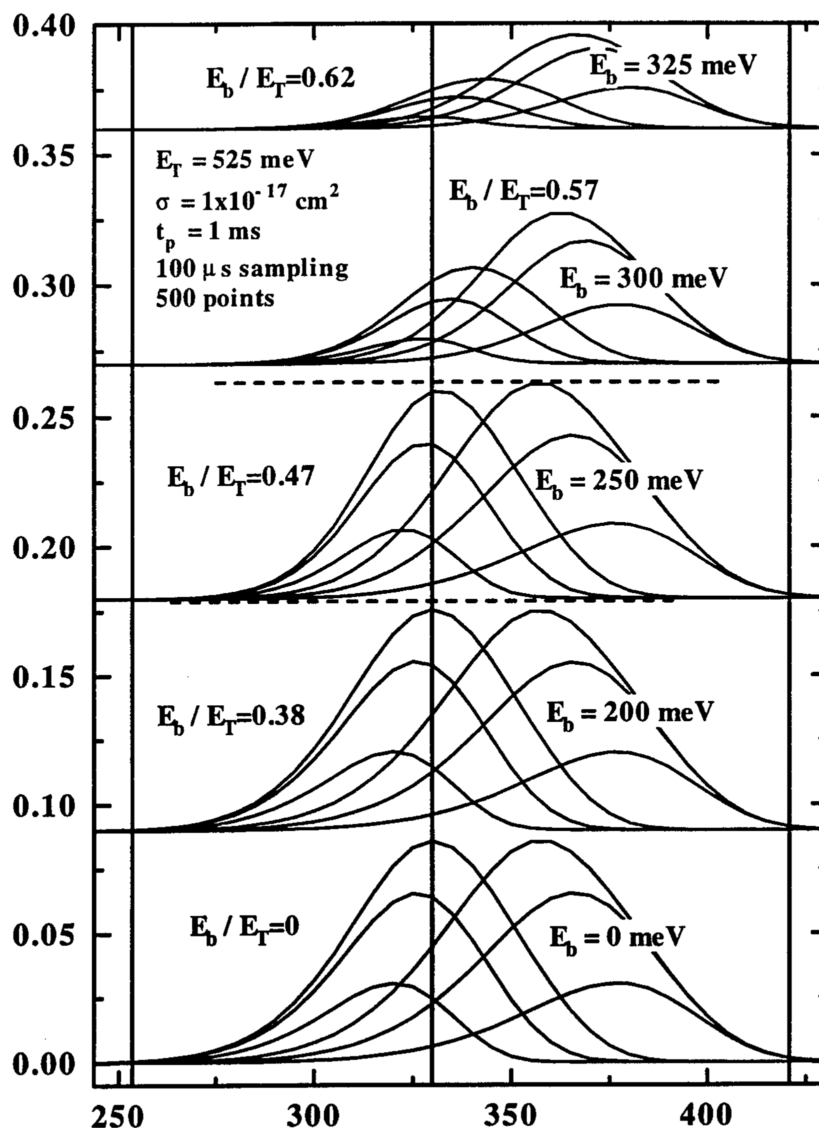

Figure VII-13. Simulated rate window spectra for an electron trap in n-type 6H-SiC. The modeled trap parameters are listed on the figure, including the trap filling pulse period of 1 ms and the transient sampling interval of 100 µs. Deep level trapping was modeled to include MPE capture kinetics. Five data sets are illustrated, which correspond to an increasing thermal capture barrier with values indicated next to each set of curves. The barrier effect on rate window symmetry is indicated for $E_b/E_T>0.47$.

reflect this behavior correctly, and support our conclusion that the capture kinetics are controlled by an exponentially activated cross section.

The large barrier rate window data of Figure VII-13 also shows a peak shift toward higher temperatures as E_b is increased. This is a manifestation of the decreasing capture cross section for a fixed temperature range as the barrier energy is increased. Since the emission rate is directly proportional to σ, the rate window peaks are shifted to higher temperatures as the cross section decreases with increasing E_b. If not considered, this effect of a large capture barrier will cause inaccuracies in the analog rate window estimates of trap ionization energies, which are used by many researchers. These errors will be realized since this estimation method utilizes the peak temperatures in conjunction with the corresponding rate window values to generate Arrhenius data.

Because the capture rate is also proportional to the free carrier concentration, which was shown to rapidly increase over various temperature ranges, it was necessary to eliminate n(T) as a cause for the rate window asymmetry and temperature shifts. To accomplish this, DLTS simulations were performed to generate rate window spectral features in the low, mid, and high temperature measurement regimes. These would then correspond to various degrees of donor ionization, allowing the identification of n(T) effects on rate window spectra. Figure VII-14 and Figure VII-15 illustrate the low and high temperature rate window spectra for electron traps at E_C-325 and E_C-850 meV, respectively. Illustrated in these figures is a comparison between the rate window spectra generated by assuming n=n(T) and then recalculating using $n=N_D$ for the trap parameters listed in the figure insets. In each case, the E_b/E_T ratio was maintained at 0.63, and the

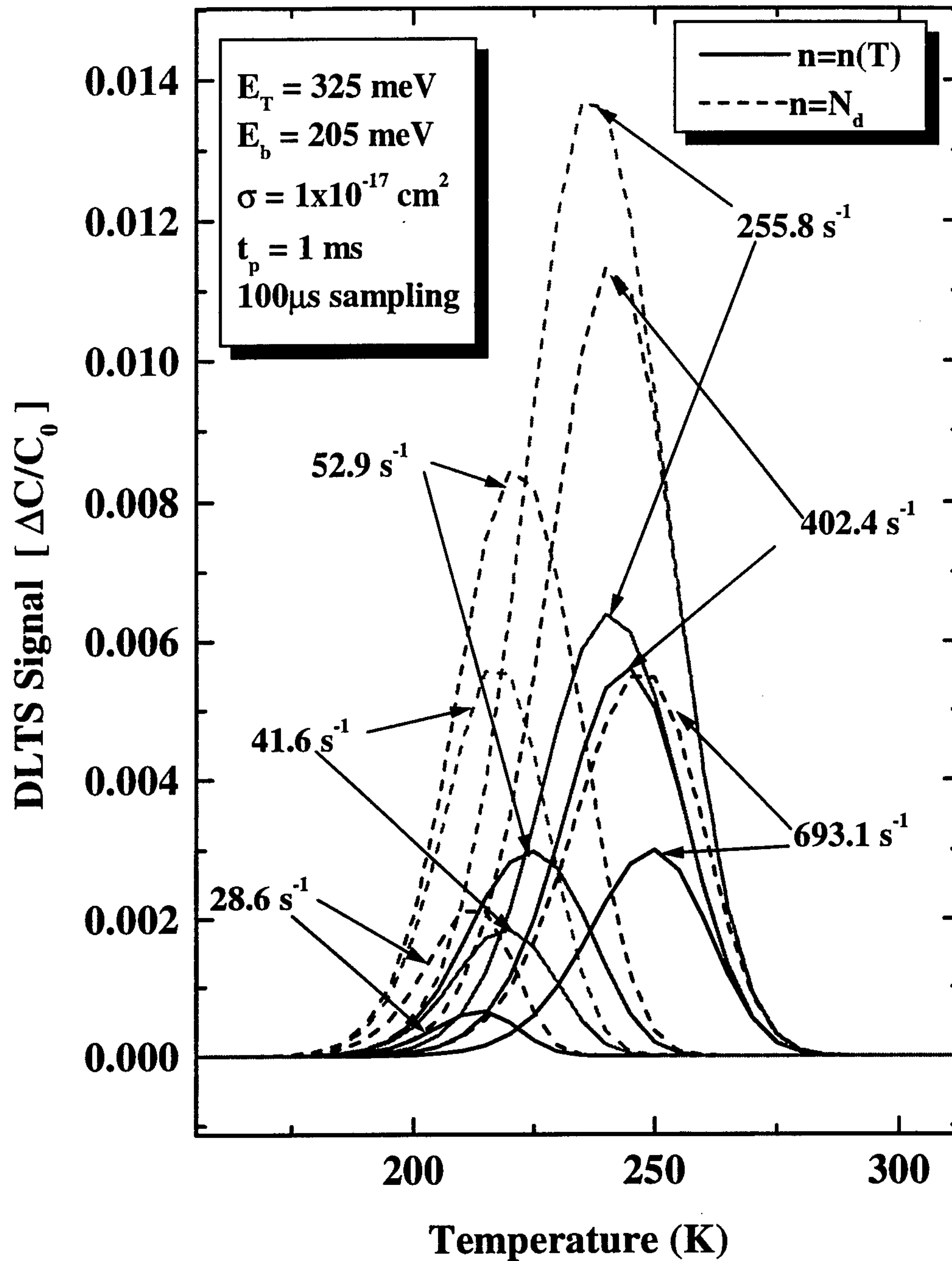

Figure VII-14. Simulated rate window data for an electron trap in n-type 6H-SiC designed to exhibit a low temperature spectral peak. Shown is a comparison between the computations assuming n=n(T) (solid lines) and n=N_D (dashed lines). The simulation parameters are listed as insets on the plot, and calculations were performed assuming carrier capture via MPE, with E_b being an appreciable fraction (0.63) of the thermal ionization energy E_T = 525 meV.

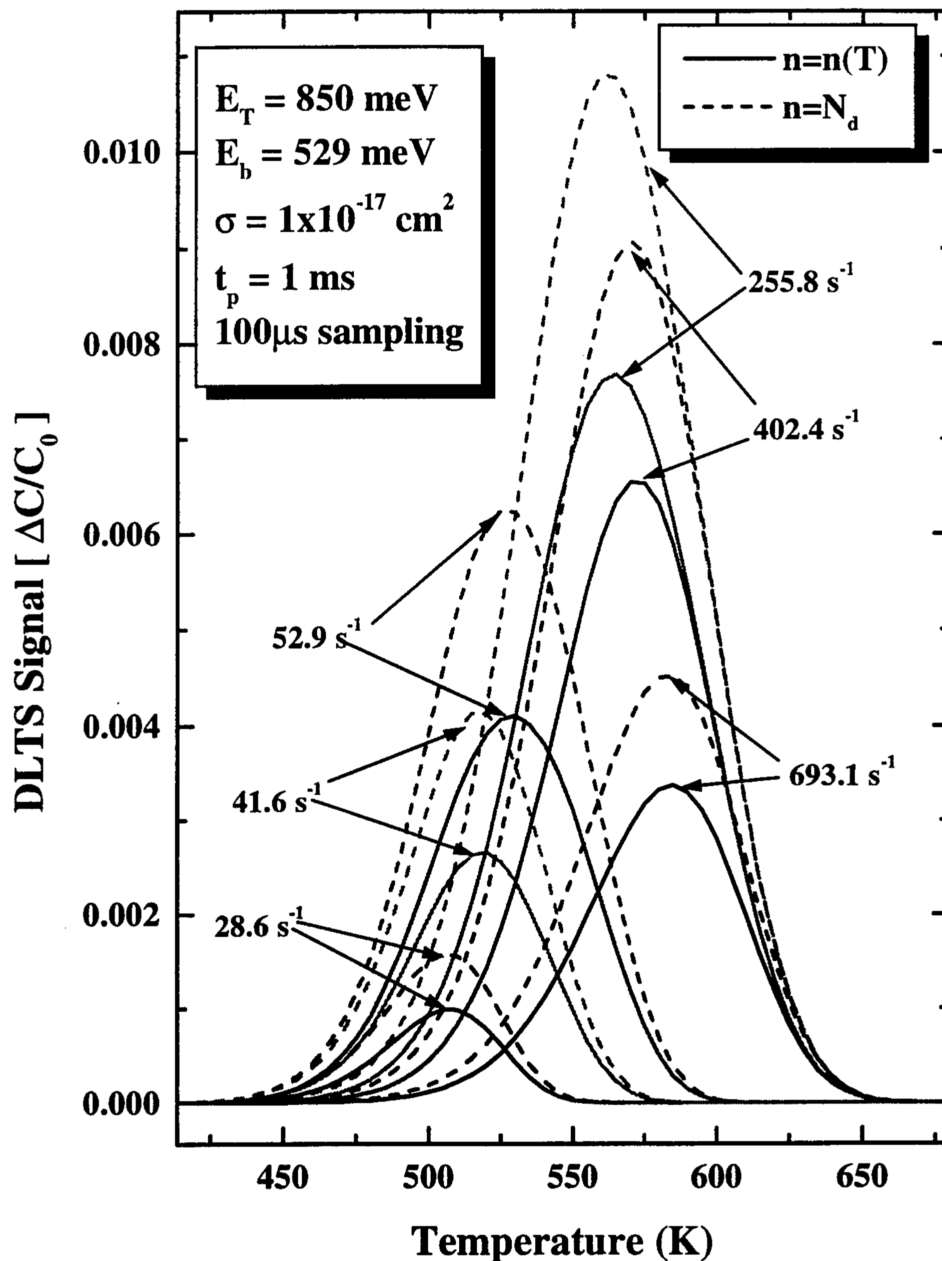

Figure VII-15. Simulated rate window data for an electron trap in n-type 6H-SiC designed to exhibit a high temperature spectral peak. Shown is a comparison between the computations assuming n=n(T) (solid lines) and n=N_D (dashed lines). The simulation parameters are listed as insets on the plot and calculations were performed assuming carrier capture via MPE, with E_b being an appreciable fraction (0.63) of the thermal ionization energy E_T = 850 meV. Data is intended to contrast the low temperature peaks of Figure VII-14, and illustrate the spectral asymmetry link to E_b and not n(T).

trap concentration was fixed at $1x10^{16}$ cm^{-3}, while the donor density was $1x10^{17}$ cm^{-3} in all trials.

Immediately apparent from the rate window comparisons of Figure VII-14 and Figure VII-15 is that the peak asymmetry is not correlated with the varying free carrier concentration. This effect is seen to occur with equal prominence in both the low temperature range, where n is a strong function of temperature, and the 500 to 600 °C range, where the carrier concentration is less variable. Thus, our original conclusion regarding the role of E_b in this phenomenon is seen to be corroborated. Additionally, from these figures, we do not observe a temperature shift for the $n=n(T)$ rate window curves when compared to the $n=N_D$ data. This conclusion supports the role of $\sigma(T)$, as related to E_b, in the spectral shifts of Figure VII-13 for large E_b/E_T ratios. The prominent effect of the incomplete ionization condition is seen to be an underestimation of the defect concentration, as illustrated by the reduced peak heights for the $n=n(T)$ curves. The underestimation is more pronounced for the low temperature peak of Figure VII-14 for the significantly lower carrier density, as expected.

VII-III-2. 6H-SiC:Mg Deep Level Pair. In addition to the bulk level electron trap in 6H-SiC, we have also observed the presence of multi-mode decay in n-6H-SiC ion-implanted with Mg. Figure VII-16 reflects typical rate window (a) and Arrhenius (b) data from DLTS measurements on 1200 °C, 120 minute annealed samples, which were implanted with Mg at an energy and dose of 195 keV and 10^{13} cm^{-2}, respectively. Implantations were performed under ambient 300 K conditions. Of interest is the high temperature spectral characteristic indicated by an arrow in Figure VII-16 (a). The

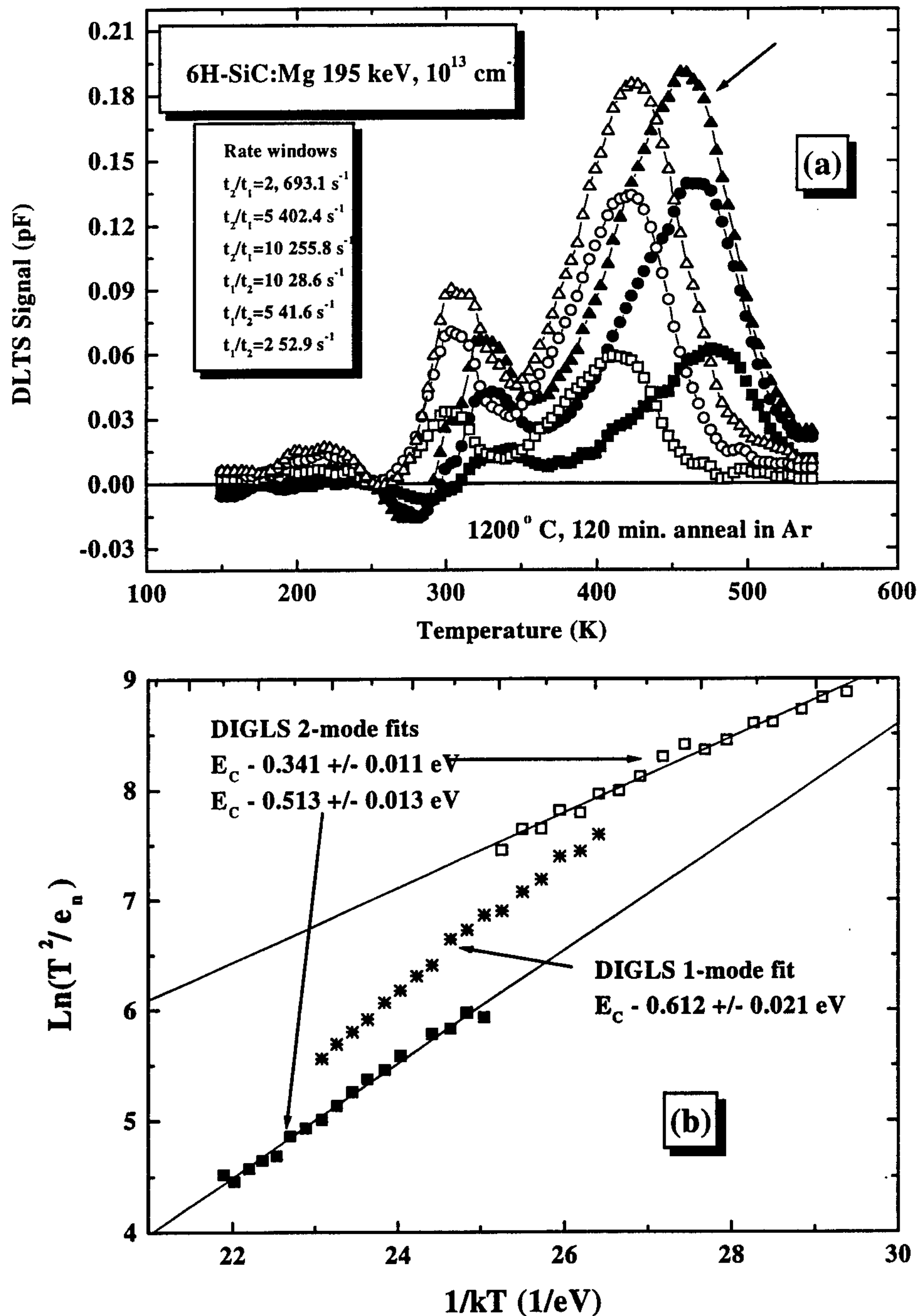

Figure VII-16. DLTS rate window spectrum (a) and Arrhenius plots (b) for data associated with Mg implanted, n-type, 6H-SiC. Mg was implanted at an energy and dose of 195 keV and 10^{13} cm^{-2}, respectively, under ambient room temperature (300 K) conditions. The high temperature spectral feature in (a) was identified as being comprised of two transient emission decay time constants, as resolved using the DIGLS fitting algorithm.

Arrhenius data in part (b) of the figure illustrate the results of transient decay fitting using both 1-mode and 2-mode DIGLS analysis for the DLTS peak indicated in (a). Again the fidelity of the DIGLS estimator is reflected by the clear resolution of a distinct time constant pair for this center. In this case, the presence of two levels is suggested by the shoulder on the low temperature side of the peaks in Figure VII-16 (a). The two mode decay analysis yielded ionization energies of 573 and 389 meV for the electron traps associated with the high temperature spectral feature of part (a). The single mode analysis yielded an energy of E_C-632 meV for this same feature.

The high temperature peak of Figure VII-16 (a) is closely related to the 657 meV 6H-SiC:Mg level described in the previous section. In that discussion, the 657 meV level was identified as one of the defects discovered to exhibit MPE capture kinetics. In the analysis of data collected from diodes containing the 657 meV level, multi-mode decay was not discriminated. The data illustrated in Figure VII-16 results from samples subjected to a higher 1200 ^{o}C anneal temperature than the 1000 ^{o}C anneal temperature used for the 657 meV level associated with the MPE data of Table VI-2. The higher anneal temperature has obviously resulted in additional rearrangement of the damaged lattice, and a more stable defect configuration has emerged. As mentioned in that earlier discussion, the peak spectral position and the E_C-657 meV energy calculated from the 1-mode analysis suggested that this center may have been related to the Z_1/Z_2 center reported for ion-implanted and electron irradiated n-type 6H-SiC [Pensl and Choyke, 1993:188]. The reported center was detected using analog methods exclusively, and was determined to be comprised of an E_C - 620 and E_C - 640 meV energetic pair. This

determination was concluded by fitting two Gaussian curves to an experimental rate window spectral feature, which as we have mentioned is fraught with uniqueness pitfalls. The Z_1/Z_2 center was implied to be related to an adjacent double vacancy, V_{Si}-V_C, which was reported [Vanier, Il'in 1981:2126] to have 6H-SiC point group symmetry, C_{3V}, thus capable of exhibiting site inequivalent energies. The assignment of their Z_1/Z_2 defect center to the double vacancy was purely speculative, as evidenced by the complete lack of physical evidence to support this claim.

Upon inspection of several samples ion implanted with Cr and Ar, we have concluded that the centers arising from both the low and high temperature anneals are directly related to the Mg impurity species. In fact, we did not observe the reported Z_1/Z_2 levels in any of our irradiated material, and concluded that the previous report was anomalous.

DDLTS measurements on the 573 and 389 meV centers, to determine emission rate field dependencies, indicated that these traps are acceptor-like in nature (neutral or repulsive when empty, therefore no coulombic attraction or emission rate effect). An acceptor-like electronic assignment was also concluded for the Z_1/Z_2 defect, based on similar measurements [Pensl, Choyke, 1993:188]. However, Mg in the SiC lattice is expected to present acceptor-like electronic levels (Mg^0/Mg^{1-}, Mg^{1-}/Mg^{2-}), and therefore this data does not support a connection with the adjacent double vacancy defect.

Analysis of the transient amplitude factors for these electron traps in the 1200 °C annealed samples indicated that electron capture at the 573 and 389 meV centers, also proceeds via MPE. This is evidenced again by the captured concentration profile as a

function of inverse temperature, which is shown in Figure VII-17. In this instance, the data was much more difficult to obtain and fit for capture barrier parameters due to interference from the signal centered at 300 K in Figure VII-16, and possibly due to the Mg concentration gradient resulting from the implantation profile. Thus, the barrier energy and the limiting cross section estimated from the peak position and curvature of the N_T^{0c}/N_S profile had a greater uncertainty than previous results. The roll-off of the experimental data on the low temperature end of the profiles in Figure VII-17 is due to the presence of the deep level represented by the ~320 K peak in Figure VII-16 (a). Thus, the amplitude factors do not approach zero as the temperature is lowered, which was characteristic of the MPE deep level data presented in the previous section.

The E_b, N_{TT}, and σ_∞ estimates for the two resolved levels are listed in Table VII-2. As was the case for the bulk 6H-SiC electron trap shown in Figure VI-19, the defect concentration ratio is very close to the 2:1 hexagonal to cubic lattice site ratio. This fact, together with the presence of an MPE capture mechanism with nearly identical E_b/E_T ratios for both levels and the connection to a specific atomic species, leads us to conclude

Table VII-2. Estimated trap emission and MPE capture parameters for the deep level electron trapping pair associated with the 1200 °C annealed 6H-SiC samples, which were ion implanted with Mg at 195 keV and 10^{13} cm^{-2}. Data supports the assignment of these two levels to inequivalent hexagonal and cubic lattice sites.

Ionization Energy	Capture Barrier	Trap Concentration	σ_∞
573 meV	246 meV	3.2×10^{16} cm^{-3}	1.6×10^{-19} cm^2
389 meV	167 meV	1.8×10^{16} cm^{-3}	3×10^{-21} cm^2

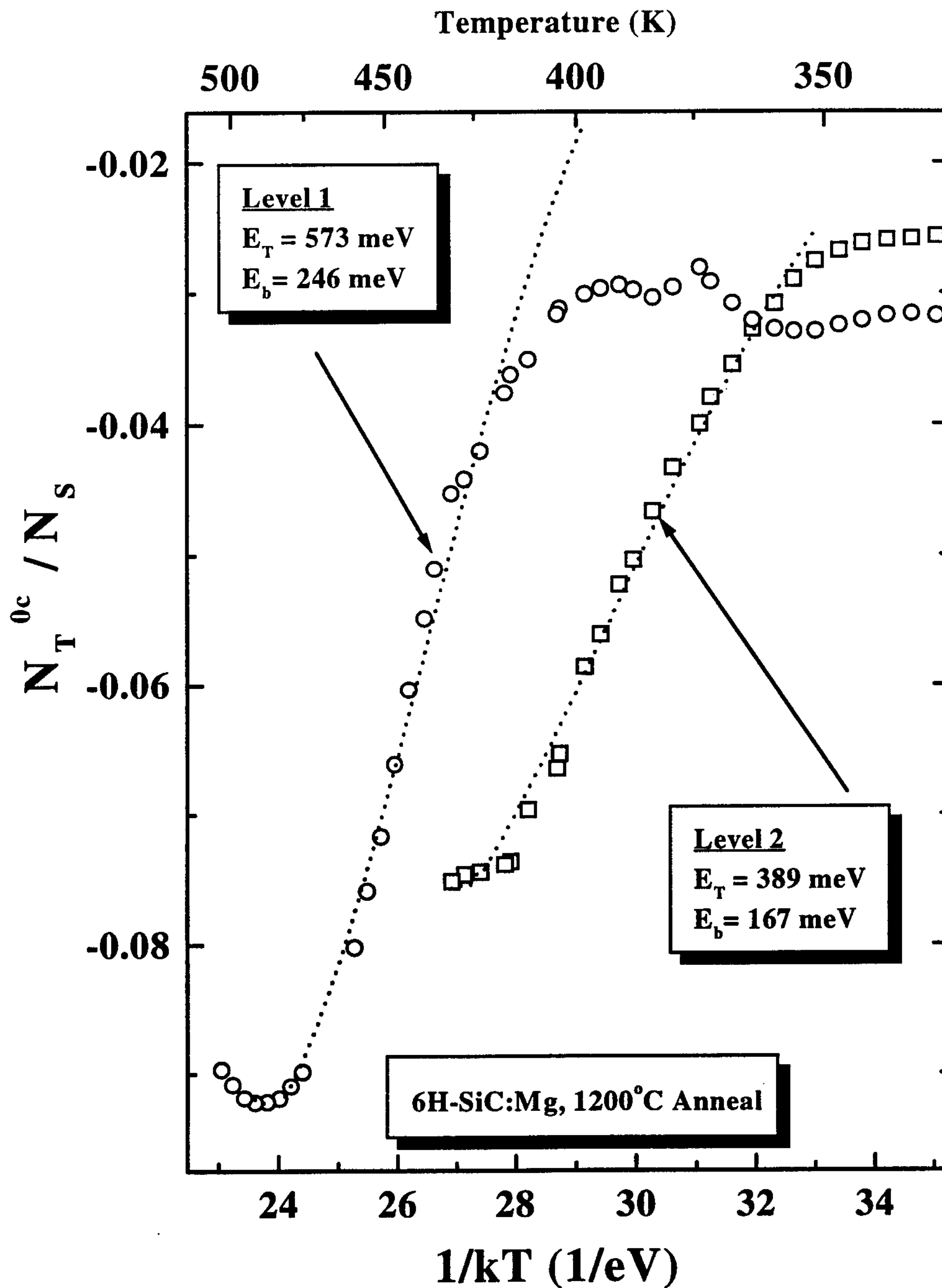

Figure VII-17. Transient amplitude variation with temperature for the energetic pair associated with the data of Figure VII-16. The dotted and dashed line fits to the symbol data yield estimated capture barrier energies of 246 and 167 meV for the 573 and 389 meV deep levels, respectively. The roll-off of the experimental data at the low temperature end of both profiles is due to the presence of the lower temperature deep level defect represented by the ~320 K peak in Figure VII-16 (a).

that these levels are site inequivalent energies associated with a Mg or Mg-complex defect. Additional support for this postulate is given by the excellent agreement between the experimental DLTS rate window spectrum and data resulting from self-consistency modeling of a two level system using the estimated trap parameters of Table VII-2. The results of these experiments are graphically illustrated in Figure VII-18, with the empirical data represented by the symbol plots and the modeled data shown as the solid line curves. This additional data strongly supports our two-mode transient decay conclusion arrived at on the basis of transient fits using the DIGLS algorithm. Furthermore, the assignment of this energetic pair to SiC inequivalent lattice sites is reasonable based on the evidence presented.

Although multi-mode decay was occasionally observed for several of the SiC deep levels investigated during this study, corroborating data enabling the assignment to hexagonal and cubic lattice sites were not realized. Typically the defect concentration ratio was not of the prescribed value, or closely related capture behavior was not observed. Thus, the connection to symmetrically distinct lattice sites could not be reasonably made without additional evidence to support such a claim. It is not unreasonable to assume that defects with complex geometries may exhibit anomalous capture kinetics or emission trends which would mask correlation to specific sites in the crystal. For example, a more complex defect potential, such as might be associated with the Mg-related defect discussed above, could account for the larger energetic splitting than was observed for the bulk SiC electron trap of Figure VII-9. However, a theoretical basis upon which to predict these defect trends is completely lacking, and

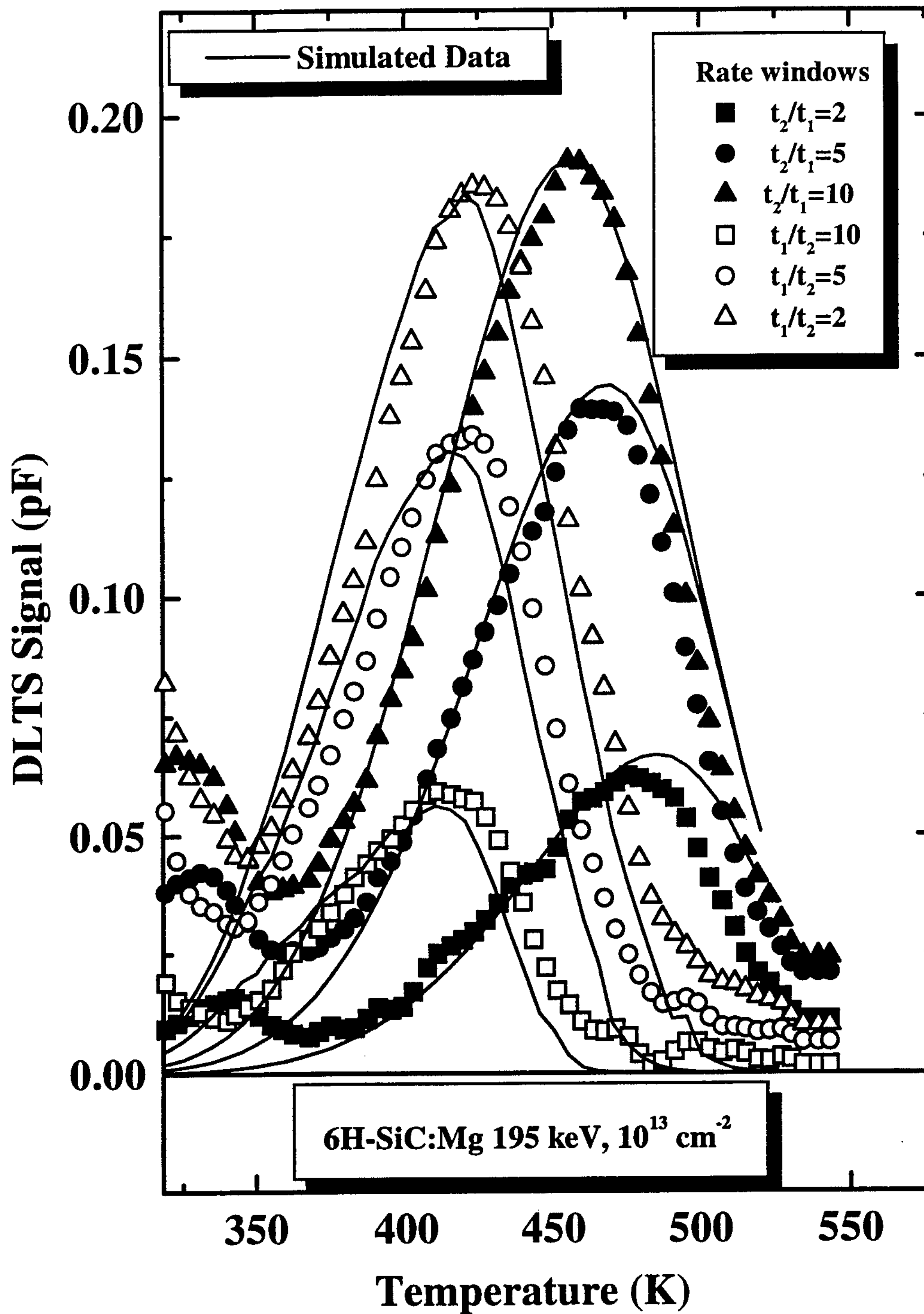

Figure VII-18. Rate window plots illustrating self-consistency between the experimental DLTS data (symbols) and numerically simulated data (solid line) for the Mg level in the 1200 °C annealed samples. The modeled data was generated using the trap capture and emission parameters listed in Table VII-2.

experimentalists must struggle with a myriad of possibilities from which to draw conclusions and interpret results. As a result of these difficulties, only the two 6H-SiC electron trapping centers illustrated in this section have been identified as exhibiting significant evidence for a connection to inequivalent lattice sites. This data represents the first conclusive evidence for this phenomenon, which has been achieved using DLTS methods.

In addition to scrutinizing all of the electron traps in the 4H and 6H materials studied during this effort, several deep level defects in p-type 6H-SiC have also been closely analyzed for multi-mode capacitance decay. However, only single-mode transient decay was observed for all of the p-6H-SiC defect emissions that we investigated, including those arising from the implantation of Mg, Cr, and Ar. Thus, this may be an indication that deep levels, which are coupled to the valence band, do not exhibit the same degree of energetic level splitting as centers that have resonances with the conduction band. This would be consistent with Hall effect observations of the ionization energy for shallow aluminum acceptors [Suttrop *et al.*, 1992:129]. These Hall effect measurements yield an average value of approximately 200 meV for the ionization energy of the Al acceptor in 6H-SiC. No dependence upon inequivalent lattice sites could be observed within the energy resolution of the Hall analysis. Furthermore, the same average value is obtained for the 4H and 3C polytypes, and illustrates an insensitivity to the particular polytype being considered. Ikeda *et al.* demonstrated that site inequivalency is applicable to the Al acceptors, but resolution of the closely spaced

energy levels (~10-20 meV) requires photoluminescence or optical absorption techniques [Ikeda *et al.*, 1979:111].

During this study, we have investigated the capture kinetics of deep trapping centers in 6H- and 4H-SiC. Free carrier trapping was found to obey the multi-phonon emission model for several of the defect centers studied. It was also determined that in each of these cases, the thermal capture barrier was an appreciable fraction of the thermal ionization energies. For a majority of centers exhibiting the MPE capture mechanism, it was discovered that the barrier to emission energy ratio, E_b/E_T, was in the range of 0.5 to 0.65. Although capture barriers of these magnitudes have been observed in other materials, these results represent the first data implicating both the MPE capture mechanism and barriers of this extent. These observations are in agreement with reports of a persistent photoconductivity effect in the hexagonal SiC polytypes, which requires the presence of an appreciable capture barrier. A new DLTS technique to identify the MPE capture mechanism was developed, which provides more accurate trap capture parameter estimates than previous analysis [Johnstone, 1996:III-27]. This method involves fitting the temperature dependent, emission transient amplitude-profiles, resulting from the incomplete filling of a trap of density N_{TT}. In addition to this analysis, direct measurement of the exponentially activated capture rate was accomplished for two of the defects associated with MPE kinetics. The results were in direct agreement with those obtained from the new amplitude analysis technique.

Although relatively simple to implement, the consideration for incompletely ionized shallow donors and acceptors was also included in the analysis of DLTS data.

The significant parameter estimate errors, which can result if this effect is not considered, were convincingly demonstrated in several instances. Surprisingly, this consideration had not previously been included or acknowledged in previous reports of SiC DLTS research.

Additionally, we investigated the model order of capacitance decay at deep levels in 6H-SiC using isothermal, digital, DLTS methods. Using our newly developed DIGLS estimator, we have identified multi-exponential decay at several deep level electron trapping centers in 6H-SiC. In each of these cases, the analog rate window spectral features did not readily indicate the presence of more than a single time constant. A center which may be related to the acceptor charge states of vanadium was shown to be comprised of two levels at E_C-551 and E_C-502 meV. Single exponential analysis yielded an ionization energy of 673 meV, which is very close to that reported for the vanadium acceptor in 6H-SiC using analog methods. Additionally, we have investigated a deep electron trapping center resulting from the ion-implantation of Mg into 6H-SiC epilayers. It was discovered that although the rate window spectra exhibited an apparent single peak structure, decomposition of the decay modes yielded convincing evidence for two level emission. Further evidence for the attribution of these multiple time constant signals to a single center was provided by the similarity of the capture cross section temperature dependencies and the concentration ratios of near the 2:1 site abundance ratio for cubic and hexagonal inequivalent sites in each case. Self-consistency with the DIGLS fitted trap parameters was achieved through computer modeling of the capture and emission kinetics for two level systems including the MPE capture mechanism. Agreement with the simulated results provided further confidence in the assignment of decay model orders

greater than one to the capacitance transients, and subsequently to the link with lattice site inequivalent energies. Finally, the experimental procedures and analytical methods used were applied to the investigation of deep levels in p-SiC to identify capacitance decay characterized by more than a single time constant. In every case, the emissions from hole trapping centers were identified with only one time constant. This result is in agreement with the observations of the shallow acceptor levels in this material, and indicates that the results obtained for the n-type material are not anomalous manifestations of our newly developed fitting algorithm or arising from other physical mechanisms.

VIII SiC Deep Levels

VIII-I. Intrinsic Deep Levels Identified

The renewed interest and activity in SiC development in recent years, owing to the availability of mono-polytypic 6H and 4H substrate material, has led to the successful development and demonstration of various devices based in these material systems. Ultraviolet photodiodes [Brown *et al.*, 1993:325], junction devices [Edmond *et al.*, 1991:487], [Kelner *et al.*, 1992:1038], numerous field effect structures [Palmour *et al.*, 1993:491], and most notably, blue light emitting diodes [Vishnevskaya *et al.*, 1987:414] have all been demonstrated to various levels of efficiency and performance. Fueling this revitalized activity in wide-gap semiconductor development is the promise of significant performance gains for microwave and power device technologies with the added benefit of increased thermal and radiation hardness. The result of these intensified efforts has been continued improvement to material quality and in device performance. However, several difficulties persist, indicating the need for greater physical understanding of the electronic properties of this unique material system. As mentioned at the end of Chapter I, SiC device technology is hampered by impurity and structurally related crystal flaws, difficulty in processing, relatively deep intentional dopant energy levels, contact metallization problems, and the lack of a controllable process for producing high quality, semi-insulating, bulk material. Metal-Oxide-Semiconductor (MOS) devices fabricated on p-6H-SiC exhibit anomalous transconductance and channel mobility behavior [Brown *et al*,. 1994:325], possibly related to the aluminum acceptor and high interface state

densities. Excessive leakage currents and pinch-off problems in MESFETS and JFETS, and unacceptably low minority-carrier lifetimes in optoelectronic devices are also representative of the difficulties encountered when building devices on these material systems. In many instances, devices built on SiC appear to behave in an unusual fashion. This is due to factors such as the anisotropy of the mobility and conductivity; marginal validity of the effective mass approximation especially in the valence band; and incomplete ionization of shallow donors and acceptors for temperatures exceeding 400 to 500 K. These conditions can be successfully accounted for by modifying the mathematical expressions used to model device performance. [See for example, Pfirsch and Ruff, 1993:2085 and references therein] Many of the device related problems, however, are directly due to the sometimes high concentrations of defects present in the material with energy levels within the forbidden gap of the semiconductor. These centers act as trap and recombination/generation centers and effectively kill minority carrier lifetimes, contribute to leakage current, and in general degrade performance. However, as outlined in Chapter III, controlled introduction of such centers may have the desirable effects of creating semi-insulating material and improving switching speed, but understanding the sources and nature of these centers is required before they can be utilized in this manner.

In order for SiC to realize its tremendous potential for high temperature, high power, and high frequency device performance, significant improvements must be made in each of these problem areas, especially in the quality of the starting bulk and epitaxial material. Although significant understanding about the radiative transition centers in SiC has been

realized [Choyke and Patrick, 1962:1868], [Dean and Hartman, 1972:4911], little is known regarding device degrading non-radiative deep traps in SiC. Therefore, a deep level study of sublimation grown bulk and MOCVD grown epitaxial 6H-SiC was undertaken on Schottky, MOS, and p-n junction devices, using DLTS over a wide temperature range up to 800 K. The results of the measurements on these devices to identify commonly occurring intrinsic defects with deep electronic trapping states are presented in following section of this Chapter. The goal was to more fully catalog and identify the commonly occurring centers in these materials, and augment the very limited data base in this area. Furthermore, the high temperature DLTS scanning capability developed and assembled during this research project represents the first extension of this technique into the temperature ranges beyond 500 K. As such, all data recorded and deep levels identified over this high temperature regime represent the first report of DLTS results for SiC or any other material in this extended range.

A thorough review of the available information regarding deep level studies of SiC bulk and epitaxial material was performed, and the results are summarized in Table VIII-1 and Table VIII-2 for 6H- and 4H-SiC, respectively. These tables summarize the observed energy levels, capture cross sections, method of identification, defect source, and material growth method. Immediately apparent from the data in these tables is that only levels induced by the addition of boron and vanadium have been reasonably studied and correlated to the specific impurity. The majority of the remaining entries in these tables were reported once and they are lacking supporting or corroborating data to verify their omnipresence in the material or assist in source identification. Additionally, the lists

Table VIII-1. Summary of all defects and deep levels identified in the 6H polytype of SiC.

Energy Level (eV)	Cross Section	Technique	Defect/Impurity	Material	Reference
E_V+1.3	n/a	ESR	V^{4+}/V^{5+} (D^o/D^+) (hex site)	Lely Bulk(n)	Schneider 1993
E_V+1.6	n/a	ESR	V^{4+}/V^{5+}(D^o/D^+) (cubic site)	Lely Bulk(n)	Schneider 1993
E_C-0.71	$6x10^{-20}$ cm^2	**DLTS**	V	Sublimation Bulk(n)	Evwaraye 1993
E_C-0.7	n/a	Theory	V	-	Stiansy 1992
E_V+1.45	n/a	Theory	V	-	Stiansy 1992
E_C-0.6	n/a	ESR	$Ti_{Si}{}^{3+}$ -N_C (D^o/D^-)	Lely Bulk(n)	Schneider 1993
E_C-0.39	$2x10^{-15}$ cm^2	**DLTS**	?	Lely Bulk(n)	Jang 1994
E_C-0.43	$4x10^{-16}$ cm^2	**DLTS**	?	Lely Bulk(n)	Jang 1994
E_C-0.69	$2x10^{-17}$ cm^2	**DLTS**	?	Lely Bulk(n)	Jang 1994
E_C-0.68	$2x10^{-14}$ cm^2	**DLTS**	?	Sublimation Bulk(n)	Uddin 1993
E_C-0.71	$5x10^{-14}$ cm^2	**DLTS**	?	LPE p^+/n	Uddin 1993
E_V+0.53	n/a	C-V, I-V-T	Al,C	SiO_2/p-SiC	Raynaud 1994
E_C-0.4 to 0.54	n/a	**DLTS**	Polishing Damage	Sublimation Bulk(n)	Evwaraye 1993
E_V+0.61	$1.5x10^{-14}$ cm^2	**DLTS**	Al irradiation	Al implant LPE(p^+/n)	Anikin 1985
E_V+0.66	$3x10^{-14}$ cm^2	**DLTS**	Boron	B diffused p-/n	Anikin 1985
E_V+0.39	n/a	TSC	V	V doped sublimation	Jenny 1995
E_V+0.3	$1x10^{-13}$ cm^2	**DLTS**	Boron	Boron implant (p-epi)	Suttrop 1990
E_V+0.58	$5x10^{-15}$ cm^2	**DLTS**	Boron D-Center	Boron implant (p-epi)	Suttrop 1990
E_V+0.55	n/a	Absorption	Boron D-Center	MOCVD (p-epi)	Ballandovich 1991

ESR=Electron spin resonance, TSC=Thermally stimulated current, LPE=Liquid phase epitaxy,

Table VIII-2. Summary of all defects and deep levels identified in the 4H polytype of SiC

Energy Level (eV)	Cross Section	Technique	Defect/Impurity	Material	Reference
E_C-1.73	n/a	OAS	V^{4+}/V^{5+} (D^o/D^+) (hex site)	PVT Bulk(n)	Evwaraye 1996
E_C-1.17	n/a	OAS	?	PVT Bulk(n)	Evwaraye 1996
E_C-1.13	$6x10^{-20}$ cm^2	OAS	?	PVT Bulk(n)	Evwaraye 1996
E_V+0.54	n/a	**DLTS/EL**	Boron D-center	-	Stiansy 1992
E_V+0.5	n/a	**DLTS/EL**	Boron i-center		Stiansy 1992
E_C-0.6 to 0.64	n/a	**DLTS/Hall**	V	PVT Bulk(n)	Schneider 1993
E_C-0.62 to 0.68	$2x10^{-15}$ cm^2	**DLTS**	?	MOCVD epi (n)	Jang 1994
E_C-0.6	$4x10^{-16}$ cm^2	**DLTS**	?	MOCVD epi (n)	Jang 1994
E_C-0.69	$2x10^{-17}$ cm^2	Hall	?	MOCVD epi(n)	Jang 1994

OAS=Optical admittance spectroscopy, PVT=Physical vapor transport

show that with the exception of boron related levels, there exists a complete lack of available deep level data for p-type materials. Thus, all commonly observed deep traps reported in this subsection for p-type 6H-SiC truly represent the initial results in this material. This is true for DLTS obtained trap data over both the low and high temperature ranges.

The SiC samples used for this portion of the work were 6H-polytype n- and p-conductivity bulk material grown by a proprietary modified Lely process and doped with nitrogen and aluminum, respectively, to concentrations between $1x10^{17}$ and $1x10^{18}$ cm^{-3}. MOCVD grown epitaxy with shallow impurity doping levels of $1x10^{16}$ to $2x10^{17}$ cm^{-3}

were also obtained and characterized. 500 μm diameter Schottky diodes and MOS capacitors were formed using the processes defined in Appendix B. DLTS measurements were taken on the computer controlled system detailed in Chapter IV. System sensitivity for defect detection has been determined to be in the mid-10^{-5} range with a noise level of approximately 5 fF.

VIII-II. Deep Levels in Bulk 6H-SiC

Both the epitaxial and bulk material investigated in this work exhibited significant numbers of deep trapping levels. Only those traps which were observed consistently throughout the range of samples measured are reported. Several new deep level centers were identified by measuring DLTS up through 800 K in as-grown bulk n- and p-type SiC. Additionally, numerous peaks in the DLTS spectra were detected, which occurred with single or insufficient frequency to allow adequate analysis and identification, and are probably related to localized structural flaws. A majority carrier electron trap observed in all n-type bulk wafers was initially determined to have a deep level energies estimated at 0.825 and 0.673 eV below the conduction band, that were estimated using rate window and DIGLS one-mode transient fitting analyses, respectively. As highlighted in the previous chapter, this discrepancy was attributed to the fact that the capacitance decay was actually characterized by two-mode emission from site inequivalent lattice positions. We have concluded that this defect is likely to be the same as that reported for the vanadium acceptor impurity center [Jenny *et al.*, 1996:1963]. This conclusion is based on the similarity between their data and ours. Our rate window DLTS spectrum analysis

yields energy and capture cross section estimates of 0.825 eV and 6.0×10^{-16} cm^2, respectively. These values are in comparison to their 0.806 eV and 1×10^{-16} cm^2 values which were obtained using identical rate window methods. On the other hand, Jenny *et al.* also estimated the V acceptor ionization energy using Hall effect analysis and obtained a value of 0.66 eV, which agrees well with our DIGLS one-mode estimate. Since their data were obtained using analog methods exclusively, they were unaware of the link to inequivalent lattice sites, which is responsible for the ionization energy discrepancy between measurement techniques. While our analysis indicates that this may be the center previously attributed to V, an anomalous field dependency was observed, and is reported for the first time. Additionally, this center was one of the defects observed to exhibit MPE activated cross section behavior, which was used to support the assignment of the resolved two-mode decay to inequivalent lattice sites.

DDLTS field dependent measurements were performed in order to determine acceptor or donor character and verify the proposed charge states of deep level under consideration. The procedure to determine emission rate field dependencies was previously outlined in Chapter VI.

Several runs were accomplished using DDLTS to detect trap emission from a narrow portion of the depletion region of the reverse biased Schottky devices. At a fixed temperature of 280 K and filling pulse biases of 0.4 and 1.0 volts with 10 ms durations, the reverse bias voltage was stepped from -1.5 to -6.5 volts in 0.15 volt increments. Using these bias values, the depth of the narrow emission region and the electric field were estimated for a Schottky diode in n-type material using

$$W = \sqrt{\frac{2\varepsilon}{qN_D}(V_{bi} - V - kT/q)}$$

and [VIII-1]

$$|F(x)| = \frac{qN_D}{\varepsilon}(W - x) \ ,$$

where the typical built-in potential, V_{bi}, for these devices was determined to be ~1.4 eV using conventional C-V analysis [Sze, 1981:286]. Using this analysis, the estimated emission depth was determined to be centered at ~0.057 μm with a width of ~0.011 μm, and estimated donor density was 5.2×10^{17} cm^{-3}. Estimates of the 280 K constant temperature deep level emission rates were obtained for each reverse bias DDLTS value, V, using the DIGLS estimator. These $1/\tau$ values were then plotted against the square root of the electric field F(x) to discern field effects, using Equations VI-9 and VI-10.

Vanadium is proposed to exist in SiC possessing three charge states $V_{si}^{5+}(3d^0)$, $V_{si}^{4+}(3d^1)$, and $V_{si}^{3+}(3d^2)$ from ESR data [Schneider *et al.*, 1990:1184], and presumably creates deep donor and acceptor states depending upon the position of the Fermi level. In n-type material, the A^0/A^- (V_{si}^{4+}/V_{si}^{3+}) electronic configuration should be prevalent. Figure VIII-1 illustrates three rate window plots of the DDLTS spectral characteristic for the deep level under consideration. The run conditions for the illustrated data are listed at the bottom of the plot. The spectral position, capture cross section, and one-mode ionization energy estimates support the conclusion that this center is related to the previously reported V acceptor. The data illustrated is from a single spatial profiling DLTS scan,

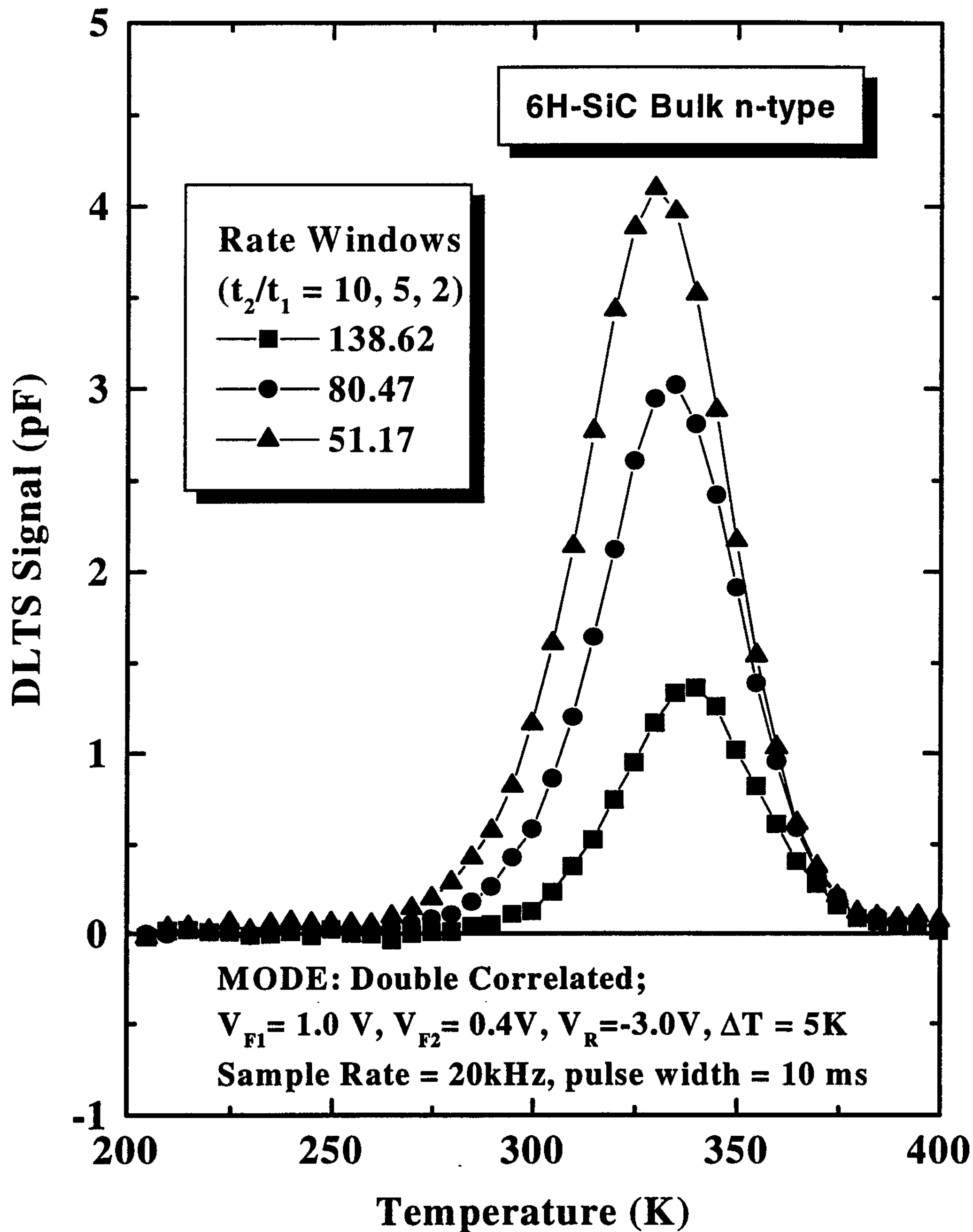

Figure VIII-1. Rate window DDLTS spectrum of the most commonly observed deep level in 6H n-type SiC. Shown here is the results of a double correlated scan utilized to ascertain spatial profile and electric field effects. Run parameters are listed at the bottom of the plot. This single peak was resolved to yield two ionization energies of 543 and 509 meV below the conduction band. This center is likely to be the acceptor level of the vanadium transition metal impurity.

which indicated that the trap was uniformly distributed with a density of $\sim 7 \times 10^{15}$ cm^{-3}. This density was found to agree well with the value of 3×10^{15} cm^{-3} obtained from secondary ion mass spectrometry (SIMS) data on these samples. As outlined in the previous chapter, this 673 meV reported level has been resolved into inequivalent lattice site energies of 543 and 509 meV below the conduction band edge. Furthermore, it was demonstrated that electron capture is facilitated by large lattice relaxation MPE. It will now be show that, in addition, there exists an anomalous electric field effect associated with this center. Figure VIII-2 is a representative emission rate versus electric field plot used to determine Poole-Frenkel barrier lowering for coulombic trap centers. In this figure, the emission rate evolution with applied electric field has been plotted for both the DIGLS one- and two-mode time constant estimates, which was done for comparison and consistency purposes. Immediately apparent from the illustrated data is that for fields $\leq$ 2.5×10^{5} volt/cm, a linear dependence on $F^{1/2}$ is observed for all three emission rates. This field effect trend is in compliance with theory as defined in Equations VI-9 and VI-10. On the other hand, when calculating the relative dielectric constant from the two-mode slope quantities (using Equation VI-9), values of $0.2 \leq \varepsilon \leq 0.7$ are obtained, depending upon the charge constant, γ, utilized. Thus, the actual induced field effect is seen to be less than that predicted by the Poole-Frenkel model for a defect, which is proposed to possess a charge of 4+ in the unoccupied condition. This discrepancy may be related to wavefunction localization associated with these deep levels. In other words, if the orbital radius is not large enough to encompass several unit cells, then the macroscopic dielectric constant has no meaning and the value estimated from this data will be undefined.

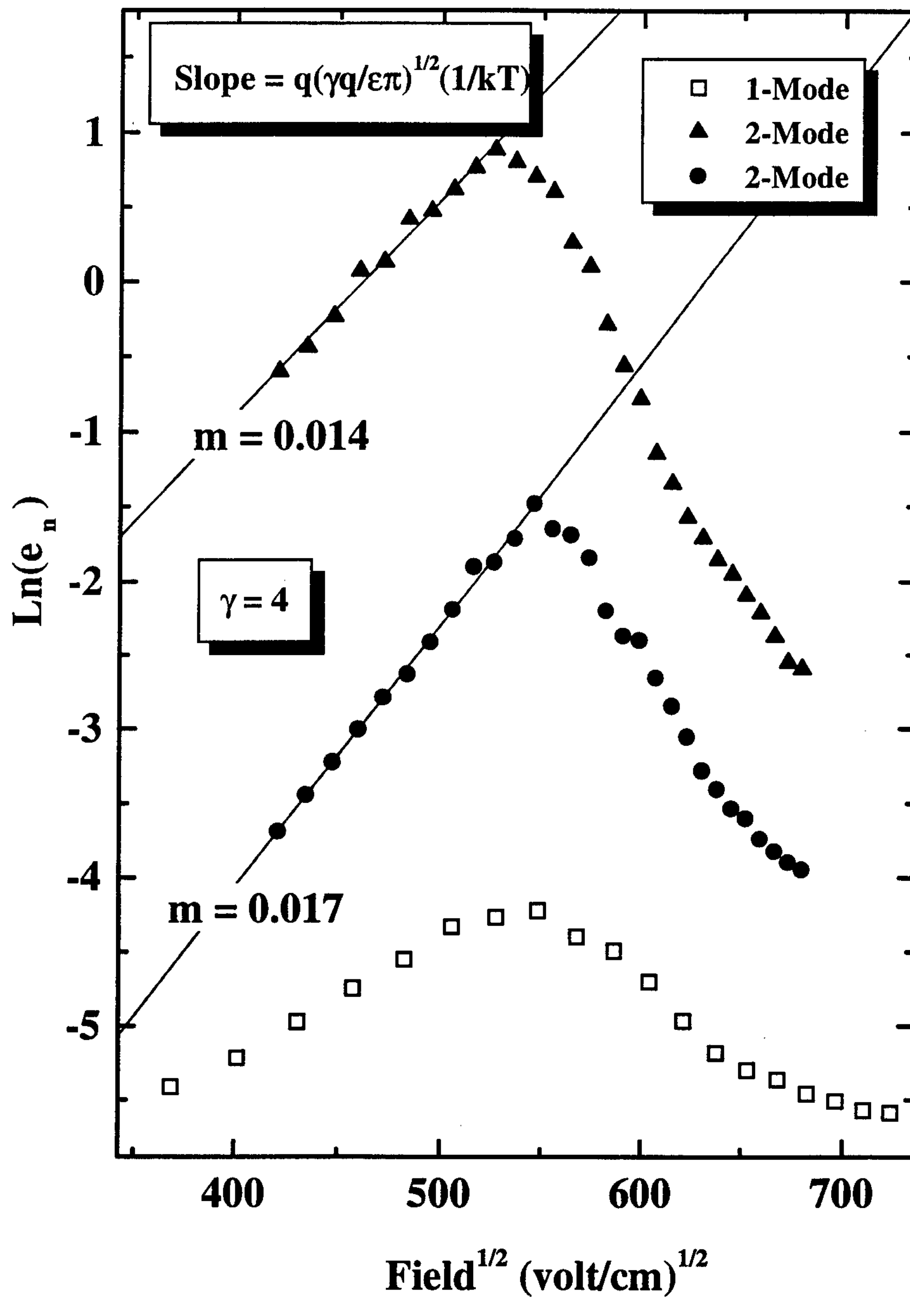

Figure VIII-2. Natural log of the DIGLS fitted emission rates for both the one- and two-mode estimates. The low field ($F<3x10^5$ V/cm) trend is seen to agree with the expected emission rate response to an applied field, however, the slope of the linear region is found to be well below that expected for γ=4+. The high field region is seen to be completely anomalous in the response to the applied field. Both effects may be related to the large MPE lattice relaxation observed for this center.

This is because the dielectric constant is related to the atomic polarizability, but more importantly, a dependence upon the arrangement of atoms in the crystal structure is the dominating consideration. A more likely cause for these low field trends is related to the presence of large thermal capture barriers, which were described for this center in the previous chapter. Buchwald and Johnson [1988:958] demonstrated that the presence of an MPE activated carrier capture mechanism and the associated thermal barriers were sufficient to suppress the Poole-Frenkel effect. They demonstrated this effect for E_b/E_T ratios as low as 0.1, both experimentally and theoretically. Furthermore, they illustrated that the primary effect was to significantly underestimate the resulting linear slope as observed for our data in Figure VIII-2. We therefore conclude that the large thermal barriers (E_b/E_T~0.6) present for this energetic pair are responsible for the observed deviation from the classical response for attractive coulombic potentials.

The most prominent feature of the field dependent data shown in Figure VIII-2 is observed for applied fields > 3.0×10^5 volt/cm. The emission rate in this region of applied field is seen to decay with increasing electric fields. There does not exist a theory which predicts this behavior for attractive, neutral, or repulsive coulombic potentials. Thus, connection to a distinct physical mechanism is not possible at this time. Considering the electron emission rate expression, this effect can be realized by a decrease in the capture cross section and/or average carrier velocity. On the other hand, an increase in the trap ionization energy with increasing field would also satisfy the observed phenomenon. A tunneling mechanism from the defect bound state to the conduction band, would serve to increase the emission rate with applied field, and can therefore be ruled out. There are

two plausible explanations which may qualitatively account for the observed behavior. First, the large field behavior of this trap potential may be related to a field enhanced screening effect. However, since the trap emission is being recorded during the biasing cycle when the depletion approximation is valid, the screening contribution could not originate from the free carriers. Thus, if screening were to be responsible, it would require a significant redistribution of the bonding valence electrons, and to a lesser extent, the inner core electrons. Thus, an electric field induced charge density would result from which a modification to the dielectric constant would occur according to Thomas-Fermi screening theory [Ashcroft and Mermin, 1976:341]. We could thus estimate a Thomas-Fermi wavevector, using the typical free electron gas approximation given as

$$\mathbf{k}_0 = \frac{2.95}{\sqrt{r_s / a_0}} \quad (\text{Å})^{-1},$$

where r_s is the screening radius, and a_0 is the Bohr radius. Using this rough estimate, a screened coulomb potential can be defined as

$$V(\mathbf{r}) = \frac{\gamma q}{r}\exp(-k_o r),$$

where γ is the charge state of the coulomb potential. The screened potential results in a defect cross section reduction, which would account for the observed emission rate decrease with increasing field. This can be seen by observing the screened and unscreened potential representations in Figure VIII-3. Using typical values for r_s/a_0 [Ashcroft and

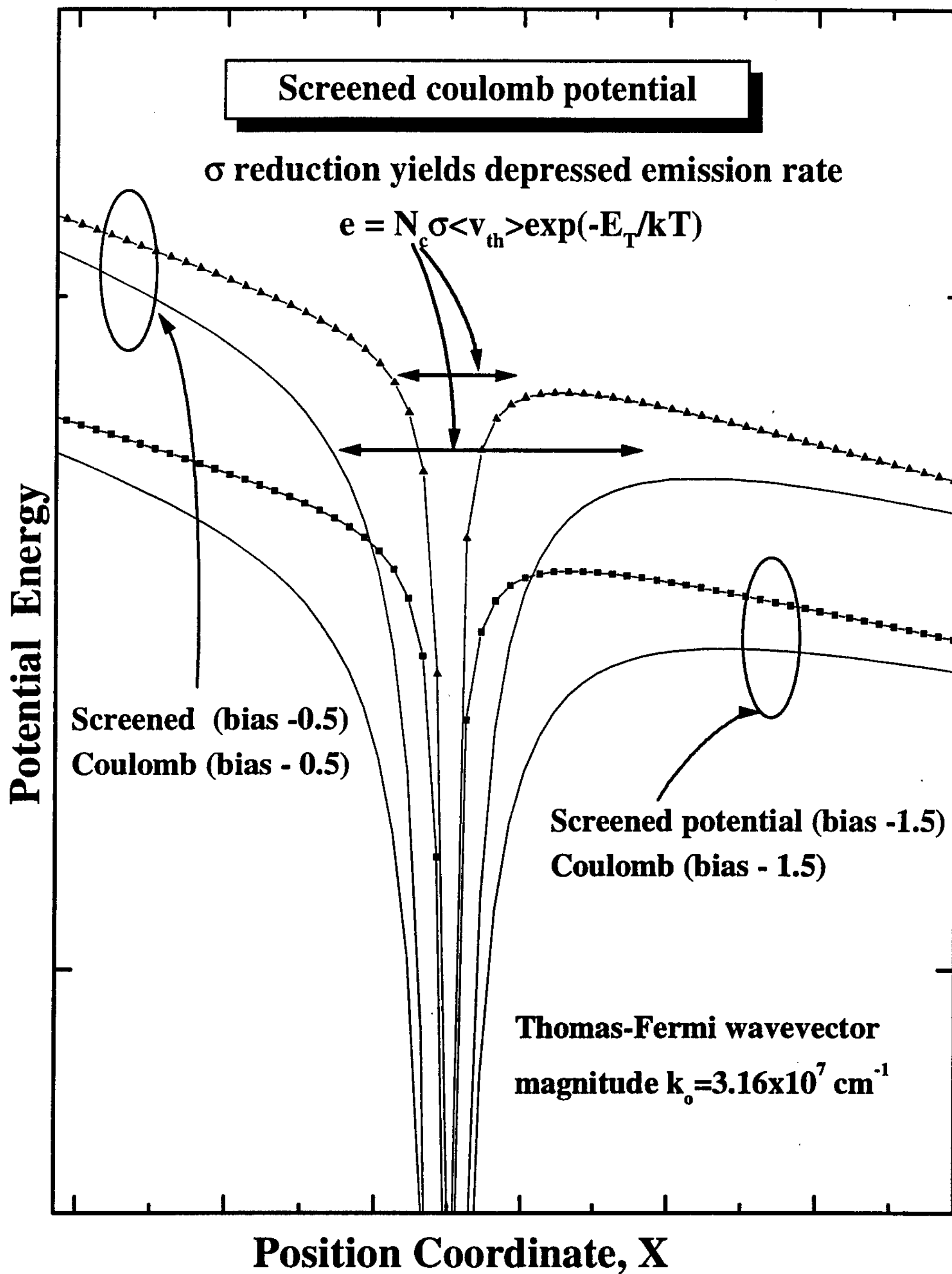

Figure VIII-3. Plots illustrating the effect of screening on a coulomb potential using the estimated Thomas-Fermi wavevector of 3.1×10^7 cm^{-1}. Shown are screened and unscreened potentials calculated at two bias values of -0.5, and -1.5 volts as illustrated on the figure. Explicitly illustrated is the physical cross section reduction for the screened potentials.

Mermin, 1976:342], the potentials were calculated for two bias values listed on the plot. These calculations are very approximate, but they serve to illustrate the cross sectional reduction, which is realized as a result of screening effects.

There are undoubtedly other plausible explanations for the depressed emission rate observed at high electric fields. For example, a field induced lattice relaxation might occur which would serve to increase the trapped carrier ionization energy. Since this center has been shown to exhibit MPE related large lattice relaxations, the potential for field induced defect motion may exist. In either case, a well founded theory does not exist to explain this phenomenon, and reports of similar field dependent behavior do not exist. Therefore, we assume that this is the first report of such an electric field effect. The low field trend exhibited by this deep level pair was found to be also anomalous, however, the connection to a capture barrier screening of the Poole-Frenkel effect was consistent with previous reports. Unfortunately, there was not found to be another deep level exhibiting this behavior in any of the SiC materials characterized, and thus a more conclusive postulate could not be formed.

Reports of deep level activity and electrical characterization of p-type hexagonal SiC are virtually nonexistent in the available literature. The lone exception is associated with ion implantation or growth of p-type SiC using boron acceptor impurities, as illustrated in Table VIII-1 and Table VIII-2. This condition has been due to two primary causes. First, the limited availability of adequate quality p-conductivity material, which is related to the difficulty in achieving a high activation fraction of the Al acceptors. Secondly, the prohibitively high cost of p-type material has restricted access to most investigators. The

first impediment to the acquisition of p-type material has been recently overcome, with a wide conductivity range of material availability. The cost factor has been relieved to some extent, following the successes realized in acceptor activation, however, significant financial restrictions exist for most institutions. Through a combination of limited purchases and generously donated samples, we have been able to adequately characterize the deep defect activity in the 6H material. As a result, all of the identified trapping centers observed and characterized in these p-type materials are being reported for the first time.

In p-type bulk 6H material, two new deep majority hole traps were observed at energies of 0.861 and 0.479 eV above the valence band. The 0.861 eV center was previously identified as one of the deep levels exhibiting MPE carrier trapping kinetics in the last chapter. It was determined to possess a high temperature limiting capture cross section of 2.2×10^{-15} cm^2. The capture cross section for the 479 meV hole trap was found to be temperature independent, and equal to 2×10^{-20} cm^2. Additionally, a minority carrier electron trap was detected at E_c-0.78 eV. Figure VIII-4 shows the DLTS rate window spectra for the three dominant trap levels consistently observed in the Al doped p-material. The 479 and 780 meV traps were found to occur in large average densities of 2% and 1.5% of the 4.1×10^{18} cm^{-3} shallow acceptor concentration, respectively.

The trap at E_c-0.78 is interesting for several reasons. The existence of such a large minority carrier signal in a Schottky device would typically not be expected, especially in a material with a large energy gap. The large bandgap of SiC precludes any possibility of thermally generated minority carriers, as illustrated at the end of Chapter I, especially in

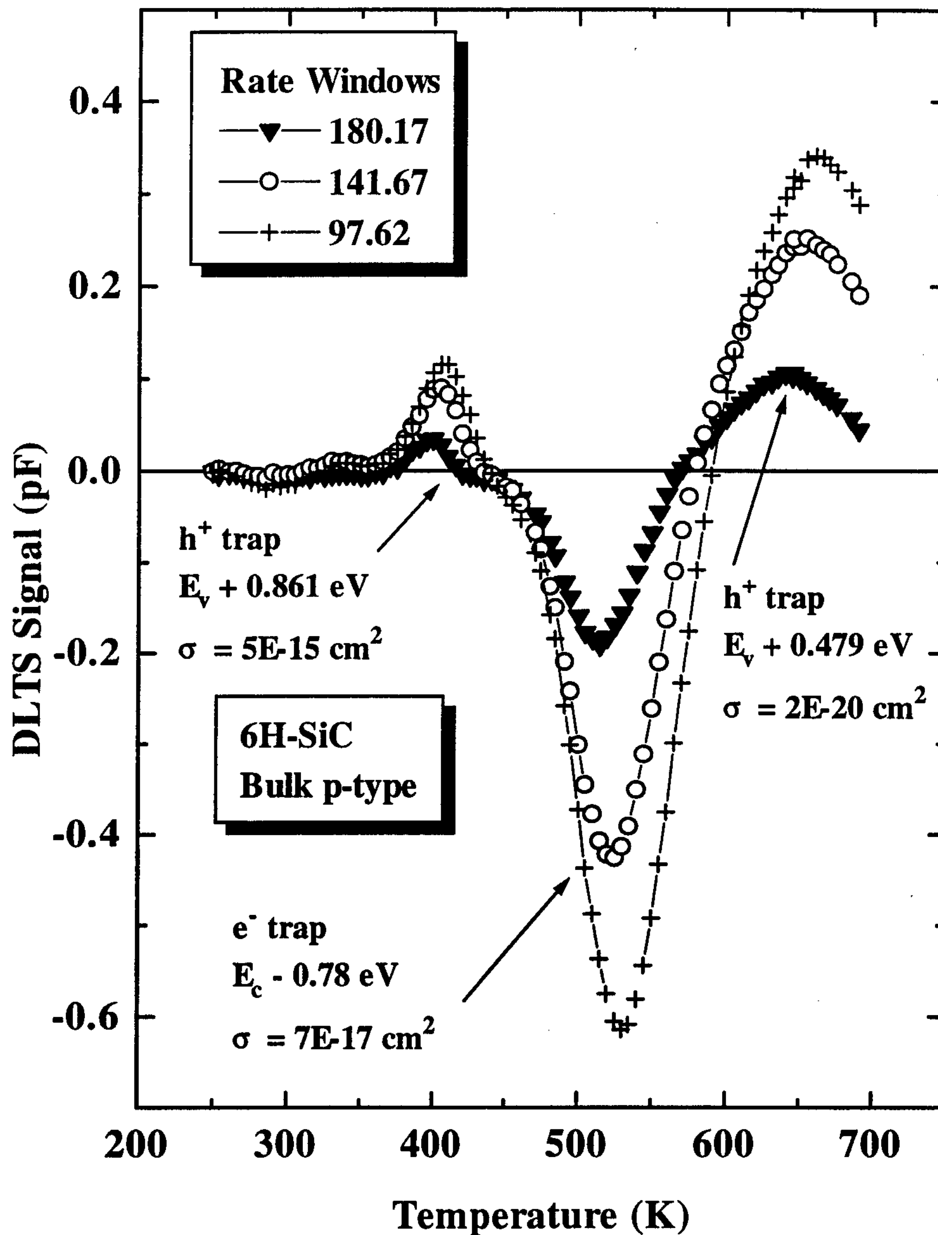

Figure VIII-4. Conventional DLTS rate window spectrum for a p-type bulk 6H-SiC sample containing the three frequently observed deep levels with energies and cross sections as labeled on the figure next to each peak. The 861 meV level was described earlier as possessing an MPE activated capture mechanism, thus the cross section labeled here represents σ_∞.

the concentrations required for filling this level. Additionally, filling pulse biases were not large enough to achieve minority carrier injection due to an enhanced drift-field component [Sze, 1981:267], and thus field injected electrons from the metal could not be the source of these signals. Additionally, this behavior was observed on several devices built on both bulk and epitaxial material having various doping densities and both conductivity types. Figure VIII-5 illustrates an analogous situation for a Schottky diode fabricated on the (0001) surface of a bulk n-type wafer sample. The rate window spectra in (a) clearly show the presence of a large concentration hole trap peak at 340 K. The Arrhenius data in part (b) of the figure reveals an activation energy of E_V+511 meV and capture cross section of $9x10^{17}$ cm^2. The majority carrier trapping peak also seen in the figure is the vanadium acceptor center, as evidenced by the two mode Arrhenius resolution illustrated in part (b). This is concluded based on the agreement of the ionization energies with those consistently observed. Although not as frequently occurring in the n-conductivity material, this apparent minority carrier injection was occasionally observed in all material types investigated. A clue to the source of this behavior was obtained by considering the Schottky barrier height dependence upon pre-fabrication wafer cleaning procedures.

Using conventional C-V profiling [Sze, 1981:286] on the samples exhibiting the minority carrier trap signal of Figure VIII-4, an average barrier height, ϕ_b, of 2.71 eV was obtained. The same measurements on the diode represented by the DLTS data of Figure VIII-5 yielded a similarly large barrier height of 2.4 eV. Since the zero field barrier height is equal to the energetic separation between the Fermi level and the valence band

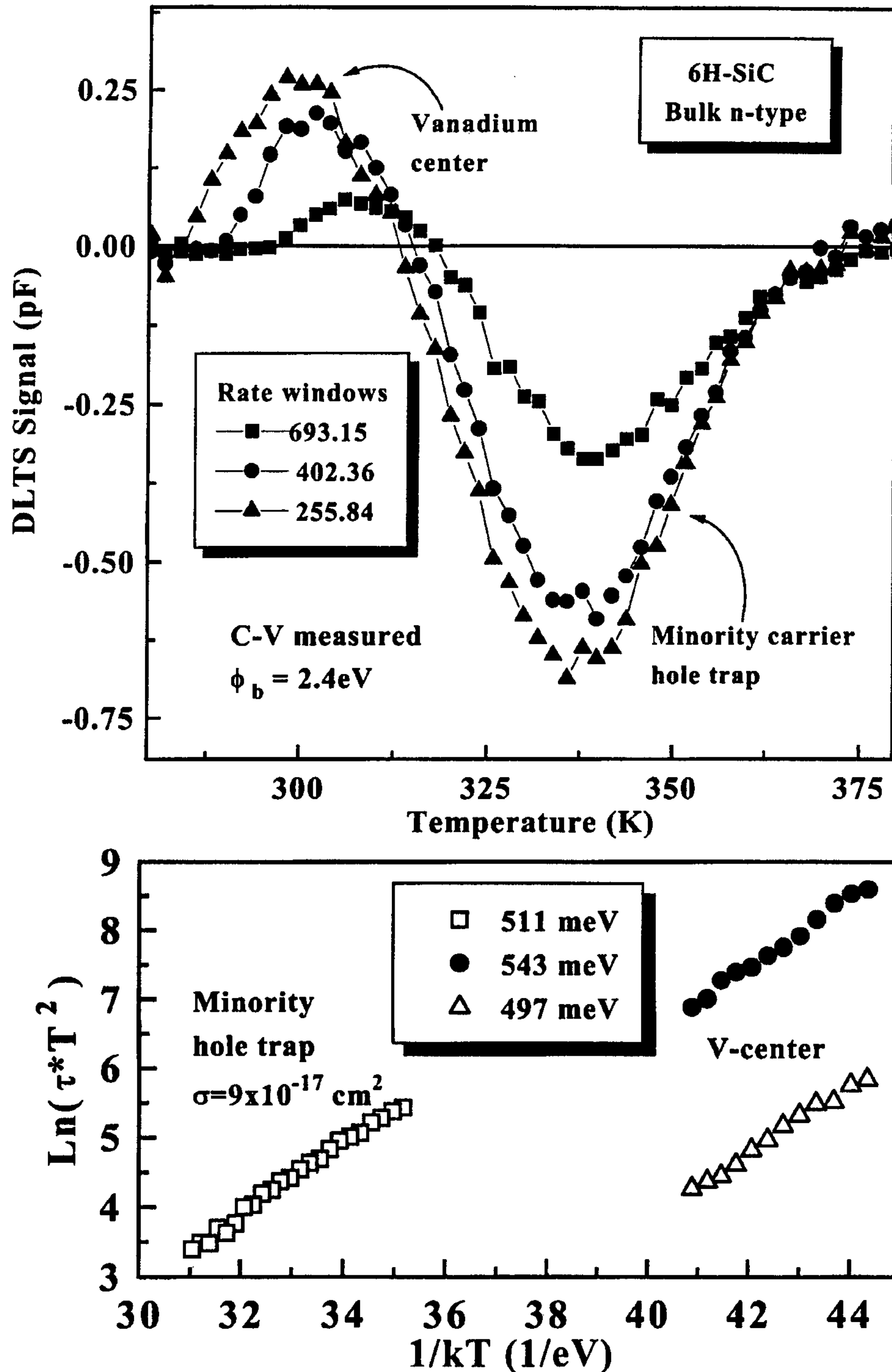

Figure VIII-5. Rate window spectra (a) and Arrhenius analyses (b) illustrating minority carrier trapping in a Schottky device. The majority carrier electron trap shown as the positive peak in (a) is the commonly observed vanadium center in the bulk n-type material. The large concentration hole trap (1.3×10^{16} cm^{-3}) was not frequently observed but serves to illustrate the condition of minority carrier injection in SiC Schottky devices.

edge at the metal-semiconductor interface, this was an indication that the Fermi level was "pinned" in the vicinity of the conduction band edge. Fermi level pinning is usually associated with mechanical surface damage or chemical contamination, which results in high concentrations of states with energy levels in the bandgap [Sze, 1981:246], [Rhoderick, 1978:3]. If this density of surface states is sufficiently large so as to accommodate additional surface charges resulting from a change in the electric field without appreciably altering the occupation level E_f, then we say that the Fermi level is pinned to this density of states. It has been reported that high concentrations of surface states plague p-type SiC MOS device interfaces, resulting in inferior performance [Brown *et al.*, 1993:325]. Reports of n-6H-SiC:SiO_2 interface studies indicate that high densities of surface states are not as prevalent for the n-type material. Additionally, bulk n-type barrier height estimates of the same Ni Schottky metallization on diodes which do not exhibit the minority carrier signal in Figure VIII-5, yielded values consistently in the 1.3 eV range.

With the Fermi level pinned in the vicinity of the conduction band edge, there exists a negligible barrier to the injection of electrons from the metal into the semiconductor. Thus, a potential source of minority carrier injection is realized, and would enable the observation of electron or hole traps in the p-type or n-type material, respectively. Verification of this behavior was obtained by careful surface preparation of new p-type diodes and subsequent characterization.

Several samples were selected from the same bulk, p-type, (0001), 6H-SiC wafers, which were used to fabricate the Schottky diodes exhibiting the deep levels illustrated in

Figure VIII-4, and prepared for device processing. The original set of samples exhibiting Fermi level pinning were prepared using a standard 4-step solvent degreasing procedure (TCE, acetone, isopropyl, H_2O) followed by a 4-step acid cleansing process (HF, H_2SO_4, HCl, H_2O). The new sample sets were processed using the sacrificial oxide deposition/removal procedure detailed as recipe Ia in Appendix C. In this process, a fresh SiC surface is exposed subsequent to the growth and removal of a 1000 Å thermally grown SiO_2 layer. The samples were then immediately loaded into a high vacuum Denton® evaporation system for deposition of the Al Schottky diode metallization.

Figure VIII-6 illustrates the DLTS spectrum resulting from diodes receiving this alternative sample cleaning procedure. Immediately apparent is the almost complete absence of the dominant minority carrier peak seen in Figure VIII-4, and the undisturbed presence of the two majority carrier hole traps at 882 and 496 meV. This result provides strong supporting evidence for the role of Fermi-level pinning as the source of minority carrier injection into the p-type material. Furthermore, C-V profiling data indicated that the alternatively processed samples had significantly lower barrier heights with an average value in the 1.42 eV range. Although the source of contamination is unknown, it would appear that high concentrations of surface defects, with a peak density near the conduction band edge, are responsible for the minority carrier injection, and enabling observation of the 780 meV p-type electron trap and the 511 meV n-type hole trap.

VIII-III. Deep Levels in Epitaxial 6H-SiC

In addition to the acquisition of n- and p-type bulk wafer material we obtained

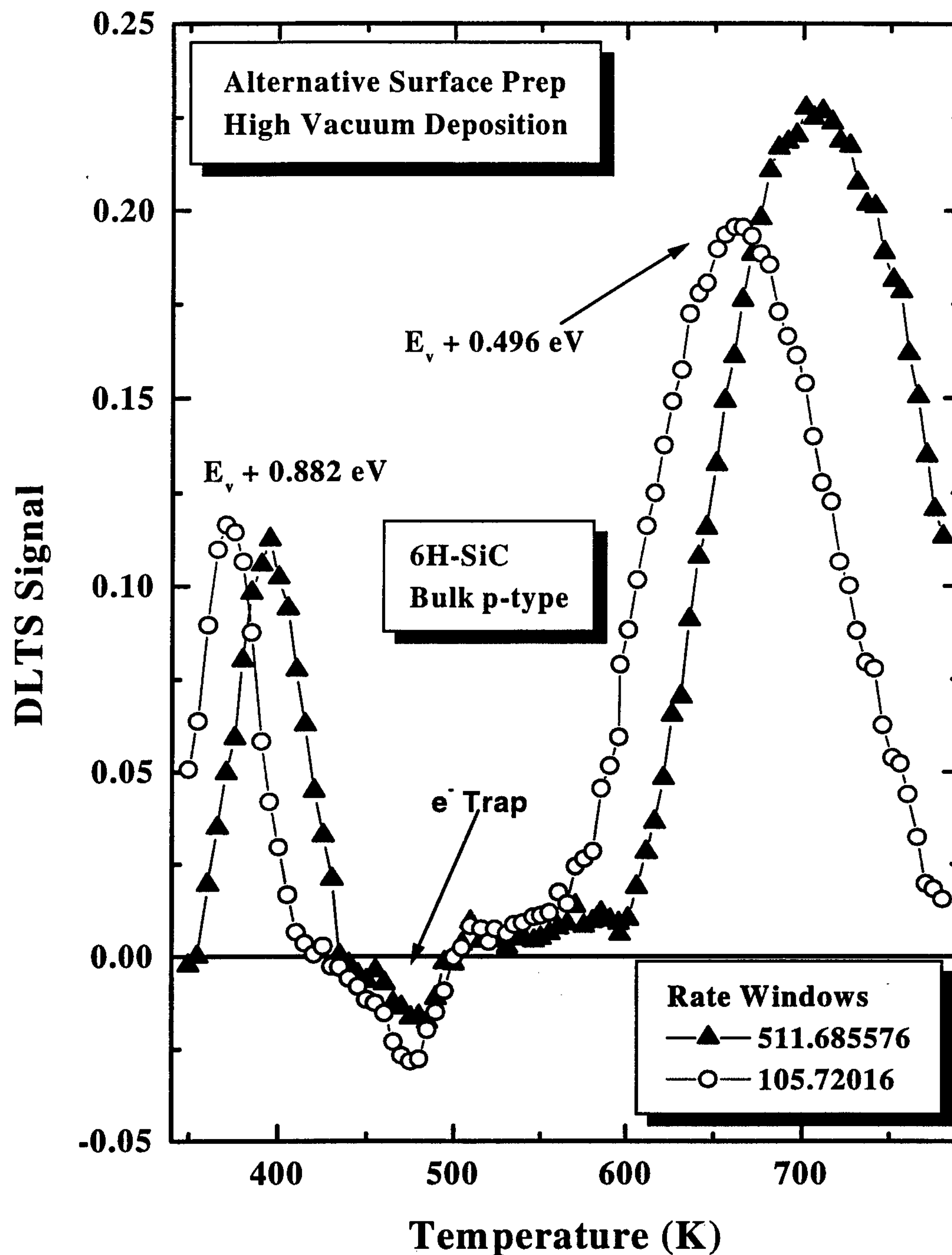

Figure VIII-6. Constant-voltage DLTS rate window spectra of the bulk p-type SiC Schottky diodes fabricated using the alternative sample cleaning process recipe Ia of Appendix C. Of significance is the near elimination of the 780 meV minority carrier electron trap seen to dominate in Figure VIII-4. These results support the role of Fermi level pinning as the source of minority carrier injection in those devices.

several wafers with 1 mm epitaxial layers grown by CREE Research, Inc. This growth was performed using metal-organic-chemical-vapor-deposition (MOCVD), and doping concentrations for both n- and p-type layers were in the 10^{17} cm^{-3} range.

Measurements of n-type epitaxial SiC layers revealed four new majority carrier traps at energies of E_c-0.89, E_c-1.3, and E_c-1.1 eV with temperature independent capture cross sections of $2x10^{-16}$, $9x10^{-13}$, $5x10^{-14}$ cm^2, and trap concentrations of $5.1x10^{13}$, $1.8x10^{14}$, and $2.3x10^{14}$ cm^{-3}, respectively. Figure VIII-7 shows the characteristic rate window plots of typical runs on the n-type epitaxial material. The 1.1 and 1.3 eV levels represented by the high temperature spectral peaks are the largest ionization energy centers observed during this entire study, and illustrates the enhanced characterization capability of the extended DLTS temperature range. On the other hand, these levels represent less than 1/2 of the 6H-SiC bandgap, and deep centers with larger ionization energies cannot be characterized due to the practical limit of thermal emission rate detection, even with an 800 K capability. As seen in the inset, there was also a shallower observed level present in the majority of diodes selected from several wafers. This center corresponds to the previously discussed 612 meV center identified in Chapter VII as possessing an MPE capture mechanism. The high temperature limiting capture cross section for this trap was $7.3x10^{-16}$ cm^2, and is listed on the figure along with the thermal ionization energy level. A field enhanced emission rate was not observed for the 612 meV level, indicating the electronic charge of the filled trap to potentially be in the ionized acceptor state, and neutral when empty.

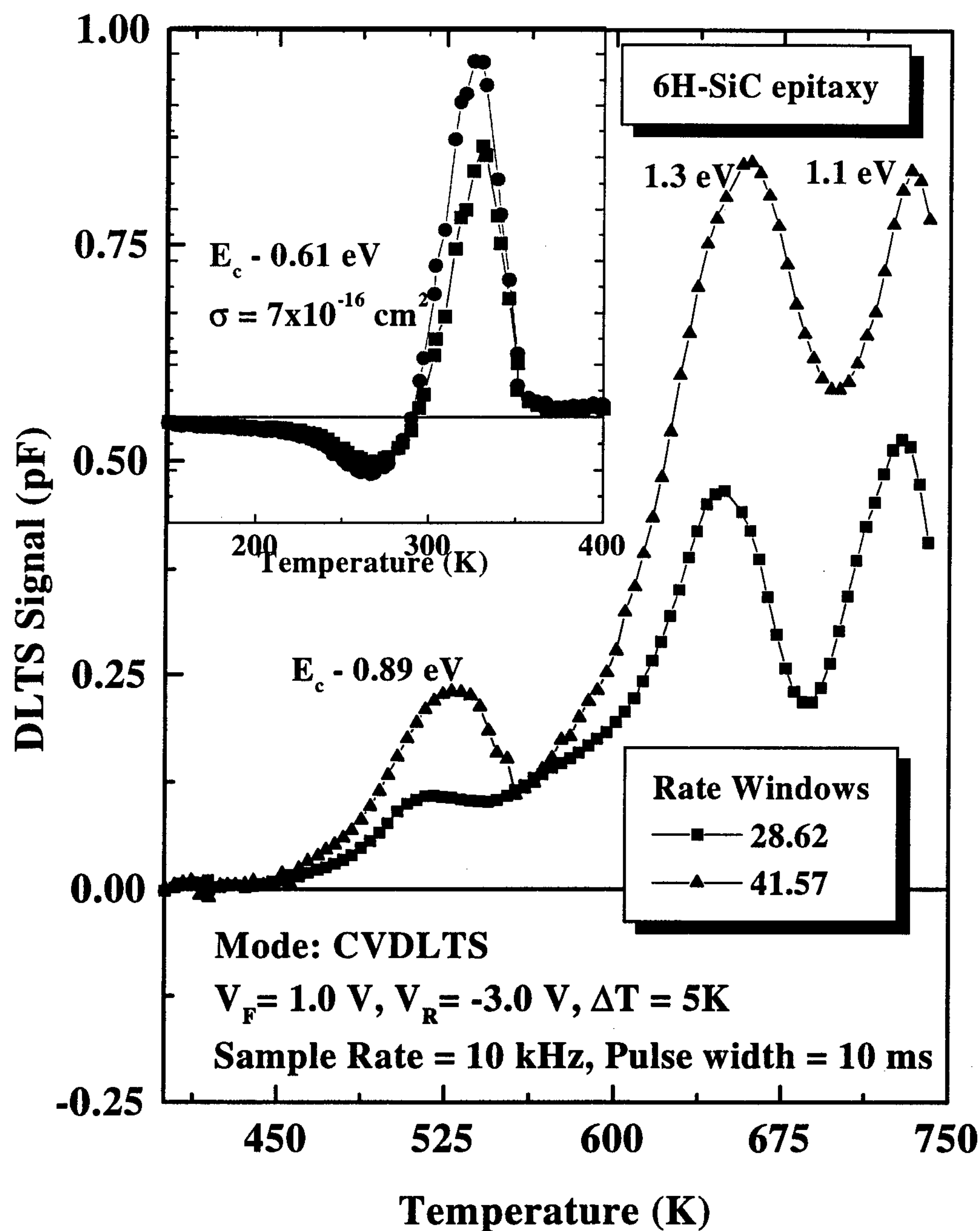

Figure VIII-7. CVDLTS rate window representation of the deep level electron trapping centers observed in the n-type 6H-SiC epitaxial material. The extended temperature range of DLTS experimental hardware is seen to enable the characterization of two very deep defects in this material. The plot in the inset is a lower temperature occurring peak in the n-epitaxy, and is the same center described in the Chapter VII discussion of MPE centers.

As is observed for the p-type bulk material, the p-epitaxial 6H-SiC also exhibits an energetically rich spectrum of deep trapping levels. Numerous hole trapping centers, with thermal ionization energies from 1.0 to 0.3 eV, were found to occur randomly in the diodes characterized. DLTS scans on a large number of Schottky diodes from six different wafers led to the observation of three centers which occurred in over 80% of the devices. The positive multiple DLTS peaks illustrated in Figure VIII-8 are from a typical sample possessing these centers. As shown in the figure, the peaks labeled A, B, and C correspond to ionization energies of 380, 473, and 789 meV above E_V, respectively. The capture cross sections for these traps were temperature independent, and measured to be $4x10^{-19}$, $2x10^{-20}$, and $1x10^{-17}$ cm^2 for the A, B, and C hole trapping levels, respectively. In this case, the multiple peaks were resolved in the analog signal using rate windows listed on the plot. Trap parameters were however, always determined using the DIGLS exponential fits of the capacitance transients at each temperature. The concentrations of the defects, which were estimated from the heights of the rate window peaks and from transient amplitude fit data, were in the range of 10^{14}, 10^{14}, and 10^{13} cm^{-3} for A, B, and C, respectively. These concentrations are significantly higher than would be expected for quality epitaxial material with minimal atomic impurity incorporation. Thus, a link to structural defects or defect-impurity complexes is suggested.

VIII-IV. Deep Level Sources

The presence of numerous deep trapping levels in the bandgap of the 6H materials investigated is indicative of significant concentrations of impurity and structural defects.

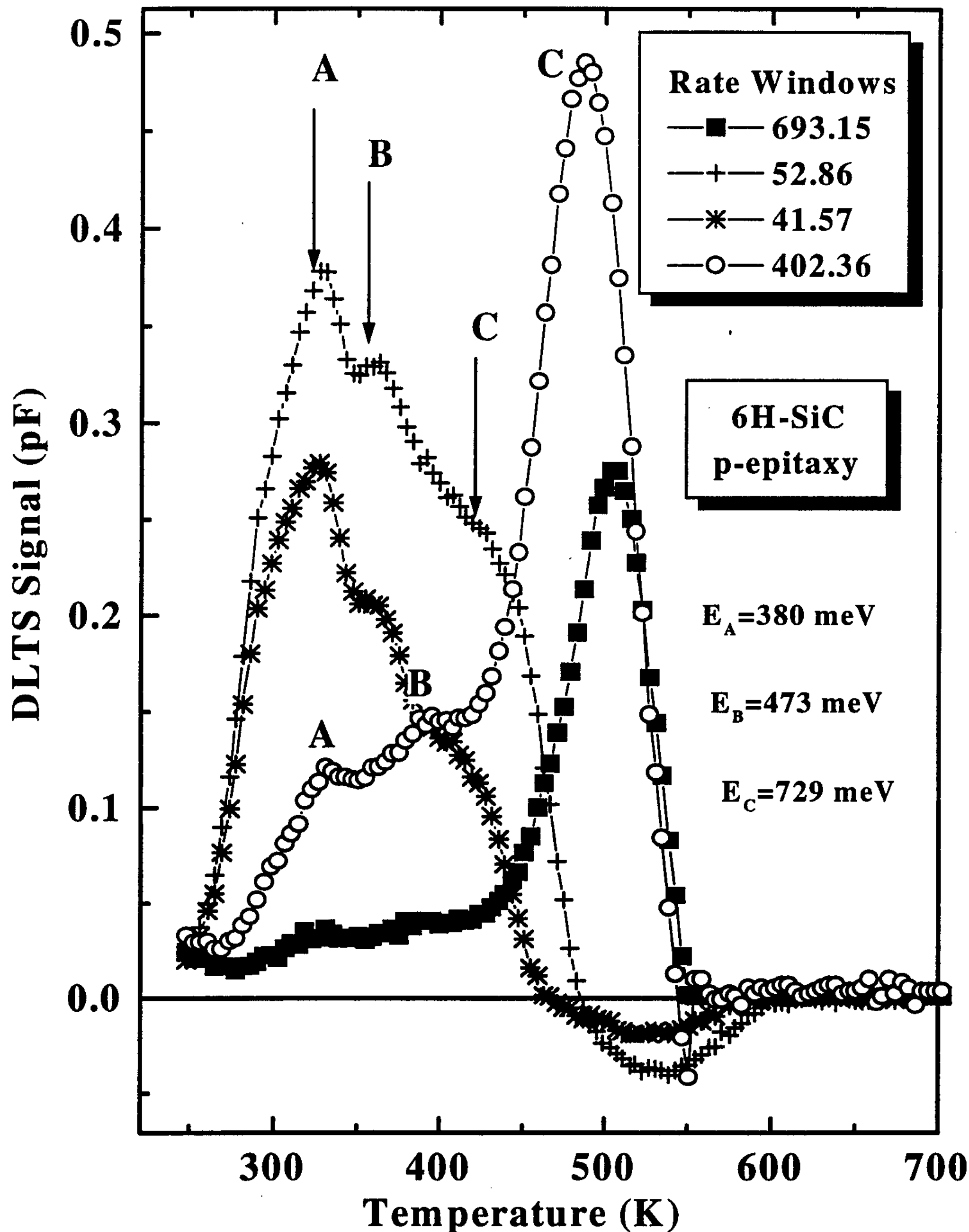

Figure VIII-8. Epitaxial p-type 6H-SiC DLTS rate window spectrum, illustrating three closely spaced emission peaks frequently observed in the p-type epitaxy. The resolved energy levels for the A, B, and C labeled peaks were determined to be 380, 473, and 729 meV above the valence band, respectively. The level A, was occasionally observed in diodes not exhibiting the B and C levels. Levels B and C were always present in pairs however, the concentration ratio of 3.5:1 and vastly differing cross section values do not suggest an inequivalent site pair.

In order to determine if there existed appreciable densities of elemental impurities, which could potentially induce deep level defects in the 6H-SiC bulk material, secondary ion mass spectrometry (SIMS) characterization was performed on samples taken from the same wafers that DLTS specimens were obtained. To eliminate the possibility of impurity contributions from handling or sample processing contamination, several angstroms of SiC material was in-situ sputter removed prior to SIMS data collection. Since there exist very few SIMS impurity calibration factors for correlating atomic mass signal counts with elemental concentration in SiC, an estimate was used based on available data for elements in Si. For example, zirconium concentrations were estimated using the known relative sensitivity factor (RSF) for boron in 6H-SiC. Using available RSF data for zirconium and boron in Si given as $RSF\ Zr_{Si} = 30xRSF\ B_{si}$, the concentration of Zr in 6H-SiC was obtained accordingly, since the RSF for B in SiC is known. The results of these measurements are summarized in Table VIII-3, but only for those atomic mass identifications which could be made definitively. As mentioned earlier in this chapter, the concentration of V in Table VIII-3 agreed rather well with the DLTS estimated concentration of the vanadium deep level in bulk n-type 6H-SiC.

Table VIII-3. Atomic concentrations of impurity species, identified using secondary ion mass spectrometry, as significant constituents in the 6H-SiC bulk wafers. The large concentrations of transition metals are likely candidates as deep level activators. Currently, no information exists regarding the electrical activity of these elements in SiC, with the lone exception of vanadium. Concentrations are given in units of cm^{-3}.

Mo	Zr	Ge	Cr	Cu	Ti	Ni	V
$3.3x10^{16}$	$5.6x10^{17}$	$1.1x10^{18}$	$1.2x10^{17}$	$1.5x10^{17}$	$5x10^{17}$	$1.6x10^{18}$	$1x10^{16}$

On the other hand, SIMS analysis of the epitaxial materials did not reveal the presence of any significant concentrations of the elements listed in Table VIII-3. This is to be expected for epitaxial material grown in highly controlled MOCVD reactors. The only unintentional species, which were commonly occurring in these materials, were found to be low level concentrations of boron and aluminum in the n-type epitaxy. The B and Al densities were determined to be below 10^{13} cm^{-3}. This is undoubtedly due to residual background levels of these common p-dopant species in the epitaxial growth chambers. This leads us to conclude that the majority of deep level traps observed in these epitaxial materials are closely correlated with structural or lattice defects, which are known to occur in significant concentrations. Micropipes, which are long range stacking voids, dislocations, inclusions of other polytypes, and stacking faults are all known impediments to the homogeneity and quality of the material being produced. Thus, we expect a connection between the large numbers of observed deep levels and these crystalline flaws, especially when considering the large concentrations found in atomically "clean" epitaxial material. This is even more relevent when considering that numerous traps which were found to occur very infrequently, and often inconsistently even across a 1/2 cm^2 sample area. Elemental impurity incorporation is typically much more homogenous and uniform when present in a semiconductor lattice.

Deep level characterization of 6H-SiC, bulk and epitaxial material of both conductivity types, was performed at temperatures up to 800 K for the first time, resulting in the observation of several new electrically active levels in the band gap. Figure VIII-9 is an illustrative summary of the newly identified deep trapping centers found in the 6H-

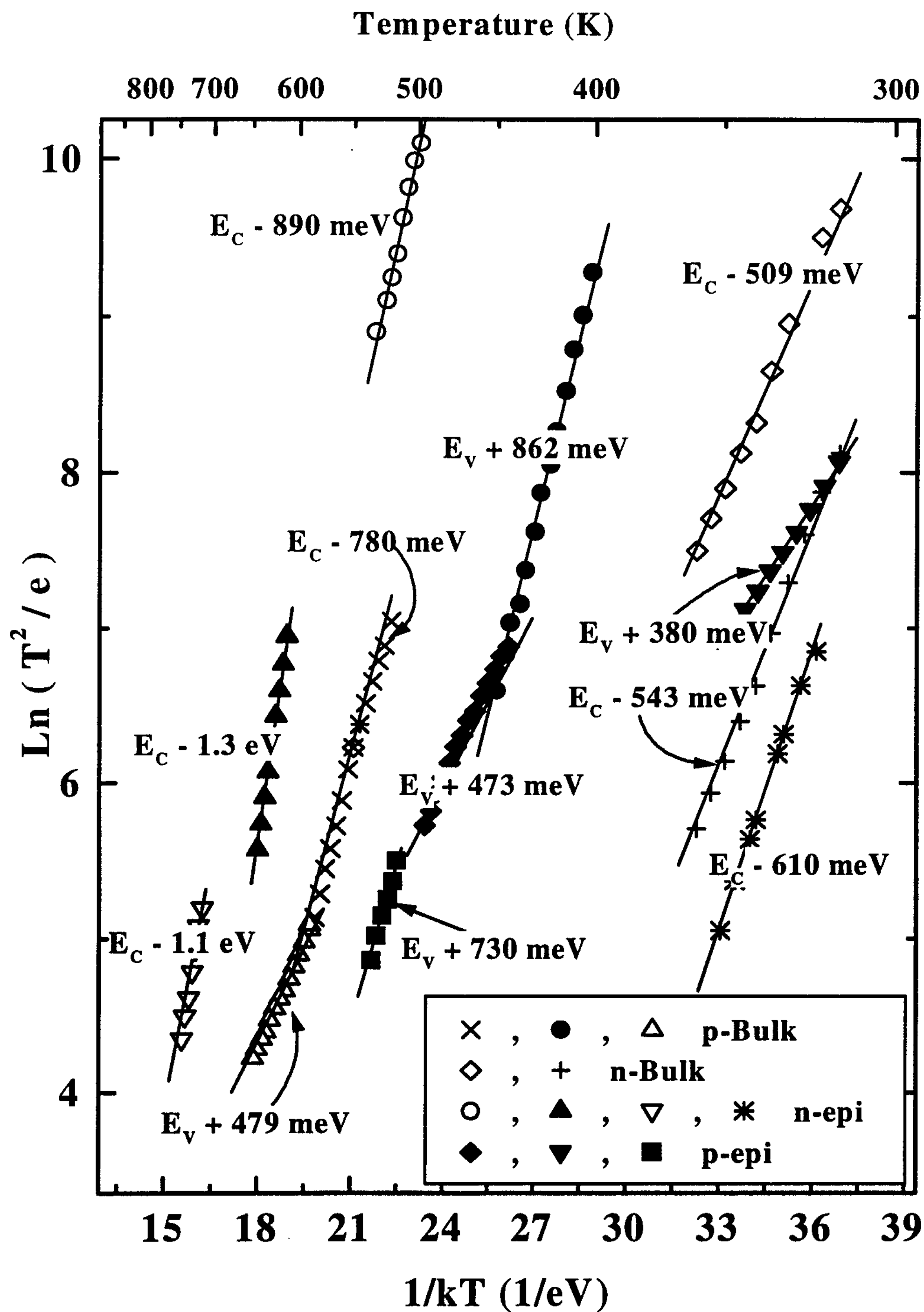

Figure VIII-9. Arrhenius activation energy summary plot of the newly identified and unreported deep traps found in the 6H-SiC bulk and epitaxial materials. Numerous additional defect levels were observed, however, the trapping centers shown in the figure were found to be consistently occurring in each of the material types illustrated by the symbol legend.

SiC materials. None of the levels shown in the figure or described in this subsection have been previously reported. SIMS analysis of the sample wafers revealed several transition metals in significantly high concentrations. These elements are well known deep level impurities in other semiconductors, and may very well play a role in the several centers identified. On the other hand, SiC is plagued by structural imperfections related to its polytypic nature, and a connection to crystalline flaws is indicated by the large density centers found in the epitaxial materials. Simulations of the free carrier concentrations and DLTS transients in 6H-SiC reveal that, even with an 800 K capability, only levels approaching midgap may be observed. This conclusion is supported by the fact that a 1.3 eV level was the largest ionization energy measured. The observation of anomalous trap potential effects and minority carrier generation mechanisms in Schottky devices illustrate a complex interaction between the electronic impurity potential and the crystal. With the study of deep levels in SiC having only recently begun, there exists a great deal of theory and experimentation to be accomplished in order to better understand the sources, how to eliminate them, and device related effects of the flaws in this material. The following section illustrates the dominance that deep level traps and recombination centers can have on the current transport and junction characteristics of power rectifiers built on the 4H polytype of SiC.

VIII-V. Defect Dominant Junction Characteristics of 4H-SiC p^+/n Diodes

In this section, we report results on electrical characterization of the junction characteristics and current conduction mechanisms of state-of-the-art p^+/n diode structures fabricated on 4H-SiC. Forward and reverse current-voltage-temperature (I-V-

T), capacitance-voltage-temperature (C-V-T), deep level transient spectroscopy (DLTS), electroluminescence (EL), and reverse breakdown measurements were all performed to correlate the observed junction characteristics with defects present in the material. It is show that while improvements to material technology have been significant with steady progression, there still exist significant concentrations of structural and impurity related defects which hamper the yield and performance of devices built on these materials.

Initially, forward and reverse current-voltage (I-V-T) measurements of MOCVD grown 4H-SiC p^+/n diodes were compared to classical recombination-generation theory over the temperature range of 100 to 750 K. Activation energy calculations from the forward bias p^+/n diode empirical data indicate that the I-V characteristics of the well-behaved devices follow a classical recombination dominant transport mechanism. Ideality factors were determined to be in the range of 1.85 to 2.09, and the forward activation energy found to be nearly ideal at E_A=1.56 eV. A majority of the devices tested under forward bias conditions were, however, found to exhibit significant leakage current components due to a tunneling dominant mechanism at forward biases of up to 2.2 volts for turn-on voltages in the 2.5 to 3.0 V range. Subsequently, DLTS was performed on the diode structures over the same wide temperature range, with deep level trap information correlated to the results obtained from reverse I-V-T characterization. Deep level defects at energies between 200 meV and 856 meV were identified from the DLTS data, and are implicated in the tunneling dominated current conduction. Additionally, electroluminescence characterization of the p^+/n rectifying devices revealed a donor to deep-acceptor pair (DAP) recombination radiation feature, which could be

correlated to a damage related deep level. Intrinsic deep levels, common to all devices tested, were investigated as possible reverse bias tunneling paths in relation to the observed lack of an avalanche mechanism for all of the 4H-SiC diodes investigated.

The SiC diodes used in our study were mesa isolated structures, 3° off-axis MOCVD grown on the (0001) surface of n-conductivity, 4H polytype wafers. Asymmetric abrupt p^{+}/n junctions were obtained by doping the p-type (Al) and n-type (N) regions to approximately $1x10^{19}$ and $5x10^{15}$ cm^{-3}, respectively, as shown in Figure VIII-10. Additionally, a $1x10^{16}$ cm^{-3} N doped buffer layer was grown on the 4H wafer surface. Aluminum and Ni standard ohmic contact metalliztions were utilized on the p-

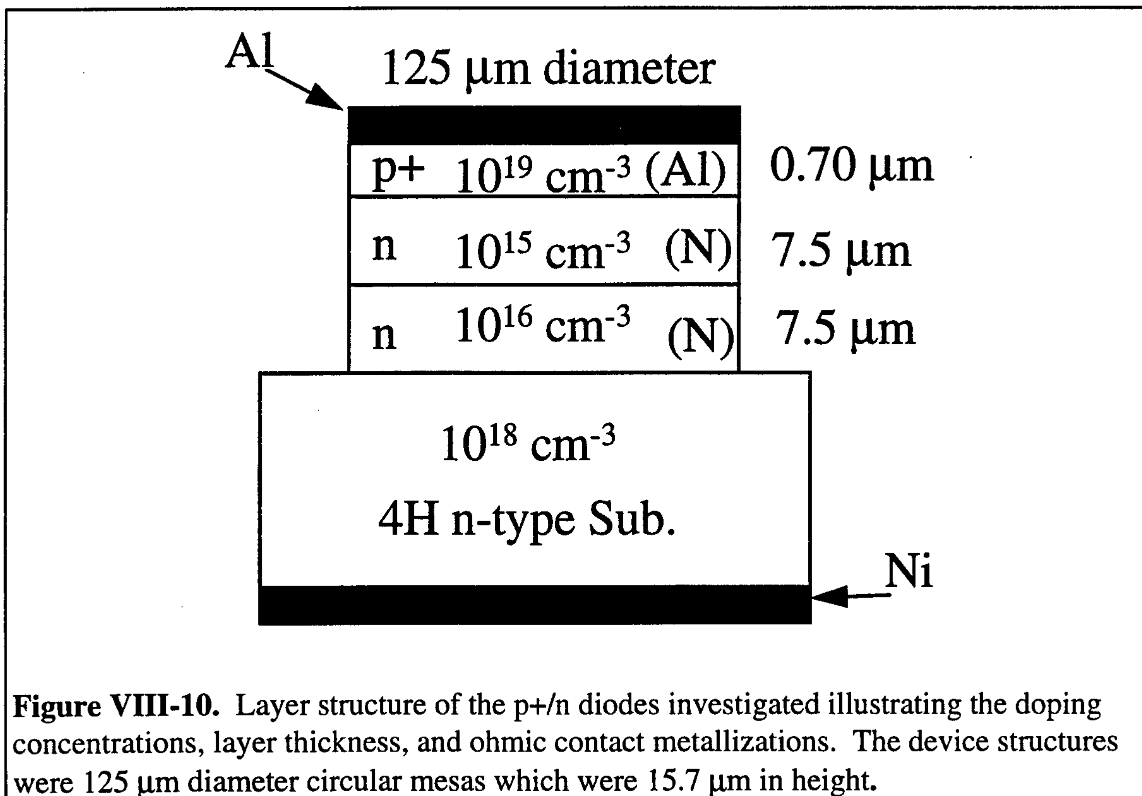

Figure VIII-10. Layer structure of the p+/n diodes investigated illustrating the doping concentrations, layer thickness, and ohmic contact metallizations. The device structures were 125 μm diameter circular mesas which were 15.7 μm in height.

and n-type surfaces, respectively, and are also illustrated in the figure. These devices were grown and fabricated by CREE Research, Inc. of Research Triangle Park, NC.

Temperature dependent current-voltage measurements were performed in the DLTS system closed cycle He refrigerated cryostat, enabling measurements up to temperatures of 800 ± 0.1 K during a single scan. Fully automated computer controlled instrumentation and data acquisition capabilities allow the performance of a wide range of detailed electrical characterizations in addition to DLTS. The software developed to automate and perform the I-V and I-V-T experiments is listed in Appendix C. Current-voltage data acquisition instrumentation consisted primarily of a Keithley 236 source measure unit (SMU).

Current transport mechanisms dictating the junction characteristics of Schottky, p-n, or other rectifying barrier can be identified, and correlated to observed current versus applied voltage experimental data. In this manner, current conduction mechanisms can be determined for a specific junction. Additionally, defect related information relating to the dominant recombination and generation centers can also be ascertained, if the I-V temperature dependence is investigated.

I-V and I-V-T analyses begin with a model for the transport of carriers across the potential barrier formed by oppositely doped regions, metal-semiconductor interfaces, or the abrupt transition between heterogeneous semiconductor materials. During this work, forward biased current conduction characteristics were found to compare favorably with the classical Sah-Noyce-Shockley (SNS) [1957:1228] recombination-generation theory. Forward biased I-V data were fit to this model, which in analytic form is given by

$$I = I_{Diff} \exp\left[\frac{qV}{A_1 kT}\right] + I_{Rec} \exp\left[\frac{qV}{A_2 kT}\right] + I_0 \exp[BV] \ , \qquad \text{[VIII-2]}$$

where I is the total forward bias dark current, and V is the applied voltage. The first term in Equation VIII-2 represents the classic Shockley diode equation, which accounts for the diffusion of carriers across the junction barrier [Sze, 1981:79]. The second term represents the current component due to recombinations of electrons and holes at deep defect levels within the junction depletion region. The last term describes the current arising from quantum mechanical tunneling across the depletion region. The expression in Equation VIII-2 is written assuming V >> kT/q so that the general term [exp(qV/AkT)-1] is simplified by the dominance of the exponential.

The primary difference between the three mechanisms of conduction current are found in their dependence upon temperature, voltage, and bandgap. The exponential arguments in the first and second terms contain the so-called "ideality" factors, A_1 and A_2, which equal 1 for ideal diffusion and approximately 2 for recombination via traps near midgap, respectively. The tunneling factors I_0 and B are empirical fitting parameters, but have a theoretical basis related to tunneling effects [Hovel, 1975:253]. Tunneling currents are theorized to be due to junction defects or damage and/or leakage at the device periphery. Expressions for the exponential coefficients of the first and second terms are given as [Sze, 1981:79-92]

$$I_{Diff} = qS\left(\frac{D_n n_p}{L_n} + \frac{D_p p_n}{L_p}\right) = J_{Diff} S \qquad \text{[VIII-3]}$$

and

$$I_{Rec} = \frac{qSn_iW_d \times f(b)}{\left(\tau_{p0}\tau_{n0}\right)^{1/2} \frac{(V_{bi} - V)q}{kT}} = J_{Rec}S \ , \qquad \text{[VIII-4]}$$

where the factor f(b) is a function of the recombination center ionization energy, ΔE, and the electron and hole minority carrier lifetimes τ_{n0} and τ_{p0}, respectively. The factors D_n and D_p, n_p and p_n, L_n and L_p are the diffusion coefficients, minority carrier densities, and the diffusion lengths of electrons and holes, respectively, and S is the diode area. All other factors carry their previous definitions. If we assume an abrupt, asymmetrically doped junction (p^+/n), then depletion will occur primarily in the n-type material and $n_p << p_n$. Using these approximations and the minority carrier density expression ($p_n = n_i^2/N_D$), we can write the exponential coefficients to explicitly reflect their temperature dependence as

$$I_{Diff} = qS\left(\frac{D_p p_n}{L_p}\right) = qS\left(\frac{D_p}{L_p}\right)\left(\frac{n_i^{\ 2}}{N_D}\right) \propto T^3 e^{-E_G/kT} \qquad \text{[VIII-5]}$$

and

$$I_{Rec} \propto T^{5/2} e^{-E_G/2kT} . \qquad \text{[VIII-6]}$$

Thus, we have the desired expressions which are used to describe the I-V dependence upon temperature as well as the applied bias. Numerical values for I_{Rec} and I_{Diff} are fitting parameters obtained by numerically applying the model of Equation VIII-2 to the experimentally obtained data. Arrhenius plots can then be constructed to yield information about the temperature dependence of the current conduction mechanisms.

Reverse bias I-V-T measurements can be used to estimate the ionization energy of deep levels, which limit reverse bias dark current if the leakage current is trap dominated [Reinhardt, 1996:5763]. If reverse leakage current, I_{Rev}, is trap dominated, then a thermally generated depletion region component, I_{Gen}, will describe carrier transport. Neglecting other components, if $I_{Rev} = I_{Gen}$, a simple expression can be written which defines the temperature dependence of the diode's reverse leakage current

$$I_{Rev} \propto W_d \exp\left(\frac{-E_a}{kT}\right), \qquad \text{[VIII-7]}$$

where

$$E_a = \begin{cases} E_C - \Delta E & \text{if } \Delta E > E_i \\ \Delta E - E_V & \text{if } \Delta E < E_i \,. \end{cases} \qquad \text{[VIII-8]}$$

E_a is the activation energy of the generation center, E_i is the intrinsic Fermi level, E_C and E_V are the conduction and valence band extrema, respectively, and W_d is the depletion region width. Details of the I-V-T hardware and procedures are found in Appendix B.

VIII-V-1. Forward I-V-T of 4H-SiC p^+/n Diodes. Forward biased current conduction characteristics of the 4H-SiC diodes were first compared to the classical SNS recombination-generation theory. Typical forward biased I-V data taken at 300 K on the 4H-SiC diodes is illustrated in Figure VIII-11 for both a well-behaved and a leaky diode with a significant shunt leakage characteristic. Solid lines in the figure are numerical fits to Equation VIII-2.

As can be seen from the figure, the 4H-SiC diodes exhibit classical forward bias characteristics, including the dominance of recombination over ideal diffusion conduction

in the well-behaved devices. This is as expected for large bandgap (E_G) materials when comparing Equation VIII-5 and Equation VIII-6. An average value for I_{rec}/I_{diff}, obtained from the numerical fits for several diodes exhibiting ideal I-V characteristics, similar to that shown in the figure, was found to be in the 10^{25} range at T=300 K, decreasing to 7×10^{12} at 700 K. The values of the diode ideality factors are illustrated next to their respective conduction regions in the figure. The A_2 factor of 2.09, which corresponds to recombination in the space charge region (SCR), is indicative of recombination via traps near the center of the bandgap. Although it is difficult to obtain due to the dominance of recombination currents at lower voltages and due to series resistance roll-over effects at larger forward biases, the diffusion ideality factor, A_1, was observed to be consistently greater than the ideal Shockley value of unity. This is attributable to current conduction due to both diffusion and recombination processes [Sze, 1981:92], and are the first indications as to the presence of significant concentrations of deep traps and/or recombination centers dominating I-V characteristics along with the large number of diodes exhibiting shunting behavior. In fact, the majority of devices characterized during our study revealed that the shunted type leaky diode characteristic was dominant for over *70%* of the devices selected from the 1.125" wafer.

Temperature dependent forward I-V data were taken to identify dark current mechanisms in the p^+/n diodes and to compute the activation energy for the $A_2 \approx 2$ current

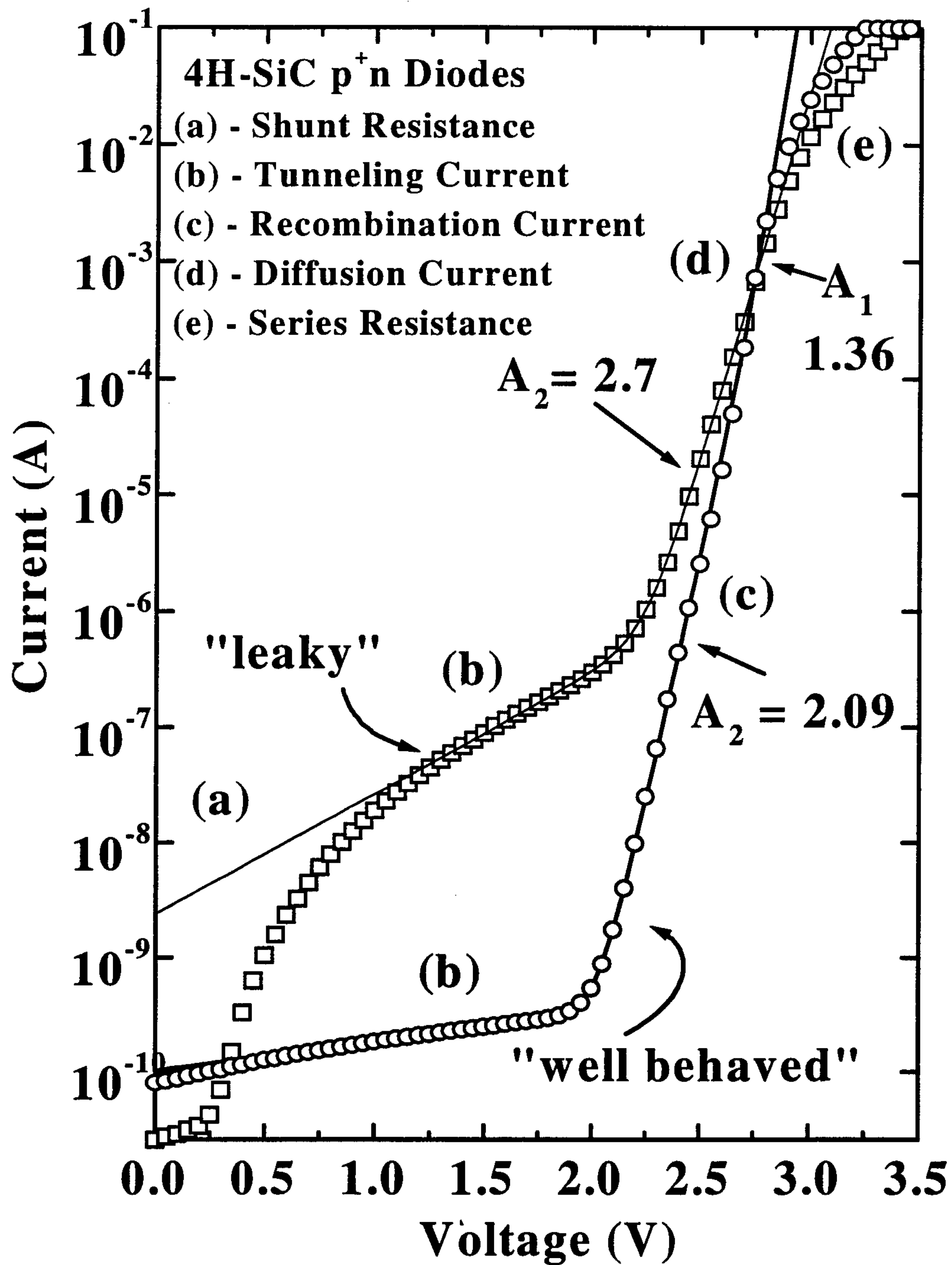

Figure VIII-11. Forward I-V characteristics for typical near ideal (o) and strongly shunted (□) p^+/n 4H-SiC diodes taken at 300 K. Solid lines are fits to Equation VIII-2, and indicate the compliance of these devices with classical SNS recombination theory. Each of the various transport mechanisms are labeled and defined on the figure as (a) through (e). The values for the ideality factors, A_1 and A_2, are listed next their respective recombination and diffusion regions as illustrated on the plot.

component. The I_{rec} value is obtained from fits to each isothermal curve, with I_{rec} expressed as $I_{rec} \propto T^{5/2}\exp(-E_A/kT)$. Then the activation energy is obtained from the Arrhenius slope by plotting $\ln(I_{rec})$ versus 1000/T. Figure VIII-12 illustrates a typical temperature dependent series of I-V data curves on a well-behaving diode along with the solid line fits to the diffusion and recombination components of conduction. The horizontal region of the I-V curves for the low bias voltages occurs due to the nonzero conductivity of the space-charge or depletion region. This results in the observed V/R_{sh} characteristic, where R_{sh} is predicted to decrease with increasing temperature [Reinhardt, 1994:5763], which is consistent with the data of Figure VIII-12. The values obtained for A_2 from I-V-T data on typical well-behaved diodes were found to be temperature independent as predicted by SNS recombination theory, and decreased roughly 7% from 250 K to 700 K.

Figure VIII-13 illustrates a typical family of I-V-T curves for one of the more frequently occurring leaky diodes. A well-behaving diode characteristic collected at 300 K is included for comparison purposes. The shunting current in the isothermal series of data plots was found to increase exponentially as $I_0\exp(BV)$. Furthermore, the slope is almost constant, and only slightly temperature dependent. This trend is predicted by tunneling-recombination theory and results in the third term of Equation VIII-2 [Riben and Feucht, 1966:1055].

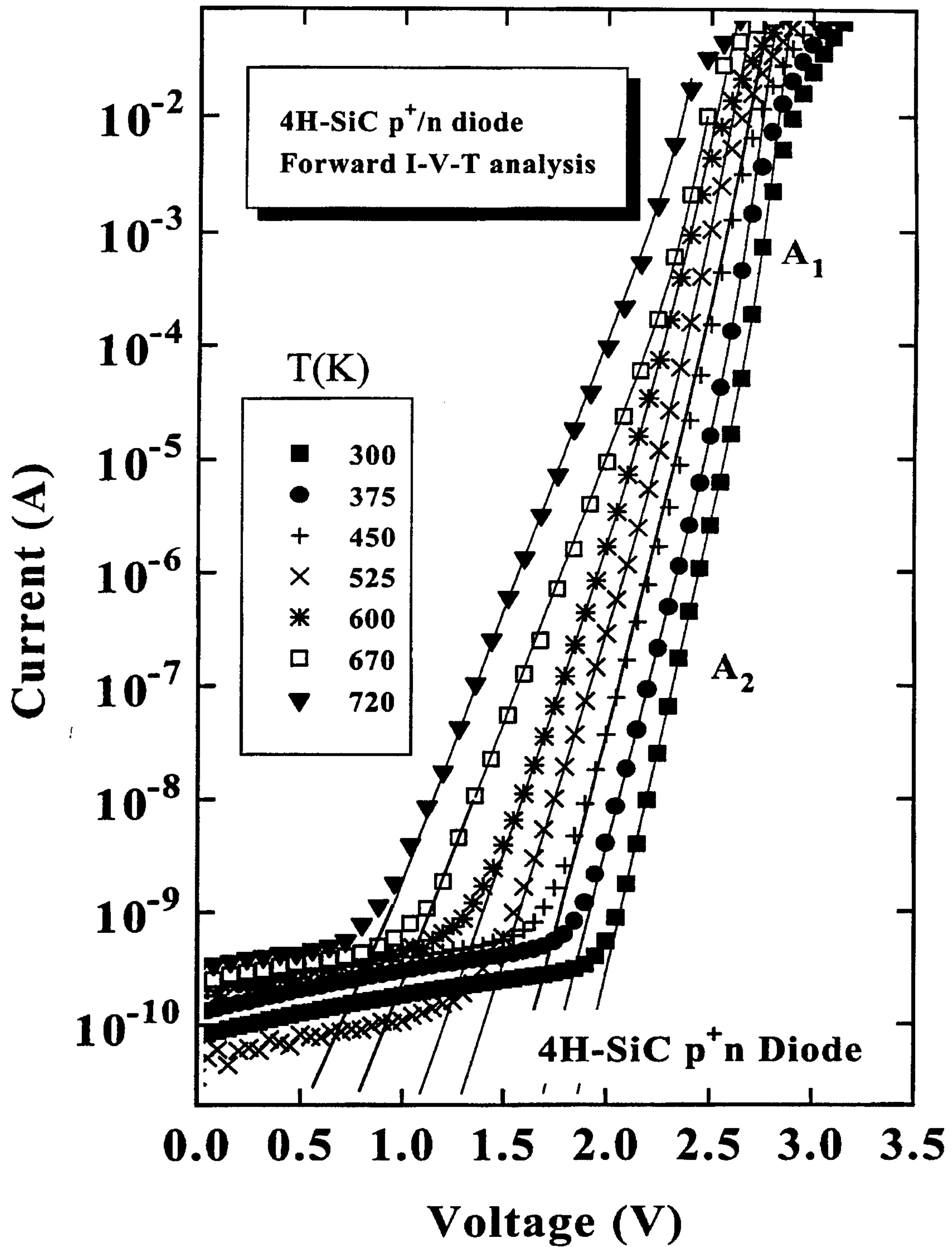

Figure VIII-12. Temperature dependent forward bias I-V family of curves for a typical well-behaved 4H-SiC p^+/n rectifier. The solid lines are fits to the SNS theory of Equation VIII-2. The data is used to identify the temperature dependence for the various transport mechanisms, and to obtain the activation energy of the A_2 recombination mechanism.

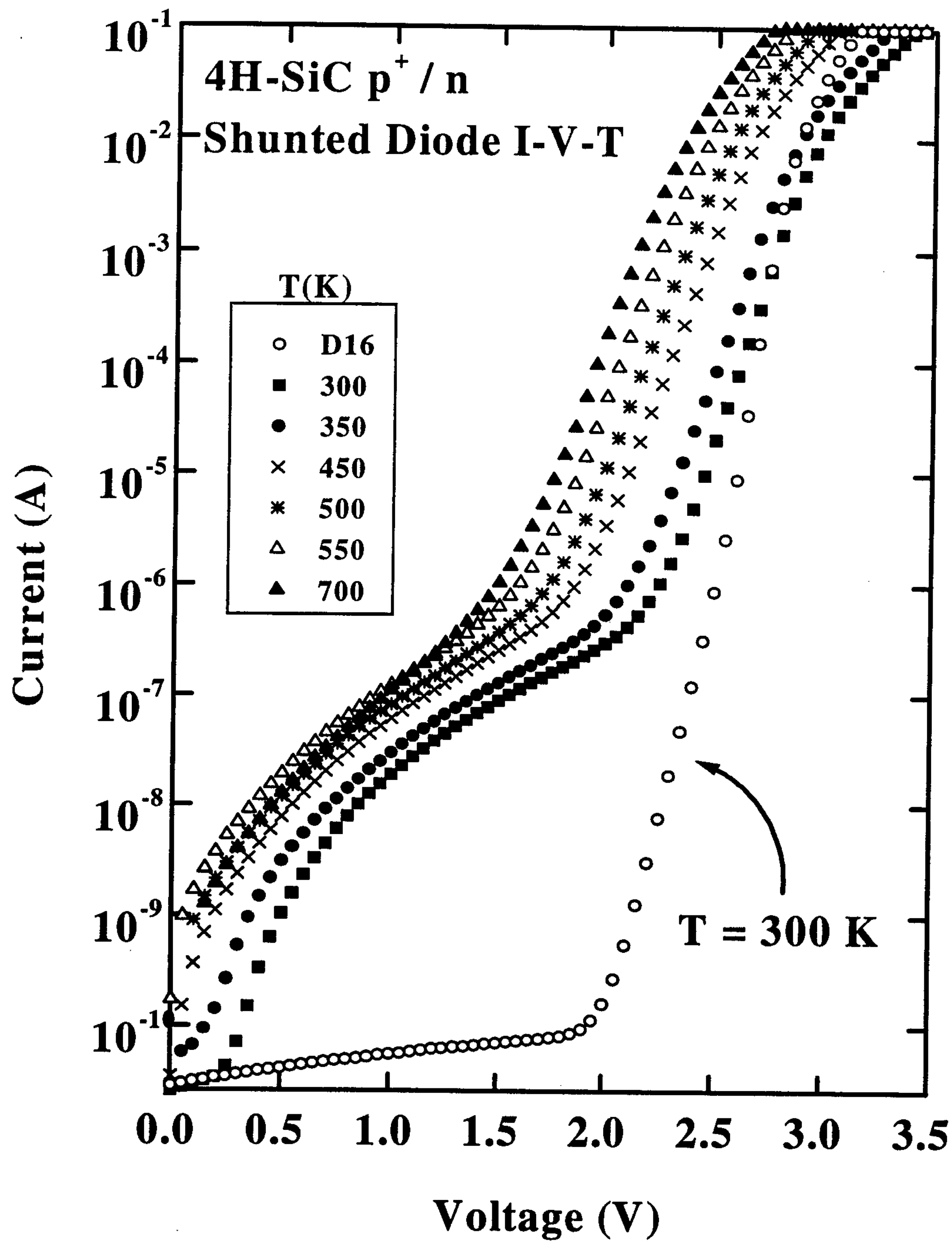

Figure VIII-13. Forward I-V-T series of curves for a shunted or leaky 4H-SiC p^{+}/n diode. The figure also includes a well-behaved 300 K I-V characteristic for comparison. As predicted by tunneling theory, the slope of the shunted region, corresponding to the third term Equation VIII-2, between 0.5 and 2.0 volts is relatively independent of temperature.

The linear region (c) of the well-behaved I-V characteristic of Figure VIII-11 is due to carrier recombination in the space charge region. The slope of the I-V curves associated with the recombination mechanism increases with decreasing temperature in accordance with the factor $\exp(qV/A_2kT)$ in Equation VIII-2. As indicated above, the activation energy for the recombination mechanism is obtained by comparing an Arrhenius slope to the exponential argument E_A/kT. When transport is controlled by ideal recombination, $E_A = E_{G0}/kT$, where E_{G0} is the bandgap of 4H-SiC at T=0 K. The estimated value of the 4H-SiC bandgap is given as 3.265 eV [Madelung, 1991:48], as obtained from low-temperature photoluminescence measurements.

Figure VIII-14 illustrates an activation energy Arrhenius plot for six p^+/n diodes with well-behaved I-V characteristics. As seen by the average value of E_A=1.56 eV listed on the plot, the recombination current in these devices is in excellent agreement with classical SNS recombination theory. Although these conclusions and studies of the transport mechanisms in 6H-SiC have been previously studied, this work is the first thorough analysis of the forward transport mechanisms in the 4H polytype of SiC.

The temperature dependence of I_{rec}/I_{diff} data was also compared to theory. Diodes with no significant leakage or shunt characteristics were utilized to determine the empirical conformity to the predicted $T^{-1/2}\exp(E_G/2kT)$ temperature dependence. The temperature dependence is obtained by taking the ratio of Equation VIII-7 to Equation VIII-6. Exponential prefactor ratios from the estimated I-V fits to Equation VIII-2 over the range of 300 to 725 K were found to be in good agreement with the exponential prediction.

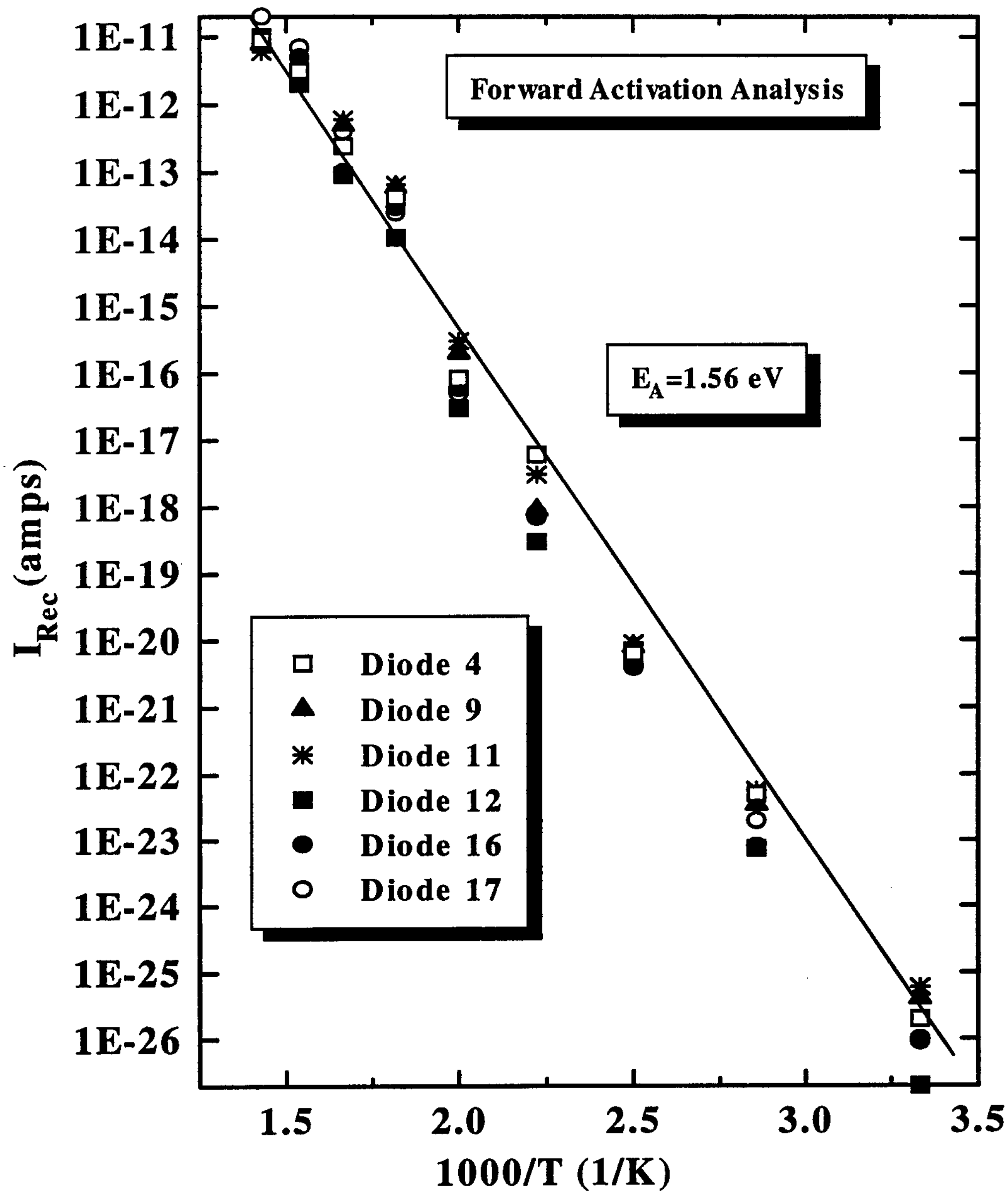

Figure VIII-14. Forward I-V-T activation energy Arrhenius analysis of the recombination mechanism for six well behaved 4H-SiC p^+/n rectifiers. An average value of E_A = 1.56 eV was obtained indicating ideal recombination in accord with SNS statistical theory, which predicts a value of $E_{G0}/2$. 4H-SiC has an estimated value of $E_{G0}/2$=1.63 eV from low temperature photoluminescence measurements.

VIII-V-2. Reverse I-V, I-V-T and Breakdown Behavior. Reverse I-V-T characterization was used to identify the activation energy of trap related generation. In general, the total reverse current is comprised of the thermally generated SCR component, I_{Gen}, a bias independent bulk diffusion component, I_{bulk}, and a surface perimeter current, I_{sur} [Sze, 1981:79]. In wide bandgap materials, we can predict that the thermally generated SCR component ($I_{rev} \approx \exp(-E_G/2kT)$) will be preeminent over bulk-diffusion ($I_{bulk} \approx \exp(-E_G/kT)$) and surface-perimeter leakage currents. This has been shown to be true for GaAs and $Ga_{0.5}In_{0.5}As$, which have bandgaps of 1.42 and 1.89 eV, respectively [Ringel *et al.*, 1989:1230], [Reinhardt *et al.*, 1995:5763]. It is therefore reasonable to assume that I_{rev} will be dominated by I_{Gen}, and the surface and bulk components will be neglected in the analysis. This analysis led to the definition of Equation VIII-7.

Figure VIII-15 displays a series of temperature dependent reverse bias I-V curves, which were observed to be typical for well-behaved diodes exhibiting a dominant recombination transport mechanism in the forward I-V characteristic. The illustrated data set reflects a consistent behavior over the wide range of measurement temperatures up to 700 K. Included in the figure is the theoretical thermal generation current, $I_{rev} \propto V^{1/2}$, curve expected for abrupt doping profiles [Sze, 1981:84], indicating that the reverse I-V characteristics of the well-behaved diodes also follow classical predictions. In contrast to the reverse characteristics for the well-behaved diodes, Figure VIII-16 reflects the typical reverse features of diodes exhibiting a significantly shunted forward I-V character. For the isothermal I-V data sets between 300 and 650 K shown in Figure VIII-16, we see that the expected $V^{1/2}$ bias variation is not obeyed, but an exponential-like variation

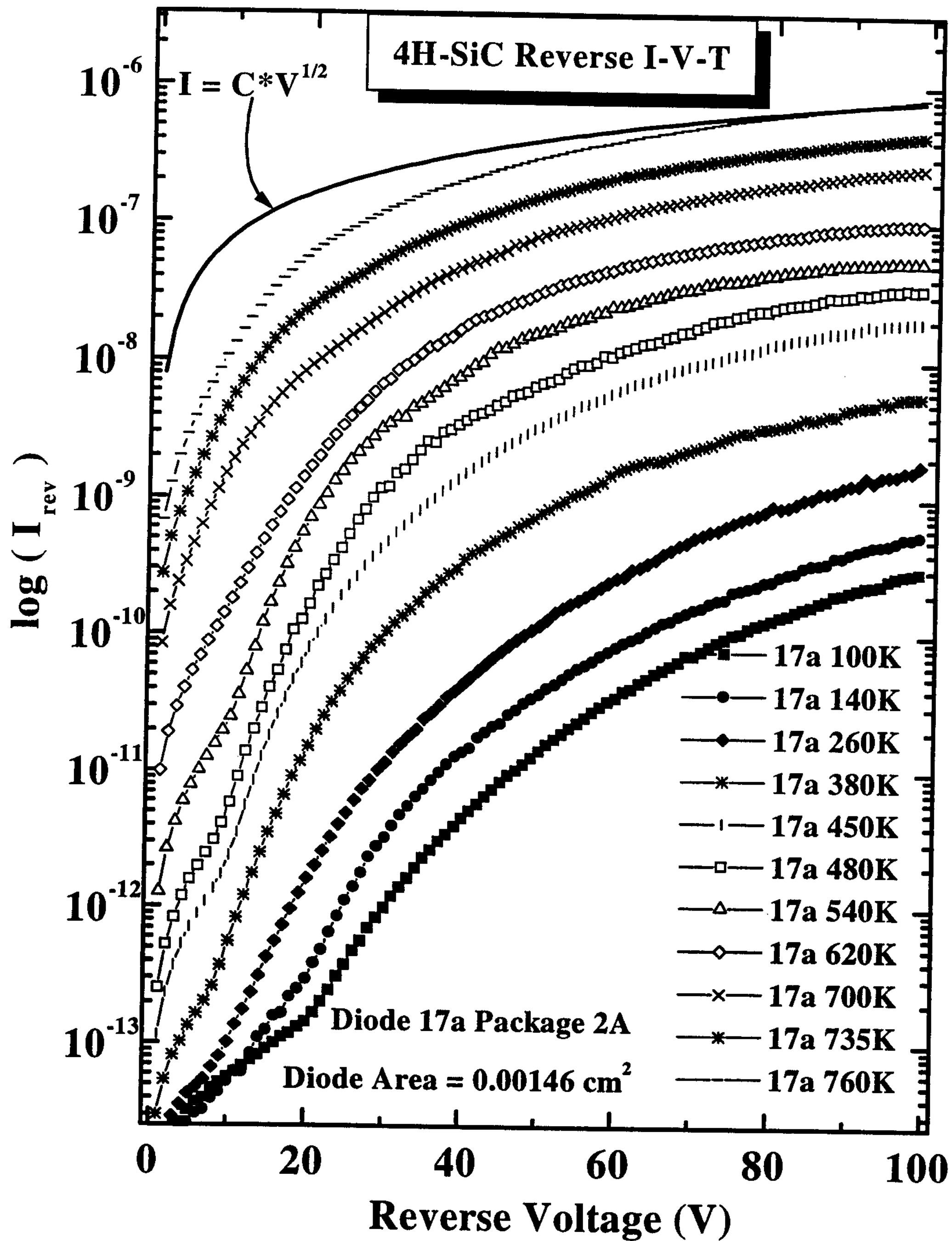

Figure VIII-15. Typical reverse-bias I-V-T series of data sets for a well-behaved diode without a forward-bias shunting characteristic. The 4H-SiC p^+/n diode curves shown from 100 to 760 K illustrate consistent performance over the wide temperature range. Included in the figure is the expected $V^{1/2}$ variation of reverse current with bias to compare with prediction for the well-behaved diodes.

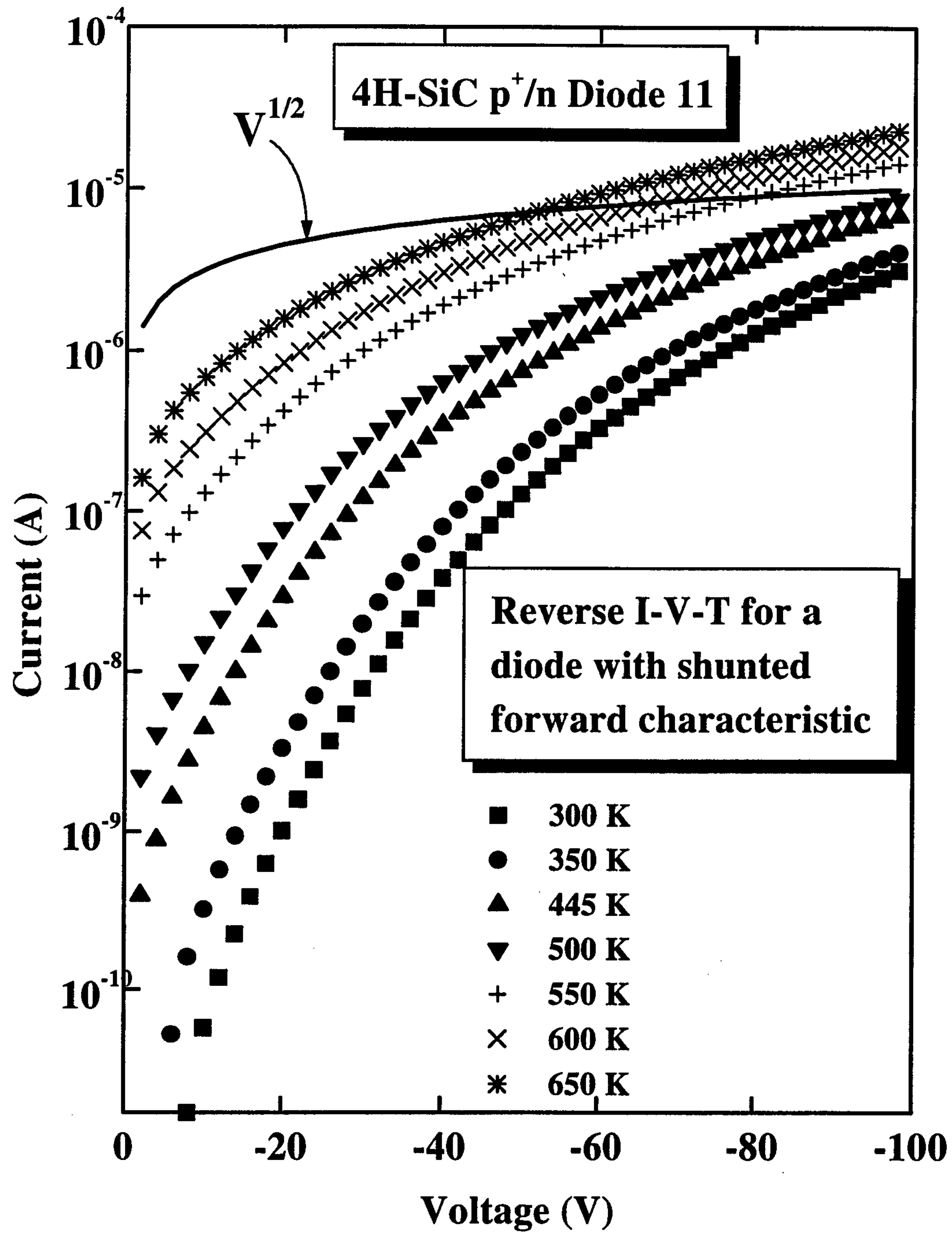

Figure VIII-16. Reverse I-V data curves for a 4H-SiC p^+/n diode that exhibited a forward bias shunting characteristic. In this case, we see that the trend is not in accordance with the $V^{1/2}$ prediction for abrupt junctions. This deviation is due to the neglected surface perimeter component and the presence of non-negligible tunneling mechanisms.

dominates. This deviation may be due to the presence of a non-negligible mesa surface perimeter reverse current component. On the other hand, Shaw *et al.* have attributed similar observations to shunting, which is correlated to a significant tunneling component. This conclusion is supported by our observations of a negative temperature coefficient for reverse breakdown and shunting in the forward I-V characteristics.

Arrhenius analysis for the reverse activation energies of the dominant generation centers in these devices met with limited success. Due to the dominant presence of non-ideal reverse characteristics like those shown in Figure VIII-16, the Ln (I_{rev}) data plots did not always yield well-defined linear features as predicted by Equation VIII-8. Figure VIII-17 illustrates the typically obtained reverse activation Arrhenius plots for diodes exhibiting non-ideal reverse characteristics and shunted forward I-V features. As seen from the plots generated at four different reverse bias values, there does not exist any well-defined linear regions from which to estimate the generation center activation energies. The lack of identifiable features from these data sets is indicative of non-negligible tunneling currents and/or the presence of multiple generation centers. As we shall see, DLTS analysis of these same devices revealed the presence of numerous deep level centers in significant concentrations, which implies both mechanisms potentially occur. It is these deep levels which are correlated to both the forward shunting characteristics and the non-ideal reverse I-V behavior.

Careful reverse I-V characterization of a large number of devices eventually led to the observation of three generation center activation energies, which were found to occur in both well-behaved diodes and some of the leaky devices. Figure VIII-18 shows

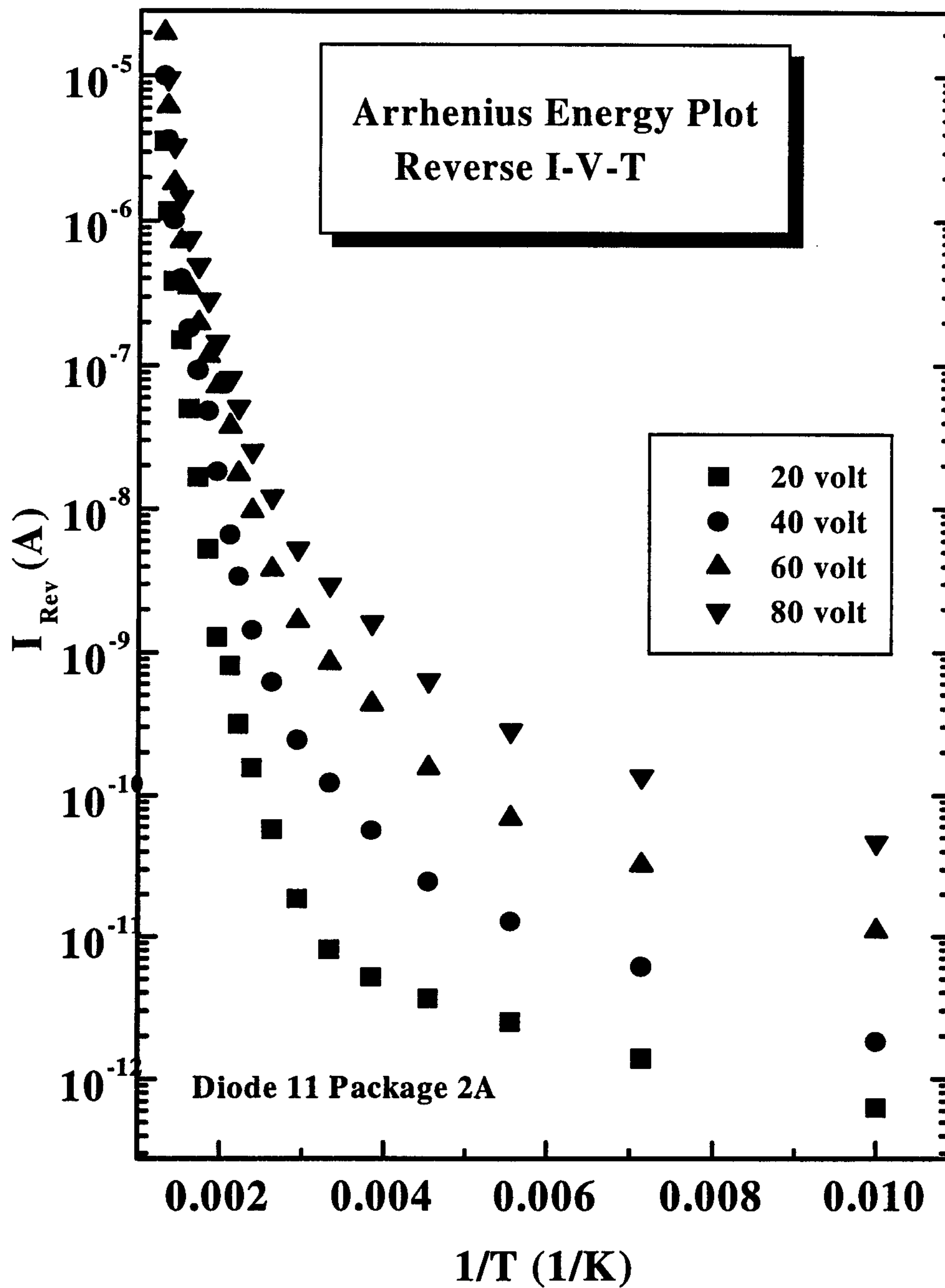

Figure VIII-17. Reverse activation energy Arrhenius plot typical of the 4H-SiC p^+/n diodes exhibiting non-ideal reverse I-V characteristics. The lack of well-defined linear regions are indicative of non-negligible tunneling components and/or the presence of multiple generation centers contributing to the reverse current. DLTS analyses of these same devices revealed the presence of numerous deep levels with large concentrations, supporting the conclusion that both mechanisms are responsible for this behavior.

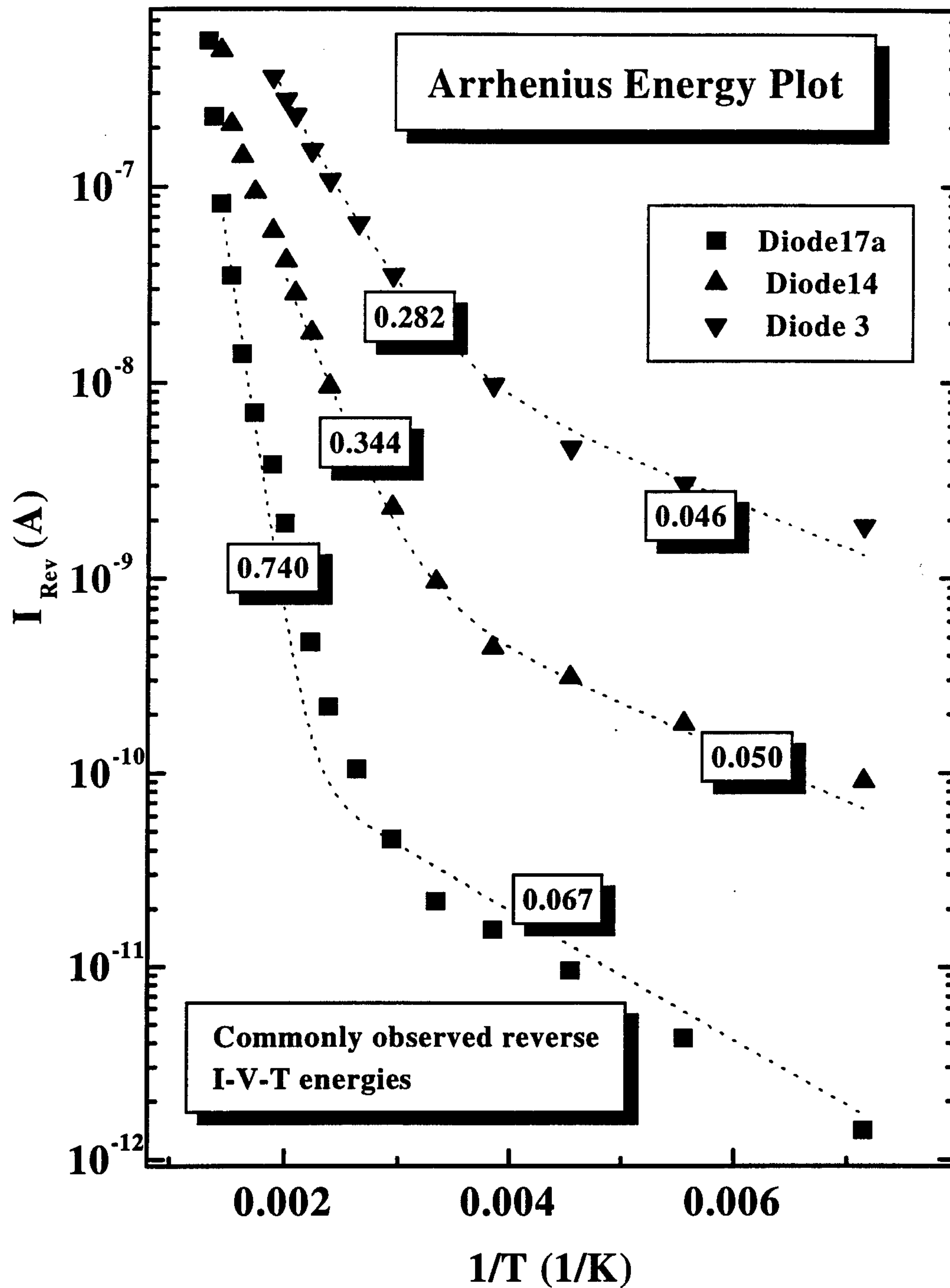

Figure VIII-18. Arrhenius plot of the three consistently observed generation centers in the 4H-SiC p^+/n diodes. The large activation energies of 740, 344, and 282 meV were all confirmed using DLTS on these and similar devices. The shallow level generation centers are approximately in the range of the nitrogen donor levels, and are consistently observed in these analyses.

activation energy data sets for three different diodes, each exhibiting one of the three most frequently observed generation centers in the 4H-SiC diodes. Within experimental uncertainty, these activation energy values were confirmed with DLTS measurements on these and similar devices. The level at 740 meV in Figure VIII-18 is significant for several reasons. It was found to occur in very large concentrations, and was correlated to a dominant radiative recombination. The shallow levels indicated in Figure VIII-18 are very close to the nitrogen donor levels in the 4H material. Since these levels are incompletely ionized over the same temperature range that the activation energies are being estimated in Figure VIII-18, it may be that a Fermi level effect is occurring with the shallow nitrogen donor levels. The connection with these impurities is supported by the nitrogen ionization fraction data illustrated in Figure VI-1 over the same temperature range.

The connection between the tunneling or shunted forward I-V characteristics, the reverse I-V features indicating tunneling in many devices, and deep defect levels is further supported by our observation of a negative temperature coefficient for reverse breakdown (TCBV) in all devices investigated. A negative TCBV is undesirable for power device applications because this behavior focuses and intensifies breakdown current at localized junction hotspots. This results in high current filamentation causing physical damage to the device. Devices exhibiting this behavior are unlikely to survive even momentary overvoltage glitches which may occur in high power control circuitry.

At 300 K, these devices had reverse breakdown voltages between 100 and 280 volts, depending upon the concentration of deep levels observed from DLTS

measurements and the I-V leakage characteristics. Illustrated in Figure VIII-19 is a series of reverse I-V-T curves, for temperatures between 300 and 700 K for a diode with shunted type forward I-V characteristics. As shown by the 650 and 700 K curves the indication of a decreasing bias value for reverse breakdown is observed at the higher temperatures. This breakdown feature was observed for all 4H-SiC p^{+}/n devices characterized. Unfortunately, in each and every instance, when the diodes were biased to full reverse breakdown, they were found to fail catastrophically, and could not be used for further analysis. This negated the possibility of a more thorough characterization of the breakdown mechanism. However, the negative TCBV was characterized by carefully biasing the diodes only until an initial indication of breakdown was observed, as illustrated by the data of Figure VIII-19.

Reports of a negative TCBV in both 6H- and 4H-SiC have been previously published [Konstantinov, 1989:31], [Neudeck and Fazi, 1996]. Anikin *et al.* demonstrated a link between the negative TCBV they observed in 6H-SiC p/n diodes and tunneling through deep levels in the semiconductor bandgap [1988:995], arguing against an intrinsic bandstructure connection previously proposed [Konstantinov, 1989:31]. Neudeck and Fazi proposed that the mechanism is related to the incomplete ionization of the shallow donor and acceptor impurities, which results in filamentation when the reverse bias electric field causes sudden impact ionization of the unionized shallow levels. Our data supports the role of a deep level tunneling mechanism to account for the TCBV we observed. This is based on the fact that we observed reduced breakdown voltages for devices showing strongly shunted forward I-V features, non-ideal tunneling

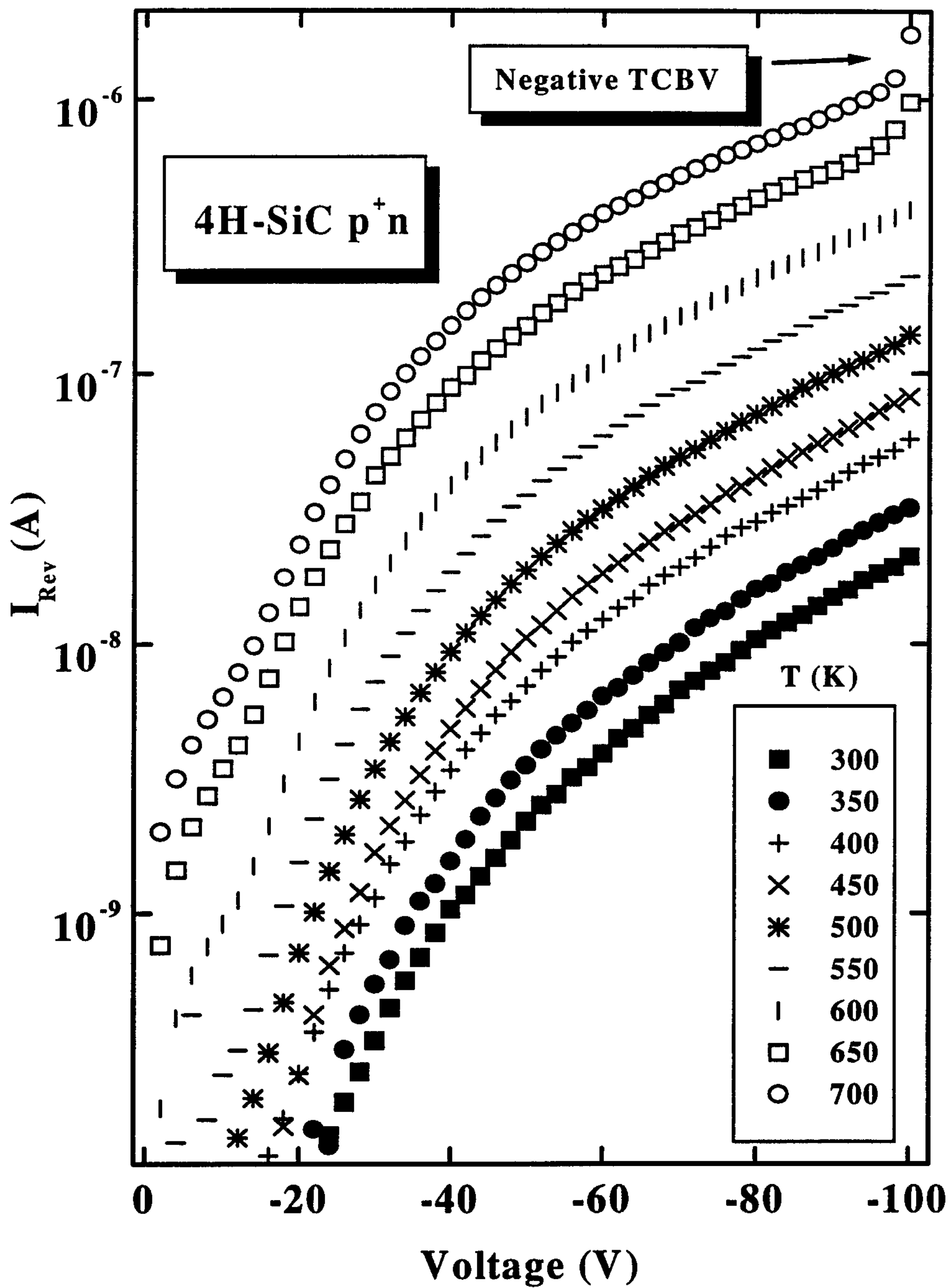

Figure VIII-19. Reverse-bias I-V-T series of data sets for a diode with a forward-bias shunting characteristic. The 4H-SiC p^+/n diode curves shown correspond to measurement temperatures from 300 to 700 K. A dominant feature of the reverse characteristics of these diodes is illustrated by the 650 and 700 K curves showing initiation of reverse breakdown at 95 volts. This negative temperature coefficient of breakdown voltage was pervasive throughout the range of devices tested.

dominant reverse I-V behavior, and a corresponding high concentration of deep levels in these same devices. Devices exhibiting these features were found to be able to sustain only 70 to 125 volts in reverse bias prior to catastrophic failure. On the other hand, well-behaving p^+/n devices were observed to sustain up to 280 volts under reverse bias conditions, and deep levels were detected in much lower densities. Thus, the devices with high defect concentrations are capable of sourcing much higher leakage current densities at smaller biases and lower temperature ranges, via tunneling. On the other hand, deep defect levels are still found to be present in the well behaved devices, however with much lower concentrations. Thus, higher bias levels and temperature ranges are required to generate a non-negligible tunneling component under reverse bias condition. This postulate is supported by the data shown in Figure VIII-20 for a pair of well-behaved diodes and two leaky devices. As seen in the figure, the higher initial voltage at the onset of breakdown, with a correspondingly lower sensitivity to temperature, are observed for the well-behaved devices in comparison to the leaky diodes. The DLTS and EL data presented in the following paragraphs further support the role of deep level defects in the observed junction characteristics of the 4H-SiC diodes.

VIII-V-3. DLTS Characterization of 4H-SiC p+/n Diodes. DLTS characterization of the diodes subjected to I-V-T analysis was typically performed using classical constant-voltage (CVDLTS) methods. In some instances, the trap concentration exceeded 10% of the shallow doping density, and thus the constant-capacitance (CCDLTS) mode of operation was utilized [Johnson, 1982:303]. Operation in this mode circumvents the assumption of low trap density when performing data reduction.

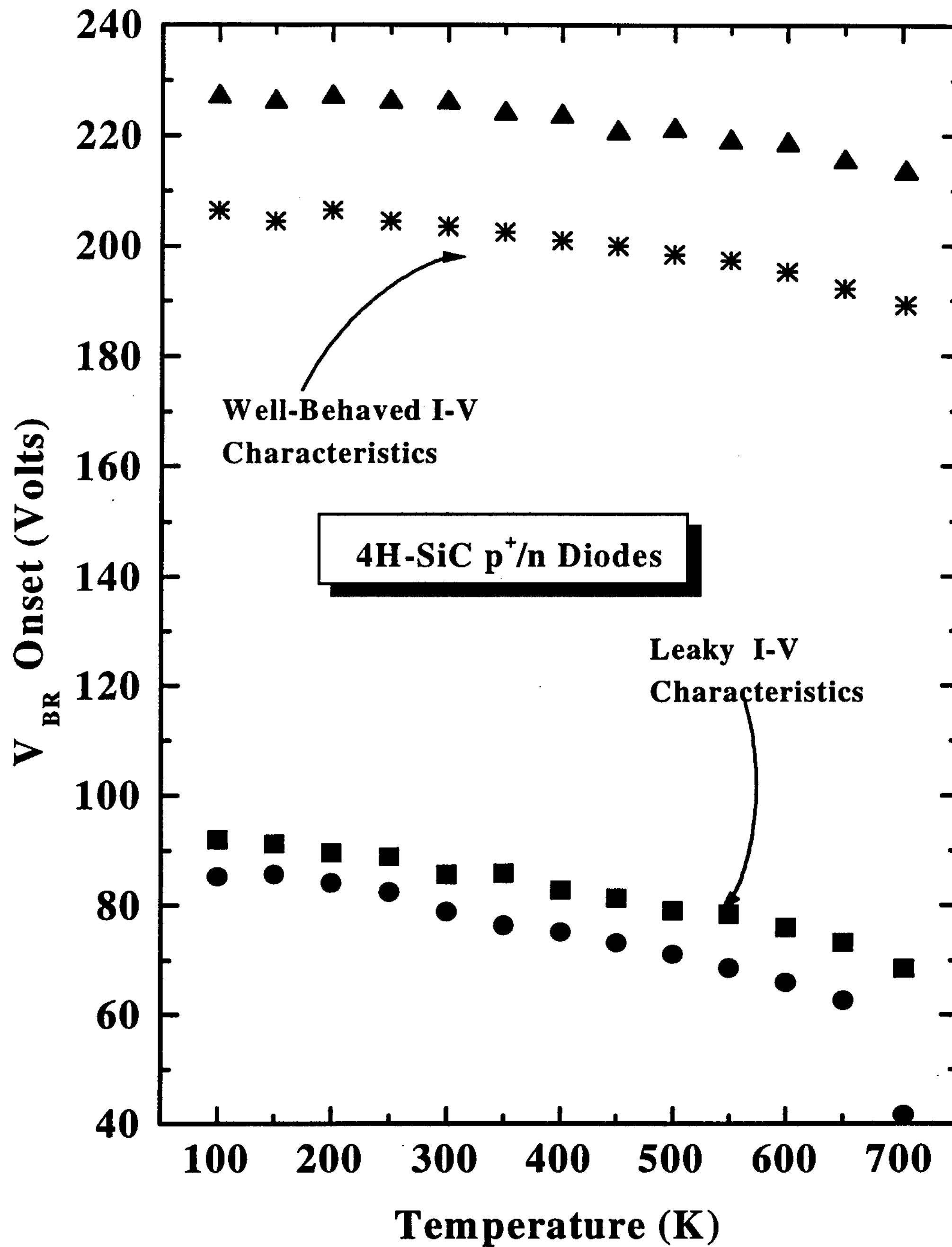

Figure VIII-20. Temperature dependent data illustrating the negative TCBV for the 4H-SiC p^+/n diodes. Shown are the results of measurements of the onset of reverse breakdown bias voltages for two diodes with well-behaved I-V characteristics and a pair of leaky diodes. The temperature coefficient for the leaky diodes is more strongly negative, supporting the role of deep centers as the tunneling mechanism controlling this behavior.

DLTS characterization of the 4H-SiC p^+/n diodes was performed on a large number of samples to determine the identifiable deep level trends in these devices. As observed for the 6H-SiC raw materials, there were found to be numerous defects with measurable trap emission rates over the 100 to 750 K temperature range of the measurements. This situation compounded the difficulty of correlating deep level behavior to the observed junction characteristics. However, several deep-level defects were consistently recorded across the matrix of samples tested, and are reported in this subsection. Furthermore, for the most commonly occurring trapping centers, a correlation to carrier transport was implied from a comparison of the I-V-T data and DLTS signatures.

Figure VIII-21 reflects the rate window plots of eight majority-electron and minority-hole deep level trapping centers observed on the n-type side of the junctions. Restriction to emission from the n-side of the junction can be made based on the $\sim 10^4$ doping level ratio between the p-type and n-type material, which results in the same large ratio, W_n/W_p, for the reverse bias depletion widths on each side of the metallurgical junction. The DLTS rate window signature of the defects, labeled A-H in Figure VIII-21, are significant in that they are found to occur in concentrations large enough to dominate device junction characteristics. Concentrations range from $0.01N_D$ for level A to $0.3N_D$ for level F, where the shallow donor doping level is $N_D \approx 5 \times 10^{15}$ cm^{-3}. These deep traps with ionization energies over the range of 200 meV to 856 meV are implicated in the shunting and leakage currents seen to dominate the majority of device I-V characteristics. Furthermore, levels B, C, and G with DLTS energies of E_C-280, E_C- 349, and E_V + 730 meV, respectively, are all implicated as the dominant reverse bias generation centers

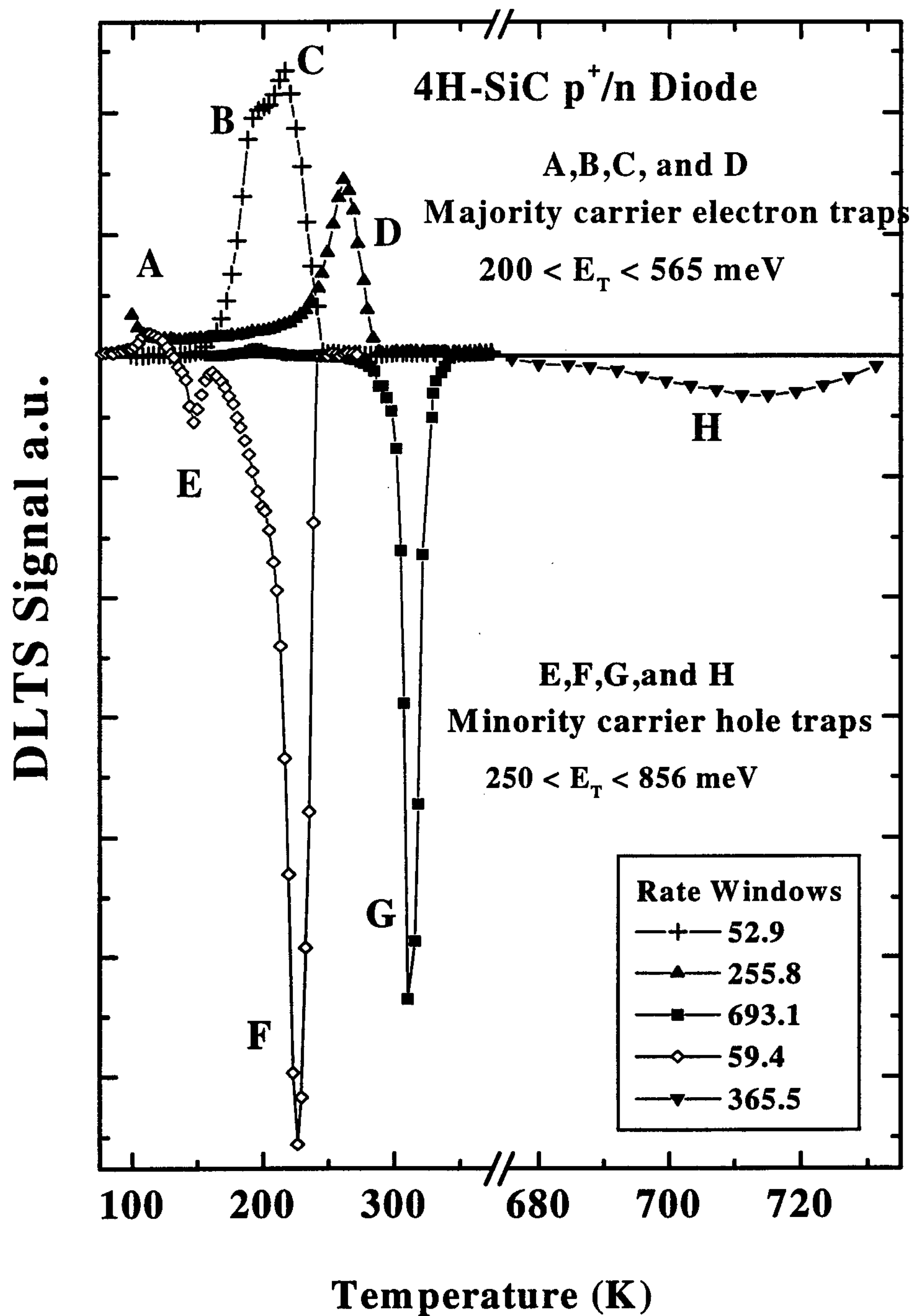

Figure VIII-21. DLTS rate window spectra of the consistently observed deep trapping centers in the 4H-SiC p^+/n junctions. The significance of these levels is in the extremely large concentrations in which they were commonly found to occur. For example, the minority carrier hole trapping center F was found in densities as high as 1.5×10^{14} cm^{-3}, which implies a strong link to crystalline imperfections such as dislocations, vacancies, or similar lattice flaw.

initially identified from reverse I-V-T analysis as shown in Figure VIII-18.

With the exception of level A, the electron and hole trapping centers shown in Figure VIII-21 were found to be omnipresent in all diodes exhibiting significant tunneling leakage currents. Furthermore, these defects are found to have characteristically large capture cross sections ranging from $5x10^{-17}$ to $2x10^{-12}$ cm^2, which increase the rate of electronic transitions through these centers significantly when occurring in conjunction with these large concentrations. Under these circumstances, the conditions exist by which these deep defect levels can dominate junction I-V characteristics. On the other hand, in no instance did we detect the presence of these large concentration trapping centers in p^+/n diodes with well-behaved I-V characteristics. This correlation again supports the role of defect related tunneling in the devices exhibiting this behavior, both in the forward and reverse bias conditions.

It should also be noted that several additional deep level electron and hole trapping centers were frequently detected in these diodes, but were found to be occurring in much lower concentrations. Figure VIII-22 shows the normalized rate window plots for these low density traps, which were only measured in the diodes with well-behaved I-V features. This is due primarily to the fact that the centers with high densities, especially large capture cross sections, will dominate carrier capture and emission in diodes possessing both low and high density centers. In addition, a fidelity limit will be exceeded for superimposed decay time constants with amplitude coefficients differing by up to several orders of magnitude.

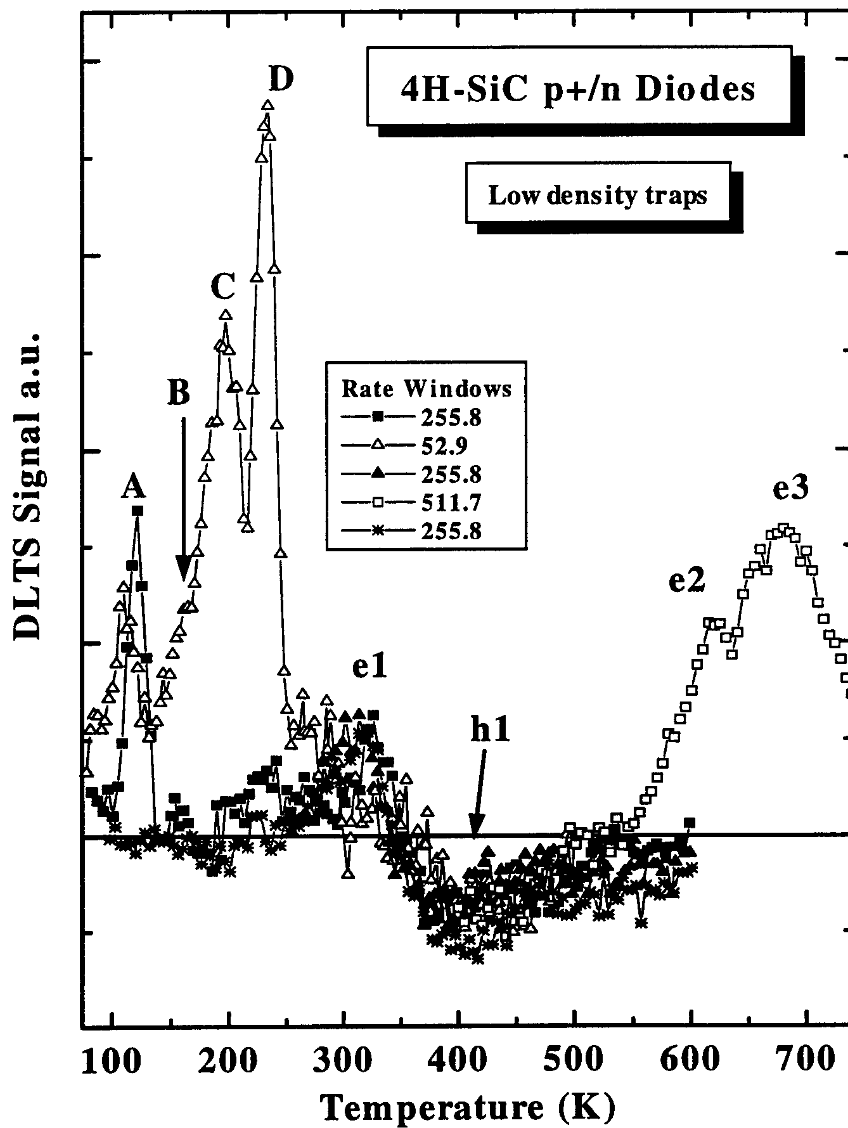

Figure VIII-22. DLTS spectral features of frequently observed traps in the 4H-SiC p^+/n diodes. These centers were found to occur in much lower concentrations than those shown in Figure VIII-21. Traps labeled e1 and h1 were found to be occurring in densities approaching the detection limit of the DLTS system, which is $\sim 10^{-4} N_S$. The levels labeled as A, B, C, and D are the same as those in Figure VIII-21, and were found in both high and low concentrations in these devices. These traps, with small transient amplitudes, were observed primarily in the diodes with well-behaved I-V features.

Table VIII-4 enumerates the estimated energy levels, capture cross sections, and trap concentrations as obtained from DLTS measurements on the levels in Figure VIII-21 and Figure VIII-22.

Capacitance-voltage-temperature versus frequency measurements were also taken on several devices at 1 MHz and 1 kHz source frequencies to estimate deep level energy values [Reinhardt *et al.*, 1995:5763],. The temperature derivative of the C-V-T scans at 0, -10, and -20 volt DC offsets were ineffective as a means to obtain or verify

Table VIII-4. Tabular summary of the deep level traps identified in Figure VIII-21 and Figure VIII-22. Ionization energies, capture cross sections, and trap densities are listed for the most consistently observed centers in the 4H-SiC p^+/n diodes.

Trap	**A**	**B**†	**C**†	**D**	**E***	**F***
^1E_T	200	280	349	564	246	680
$^2\sigma$	$2x10^{-17}$	$4x10^{-17}$	$1x10^{-16}$	$6x10^{-13}$	$1x10^{-18}$	$2x10^{-12}$
$^3N_{TT}$	0.01	0.06	0.09	0.07	0.03	0.3
Trap	**G***†	**H***	**e1**	**e2**	**e3**	**h1***
^1E_T	750	856	585	611	536	350
$^2\sigma$	$4x10^{-13}$	$1x10^{-18}$	$2x10^{-14}$	$5x10^{-20}$	$3x10^{-21}$	$1x10^{-19}$
$^3N_{TT}$	0.25	0.03	0.002	0.002	0.003	0.002

*-Minority carrier hole traps. †-Observed using reverse I-V-T technique also. **1**-Energies in meV, **2**-cross sections in cm^2, and **3**-trap concentrations normalized to the shallow donor concentration of $5x10^{15}$ cm^{-3}.

deep level defect activation energies. This was due to the presence of numerous overlapping peaks and troughs in the dC/dT vs. T data, indicating the presence of several competing emission rate resonances superimposed over coincident temperature ranges. Since the fidelity of the C-V-T technique is limited to single or two energetically well separated levels, the failure of this technique further illustrates that the device terminal characteristics are dominated by deep levels in the 4H-SiC junctions. Additionally, the 1 MHz peak locations were found to lead the corresponding 1 kHz peaks with respect to temperature. This deviation from theory is not understood, but invalidates the resulting deep level energy analysis. Thus, C-V-T measurements could not be used to identify defect levels in these diodes.

Due to the fact that 4H-SiC is a much more immature technology than its counterpart 6H polytype, we expect greater concentrations of structural lattice imperfections to be present in 4H-SiC. Substrate material of very limited quality has only recently become available, and reported efforts to characterize the defects in this polytype are even more limited than for the 6H material. Thus, as indicated by the data of Tables VIII-1 and VIII-2, even less information is available regarding the nature and/or sources of the deep level activity in the 4H polytype of SiC. Of the twelve levels identified and enumerated in Table VIII-4, none appears to have been previously reported when comparing to the literature summary of Table VIII-2.

In addition to being directly correlated with shunted or tunneling related I-V transport characteristics of the 4H-SiC p^+/n diodes, the observed deep level trapping data implies a link to crystalline damage for the large concentration defects A through H, and

especially B, C, D, F, and G. This implication is based solely upon the extremely large concentrations associated with these levels. We observed that the concentration of 4H-SiC deep levels approaches the donor doping density, and thus atomic impurity incorporation at these high levels is for all practical purposes impossible. This is due to the integrity of MOCVD epitaxial growth systems, and the extreme care that is taken to minimize system contamination. However, without definite corroborating evidence to verify the connection to crystalline imperfections, we can only postulate this correlation at this time.

In the following section, we summarize the connection between the deep level labeled F in Figure VIII-21 and a dominant green electroluminescence observed only in diodes possessing this center. Furthermore, a connection to structural damage is again implied by the occurrence of a similar green luminescence reported to be present in 6H-SiC junctions formed by ion implantation [Neudeck, 1995].

VIII-V-4. Electroluminescence of the 4H-SiC p^+/n Junctions. As indicated in the DLTS summary above, the large concentrations and cross sections of deep levels are implicated in the forward I-V shunting characteristic because their presence in all diodes exhibiting significant leakage and tunneling currents. Additionally, the minority carrier hole trap labeled F in Figure VIII-21 has also been observed in diodes with similar shunting I-V behavior, but is present only in those diodes also exhibiting a green (2.42, 2.35 eV) defect electroluminescence. The energetic separation between spectral peaks indicates that this luminescence is a nitrogen-donor to deep-acceptor pair recombination.

Figure VIII-23 illustrates the spectral characteristic for an injection dependent

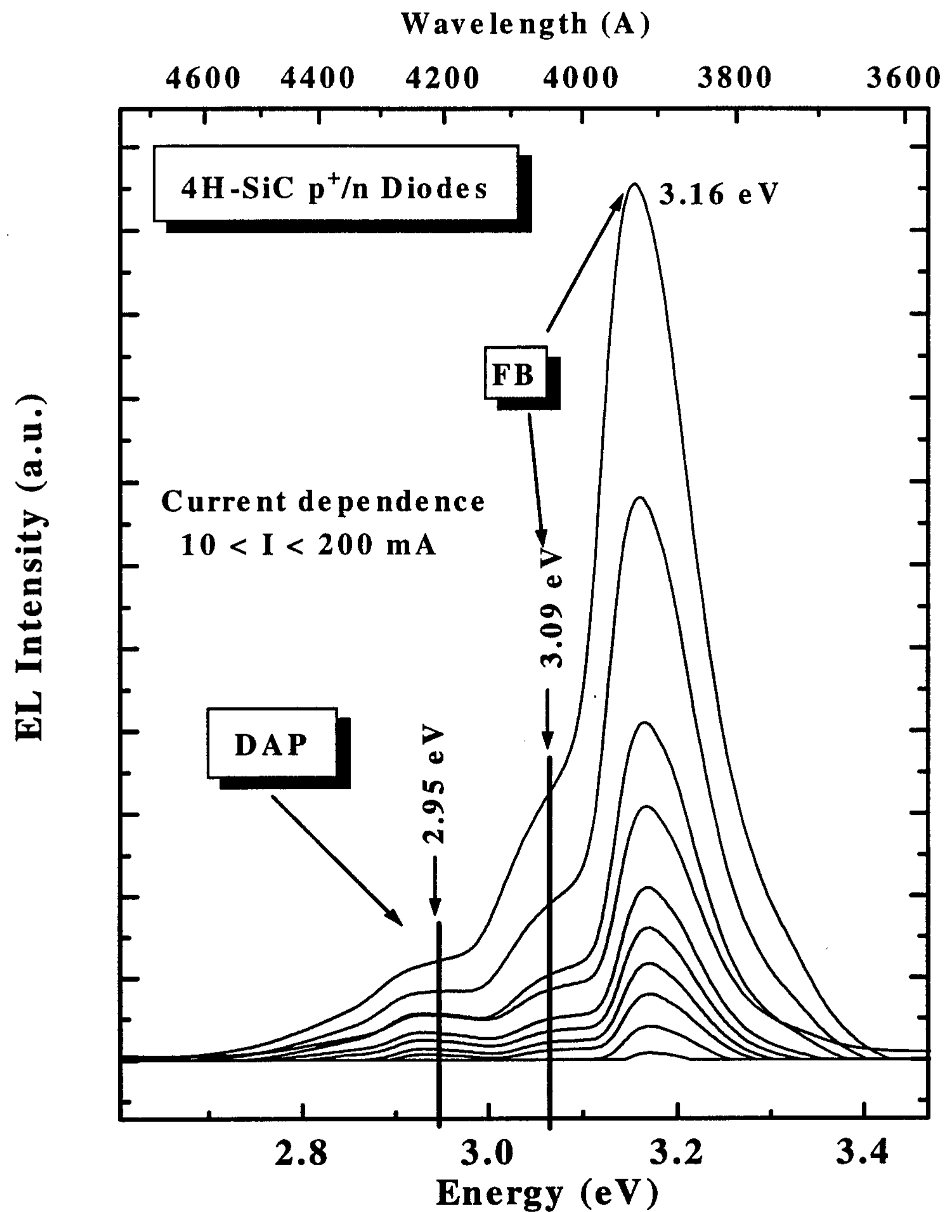

Figure VIII-23. Injection dependent series of electroluminescence curves collected on 4H-SiC diodes with well-behaved I-V characteristics. The 3.16 and 3.09 eV ultraviolet peaks are due to the recombination of free holes at hexagonal and cubic site nitrogen donors, respectively. This ultraviolet feature dominated the EL spectra only for diodes with the most well-behaved I-V features. The feature just becoming discernible at 2.95 eV is the well known N-Al violet DAP recombination spectra. Small amplitude curves are for low injection currents.

series of measurements on a p^+/n diode. The 3.16 eV peak is the ultraviolet radiation resulting from the recombination of free holes (FB) with nitrogen donor atoms at occupied hexagonal sites, which are located at ~50 meV below the conduction band in the 3.2 eV bandgap material [Dmitriev *et al.*, 1988:23]. The low energy shoulder of this spectral feature, at roughly 3.09 eV is also due to the recombination of free holes with donor atoms occupied at cubic sites, which are located at ~100 meV above the valence band edge [Violin *et al.*, 1964:1331]. Finally, the lower energy feature at 2.95 eV is the well studied violet N-Al DAP recombination peak [Hagen *et al.*, 1973:18]. The dominance of the FB transitions over the DAP recombinations was observed only in devices void of significant deep level activity and exhibiting superior I-V features.

The majority of well-behaved and in some instances, shunted diodes exhibited an electroluminescence spectra like that illustrated in Figure VIII-24. The typical violet N-Al DAP recombination peaks at 2.92 and 2.85 eV originate from hole annihilation with electrons on the two nitrogen energy levels [Tairov and Vodakov, 1977:CH.2]. It is the dominance of this intense DAP radiation which has enabled the only true commercial product currently fabricated on SiC.

While the features of the spectra illustrated in Figure VIII-23 and Figure VIII-24 were pervasive throughout the majority of devices investigated, there was an additional, interesting spectrum observed in several diodes. It was consistently observed that diodes containing the deep level labeled F in Figure VIII-21 were identifiable by their bright green (2.4 eV) luminescence. In addition, these diodes were found to be characterized by

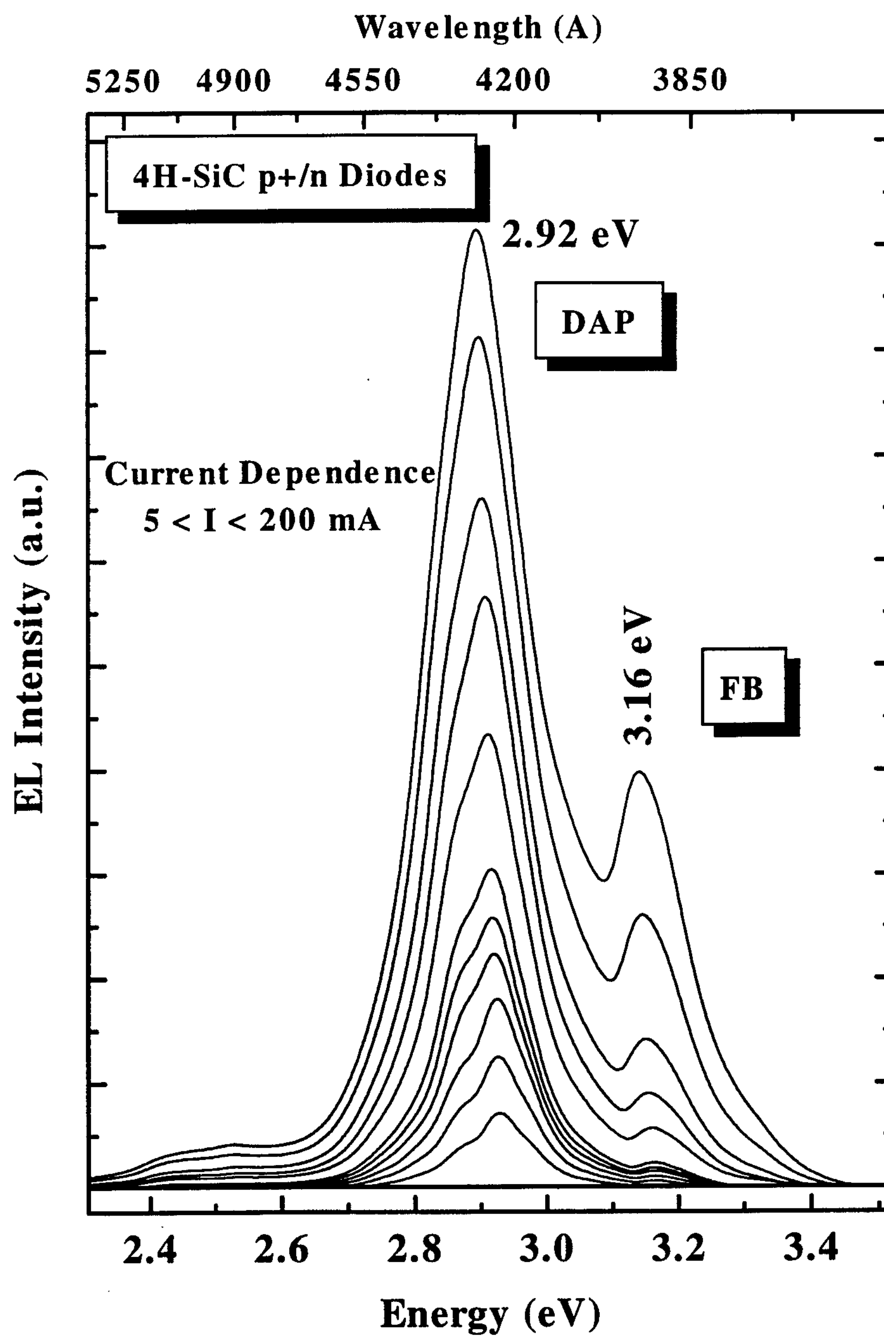

Figure VIII-24. More commonly observed electroluminescence spectra for the 4H-SiC p^+/n diodes, exhibiting the dominance of the violet N-Al DAP recombination peaks. As seen in the low injection bottom curves, the spectral feature is characterized by two peaks corresponding to the inequivalent donor energies.

strongly shunted I-V characteristics. Figure VIII-25 and Figure VIII-26 are representative examples of the electroluminescence and forward I-V features of typical diodes possessing this deep defect level, respectively. As seen in Figure VIII-25, the characteristic violet free-to-bound transitions involving the two nitrogen inequivalent lattice sites are seen to be still present. However, the N-Al donor-acceptor pair (DAP) recombination is seen to be quenched, which was found to be the case in all diodes exhibiting the green EL feature. We see a large intensity DAP peak, which is associated with what appears to be recombination between the two nitrogen levels and a deep acceptor at about $\sim E_V+730$ meV. This energy is 50 meV larger than the DLTS measured value of 680 meV for the F-defect. This difference is insignificant when considering that typical uncertainties in DLTS estimated energies can approach 30 to 50 meV. Additionally, we must remember that DLTS and other thermally stimulated techniques actually yield enthalpy estimates, whereas optical techniques give actual free energy values. The difference between these two quantities is the system entropy, in terms of the Gibbs free energy formalism. This is the reason that thermal techniques almost universally underestimate ionization energies, in comparison to corresponding optical results on the same centers. The fact that the F-defect was always present in the diodes exhibiting the green EL and never present in diodes without this luminescence feature, strongly implicate the F-defect as the luminescence activator.

Additionally, field dependent DLTS emission rate measurements revealed no electric field enhancement of the capacitance decay rate, indicating acceptor-like charge states for the F-defect. This fact together with the presence of this center in all diodes

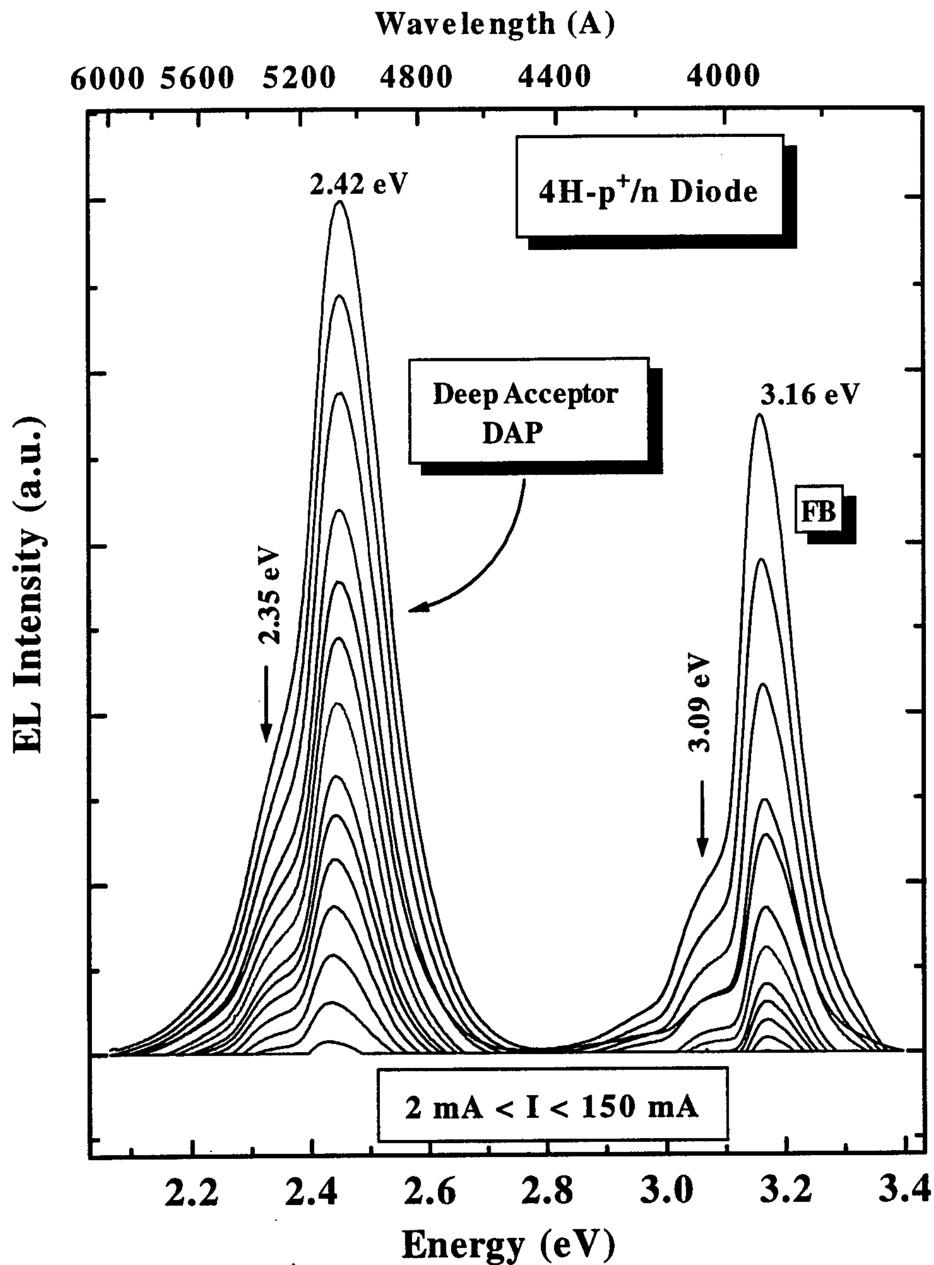

Figure VIII-25. Electroluminescence spectra observed only for diodes possessing high concentrations of the deep level labeled F in Figure VIII-21. Although the FB radiative transitions are seen to persist, the N-Al DAP spectra have been completely quenched. This is a result of the higher transition probability for the deeper acceptor level created by the F defect. The lower curves correspond to lower injection current values.

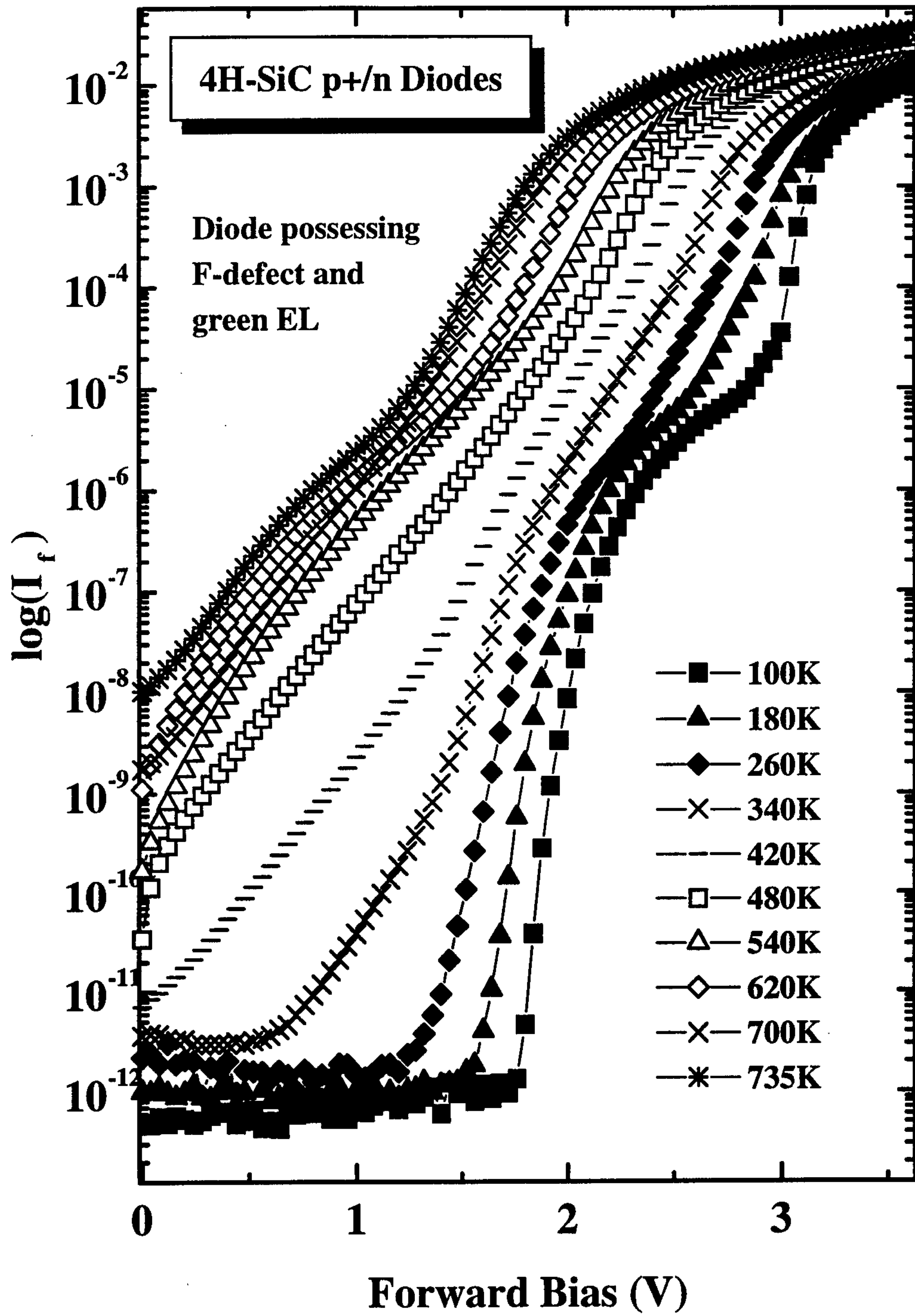

Figure VIII-26. Forward I-V-T family of curves for the diode exhibiting the green defect electroluminescence shown in Figure VIII-25. The identification of diodes exhibiting both the shunted I-V characteristic shown here and the green EL were found to also possess the F-defect center in every instance investigated.

exhibiting a bright green luminescence lead us to conclude that the 680 meV, DLTS detected center, is the activator responsible for the bright green luminescence observed. The complete quenching of the N-Al DAP spectra provides additional support for the assignment of a deep DAP recombination to the green spectrum. This is because the relative recombination probabilities for deep DAP transitions are significantly greater for deep levels. Deep centers provide a much more efficient mechanism for momentum conservation because of the larger number of **k**-vectors required to define the bound state wavefunction. The result is a more significant overlap between the wavefunctions of the bound nitrogen electron and the deeply bound hole, which in fact defines the transition probability. Additionally, the large cross section (10^{-12} cm^2), deep energy level (680 meV), and measured large concentrations (10^{14} cm^{-3}) will also increase the recombination probability resulting in short radiative lifetime for this process. All these factors support the role of a N-F center DAP transition, and explain the lack of a N-Al DAP radiative recombination in these diodes.

State-of-the-art p^+/n 4H-SiC rectifiers have been studied to determine current conduction mechanisms using I-V-T, DLTS, and EL. The majority of diodes tested were found to exhibit shunted I-V behavior which was found to obey a tunneling conduction model. DLTS measurements of the devices revealed the presence of numerous deep trapping centers, several of which are implicated in the large reverse saturation currents observed in many devices. Additionally, investigation of a green DAP luminescence in these same diodes was correlated to a large concentration acceptor-like hole trap which appears to be the luminescence activator. Finally, reverse breakdown measurements were

characterized by a lack of an avalanche mechanism and by the catastrophic failure of each device after biasing to breakdown. The negative temperature coefficient trends are indicative of reverse bias tunneling through allowed states in the bandgap. The detection of several deep level defects with significant concentrations support this supposition. Furthermore, the number of DLTS detected defect centers observed within roughly $E_G/3$ of the bandedges is an indication that additional undetected deeper levels may exist in the material. These levels, if present, will also contribute to the defect dominated junction characteristics observed. The sources of the defects observed in these devices are unknown. However, a link to intrinsic defects may be implied in some instances by noting that a similar green luminescence with an approximate peak at 2.2 eV is commonly observed in p/n junctions formed by ion-implantation in 6H-SiC [Violin and Kholuyanov, 1963:1331]. The difference between this reported EL and that measured in our 4H-SiC sample devices is approximately equal to the bandgap difference between the 6H and 4H polytypes. Additionally, the unintentional introduction of atomic impurities at the observed concentrations for some of the defects is unlikely in high quality epitaxial CVD reactors. Thus, if lattice imperfections are dominating junction characteristics, scaling the device areas to dimensions appropriate for applications such as power rectifiers will only exacerbate the problems. The results here indicate the need for additional study of the defects in these materials, especially their sources, and the need for continued attention and improvements to material quality.

IX. Summary and Conclusions

The primary objectives of this study were to characterize and identify the deep levels in SiC hexagonal polytypes of 4H and 6H, with the goal of achieving an increased understanding of the device detracting mechanisms in these materials. Secondary objectives were to utilize deep level transient spectroscopy (DLTS) techniques to investigate the non-radiative carrier capture mechanisms, to determine inequivalent lattice site correlations between deep energy levels, and to increase the capabilities of DLTS methodology in the areas of parameter estimation and thermal scanning capability. Each of these goals and objectives were accomplished. During the course of this effort, an opportunity arose to collaborate on a project that ultimately resulted in the development and demonstration of a novel transient fitting algorithm, which extends the capability of all DLTS researchers using isothermal, digital methods. The contributions resulting from these efforts are:

1). Identified and characterized several new deep level centers in bulk and epitaxial 4H- and 6H-SiC, which had previously been unreported. Electron traps in n-6H-SiC bulk material at energies of E_C-509 and 543 meV; hole traps in p-6H-SiC bulk material at E_V+479 and 862 meV, and a minority carrier electron trap at E_C-780 meV; 4 deep level electron traps at energies of E_C-610, 890, 1100, 1300 meV in n-type 6H-SiC epitaxy; and hole trapping centers in p-6H-SiC epitaxial materials with ionization potentials of E_V+380, 473, and 730 meV. Electron traps in 4H-SiC epitaxy were identified with

energies ranging from 200 to 611 meV below the conduction band and hole traps were revealed with levels above the valence band of 246 to 856 meV.

2). Collaborated on the development of a novel parameter estimation algorithm called the differenced iterative generalized least squares (DIGLS) formalism. This technique was demonstrated to be superior to previous algorithms applied to DLTS transient signals comprised of decaying exponentials.

3). Developed a new analysis methodology for the identification of carrier capture kinetics, such as multi-phonon emission, at deep level centers. This involves using fitting the capacitive decay transient amplitude variations with temperature in accordance with specific model kinetics. As a result of these developments it was discovered that the dominant capture mechanism for traps in 4H and 6H-SiC was lattice relaxation multi-phonon emission. The identifying feature of this mechanism, the large thermally activated capture barrier, was measured for several centers using the new methodology and in two cases by direct measurement of the capture rates. Carrier trapping kinetics had previously not been studied or reported for these materials, and this represents the first data in this area.

4). Demonstrated that the commonly ignored shallow impurity ionized fraction could result in serious DLTS parameter estimation errors for SiC traps if not considered. This was shown through extensive modeling of deep level capture and emission processes in SiC, including calculations for the free carrier concentrations when conductivity is controlled by two or three impurity levels.

5). Demonstrated strong evidence for the assignment of closely spaced deep level energetic pairs to lattice site inequivalencies for two different deep level centers. This had previously not been accomplished using DLTS methods.

6). Investigated and demonstrated the link between diode junction transport characteristics and electroluminescence, to deep level trapping centers in 4H-SiC p^+/n rectifiers. This accomplishment illustrated for the first time the direct connection between the high concentrations of flaws in this material and the limited device development success, which has been realized in these materials to date.

7). Extended the DLTS thermal scanning and measurement capabilities to 800 K, which enables investigation of the wide SiC bandgap to levels previously unexplored. This accomplishment enabled contribution 1).

Efforts focused on identifying and cataloging the frequently occurring deep level traps in both epitaxial and bulk 6H- and 4H-SiC were accomplished by investigating a large number of samples from a wide range of wafer materials. This task was motivated by the lack of information in this area, which is crucial to the successful future development of SiC as a high power, high frequency, and high temperature electronic device material. The need for an extensive data base of the device degrading deep level traps and their sources is fundamental information for crystal growers to utilize in efforts to improve material quality to the levels required for a commercially viable SiC device technology. In order to accomplish this goal, the modifications necessary to extend the temperature capability of the DLTS system from refrigerated helium temperatures to 800

K were acquired and implemented. During this time, additional techniques such as constant capacitance (CCDLTS) transient methods were implemented along with extensive data acquisition and experiment automation software developments. These accomplishments have resulted in the development an implementation of a defect characterization DLTS system which surpasses the capabilities of any other known systems in use today and led to the identification and characterization of the frequently observed deep level defects in 4H- and 6H-SiC which are summarized below in Table IX-1 and Table IX-2. Secondary ion mass spectrometry (SIMS) characterization of the 6H-SiC wafers was also obtained in an effort to identify possible sources for the deep levels characterized in these materials. These measurements revealed the presence of several transition metal (V, Cr, Zr, Cu, Ti, Ni, Mo) impurities in significant concentrations, sometimes exceeding 10^{18} cm^{-3}.

These DLTS system improvements were further enhanced by the collaborative development and demonstration of a novel parameter estimation algorithm which was shown to improve the fidelity and range of useful DLTS data for defect characterization. The differenced iterative generalized least squares (DIGLS) formalism was demonstrated to perform better than previous linear prediction based algorithms. This was shown for simulated exponential decay signals plus noise and on challenging real DLTS data. DIGLS performance in estimating trap parameters from capacitance decay transients from the EL2 level in GaAs and two deep levels in 6H-SiC provided convincing evidence of the significant improvements afforded by the new algorithm.

Table IX-1. Summary of the deep level traps identified in 4H-SiC epitaxial material. Ionization energies, capture cross sections, and trap densities are listed for the most consistently observed centers in the 4H-SiC p^+/n diodes.

Energy Level (meV)	Cross section (cm^2)	Concentration (cm^{-3}) times $5x10^{15}$	Source
E_C-200	$2x10^{-17}$	0.01	Unknown
E_C-280	$4x10^{-17}$*	0.06	Unknown
E_C-349	$1x10^{-16}$	0.09	Unknown
E_C-536	$3x10^{-21}$	0.003	Unknown
E_C-564	$6x10^{-13}$	0.07	Unknown
E_C-585	$2x10^{-14}$	0.002	Unknown
E_C-611	$5x10^{-20}$	0.002	Unknown
E_V+246	$1x10^{-18}$	0.03	Damage ?
E_V+350	$1x10^{-19}$	0.002	Unknown
E_V+680	$2x10^{-12}$	0.3	Damage
E_V+750	$4x10^{-13}$	0.25	Damage
E_V+856	$1x10^{-18}$	0.03	Unknown

* : Identified with MPE capture mechanism, and therefore entry is equal to σ_∞.

Table IX-2. Summary of the deep level traps identified in bulk and epitaxial 6H-SiC material. Ionization energies, capture cross sections, and trap densities are listed for the most consistently observed centers.

Energy Level (meV)	Cross section (cm^2)	Concentration (cm^{-3})	Material	Source
E_C-509	$6x10^{-18}$*	$2.4x10^{16}$	n-bulk	vanadium
E_C-543	$1.75x10^{-16}$*	$4.5x10^{16}$	n-bulk	vanadium
E_C-780	$7x10^{-17}$	$8x10^{16}$	p-bulk	Unknown
E_V+479	$2x10^{-20}$	$1x10^{15}$	p-bulk	Unknown
E_V+862	$2.2x10^{-15}$*	$1.4x10^{16}$	p-bulk	Damage
E_C-610	$7.3x10^{-16}$*	$2.3x10^{16}$	n-epi	Unknown
E_C-890	$2x10^{-16}$	$5.1x10^{13}$	n-epi	Unknown
E_C-1100	$5x10^{-14}$	$2x10^{14}$	n-epi	Unknown
E_C-1300	$9x10^{-13}$	$1.8x10^{14}$	n-epi	Unknown
E_V+380	$4x10^{-19}$	10^{13}	p-epi	Unknown
E_V+473	$2x10^{-20}$	10^{13}	p-epi	Unknown
E_V+730	$1x10^{-17}$	10^{14}	p-epi	Unknown

* : Identified with MPE capture mechanism, and therefore entry is equal to σ_∞.

Investigation of the capture mechanism at deep level defects in 6H- and 4H-SiC led to the discovery that for a significant number of deep levels in both SiC polytypes, free carrier trapping proceeds via lattice relaxation multi-phonon emission. This contribution is being reported for the first time, and results from the development of a new data analysis technique. This method involves fitting the transient amplitude variations as a function of temperature and estimating the MPE trap parameters which predict this variation. The ability to estimate trap parameters in this manner was demonstrated on simulated DLTS transient data that included MPE capture kinetics. The resulting profiles were shown to be proportional to a non-equilibrium quasi-distribution occupation function. The defects identified with this mechanism were found to possess large thermal capture barriers (E_b), which were on the order of the thermal detrapping energy (E_T) of traps studied. This implies a possible link to the semiconductor bandstructure, although additional study and theoretical development are required to verify or deny this possibility.

A solid link to SiC inequivalent lattice sites was demonstrated for a vanadium induced deep center and for a Mg implantation induced deep level pair in bulk 6H-SiC. This connection was made on the basis of the DIGLS resolution of deep level energetic pairs associated with a single rate window peak. Additionally, both the V and Mg centers were found to possess capture mechanisms obeying MPE kinetics with the temperature variation of the cross sections for both energy pairs varying in a manner consistent with the behavior of a single deep level source. Furthermore, the ratios of the trap concentrations for each pair of levels was found to be in almost a 2:1 ratio corresponding

to the natural abundance of the hexagonal and cubic lattice sites in the 6H-SiC crystal. Further verification of site inequivalent pairs was accomplished by comparing the raw experimental data and simulated DLTS data, which were generated by utilizing the estimated inequivalent lattice site trap parameters obtained from empirical data analysis, showing excellent agreement.

In conjunction with the DLTS modeling efforts, it was discovered that the incomplete ionization of the dopant impurities in SiC could affect significant errors in the estimation of deep level trap parameters. The result of ignoring of this condition, which is unique to SiC, was demonstrated on both experimental and simulated data. Surprisingly, this well-known condition has never previously been considered in reports of DLTS or other deep level data on SiC.

The final contribution from this work is related to the identification of the junction transport characteristics and deep level dominated behavior of p^+/n junctions fabricated on 4H-SiC. Well-behaved diodes were shown to have I-V characteristics which were in excellent agreement with the statistical Sah-Noyce-Shockley (SNS) theory. However, significant shunting of both forward and reverse I-V characteristics were observed for the majority of diodes tested, and correlated to the high density of deep level defects found in these samples. Furthermore, the extremely high concentrations of several defect centers observed in this material implied a link to lattice imperfections as their sources. A deep hole trap at E_V+680 meV was found to be the activator for a bright green electroluminescence (EL) as determined by correlating DLTS, I-V-T, and EL data for diodes exhibiting leaky behavior.

Future efforts in the area of SiC defect identification and characterization must emphasize an unequivocal determination of the microscopic sources of the numerous deep levels found in these materials. This can be accomplished by through ion implantation of transition metals and other impurities, and subsequent characterization. This would also allow the investigation of deep level activation related to lattice structural imperfections and damage, which are strongly implicated in the data collected during this effort. Additionally, the need to fully characterize the entire bandgap of SiC or any other wide gap material is crucial to the understanding of the complete deep level picture in these materials. This cannot be accomplished exclusively with thermal techniques, and thus must involve an additional excitation source such as photons. Techniques such as optical admittance spectroscopy and optical DLTS can easily be added to the existing system with only minor modifications to both hardware and data acquisition software routines. These additions would significantly extend the defect characterization capabilities for all wide band gap material systems of interest.

Appendix A

Publication Summary

The following is the complete list of publications resulting from the data and conclusions arrived at during the course of this dissertation. The entries are categorized by publication type. Papers labeled as "to be submitted" indicate articles which have already been prepared in draft form.

Journal Articles:

Improved linear prediction for deep level transient spectroscopy analysis, Ingham E., Scofield J., Pachter M., J. Appl. Phys. **80** (5), 2805 (1996).

Observation of inequivalent lattice site energies for deep level traps in 6H-SiC by isothermal deep level transient spectroscopy, Scofield J., Ingham E., Yeo Y.K., Hengehold R., To be submitted J. Appl. Phys. 1996.

Evidence for nonradiative carrier capture by multi-phonon emission in hexagonal SiC polytypes 4H and 6H, Scofield J., Yeo Y.K., Hengehold R., To be submitted J. Appl. Phys. 1996.

Refereed Conference Proceedings

Deep level investigation of bulk and epitaxial 6H-SiC at high temperatures, Scofield J., Yeo Y., Hengehold R, Inst. Phys. Conf. Ser. No 145, Ch 3, IOP Publishing Bristol UK, (1995).

Deep level study of as-grown and ion implanted bulk and MOCVD grown epitaxial 6H-SiC, Scofield J., Yeo Y., Hengehold R., Inst. Phys. Conf. Ser. No 145, Ch 2, IOP Publishing Bristol UK, (Kyoto, Japan 1995).

Defect dominant junction characteristics of 4H-SiC p+/n diodes, Scofield J., Dunn M., Reinhardt K., Yeo Y., Hengehold R., Proc. Mat. Res. Soc. Spring Meeting, (San Francisco CA), (1996).

Comparative Study of the Junction Characteristics and Performance of SiC p+/n and Schottky Power Rectifiers, Scofield J., Dunn M., Weimeri J., Reinhardt K., Yeo Y.K., and Hengehold R.L., To be published in Compound Semiconductors, Inst. Phys. Conf.

Ser., IOP Publishing Bristol UK Presented at the International Symposium on Compound Semiconductors, (St. Petersburg, Russia September 1996).

Non-refereed Conference Proceedings

Deep level studies specific to the SiC polytypes 6H and 4H, Scofield J., Yeo Y.K., Hengehold R., To be published in Physics of Semiconductors, Proc. International Conf. Phys. Semiconductors, Presented at the conference in Berlin, Germany, (July 1996).

Presentations

American Physical Society Spring Meeting, San Jose, CA (March 1995).

International Symposium on Compound Semiconductors, Cheju S. Korea (August 1995).

Materials Research Society Spring Meeting, San Francisco, CA (April 1996).

International Symposium on Compound Semiconductors, St. Petersburg, Russia (September 1996).

Appendix B

B-I. Secondary Experimental Techniques

B-I-1. Photoluminescence and Electroluminescence. Defect characterization can often be enhanced by the addition of techniques designed to collect and record the optical energy produced by a trapping or recombination event. Recalling the discussions of Chapter III we concluded that the probability of energy conservation, resulting from the emission of optical photons, was much lower than that associated with transitions mediated by collisional or lattice vibrational mechanisms. The key point to remember in dealing with these quantum mechanical probabilities is that each of the transitions will always have a *nonzero* probability of occurance. In other words, a recombination or trapping event will be characterized by the realization of all three processes, although only one will usually dominate. The dominating process was shown to be non-radiative recombination via energy mediated phonon emission. However, under carefully contrived experimental conditions, a competing process can be encouraged to dominate the trapping and recombination kinetics or other processes can be minimized with similar results. As alluded to in Chapter III, temperature control is the most often applied parameter variation utilized to enhance one mechanism while precluding another. As temperature is lowered, occupation numbers of the normal modes are decreased. There will be similar reductions in the numbers associated with free particle distributions with large kinetic energies. Thus, phonon and Auger mechanisms will experience a decrease in recombination probability relative to photon emission, as predicted by Equations III-

18, -19, and -20 for band-to-band transition rates. Photon emission processes will almost never dominate even at the lowest temperatures, however, the intensity of luminescence can frequently be increased to levels sufficient for experimental observation.

Two closely related luminescence techniques were utilized during this study, photoluminescence (PL) and electroluminescence (EL). They differ by the excitation mechanism with which the samples are stimulated to a non-equilibrium state and in their respective sample requirements. Photoluminescence utilizes optical energy to increase the population of upper level excited states by illumination with coherent laser energy, and the resulting photon emission induced by the relaxation back toward equilibrium is recorded and subsequently analyzed. Electroluminescence occurs when the upper state excess population occurs due to the application of an electric field induced injection of energetic free carriers. In the former case, samples are typically restricted to bulk material, while in the latter case p/n junctions are required to realize the necessary concentrations of minority carriers to enable recombination. Similar emission spectra are typically realized between the two techniques. DAP, exciton, and band-to-band recombinations are all found to be observable using both methods. The primary advantage of low temperature PL is in providing greater detail to the sharp excitonic spectral features, which are significantly broadened or quenched by junction heating effects associated with the large current densities often required for EL. Electroluminescence provides an experimental technique which allows the optical exploration of various junctions or barriers, especially those designed for light emission such as heterojunction structures. This enables the determination of recombination

mechanisms in the junction region, which may not be accessable to the exciting laser probe of PL. As such, the two methods are typically complimentary with PL utilized to determine bulk material properties and EL being applied to device-type structures more closely related to the proposed or designed structure.

Photoluminescence was primarily utilized for the determination of radiation damage recovery in 6H-SiC samples subsequent to ion implantation and thermal anneals. The extent of lattice damage recovery was monitored by comparing pre- and post-implantation anneal spectra. Using identical experimental conditions the luminescence intensity peaks of the nitrogen excitonic and N-Al DAP spectra yielded qualitative indications of recrystallization and lattice recovery.

Electroluminescence was successfully used to identify a dominant recombination center in the junction region of p/n rectifying diodes fabricated on 4H-SiC. The associated spectral characteristic was attributed to hole recombination with an electron bound to a deep level proposed to be due to crystalline imperfections in the epitaxial junction region. This conclusion was based on observations of this spectral feature in p/n junctions formed by implantation of energetic Al^- ions. Experimental data and details of the specific parametric conditions for the results obtained using these techniques will be included in the relevent results discussions of following chapters.

Figure B-1 illustrates the block diagram of the hardware and and automated data acquisition controller used for the PL and EL experiments. SiC sample excitation is provided by the Kr^+ ion laser operating on the 350.1 nm ultraviolet frequency line.

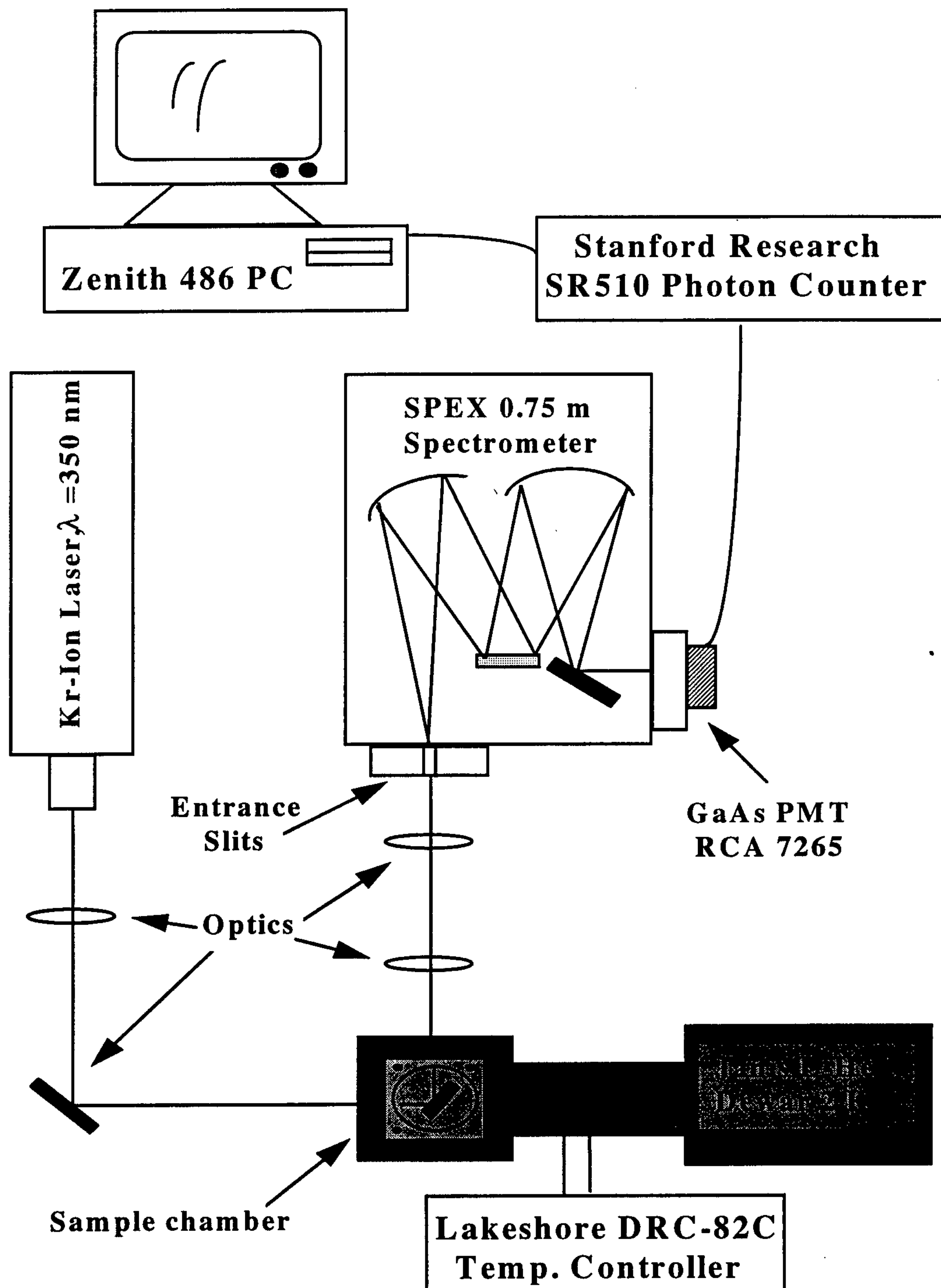

Figure B-1. Photoluminescence experimental hardware block diagram and automated data acquisition controller. Kr^+ laser used to excite non-equilibrium conditions in the SiC bulk material. Electroluminescence utilizes the same hardware minus the laser. Current injection in the junction devices is accomplished using a Keithley 236 source-measure-unit.

Electroluminescence experiments are enabled by replacement of the Kr+ ion laser with a Keithley 236 source-measure-unit to provide the biasing and current sourcing requirements.

Total instrument linewidth (grating + slit width) calculations, for a 3.875 cm wide, 1200 line/mm grating and a typical spectrometer slit width of 25 μm, yield values in the range of 0.3 to 0.31 Å for 300 to 550 nm light. This enabled the reproduction of sharp spectra, such as that exhibited by the SiC nitrogen excitonic transitions.

B-I-2. Temperature Dependent Hall Effect Measurement. Characterization of the free carrier concentration as a function of temperature, using the Hall effect, will yield information regarding the shallow energy levels in a material. Insight into the dominant carrier scattering mechanisms can be obtained by evaluating the temperature dependence of Hall mobility. This technique, while originally developed for characterization of metals, has become an invaluable tool for the determination of shallow impurity ionization energies, through their effect on free carrier concentration. The theory is based on measuring the induced voltage, E_y, resulting from the interactions of an electric current, $\vec{\mathbf{I}}$ and an orthogonal, static, magnetic field, $\vec{\mathbf{B}}$. Figure B-2 graphically illustrates the directions and geometry of the relevent Hall effect quantities on a rectangular slab of material. The Lorentz force on a particle of charge q, moving with velocity $\vec{\mathbf{v}}$, and in the presence of and electric field $\vec{\mathbf{E}}$, and magnetic field $\vec{\mathbf{B}}$, is given by

$$\vec{\mathbf{F}} = q(\vec{\mathbf{E}} + \frac{1}{c}\vec{\mathbf{v}} \times \vec{\mathbf{B}}), \qquad \text{[B-1]}$$

where c = 2.99 x 10^8 m/s is the speed of light. A rigorous solution of the Boltzmann transport equation, using the Lorentz force and the relaxation time approximation, is required to obtain the general solution involving the inverse effective mass, $[m^*]^{-1}$, as a matrix represented tensor quantity [McKelvey, 1986:299]. The relaxation time approximation is an assumption which simplifies the temporal derivative (due to collisions) of the probability distribution function in Boltzmann's equation. In short, the simplification involves replacing the derivative with the difference of the perturbed, non-

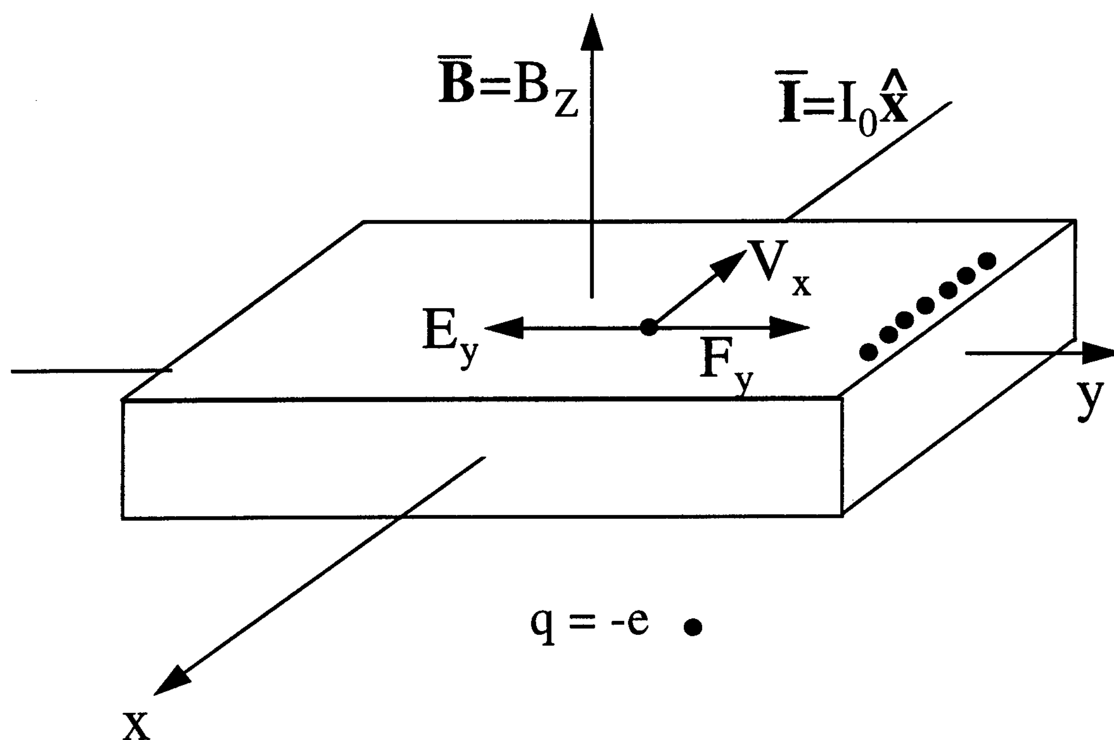

Figure B-2. Diagram illustrating the magnetic $\vec{\mathbf{B}}$-field, current flow $\vec{\mathbf{I}}$, and Lorentz force F_y, which conspire to induce an equilibrating electric field E_y, which characterizes the Hall effect in metals and semiconductors.

equilibrium distribution function (f), and the equilibrium function (f_0) divided by the relaxation or mean free time between collisions (τ). Explicitly,

$$\left(\frac{\partial f}{\partial t}\right)_{Coll} = -\frac{f - f_0}{\tau} .$$

These results are available in most advanced solid state physics texts and will not be reproduced here. Instead a phenomenological description will be given.

As shown in Figure B-2, electrons moving in the x-direction and transverse to a static magnetic field will experience a force equal to (q/c)($\vec{\mathbf{v}}$ x $\vec{\mathbf{B}}$) in the y-direction. Now, if we accept the definition of steady state conditions, which necessitate that there are no net forces on the electron, then a balancing force must exist to exactly balance q($\vec{\mathbf{v}}$ x $\vec{\mathbf{B}}$). This force results from the build-up of electrons along the y-edge of the sample orientation as shown in Figure B-2. When the electrostatic force, E_y, exactly balances the magnetic deflection, then we can write

$$F_y = \frac{q}{c}(\vec{\mathbf{v}} \times \vec{\mathbf{B}}) - eE_y = \frac{ev_x B_z}{c} - eE_y = 0 . \quad \text{[B-2]}$$

Solving Equation B-2 for the induced field, E_y, and using the expression $I_0 = -nev_x$, we obtain the desired simplified result

$$E_y = \frac{v_x B_z}{c} = \frac{-I_0 B_z}{nec} = RI_0 B_z . \quad \text{[B-3]}$$

The quantity R = -(1/nec) is defined as the Hall coefficient which can be seen to be merely the proportionality constant between the Hall field and the current magnetic field

product. The experimental procedure involves sourcing a current, I_0, and measuring the Hall voltage, $V_H = y_0 E_y$, across the width of the sample in the y-direction (y_0) in the presence of an applied magnetic field. The Hall coefficient and the free carrier concentration n can be calculated using the potential-electric field relationship and Equation B-3, respectively. This provides a simple procedure for measuring the free carrier concentration as a function of the controlled sample temperature, yielding information about the ionization energies of the dominant (largest density) impurity in the material. Additionally, if resistivity measurements ($\rho = (ne\mu)^{-1}$) are combined with the Hall coefficient the carrier mobility, μ, may be obtained by

$$R\rho^{-1} = -\frac{1}{nec}(ne\mu) = -\frac{\mu}{c}\,. \qquad [B-4]$$

Of course, this simplified picture must be modified in reality to account for the actual distribution of velocity components, v_x, which will change the values of R slightly. Additionally, the mobility defined in Equation B-4 is not the true drift mobility and is called the Hall mobility. The relationship between the two quantities involves detailed information regarding the actual carrier scattering mechanisms dictating transport in the crystal being characterized. The drift and Hall mobilities are related by

$$\mu = \mu_H \frac{\langle \tau \rangle^2}{\langle \tau^2 \rangle}\,,$$

where the brackets <*> denote the average value and τ is the relaxation time of the dominant scattering mechanism. Fortunately, the ratio of the scattering time constants in most cases deviates only slightly from unity and the Hall mobility is a good

representation of actual drift or conductivity mobilities in the material. Figure B-3 shows a block diagram of the automated Hall measurement system used during this effort. Temperature control was modified for SiC and other wide bandgap materials to enable operation from 77 K to 725 K, enabling characterization of large ionization energy donors and acceptors.

B-I-3. Current Voltage (I-V) and I-V-Temperature Measurements. Current transport mechanisms dictating the junction characteristics of Schottky, p-n or other rectifying barrier can be identified and correlated to observed current versus applied voltage experimental data. In this manner current conduction mechanisms can be determined for a specific junction. Additionally, defect related information relating to the dominant recombination and generation centers can also be ascertained, if the I-V temperature dependence is investigated.

These techniques were applied to 4H-SiC p/n junction diodes and 4H- and 6H-SiC Schottky rectifiers, which were designed as blocking elements for power control circuitry and were obtained from extramural sources. The results of these experiments are disclosed in Chapter VIII.

I-V and I-V-T analysis begins with a model for the transport of carriers across the potential barrier formed by oppositely doped regions, metal-semiconductor interfaces, or the abrupt transition between heterogenous semiconductor materials. During this work, forward biased current conduction characteristics were found to compare favorably with the classical Sah-Noyce-Shockley (SNS) [1957:1228] recombination-generation theory.

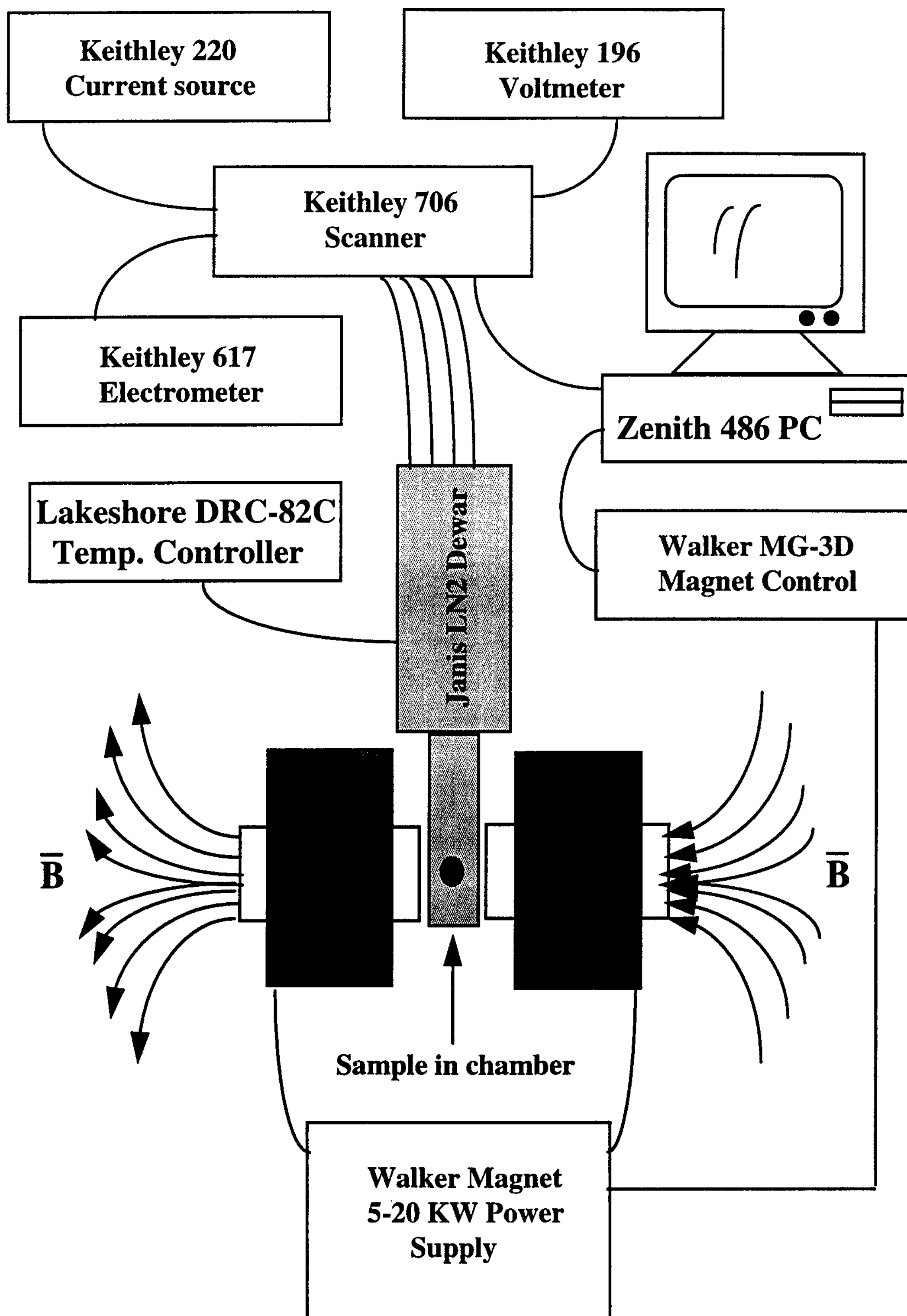

Figure B-3. Automated Hall effect experimental-setup block diagram. System used to characterize n(T), μ, and ΔE for the dominant impurity in a semiconductor.

Forward biased I-V data were fit to this model which in analytic form is given by

$$I = I_{Diff}\exp\left[\frac{qV}{A_1kT}\right] + I_{Rec}\exp\left[\frac{qV}{A_2kT}\right] + I_0\exp[BV] \,, \qquad \text{[B-5]}$$

where I is the total forward bias dark current and V is the applied voltage. The first term in Equation B-5 represents the classic Shockley diode equation, which accounts for the diffusion of carriers across the junction barrier [Sze, 1981:79]. The second term represents the current component due to recombinations of electrons and holes at deep defect levels within the junctions depletion region. The last term describes the current arising from quantum mechanical tunneling across the depletion region. The expression in Equation B-5 is written assuming $V \gg kT/q$ so that the general term $[\exp(qV/AkT)-1]$ is simplified by the dominance of the exponential.

The primary difference between the three mechanisms of conduction current are found in their dependence upon temperature, voltage, and bandgap. The exponential arguments in terms one and two contain the so-called "ideality" factors, A_1 and A_2, which equal 1 for ideal diffusion and approximately 2 for recombination via traps near midgap, respectively. The tunneling factors I_0 and B are empirical fitting parameters but have a theoretical basis related to tunneling effects [Hovel, 1975:253]. Tunneling currents are theorized to be due to junction defects or damage and/or leakage at the device periphery. Expressions for the exponential coefficients of terms one and two are given as [Sze, 1981:79-92]

$$I_{Diff} = qS\left(\frac{D_n n_p}{L_n} + \frac{D_p p_n}{L_p}\right) = J_{Diff}S \qquad \text{[B-6]}$$

and

$$I_{Rec} = \frac{qSn_i W_d \times f(b)}{\left(\tau_{p0}\tau_{n0}\right)^{1/2} \frac{(V_{bi} - V)q}{kT}} = J_{Rec}S \ , \qquad \text{[B-7]}$$

where the factor f(b) is a function of the recombination center ionization energy, ΔE, and the electron and hole minority carrier lifetimes τ_{n0} and τ_{p0}, respectively. The factors D_n and D_p, n_p and p_n, L_n and L_p are the diffusion coefficients, minority carrier densities, and the diffusion lengths of electrons and holes, respectively, and S is the diode area. All other factors carry their previous definitions. If we assume an abrupt, assymetrically doped junction (p^+/n), then depletion will occur primarily in the n-type material and $n_p << p_n$. Using these approximations and the minority carrier density expression ($p_n = n_i^2/N_D$) we can write the exponential coefficients to explicitly reflect their temperature dependence as

$$I_{Diff} = qS\left(\frac{D_p p_n}{L_p}\right) = qS\left(\frac{D_p}{L_p}\right)\left(\frac{n_i^2}{N_D}\right) \propto T^3 e^{-E_G/kT} \qquad \text{[B-8]}$$

and

$$I_{Rec} \propto T^{5/2} e^{-E_G/2kT} . \qquad \text{[B-9]}$$

Thus, we have the desired expressions which are used to describe the I-V dependence upon temperature as well as the applied bias. Numerical values for I_{Rec} and I_{Diff} are fitting

parameters obtained by numerically applying the model of Equation B-5 to the experimentally obtained data. Arrhenius plots can then be constructed to yield information about the temperature dependence of the current conduction mechanisms. Explicit examples of these procedures are given in Chapter VIII.

Reverse bias I-V-T measurements can also be used to estimate the ionization energy of deep levels, which limit reverse bias dark current if the leakage current is trap dominated [Reinhardt, 1996:5763]. If reverse leakage current, I_{Rev}, is trap dominated, then a thermally generated depletion region component, I_{Gen}, will describe carrier transport. Neglecting other components, if $I_{Rev} = I_{Gen}$, a simple expression can be written which defines the temperature dependence of the diodes reverse leakage current

$$I_{Rev} \propto W_d \exp\left(\frac{-E_a}{kT}\right), \qquad \text{[B-10]}$$

where

$$E_a = \begin{cases} E_C - \Delta E & \text{if } \Delta E > E_i \\ \Delta E - E_V & \text{if } \Delta E < E_i \end{cases}. \qquad \text{[B-11]}$$

E_a is the activation energy of the generation center, E_i is the intrinsic Fermi level, E_C and E_V are the conduction and valence band extrema, respectively, and recall, W_d is the depletion width.

Reverse bias I-V-T data for the 4H-SiC p/n diodes provided corroboration of several deep defect levels characterized using DLTS and EL techniques. This data summary is presented in Chapter VIII.

I-V and I-V-T characterization of Schottky barrier diode junction characteristics proceeds in exactly the same manner as that for p/n junction diodes. The only modification required is obviously to utilize models appropriate for the current conduction mechanisms in a Schottky barrier diode. Assuming operation under the Schottky limit, there are four basic current transport processes, which are illustrated in Figure B-4 for an n-type semiconductor. Operation within the Schottky limit results when the junction barrier height, ϕ_B can be described as the difference between the work functions of the metal, ψ_M, and the semiconductor, ψ_{SC} ($\phi_B = \psi_M - \psi_{SC}$). The work

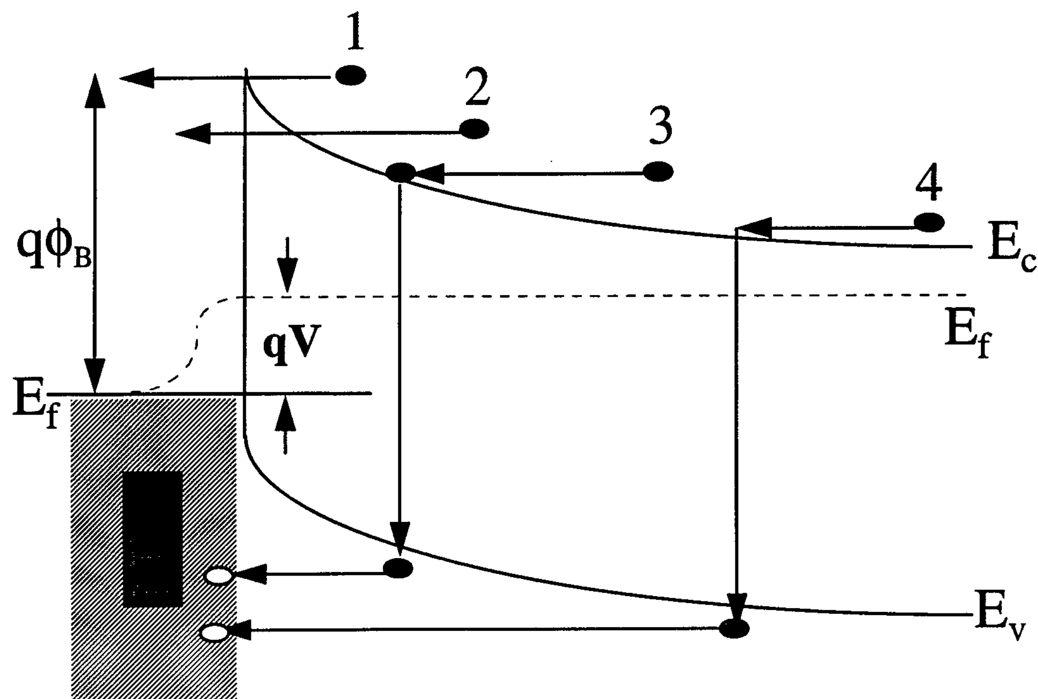

Figure B-4. The four basic current transport processes in a Schottky barrier diode with an applied bias, V. Thermonic emission and diffusion 1), tunneling 2), depletion region recombination 3), and minority carrier injection from the metal 4) (equivalent to 3).

function being defined as the energy required to remove an electron from the Fermi level, E_f, to the vacuum outside the material, upon which it possess zero kinetic energy. Referring to Figure B-4, the mechanism which typically dominates is the flow of electrons over the barrier, labeled by 1 in the figure. This component was originally described by Bethe's [1942:12-43] thermonic emission theory and by the diffusion theory of Schottky [1938:843]. However, Crowell and Sze subsequently developed a concise theory, successfully incorporating both mechanisms [Sze, 1981:254]. Their expression for thermonic-diffusion current is given as

$$I_{T-D} = SA^{**}T^2 \exp\left(\frac{-q\phi_B}{kT}\right)\left[\exp\left(\frac{qV}{\alpha kT}\right)-1\right] = I_S\left[\exp\left(\frac{qV}{\alpha kT}\right)-1\right], \qquad \text{[B-12]}$$

with A** being the effective Richardsons constant modified to account for electron-phonon interactions and quantum mechanical reflections from the Schottky barrier, and S is again the diode area. The empirical ideality factor, α, in Equation B-12 is a measure of the transport contribution from tunneling (also called field emission), equaling one (1) when this effect is absent. Analogous to the situation described for p/n junctions above, we again have an I-V relationship with a well defined temperature dependence from which factors ϕ_B and α may be extracted from experimental data.

If α in Equation B-12 becomes significantly greater than one (1), then tunneling effects are dominant and the I-V theory must be modified to include this effect. The tunneling mechanism corresponds to the transport represented by label 2 in the illustration of Figure B-4. Normally this characteristic dominates only when high doping concentrations are present, and is the mechanism most often responsible for linear I-V

behavior associated with ohmic contacts. The expression representing this second carrier transport mechanism in Schottky diodes is

$$I_T = C\exp\left(\frac{-q\phi_B}{E_{00}}\right) \quad \text{where} \quad E_{00} = \frac{q\hbar}{2}\sqrt{\frac{N_D}{\varepsilon_s m^*}}\ , \qquad \text{[B-13]}$$

where ε_s is the dielectric constant of the semiconductor, and C is a constant.

The third current conduction mechanism is attributed to recombination in the depletion or space-charge region of the junction. This component is identical to the recombination theory of p/n junctions and is labeled 3 in Figure B-4. If the diode bias is such that V >> kT/q then the recombination current is given by the second term of Equation B-5 and varies as

$$I_{Rec} \propto \exp\left(\frac{qV}{2kT}\right).$$

The Schottky diode transport component 4 in Figure B-4 is due to minority carrier (holes in this example) injection from the metal. Conversely, it is easier to understand this mechanism as originating from electrons in occupied valence band states whose wavefunctions have a significant overlap with available states in the distribution function of electrons in the metal. These electrons are thus "injected" into the metal leaving behind empty valence band states (holes). The 1-D equation for minority carrier (hole) current is obtained from the difference between drift and diffusion components

$$I_p = S\left(q\mu_p p_n E - qD_p \frac{\partial p_n}{\partial x}\right),$$

where E is the applied electric field, p_n is the hole density, and μ_p is the hole mobility. Under low forward bias conditions the diffusion term dominates and assuming that the diffusion length, L_p, is greater than the depletion width, W, the minority carrier hole current corresponding to Figure B-4 can be written as

$$I_p = \frac{SqD_p}{W} p_n \left[\exp\left(\frac{qV}{kT}\right) - 1 \right] = \frac{SqD_p}{W} \frac{n_i^2}{n} \left[\exp\left(\frac{qV}{kT}\right) - 1 \right], \qquad \text{[B-14]}$$

where the equilibrium concentration expression $n_i^2 = p_n n$ has been used.

The injection of minority carriers in a Schottky diode is typically a small fraction of the total current flow. Minority carrier to total current ratios have been predicted to be in the 10^{-5} range for low injection conditions in Si [Sze, 1981:269]. Additionally, this ratio is proportional to n_i^2 and therefore exponentially dependent upon the semiconductor bandgap ($\exp[-E_G/2kT]$). Thus, minority carrier injection is expected to be negligible for wide bandgap materials such as SiC. This conclusion is supported by the I-V and I-V-T characteristics observed on the SiC Schottky diodes which were investigated during this study.

A software program was developed to automate the I-V and I-V-T data collection. A Keithley 236 source-measure-unit, which incorporates both power supply and electrometer functions, was the primary instrument used to perform these measurements. The LabWindows® programming environment was utilized to accomplish implement these instrumentation and data collection routines. A listing of the software is included in Appendix D.

Figure B-5 shows the various simple device structures characterized using the electrical measurement techniques outlined in Chapter IV and this appendix. These structures enabled the determination of current conduction mechanisms, deep trapping

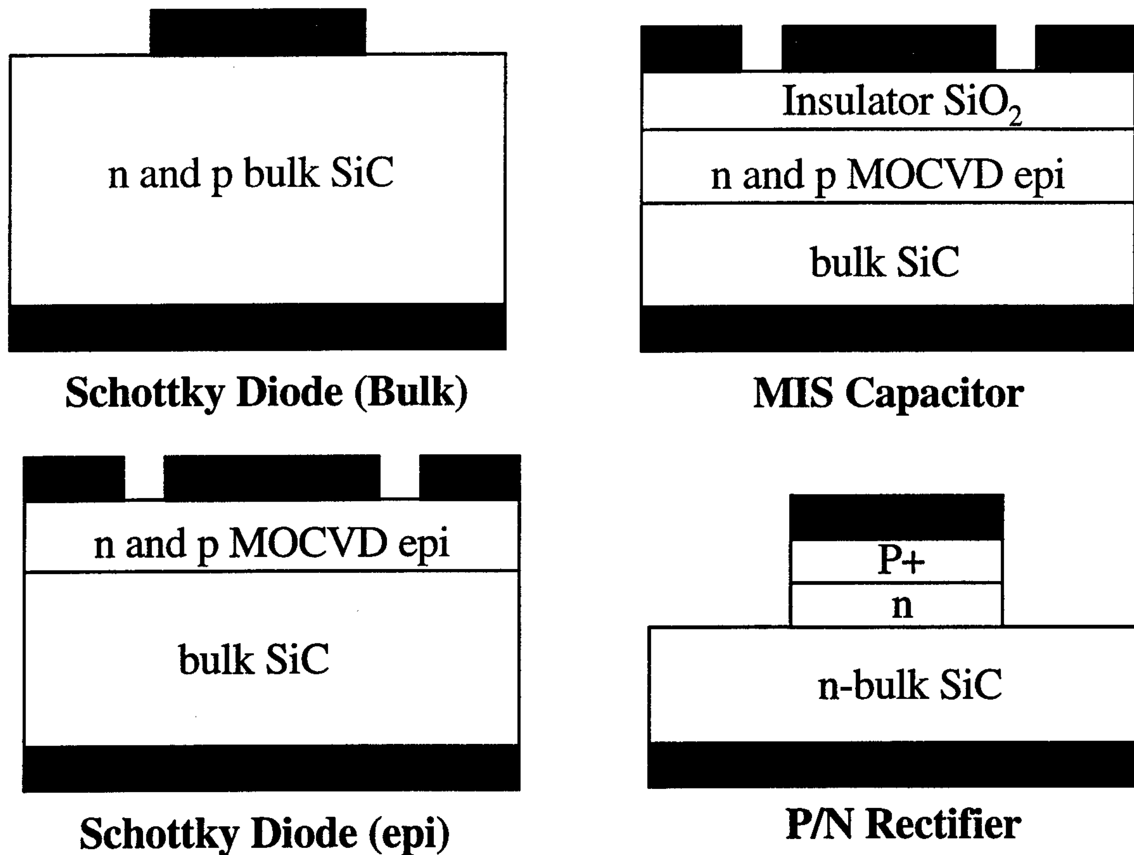

Figure B-5. Device structures utilized to perform electrical characterizations during the SiC study. The shaded regions correspond to device metallizations, which form either ohmic or rectifying (Schottky) contacts on the various bulk and epitaxial surfaces. Typical substrate doping concentrations were in the 10^{17} to 10^{18} cm^{-3} range, and epitaxial conductivities were determined by doping densities from between $5x10^{15}$ to 10^{17} cm^{-3}.

level identification, and electrically induced photon emission spectra. All substrate doping densities were in the 10^{17} to 10^{18} cm^{-3} range and epitaxial doping varied from between $5x10^{15}$ to 10^{17} cm^{-3}.

Due to the very chemically inert nature of the SiC crystal, device processing to form even these simple structures required significant iteration to develop a procedure which would yield functional devices. Difficulty in realizing ohmic contacts with linear I-V characteristics, Schottky junctions with minimal leakage current densities, and uniform SiO_2 coverage with desired insulating characteristics was exacerbated by the non-reactive nature of the SiC surfaces. Acids and caustics were very ineffective in cleaning the sample surfaces prior to metallization and residual contamination plagued device performance. Gleaning information regarding sample preparation chemistry from the literature and performing numerous trial-and-error experiments led to the identification of four device processing recipes, which are detailed in Appendix C.

Appendix C

Due to the very chemically inert nature of SiC, sample preparation for device fabrication is not a trivial matter. The four recipes outlined and listed below were designed after numerous trial and error experiments. The resulting procedures, although lengthy, have been determined to yield SiC surfaces suitable for simple device fabrication.

Process I and Ia involve a sacrificial thermal oxide growth for MIS and Schottky devices, respectively. The oxide is grown in a quartz tube furnace heated to 1100°C, with a wet O_2 atmosphere introduced by bubbling O_2 through H_2O maintained at 90°C. During the SiO_2 growth, a thin SiC surface layer is consumed in order to liberate the Si required to complete the growth chemistry. As a result, when the grown SiO_2 layer is subsequently etch removed in concentrated hydrofluoric acid, a fresh SiC surface for metal deposition is realized. Processes II and IIb are chemical-only recipes, which were identified as adequate for the preparation of SiC surfaces. These two processes were primarily used for the preparation of surfaces which were intended for ohmic contact metallization. For all SiC samples, the ohmic contact metallizations used were Al (p-type) and Ni (n-type) annealed at 830°C and 1050°C, respectively, for 10 minutes in an Ar atmosphere. N- and p-type Schottky diodes were formed using various as-deposited metals (Al, Ni, Au, Ti, Pt) without a thermal anneal step. Molybdenum was the contact metal utilized for the SiO_2 surface of the MIS devices.

Sample Processes for SiC Capacitor/Diode pre-Fabrication Surface Prep

Process I. Oxide Growth/Etch Removal for MIS Devices

Step 1) Organic Solvent Degrease
- i) Acetone (5 min @ 30°C)
- ii) TCE (5 min @ 30°C)
- iii) Acetone (5 min @ 30°C)
- iv) Methanol (5 min @ 30°C)
- v) Propanol (5 min @ 30°C)
- vi) H_2O Rinse, N_2 Blow Dry

Step 2) Acid Cleanse
- i) H_2SO_4 (5 min @ 50°C)
- ii) $NH_4OH:H_2O_2$ (1:1) (5 min @ 30°C)
- iii) HF (1 min @ 30°C)
- iv) H_2O Rinse, N_2 Dry

Step 3) Wet Oxide Growth
- i) Heat Tube furnace 1050°C to 1100°C
- ii) Place samples in tube with wet O_2 gas flow (O_2 bubbling through D.I. H_2O @ 90°C)
- iii) Insert tube in pre-heated furnace
- iv) Duration 3 to 5 hours

Step 4) Oxide Removal
- i) HF (5 min @ 30°C)
- ii) K_2CO_3 (10 min @ 50°C) (20% solution 5g K_2CO_3 powder with 25g H_2O)
- iii)HCL:H_2O (1:9, 10% solution) (5 min @ 30°C)
- iv) H_2O Rinse N_2 Dry

(**NOTE:** Step 4 should only be performed immediately prior to subsequent insulator deposition. Storage in methanol during transportation is acceptable to inhibit clean surface contamination)

Step 5) Oxide Regrowth/Insulator Deposition
- i) oxide growth using Step 4)/insulator deposition CVD etc.
- i) for SiO2 insulator follow the next three steps at completion of growth run
- ii) Slow or fast cool samples to < 50°C
- iii) Flow Ar gas in tube
- iv) Anneal oxidized samples at growth temperature for 30 min.
- v) Slow cool samples to ambient by shutting down furnace with tube and samples remaining loaded

Step 6) Device Processing
- i) front contacts deposit
- ii) spin/bake PR on top
- iii) oxide removal, dilute HF (10% w/H_2O)
- iv) deposit ohmic
- v) remove PR
- vi) anneal ohmic
- vii) slow cool samples

Process II Chemical Only Surface Prep for MIS Devices

Step 1) Organic Solvent Degrease
- i) Acetone (5 min @ 30°C)
- ii) TCE (5 min @ 30°C)
- iii) Acetone (5 min @ 30°C)
- iv) Methanol (5 min @ 30°C)
- v) Propanol (5 min @ 30°C)
- vi) H_2O Rinse N_2 Dry

Step 2) Acid "Etch"
- i) H_2SO_4:H_2O_2 (1:1, 15 min @ 30°C)
- ii) H_2O Rinse
- iii) Buffered HF (5 min @ 30°C)
- iv) NH_4OH:H_2O_2:H_2O (1.5:1.5:5, 5 min 2 boil)
- v) H_2O Rinse
- vi) HCl:H_2O_2:H_2O (1.5:1.5:5, 5 min @ boil)
- vii) H_2O Rinse

Step 3) Oxide Growth/Insulator Deposition
- i) oxide growth using Step 4 Process I)/insulator deposition CVD etc.
- i) for SiO_2 insulator follow the next three steps at completion of growth run
- ii) Slow or fast cool samples to < 50°C
- iii) Flow Ar gas in tube
- iv) Anneal oxidized samples at growth temperature for 30 min.
- v) Slow cool samples to ambient by shutting down furnace with tube and samples remaining loaded

Step 4) Device Processing
- A) **MIS** devices
  - i) front contacts deposit
  - ii) spin/bake PR on top
  - iii) deposit ohmic
  - iv) remove PR
  - v) anneal ohmic
  - vi) slow cool samples

Process Ia. Oxide Growth/Etch Removal for Schottky Devices

Step 1) Organic Solvent Degrease
- i) Acetone (5 min @ 30°C)
- ii) TCE (5 min @ 30°C)
- iii) Acetone (5 min @ 30°C)
- iv) Methanol (5 min @ 30°C)
- v) Propanol (5 min @ 30°C)
- vi) H_2O Rinse N_2 Dry

Step 2) Acid Cleanse
- i) H_2SO_4 (5 min @ 50°C)
- ii) NH_4OH:H_2O_2 (1:1) (5 min @ 30°C)

iii) HF (1 min @ 30°C)
iv) H_2O Rinse N_2 Dry

Step 3) Wet Oxide Growth
i) Heat Tube furnace 1050°C to 1100°C
ii) Place samples in tube with wet O_2 gas flow
iii) Insert tube in pre-heated furnace
iv) Duration 3 to 5 hours

Step 4) Oxide Removal
i) HF (5 min @ 30°C)
ii) K_2CO_3 (10 min @ 50°C) (20% solution 5g K_2CO_3 powder with 25g H_2O)
iii)HCL:H_2O (1:9, 10% solution) (5 min @ 30°C)
iv) H_2O Rinse N_2 Dry

(NOTE: This step should only be performed immediately prior to subsequent metallization deposition. Storage in methanol prior to deposition is acceptable.)

Step 5) Device Processing backside ohmic contacts
i) spin/bake PR on front surface of sample
ii) deposit ohmic metal
iii) remove PR front surface
iv) anneal ohmic (Ni 5 min @ 1030°C, Al 5 min @ 830°C)

Step 6) Process diode contacts
i) Clean front surface using Step 2) above and substitute 1 min for 5 min acid dips
ii) Pattern PR
iii) Deposit metal
iv) Liftoff

Process IIa Chemical Surface Prep Schottky Devices

Step 1) Organic Solvent Degrease
i) Acetone (5 min @ 30°C)
ii) TCE (5 min @ 30°C)
iii) Acetone (5 min @ 30°C)
iv) Methanol (5 min @ 30°C)
v) Propanol (5 min @ 30°C)
vi) H_2O Rinse N_2 Dry

Step 2) Acid "Etch"
i) H_2SO_4:H_2O_2 (1:1, 15 min @ 30°C)
ii) H_2O Rinse
iii) Buffered HF (5 min @ 30°C)
iv) NH_4OH:H_2O_2:H_2O (1.5:1.5:5, 5 min 2 boil)
v) H_2O Rinse
vi) HCl:H2O2:H2O (1.5:1.5:5, 5 min @ boil)
vii) H_2O Rinse

Step 3) Device Processing Ohmic contacts
i) spin/bake PR on front surface of sample
ii) deposit ohmic metal

iii) remove PR front surface
iv) anneal ohmic (Ni 5 min @ 1030°C, Al 5 min @ 830°C)

Step 4) Process diode contacts
i) Clean front surface using Step 2) above and substitute 1 min for 5 min acid dips
ii) Pattern PR
iii) Deposit metal
iv) Liftoff

Appendix D

I-V-T Data Acquisition and Experiment Automation Software

The following program listing represents the Basic programming code for the automation of the I-V and I-V-T data acquisition procedures. This code was written as part of the research project and represents one of the tasks accomplished during the course of this project. The software is executed in the LabWindows® programming and development environment.

I-V-T Basic Code Listing.

```
'MEASURE, PLOT AND SAVE I-V-T MEASUREMENTS FOR CORRECTION OF C-V
'PROFILES, DETERMINATION OF CURRENT CONDUCTION MECHANISMS, DEEP LEVEL
'ACTIVATION ENERGIES ETC. FOR C-V CORRECTION, VOLTAGES USED SHOULD BE
'IN'THE SAME RANGE AS THOSE USED IN THE C-V PROFILE.
'Last edit 2-9-96 jds

DECLARE SUB RUNIT (FILBUF$)
DECLARE SUB IVRUN (FILBUF$)
DECLARE SUB PLOTSCRN ()
DECLARE SUB SAVEIT (FILBUF$)
DECLARE SUB SETGAIN (vdamax#, vdamin#, gain%)
DECLARE SUB TEMPCONTROL (CONTEM%)
DECLARE SUB TEMPCONTROL1 (IVHANDLE%,TEMNOW#)
DECLARE SUB TEMPCONTROL2 (IVHANDLE%,TEMNOW#)
DIM VOLTSOUT#(1200), VOLTSIN#(1200),VOLTSIND#(1200)
DIM CURRENT#(1200), CURRENT2#(1200),CURRENT3#(1200)
DIM FILBUF AS STRING * 80
COMMON SHARED /VOLTSOUT/VOLTSOUT#()
COMMON SHARED /VOLTSIN/VOLTSIN#()
COMMON SHARED /VOLTSIND/VOLTSIND#()
COMMON SHARED /CURRENT/CURRENT#()
COMMON SHARED /CURRENT2/CURRENT2#()
COMMON SHARED /CURRENT3/CURRENT3#()
COMMON SHARED /IVHANDLE/IVHANDLE%
COMMON SHARED /BARHAN1/BARHAN1%
COMMON SHARED /count/count%
COMMON SHARED /gain/gain%
COMMON SHARED /NPTS/NPTS%
COMMON SHARED /TEMPARRAY/TEMPARRAY#()
COMMON SHARED /TEMNOW/TEMNOW#
COMMON SHARED /TRANUM/TRANUM%
```

```
COMMON SHARED /TGAIN/TGAIN%
COMMON SHARED /TRATE/TRATE%
COMMON SHARED /TRESET/TRESET%
COMMON SHARED /DONE1TEMP1/DONE1TEMP1%
COMMON SHARED /DONE1TEMP2/DONE1TEMP2%
COMMON SHARED /DONE1/DONE1%
COMMON SHARED /CONTEM/CONTEM%
COMMON SHARED /FLAGFILE/FLAGFILE%
COMMON SHARED /TOOK1/TOOK1%
COMMON SHARED /NUMACC/NUMACC%
REM $INCLUDE: 'IVMEASUR.INC'
i..ret% = DAQ.Config (1, 1, 0)
i..ret% = AI.Configure (1, -1, 1, 10, 0, 0)
i..ret% = Set.DAQ.Device.Info% (1, 14000&, 35300&)
i..ret% = Timeout.Config% (1, 3200&)
NUMACC%=90 'Timeout stop number
TRANUM%=0  'INDEX FOR THE NUMBER OF TRANSIENTS TAKEN
const true=1
const false=0
done1temp2%=0
done1temp1%=0
TOOK1%=0
IVHANDLE% = LoadPanel ("IVMEASUR.UIR", IVMEAS)
BARHAN1%=LOADMENUBAR ("IVMEASUR.UIR",IVMENBAR)
DIM TEMPARRAY#(0)
quit.app%=0

REM      ****** MAIN PROGRAM *********

WHILE quit.app%=0
   t..00000% = DisplayPanel (IVHANDLE%)
   ER% = GetUserEvent% (1, BARHAN1%, CTRLM%)

   SELECT CASE CTRLM%
    CASE IVMENBAR.SAMPL1
       CALL RUNIT (FILBUF$)
    CASE IVMENBAR.SAVEIT
       CALL SAVEIT (FILBUF$)
    CASE IVMENBAR.RUNIT
       CALL IVRUN (FILBUF$)
    CASE IVmenbar.fiLMAN
       FLAGFILE% = FileSelectPopup ("c:\lw\IVCURVES\", "noname.IV", "I-V DATA FILE", 0, 0, 1,
FILBUF$)
    CASE IVMENBAR.TEMPSTAB
       ' USER PRESSED THE STABILIZE TEMPERATURE BUTTON
       CALL TEMPCONTROL (CONTEM%)
    CASE IVMENBAR.PLOTIT
      IF FLAGFILE% THEN
        I..DUMMY% = SetCtrlVal% (IVHANDLE%, IVMEAS.MESBOX%, FILBUF$)
      END IF
      i..ret% = OutputPanel (0, "", 1, IVHANDLE%)
    CASE IVMENBAR.QUITIT
       REM USER PRESSED THE QUIT BUTTON
```

```
        QUIT.APP%=1
      CASE IVMEAS.PLOTYP
        CALL PLOTSCRN
      CASE ELSE
        I..DUMMY% = SetCtrlVal% (IVHANDLE%, IVMEAS.MESBOX%, "Set parameters or select
menu command")
    END SELECT
WEND

er% = CloseInterfaceManager

REM   *********** SUBROUTINES ********************

SUB PLOTSCRN
  i..ret% = GetCtrlVal (IVHANDLE%, IVMEAS.PLOTYP%, PLOTYP%)
  IF PLOTYP%=0 THEN     'SWITCH TO LINEAR PLOT
    IF TOOK1%=1 THEN
      i..ret% = DeletePlots (IVHANDLE%, IVMEAS.CURVVOL%)
    END IF
    i..ret% = SetGraphAttribute (IVHANDLE%, IVMEAS.CURVVOL%, 21, 0)
    i..ret% = PlotXY (IVHANDLE%, IVMEAS.CURVVOL%, VOLTSIN#(), CURRENT2#(), NPTS%,
4, 4, 0, 0, 1, 15)

  ELSE              'SWITCH TO LOG PLOT
    IF TOOK1%=1 THEN
      i..ret% = DeletePlots (IVHANDLE%, IVMEAS.CURVVOL%)
    END IF
    i..ret% = SetGraphAttribute (IVHANDLE%, IVMEAS.CURVVOL%, 21, 1)
    i..ret% = PlotXY (IVHANDLE%, IVMEAS.CURVVOL%, VOLTSIN#(), CURRENT3#(), NPTS%,
4, 4, 0, 0, 1, 15)
  END IF
  TOOK1%=1
END SUB

SUB IVRUN(FILBUF$)
  WHILE DONE1%<>1
   I..DUMMY% = SetCtrlVal% (IVHANDLE%, IVMEAS.MESBOX%, "Stabilizing Temperature")
   CALL TEMPCONTROL (CONTEM%)
   IF DONE1%=0 THEN
     CALL RUNIT (FILBUF$)
     I..DUMMY% = SetCtrlVal% (IVHANDLE%, IVMEAS.MESBOX%,"Recording transients")
     CALL SAVEIT (FILBUF$)
     I..DUMMY% = SetCtrlVal% (IVHANDLE%, IVMEAS.MESBOX%,"Saving data")
   END IF
  WEND
  DONE1%=0
  TRANUM%=0
  i..ret% = MessagePopup% ("Done")
END SUB

SUB RUNIT(FILBUF$)

  DIM ISTRING AS STRING *26
```

```
   DIM VOLDATA AS STRING *80
   DIM DUM AS STRING *80
   DIM PROG AS STRING *80
   DIM ENTER AS STRING *80
   I..DUMMY% = GetCtrlVal (IVHANDLE%, IVMEAS.STAVOL%, STAVOL#)
   I..DUMMY% = GetCtrlVal (IVHANDLE%, IVMEAS.ENDVOL%, ENDVOL#)
   I..DUMMY% = GetCtrlVal (IVHANDLE%, IVMEAS.NPTS%, NPTS%)
   i..ret% = GetCtrlVal (IVHANDLE%, IVMEAS.DELA%, DELA#)
   STEPV#=(STAVOL#-ENDVOL#)/NPTS%
   CALL ibfind ("GPIB0", ieee%)
   CALL ibfind ("DEV6", HCSMU%)
   CALL ibclr (HCSMU%)
   CALL Clear1D (VOLTSOUT#(), NPTS%)
   CALL Clear1D (VOLTSIN#(), NPTS%)
   CALL Clear1D (VOLTSIND#(), NPTS%)
   CALL Clear1D (CURRENT#(), NPTS%)
   LOOPVOL1#=STAVOL#
   CALL IBWRT(HCSMU%, "F0,0X"+CHR$(13)+CHR$(10))
   CALL IBWRT(HCSMU%, "L1e-1,0X"+CHR$(13)+CHR$(10))
   CALL IBWRT(HCSMU%, "S2X"+CHR$(13)+CHR$(10))
   CALL IBWRT(HCSMU%, "P0X"+CHR$(13)+CHR$(10))
   CALL IBWRT(HCSMU%, "N1X"+CHR$(13)+CHR$(10))
   FOR I=0 TO NPTS%
    LOOPVOL#=LOOPVOL1# - i*STEPV#
    CALL fillbytes (prog$,0,30,32)
    NB%=FMT(prog$, "%s<B%f,0,%f[p0]X"+CHR$(13)+CHR$(10), LOOPVOL#,DELA#)
    L&=STRINGLENGTH(prog$)
    I..RET%=ILWRT(HCSMU%, PROG$,L&)
    CALL IBWRT(HCSMU%, "H0X"+CHR$(13)+CHR$(10))
    CALL IBWRT(HCSMU%, "G5,2,0X"+CHR$(13)+CHR$(10))
    CALL ibrd (HCSMU%, ISTRING$)
    N%=SCAN (ISTRING$, "%s[i12]>%f",CURRENT#(I))
    N%=SCAN (ISTRING$, "%s[w11]>%f",VOLTSIN#(I))
    CURRENT2#(I)=CURRENT#(I)
    CURRENT3#(I)=ABS(CURRENT#(I)) 'ABSOLUTE VALUE OF CURRENT FOR LOG PLOT
    I..DUMMY% = SetCtrlVal% (IVHANDLE%, IVMEAS.CURMEA%, CURRENT#(I))
   NEXT I
   i..ret% = SetCtrlAttribute (IVHANDLE%, IVMEAS.PLOTYP%, 15, 1)
   CALL IBWRT(HCSMU%, "B0,0,50X"+CHR$(13)+CHR$(10))
   CALL IBWRT(HCSMU%, "N0X"+CHR$(13)+CHR$(10))
   CALL PLOTSCRN
   BEEP
END SUB

SUB SAVEIT (FILBUF$)
   IF FLAGFILE%=0 THEN
     FLAGFILE% = FileSelectPopup ("C:\LW\IVCURVES", "noname.IV", "I-V CURVE", 0, 0, 1,
FILBUF$)
   END IF
   FILHAN%=OPENFILE (FILBUF$,2,1,1)
   N%=FmtFile (filhan%, "%s<%s"+ CHR$(10), date$)
   N%=FmtFile (filhan%, "%s<%f"+ CHR$(10),TEMNOW#)
   N%=FmtFile (filhan%, "%s<V,I"+ CHR$(10))
```

```
    FOR I=0 TO NPTS%-1
     N%=FMTFILE (FILHAN%, "%s<%f %f" + CHR$(10),VOLTSIN#(I), CURRENT#(I))
    NEXT I
    N%=FmtFile (filhan%, "%s<"+ CHR$(10))
    i..ret% = CloseFile (FILHAN%)
    TRANUM% = TRANUM% + 1
END SUB

SUB TEMPCONTROL (CONTEM%)
  I..DUMMY% = GetCtrlVal (IVHANDLE%, IVMEAS.CONTEM%,CONTEM%)
  IF CONTEM%=1 THEN  'RMC cold head w/Lakeshore control selected
     if done1temp2% =0 then
       TGAIN%=12
       TRATE%=0
       TRESET%=2
       done1temp2%=1
     end if
     CALL TEMPCONTROL1 (IVHANDLE%,TEMNOW#)
  ELSEIF CONTEM%=2 THEN 'Janis-Lakeshore cold head selected
     if done1temp1% =0 then
       TGAIN%=200
       TRATE%=0
       TRESET%=100
       done1temp1%=1
     end if
     CALL TEMPCONTROL2 (IVHANDLE%,TEMNOW#)
  END IF
END SUB

SUB TEMPCONTROL1 (IVHANDLE%,TEMNOW#)
   i..ret% = GetCtrlVal (IVHANDLE%, IVMEAS.STATEM%, STATEM#)
   i..ret% = GetCtrlVal (IVHANDLE%, IVMEAS.ENDTEM%, ENDTEM#)
   i..ret% = GetCtrlVal (IVHANDLE%, IVMEAS.TEMINC%, TEMINC#)
   SPOINT#=STATEM#+TRANUM%*TEMINC#
   TEMNOW#=SPOINT#
   CALL ibfind ("GPIB0", IEEE%)
   CALL ibfind ("DEV7", LSTEMP%)
   CALL ibfind ("DEV2", PULSER%)
dim temout as string * 5
dim TEMPROG AS STRING * 23
DIM TEMP AS STRING * 10
dim TEMPROGin AS STRING * 38
dim buf as string * 5
dim buf2 as string * 7
dim buf4 as string * 13
DONE1%=0
IF SPOINT#>ENDTEM# THEN
  if contpul%=1 then
    i..ret% = WFM.Group.Control (1, 1, 0)
  end if
  i..ret% = AO.VWrite (1, 0, 0.0#)
  TEMNOW#=290
  DONE1%=1
```

```
END IF
IF i..ret%<>256 then
   call ibwrt (LSTEMP%, "*RST"+CHR$(13)+CHR$(10))'reset if error condition
END IF
CALL ibwrt (LSTEMP%, "*ESR?"+CHR$(13)+CHR$(10))
CALL ibrd (LSTEMP%, TEMP$)
   'SETPOINT
n%= fmt (buf2$, "%s<%f[p2]", temnow#)
N%=FMT (BUF$, "%s<SETP")
n%= fmt (buf4$, "%s<%s%s"+CHR$(13)+CHR$(10), buf$, buf2$)
l&=stringlength(buf4$)
i..ret% = ilwrt (LSTEMP%, buf4$,l&)

   'GAIN
n%= fmt (buf2$, "%s<%i", tGAIN%)
N%=FMT (BUF$, "%s<GAIN")
n%= fmt (buf4$, "%s<%s%s"+CHR$(13)+CHR$(10), buf$, buf2$)
l&=stringlength (buf4$)
i..ret% = ilwrt (LSTEMP%, buf4$,l&)

   'RATE
n%= fmt (buf2$, "%s<%i", tRATE%)
N%=FMT (BUF$, "%s<RATE")
n%= fmt (buf4$, "%s<%s%s"+CHR$(13)+CHR$(10), buf$, buf2$)
l&=stringlength (buf4$)
i..ret% = ilwrt (LSTEMP%, buf4$,l&)

   'RESET
n%= fmt (buf2$, "%s<%i", tRESET%)
N%=FMT (BUF$, "%s<RSET")
n%= fmt (buf4$, "%s<%s%s"+CHR$(13)+CHR$(10), buf$, buf2$)
l&=stringlength (buf4$)
i..ret% = ilwrt (LSTEMP%, buf4$,l&)

call ibwrt (LSTEMP%, "SDAT?"+CHR$(13)+CHR$(10))
CALL ibrd (LSTEMP%, TEMP$)
Nm=0
i..ret% = ConfigureAxes (IVHANDLE%, IVMEAS.TEMPGRA%, -1, 0.0, 1.0, 0, SPOINT#-
teminc#,SPOINT#+teminc#)
IF DONE1%=0 THEN  'OTHERWISE END THE SUBROUTINE
  i..ret% = UnloadMenuBar
  TEMBARHAN% = LoadMenuBar ("IVMEASUR.UIR", TEMBAR%) 'MENU BAR HANDLE
(BARHAN1%), MENUBAR ID IVMENBAR%
  P=0
  WHILE Nm<NUMACC%                    'continuous loop
    CALL ibwrt (LSTEMP%, "SDAT?"+CHR$(13)+CHR$(10))
    CALL ibrd (LSTEMP%, TEMP$)
    EN%=SCAN(TEMP$,"%s>%s[dt#]%f",TEMPARRAY#(0))  'pick out the temperature from the string
    P=1
    IF TRANUM%=0 THEN
      TEMTOL#=TEMINC#/5
    ELSE
      TEMTOL#=TEMINC#/10
```

```
END IF
IF TEMPARRAY#(0)>SPOINT#-TEMTOL# AND TEMPARRAY#(0)<SPOINT#+TEMTOL# THEN
 Nm=Nm+1
END IF
IF TEMPARRAY#(0)<SPOINT#-TEMTOL# OR TEMPARRAY#(0)>SPOINT#+TEMTOL# THEN
 Nm=0
END IF
INTER% = GetUserEvent (0, HAN%, CTRL%)
SELECT CASE CTRL%
  CASE TEMBAR.QUITEM%
     Nm=NUMACC%+1
  CASE TEMBAR.CONPAR%
     i..ret% = HidePanel (IVHANDLE%)
     CONPARHAN% = LoadPanel ("IVMEASUR.UIR", CONPARPAN)
     i..ret% = DisplayPanel (CONPARHAN%)
     i..ret% = SetActivePanel (CONPARHAN%)
     i..ret% = SetCtrlVal (CONPARHAN%, CONPARPAN.NUMACC%, NUMACC%)
     i..ret% = SetCtrlVal (CONPARHAN%, CONPARPAN.TGAIN%, TGAIN%)
     i..ret% = SetCtrlVal (CONPARHAN%, CONPARPAN.TRATE%, TRATE%)
     i..ret% = SetCtrlVal (CONPARHAN%, CONPARPAN.TRESET%, TRESET%)
     TADDR% = GetUserEvent (1, PANBAR%, CTRA%)
     DONET%=0
     WHILE DONET%<>1
       SELECT CASE CTRA%
         CASE CONPARPAN.CONRET%
            Nm = 0
            DONET%=1
            i..ret% = GetCtrlVal (CONPARHAN%, CONPARPAN.NUMACC%, NUMACC%)
            i..ret% = GetCtrlVal (CONPARHAN%, CONPARPAN.TGAIN%, TGAIN%)
            i..ret% = GetCtrlVal (CONPARHAN%, CONPARPAN.TRATE%, TRATE%)
            i..ret% = GetCtrlVal (CONPARHAN%, CONPARPAN.TRESET%, TRESET%)
            i..ret% = HidePanel (CONPARHAN%)
            i..ret% = DisplayPanel (IVHANDLE%)
            i..ret% = SetActivePanel (IVHANDLE%)
       'GAIN
            n%= fmt (buf2$, "%s<%i", tGAIN%)
            N%=FMT (BUF$, "%s<GAIN")
            n%= fmt (buf4$, "%s<%s%s"+CHR$(13)+CHR$(10), buf$, buf2$)
            l&=stringlength (buf4$)
            i..ret% = ilwrt (LSTEMP%, buf4$,l&)
       'RATE
            n%= fmt (buf2$, "%s<%i", tRATE%)
            N%=FMT (BUF$, "%s<RATE")
            n%= fmt (buf4$, "%s<%s%s"+CHR$(13)+CHR$(10), buf$, buf2$)
            l&=stringlength (buf4$)
            i..ret% = ilwrt (LSTEMP%, buf4$,l&)
       'RESET
            n%= fmt (buf2$, "%s<%i", tRESET%)
            N%=FMT (BUF$, "%s<RSET")
            n%= fmt (buf4$, "%s<%s%s"+CHR$(13)+CHR$(10), buf$, buf2$)
            l&=stringlength (buf4$)
            i..ret% = ilwrt (LSTEMP%, buf4$,l&)
         CASE ELSE
```

```
            END SELECT
          WEND
          i..ret% = DisplayPanel (IVHANDLE%)
      END SELECT
'     add the point to the strip chart
      count% = Nm
      I..DUMMY% = SetCtrlVal% (IVHANDLE%, IVMEAS.TIMENOW%, count%)
'      IF CNT = 1
'        TFIRST# = TEMPARRAY(0)
'      END IF
'      IF CNT = 11
'        TLAST# = TEMPARRAY(0)
'        CNT = 0
'        TDIF# = TLAST# -TFIRST#
'        TDIF# = abs(TDIF#)
'        IF TDIF# < (TEMINC#/50) thEN

      I..ret% = PlotStripChart (IVHANDLE%, IVMEAS.TEMPGRA%, TEMPARRAY#(), 1, 0, 0, 4)
      CALL Delay (1)
    WEND
    DLTSBAR% = LoadMenuBar ("IVMEASUR.UIR", IVMENBAR%) 'MENU BAR HANDLE
(BARHAN1%), MENUBAR ID IVMENBAR%
    call ibwrt (LSTEMP%, "SDAT?"+CHR$(13)+CHR$(10))
    CALL ibrd (LSTEMP%, TEMP$)
    EN%=SCAN(TEMP$,"%s>%s[dt#]%f",TEMPARRAY#(0)) 'pick out the temperature from the string
    TEMNOW#=TEMPARRAY#(0)
' call ibwrt (pulser%, "TRMD SINGLE"+CHR$(13)+CHR$(10)) 'configure for external width
END IF
END SUB


SUB TEMPCONTROL2 (IVHANDLE%,TEMNOW#)
    i..ret% = GetCtrlVal (IVHANDLE%, IVMEAS.STATEM%, STATEM#)
    i..ret% = GetCtrlVal (IVHANDLE%, IVMEAS.ENDTEM%, ENDTEM#)
    i..ret% = GetCtrlVal (IVHANDLE%, IVMEAS.TEMINC%, TEMINC#)
'   i..ret% = GetCtrlVal (mainpan%, DLTSPAN.STATEM%, STATEM#)
'   i..ret% = GetCtrlVal (mainpan%, DLTSPAN.ENDTEM%, ENDTEM#)
'   i..ret% = GetCtrlVal (mainpan%, DLTSPAN.TEMINC%, TEMINC#)
    IF TRANUM%=0 THEN
      DELTAT#=0
    END IF
    SPOINT#=STATEM#+TRANUM%*TEMINC#
    TEMNOW#=SPOINT#+DELTAT#
    CALL ibfind ("GPIB0", IEEE%)
    CALL ibfind ("DEV3", LSTEMP%)
'   CONTINUOUSLY PULSE (THIS MAY EFFECT THE FILLING OF THE TRAPS)
    CALL ibfind ("DEV2", PULSER%)
'   CALL IBWRT (PULSER%, "PER 100m"+CHR$(13)+CHR$(10))
'   CALL IBWRT (PULSER%, "A:WID 10m"+CHR$(13)+CHR$(10))
'   CALL IBWRT (PULSER%, "B:WID 10m"+CHR$(13)+CHR$(10))
'   CALL IBWRT (pulser%, "TRMD NORMAL"+CHR$(13)+CHR$(10))
    dim temout as string * 5
    dim TEMPROG AS STRING * 23
```

```
  DIM TEMP AS STRING * 10
  dim TEMPROGin AS STRING * 38
  dim buf as string * 5
  dim buf2 as string * 7
  dim buf4 as string * 13
  DONE1%=0
  IF SPOINT#>ENDTEM# THEN
'   call ibwrt (pulser%, "A:DISA ON"+CHR$(13)+CHR$(10))
'   call ibwrt (pulser%, "B:DISA ON"+CHR$(13)+CHR$(10))
   if contpul%=1 then
     i..ret% = WFM.Group.Control (1, 1, 0)
   end if
   i..ret% = AO.VWrite (1, 0, 0.0#)
   TEMNOW#=290
   DONE1%=1
  END IF
  IF i..ret%<>256 then
    call ibwrt (LSTEMP%, "*RST"+CHR$(13)+CHR$(10))'reset if error condition
  END IF
  CALL ibwrt (LSTEMP%, "*ESR?"+CHR$(13)+CHR$(10))
  CALL ibrd (LSTEMP%, TEMP$)
' IF temnow#<50 then
'  call ibwrt (LSTEMP%, "RANG2"+CHR$(13)+CHR$(10))
' ELSE
  call ibwrt (LSTEMP%, "RANG3"+CHR$(13)+CHR$(10))
' END IF
'SETPOINT
n%= fmt (buf2$, "%s<%f[p2]", temnow#)
N%=FMT (BUF$, "%s<SETP")
n%= fmt (buf4$, "%s<%s%s"+CHR$(13)+CHR$(10), buf$, buf2$)
l&=stringlength(buf4$)
i..ret% = ilwrt (LSTEMP%, buf4$,l&)
'GAIN
n%= fmt (buf2$, "%s<%i", tGAIN%)
N%=FMT (BUF$, "%s<GAIN")
n%= fmt (buf4$, "%s<%s%s"+CHR$(13)+CHR$(10), buf$, buf2$)
l&=stringlength (buf4$)
i..ret% = ilwrt (LSTEMP%, buf4$,l&)
'RATE
n%= fmt (buf2$, "%s<%i", tRATE%)
N%=FMT (BUF$, "%s<RATE")
n%= fmt (buf4$, "%s<%s%s"+CHR$(13)+CHR$(10), buf$, buf2$)
l&=stringlength (buf4$)
i..ret% = ilwrt (LSTEMP%, buf4$,l&)

  'RESET
n%= fmt (buf2$, "%s<%i", tRESET%)
N%=FMT (BUF$, "%s<RSET")
n%= fmt (buf4$, "%s<%s%s"+CHR$(13)+CHR$(10), buf$, buf2$)
l&=stringlength (buf4$)
i..ret% = ilwrt (LSTEMP%, buf4$,l&)

call ibwrt (LSTEMP%, "SDAT?"+CHR$(13)+CHR$(10))
```

```
CALL ibrd (LSTEMP%, TEMP$)
Nm=0
i..ret% = ConfigureAxes (IVHANDLE%, IVMEAS.TEMPGRA%, -1, 0.0, 1.0, 0, SPOINT#-
5,SPOINT#+5)
'i..ret% = ConfigureAxes (mainpan%, dltspan.TEMPGRA%, -1, 0.0, 1.0, 0, SPOINT#-5,SPOINT#+5)

IF DONE1%=0 THEN  'OTHERWISE END THE SUBROUTINE
  i..ret% = UnloadMenuBar
  TEMBARHAN% = LoadMenuBar ("IVMEASUR.UIR", TEMBAR%) 'MENU BAR HANDLE
(BARHAN1%), MENUBAR ID IVMENBAR%
'   TEMBARHAN% = LoadMenuBar ("DDLTS1.UIR", TEMBAR%) 'MENU BAR HANDLE
(DLTSBAR%), MENUBAR ID DLTSMENBAR%
  P=0

WHILE Nm<NUMACC%                 'continuous loop
call ibwrt (LSTEMP%, "SDAT?"+CHR$(13)+CHR$(10))
 CALL ibrd (LSTEMP%, TEMP$)
 EN%=SCAN(TEMP$,"%s>%s[dt#]%f",TEMPARRAY#(0)) 'pick out the temperature from the string
 P=1
IF TRANUM%=0 THEN
  TEMTOL#=14
ELSE
  TEMTOL#=2
END IF
IF TEMPARRAY#(0)>SPOINT#-TEMTOL# AND TEMPARRAY#(0)<SPOINT#+TEMTOL# THEN
  Nm=Nm+1
END IF
 INTER% = GetUserEvent (0, HAN%, CTRL%)
  SELECT CASE CTRL%
    CASE TEMBAR.QUITEM%
      Nm=NUMACC%+1
    CASE TEMBAR.CONPAR%
    i..ret% = HidePanel (IVHANDLE%)
    CONPARHAN% = LoadPanel ("IVMEASUR.UIR", CONPARPAN)
'    i..ret% = HidePanel (MAINPAN%)
'    CONPARHAN% = LoadPanel ("DDLTS1.UIR", CONPARPAN)
    i..ret% = DisplayPanel (CONPARHAN%)
    i..ret% = SetActivePanel (CONPARHAN%)
    i..ret% = SetCtrlVal (CONPARHAN%, CONPARPAN.NUMACC%, NUMACC%)
    i..ret% = SetCtrlVal (CONPARHAN%, CONPARPAN.TGAIN%, TGAIN%)
    i..ret% = SetCtrlVal (CONPARHAN%, CONPARPAN.TRATE%, TRATE%)
    i..ret% = SetCtrlVal (CONPARHAN%, CONPARPAN.TRESET%, TRESET%)
    TADDR% = GetUserEvent (1, PANBAR%, CTRA%)
    DONET%=0
    WHILE DONET%<>1
      SELECT CASE CTRA%
          CASE CONPARPAN.CONRET%
            DONET%=1
            i..ret% = GetCtrlVal (CONPARHAN%, CONPARPAN.NUMACC%, NUMACC%)
            i..ret% = GetCtrlVal (CONPARHAN%, CONPARPAN.TGAIN%, TGAIN%)
            i..ret% = GetCtrlVal (CONPARHAN%, CONPARPAN.TRATE%, TRATE%)
            i..ret% = GetCtrlVal (CONPARHAN%, CONPARPAN.TRESET%, TRESET%)
            i..ret% = HidePanel (CONPARHAN%)
```

```
            i..ret% = DisplayPanel (IVHANDLE%)
            i..ret% = SetActivePanel (IVHANDLE%)
    'GAIN
  n%= fmt (buf2$, "%s<%i", tGAIN%)
  N%=FMT (BUF$, "%s<GAIN")
  n%= fmt (buf4$, "%s<%s%s"+CHR$(13)+CHR$(10), buf$, buf2$)
  l&=stringlength (buf4$)
  i..ret% = ilwrt (LSTEMP%, buf4$,l&)


    'RATE
  n%= fmt (buf2$, "%s<%i", tRATE%)
  N%=FMT (BUF$, "%s<RATE")
  n%= fmt (buf4$, "%s<%s%s"+CHR$(13)+CHR$(10), buf$, buf2$)
  l&=stringlength (buf4$)
  i..ret% = ilwrt (LSTEMP%, buf4$,l&)

    'RESET
  n%= fmt (buf2$, "%s<%i", tRESET%)
  N%=FMT (BUF$, "%s<RSET")
  n%= fmt (buf4$, "%s<%s%s"+CHR$(13)+CHR$(10), buf$, buf2$)
  l&=stringlength (buf4$)
  i..ret% = ilwrt (LSTEMP%, buf4$,l&)

        CASE ELSE
      END SELECT
    WEND
    i..ret% = DisplayPanel (IVHANDLE%)

  END SELECT

  'add the point to the strip chart
I..ret% = PlotStripChart (IVHANDLE%, IVMEAS.TEMPGRA%, TEMPARRAY#(), 1, 0, 0, 4)
CALL Delay (1)
WEND
DLTSBAR% = LoadMenuBar ("IVMEASUR.UIR", IVMENBAR%) 'MENU BAR HANDLE
(BARHAN1%), MENUBAR ID IVMENBAR%
'I..ret% = PlotStripChart (mainpan%, dltspan.TEMPGRA%, TEMPARRAY#(), 1, 0, 0, 4)
'CALL Delay (1)
'WEND
'DLTSBAR% = LoadMenuBar ("DDLTS1.UIR", dLTSmenBAR%) 'MENU BAR HANDLE
(DLTSBAR%), MENUBAR ID DLTSMENBAR%
call ibwrt (LSTEMP%, "SDAT?"+CHR$(13)+CHR$(10))
CALL ibrd (LSTEMP%, TEMP$)
EN%=SCAN(TEMP$,"%s>%s[dt#]%f",TEMPARRAY#(0)) 'pick out the temperature from the string
TEMNOW#=TEMPARRAY#(0)
'call ibwrt (pulser%, "TRMD SINGLE"+CHR$(13)+CHR$(10)) 'configure for external width
END IF
  'ADJUST THE NEXT TEMPERATURE SETPOINT TO TAKE OFF THE OFFSET
  DELTAT#=STATEM#+TRANUM%*TEMINC#-TEMPARRAY#(0)+DELTAT#
END SUB
'*********************************
' ADJUST FOR MAXIMUM GAIN
```

```
'**********************************
sub setgain (vdamax#, vdamin#, gain%)
   g#=10/(vdamax#-vdamin#+.5*(vdamax#-vdamin#))
if g#<2 then
    gain%=1
   elseif g#<5 then
    gain%=2
   elseif g#<10 then
   gain%=5
   elseif g#<20 then
   gain%=10
   elseif g#<50 then
    gain%=20
   elseif g#<100 then
    gain%=50
   else
   gain%=100
end if
end sub
```

BIBLIOGRAPHY

Acheson E., *On carborundum*, Chem. News **68**, 179 (1893).

Adams W., Day R., *The action of light on selenium*, Proc. Roy. Soc. (London) **25**, 113 (1876).

Andreev A., Anikin M., Syrkin A., Chelnokov V, *Method for purifying a silicon carbide surface in high vacuum*, Semiconductors **28** (6), 577 (1994).

Anikin M.M., Levinshtein M.E., Popov I.V., Rastegaev V.P., Strel'chuk A.M., Syrkin A.L., *Temperature dependence of the avalanche breakdown voltage of silicon carbide p-n junctions*, Sov. Phys. Semicond. **22** (9), 995 (1988).

Anikin MM., Lebedev A.A., Syrkin A.L., Suvorov A.V., *Capacitance spectroscopy of p-n junctions made of epitaxial 4H-SiC doped by implantation of Al ions*, Sov. Phys. Semicond. **20** (12), 1357 (1986).

Anikin MM., Lebedev A.A., Syrkin A.L., Suvorov A.V., *Investigation of deep levels in SiC by capacitance spectroscopy methods*, Sov. Phys. Semicond. **19** (1), 69 (1985).

Ashcroft N., Mermin N. Solid State Physics. Philadelphia:Saunders College HRW, 1976.

Baliga J., *Evolution of MOS bipolar power semiconductor technology*, Proc. of the IEEE **76** (4), 409 (1988).

Baranov P., Khramtsov V., Mokhov E., *Chromium in silicon carbide: electron paramagnetic resonance studies*, Semicond. Sci. Technol. **9**, 1340 (1994).

Becquerel A. *On electric effects under the influence of solar radiation*, Compt. Rend. **vol 9**, 711 (1839).

Bardeen J., Brattain W., *The transistor: a semiconductor triode*, Phys. Rev. **74**, 230 (1948).

Benton J., *Characterization of defects in semiconductors by deep level transient spectroscopy*, J. Cryst. Growth **106**, 116 (1990).

Bermudez V., *Auger and electron energy loss study of the Al/SiC interface*, Appl. Phys. Lett. **42** (1), 70 (1983).

BermudezV., *Growth and structure of aluminum films on (001) silicon carbide*, J. Appl. Phys. **63** (10), 4951 (1987).

Bernholc J., Kajihara S., Wang C., Antonelli A., *Theory of native defects, doping, and diffusion in diamond and silicon carbide*, Mat. Sci. and Eng. B11, p265 (1992).

Bess L., *Radiationless recombination in phosphors*, Phys. Rev. **111** (1), 129 (1958).

Bethe, H., *Theory of the boundary layer of crystal rectifiers*, M.I.T. Radiation Laboratory Report pp 12-43 (1942).

Bhatnagar M., Baliga J., *Analysis of silicon carbide power device performance*, in Proc. 3rd Int. Symp. Power Semic. Dev. and IC's, p176 (1991).

Bhatnagar M., McLarty P., *Silicon carbide high-voltage (400V) Schottky barrier diodes*, IEEE Elec. Dev. Lett. **13** (10), 501 (1992).

Birman J., *Simplified LCAO method for zincblende wurtzite and mixed crystal structures*, Presented at the American Physical Society Meeting, Chicago (1958).

Blakemore J. Semiconductor Statistics. New York: Dover Publications, 1987.

Bloch F., Z. Phys. **52**, 555 (1928).

Bonch-Bruevich V., Glasko V., *The theory of "cascade" carrier recombination in homopolar semconductors*, Sov. Phys. Solid State **4** , 599 (1962)

Borgoin J. and Lannoo M., Point Defects in Semiconductors II. Berlin:Springer-Verlag, Ch. 6, 1983.

Bose J.C., U.S. Patent 755840, (1904).

Brattain W., Bardeen J., *The nature of the forward current in germanium point contacts*, Phys. Rev. **74**, 232 (1948).

Braun F., *Uber die Stromleitung durch Schwefelmetalle*, Ann. Physik. Chem. **153** (4), 556 (1874).

Braun S., Grimmeiss H., *Optical properties of gold acceptor and donor levels in Si*, J. Appl. Phys. **45** (6), 2658 (1974).

Broniatowski A., Blosse A., Srivastava P., Bourgouin J., *Transient capacitance measurements on resistive samples*, J. Appl. Phys. **54** (6), 2907 (1983).

Brown D., Downey E., Ghezzo M., Kretchmer J., Saia R., Liu Y.S., Edmond J., Gati G., Pimbley J., Schneider W., *Silicon carbide UV photodiodes*, IEEE Trans. Elec. Dev. **40** (2), 325 (1993).

Buchwald W., Johnson N., *Revised role for the Poole-Frenkel effect in deep-level characterization*, J. Appl. Phys. **64** (2), 958 (1988).

Burford W., Verner H. Semiconductor Junctions and Devices-Theory to Practice. New York:McGraw-Hill Book Company, 1965.

Chakravarty S., Subramanian S., Sharma D., Arora B., *Deep level admittance spectroscopy of DX centers in AlGaAs:Sn*, J. Appl. Phys. **66** (8), 3955 (1989).

Chelenokov V., *SiC bipolar devices*, Mat. Sci.and Egr., B11, p103 (1992).

Choyke W. Patrick L., *Exciton recombination radiation and phonon spectrum of 6H SiC*, Phys. Rev. **127** (6), 1868 (1962).

Choyke W., Patrick L., *Higher absorption edges in 6H SiC*, Phys. Rev. **172** (3), 769 (1968).

Christenson D., *High temperature electronics for supersonic aircraft*, Proc. 26th AIAA Joint Prop. Conf., Orlando FL p245 (1990).

Clemen L., Devaty R., MacMillan M., Yoganathan M., Choyke W., Larkin D., Powell J., Edmond J., Kong H., *Aluminum acceptor four particle bound exciton complex in 4H, 6H, and 3C SiC*, Appl. Phys. Lett. **62** (23), 2953 (1993).

Cohen M., Heine V., *Cancellation of kinetic and potential energy in atoms, molecules, and solids*, Phys. Rev. **122** (6), 1821 (1961).

Colwell P., Klein M., *Raman scattering from electronic excitations in n-type silicon carbide*, Phys. Rev. B. **6** (2), 498 (1972).

Davis R., *Deposition and characterization of diamond, silicon carbide, and gallium nitride thin films*, J. of Cryst. Growth 173, 161 (1994).

Davis R., Kelner G., Shur M., Palmour J., Edmond J., *Thin film deposition and microelectronic and optoelectronic device fabrication and characterization in monocrystalline alpha and beta silicon carbide*, Proc. of the IEEE **79** (5), 677 (1991).

Davis R., Sitar Z., Williams B., Kong H., Kim H., Palmour J., Edmond J., Ryu J., Glass J., Carter C., *Critical evaluation of the status of the areas for future research regarding the wide band gap semiconductors diamond, gallium nitride, and silicon carbide*, Mat. Sci. and Engineering **B1**, 77 (1988).

Day D., Tsai M., Streetman B., Lang D., *Deep level transient spectroscopy: System effects and data analysis*, J. Appl. Phys. **50** (8), 5093 (1979).

Dean P., Faulkner R., Kimura S., Ilgems M., *Optical properties of excitons bound to neutral acceptors in GaP*, Phys. Rev. B **4** (6), 1926 (1971).

Dean P., Hartman R., *Magneto-optical properties of the dominant bound excitons in undoped 6H-SiC*, Phys. Rev. B **5** (12), 4911 (1972).

Dean P., Yafet Y., Haynes J., *Valley-orbit splitting of the indirect free exciton in silicon*, Phys. Rev. **184** (3), 837 (1969).

Dmitriev V., Kogan L., Morozenko Y., Tsarenkov B., Chelnokov V. Cherenkov A., *Violet light emitting SiC-4H diodes*, Sov. Phys. Semicond. **23** (1), 23 (1989).

Doolittle W., Rohatgi A., Review of Scientific Instrumentation **63**, 5733 (1992).

Doolittle W., Rohatgi A., *A new figure of merit and methodology for quantitatively determining defect resolution capabilities in deep level transient spectroscopy andlysis*, J. Appl. Phys. **75** (9), 4570 (1994).

Doolittle W., Rohatgi A., *Comparison of covariance linear predictive modeling to the modulation function method for use in deep level transient spectroscopy*, J. Appl. Phys. **75** (9), 4560 (1994).

Dozsa L., *A new method to measure fast defect transients in semiconductor and/or insulator samples*, Solid State Electronics **35** (2), 228 (1991).

Dyson R., Isenberg I., *Analysis of exponential curves by a method of moments, with special attention to sedimentation equilibrium and flourescence decay*, Biochemistry **10** (17), 3233 (1971).

Edmond J., Palmour J., Carter C., *Junction Devices in 6H-SiC*, Proc. 1st Int. Conf. Hi. Temp. Elec., D.B. King F. Thome Eds., Albuquerque NM, p487 June 1991.

Eicke D., Hodge E., Price W., Ravaris P., Talati S., *Advanced secondary power system study*, Final report, USAF Contract F33657-84-C-0247, CDRL 3402, 1992, General Dynamics, Fort Worth Division, 76101.

Elkin E., Watkins G., *Defects in irradiated silicon: electron paramagnetic resonance and electron double nuclear resonance of the arsenic and antimony vacancy pairs*, Phys. Rev. **174** (3), 881 (1968).

Englman R., Jortner J., *The energy gap law for radiationless transitions in large molecules*, Molecular Physics **18** (2), 145 (1969).

Evstropov V., Linkov I., Morozenko Y., Pikus F., *Exciton luminescence of compensated SiC 6H*, Physica B **185**, 313 (1993).

Evwaraye A.O., Smith S.R., Mitchel W., *Characterization of defects in n-type 6H-SiC single crystals by optical admittance spectroscopy*, Proc. Fall Meeting of the MRS, Boston MA, p543 (1993).

Evwaraye A.O., Smith S.R., Mitchel W., *Shallow levels in n-type 6H-silicon carbide as determined by admittance spectroscopy*, J. Appl. Phys. **75** (7), 3472 (1994).

Evwaraye A.O., Smith S.R., Mitchel W.C., *Electrical properties of deep levels in bulk n-type silicon carbide*, J. Appl. Phys. **76**, 5769 (1994).

Evwaraye A.O., Smith S.R., Mitchel W.C., *Kinetics of slow buildup of photoconductance in 6H-SiC*, Appl. Phys. Lett. **66** (20), 2691 (1995).

Evwaraye A.O., Smith S.R., Mitchel W.C., *Observation of surface defects in 6H-SiC wafers*, J. Appl. Phys. **74** (8), 5269 (1993).

Evwaraye A.O., Smith S.R., Mitchel W.C., *Shallow and deep levels in n-type 4H-SiC*, J. Appl. Phys. **79** (10), 7726 (1996).

Faraday M. Experimental Researches in Electricity Vol I. London:Bernard Quaritch, 1839.

Frenkel J., Phys. Rev. **54**, 647 (1938).

Fritts C., *A new form of selenium cell*, Am. J. Sci. **26**, 465 (1883).

Gardner C., Cooper J., Melloch M., Palmour J., Carter C., *Dynamic storage in 6H-SiC*, Appl. Phys. Lett. **61** (10), 1185 (1992).

Gavrilenko V., Postnikov A., Klyui N., Litovchenko V., *Energy band structure and optical properties of wurtzite structure silicon carbide crystals*, Phys. Stat. Sol. **162**, 477 (1990).

Gibb R., Rees G., Thomas B., Wilson B., Hamilton B., Wight D., Mott N., *A two stage model for deep level capture*, Philosophical Magazine **36** (4), 1021 (1977).

Gotz W., Schoner A., Pensl G., Suttrop W., Choyke W., Stein R., Leibenzeder S., *Nitrogen donors in 4H-silicon carbide*, J. Appl. Phys. **73** (7), 3332 (1993).

Grimmeiss H., *Deep level impurities in semiconductors*, in the Ann. Rev. Mat. Sci. Edited by Huggins R.A., Bube R.H., Roberts R.W., p341-376 (1977).

Grimmeiss H., Kullendorff N., *A steady state constant capacitance method for the characterization of deep energy levels in semiconductors*, J. Appl. Phys. **51** (11), 5852 (1980).

Grimmeiss H., Ledebo L., Meijer E., *Capture from free-carrier tails in the depletion region of junction barriers*, Appl. Phys. Lett. **36** (4), 307 (1980).

Haberstroh C., Helbig R., Stein R., *Some new features of the photoluminescence of SiC(6H), SiC(4H, and SiC(15R),* J. Appl. Phys. **76** (1), 509 (1994).

Hagen S., Van Kemmenade A., Van Der Does Debye J., *Donor-acceptor pair spectra in 6H and 4H SiC doped with nitrogen and aluminum*, J. of Luminescence **8**, 18 (1973).

Hall E., *On a new action of the magnet on electric currents*, Am. J. Math. **2**, 287 (1879).

Hall R., *Electron-hole recombination in germanium*, Phys. Rev. **87**, 387 (1952).

Harris G.L. *Properties of Silicon Carbide*. London:INSPEC, 1995.

Hartke J., *The three dimensional Poole-Frenkel effect*, J. Appl. Phys. **39**, 4871 (1968).

Hasegawa F., *Deep energy levels in the high resistance region at GaAs vapor epitaxial film substrate interface*, Jap. J. Appl. Phys. **9** (6), 638 (1970).

Haynes J., *Experimental proof of the existence of a new electronic complex in silicon*, Phys. Rev. Lett. **4** (7), 361 (1960).

Hemstreet L., Fong C., *Recent band structure calculations of cubic and hexagonal polytypes of silicon carbide*, Proc. 3rd International Conf. SiC, (Miami, FL), University of South Carolina Press, 1973.

Henry C., Kukimoto H., Miller G., Merritt F., *Photocapacitance studies of the oxygen donor in GaP. II. Capture cross sections*, Phys. Rev. B **7** (6) 2499 (1973).

Henry C., Lang D., *Nonradiative capture and recombination by multi-phonon emission in GaAs and GaP*, Phys. Rev. B **15** (2), 989 (1975).

Henry C., *Some fundamental advances in radiative and non-radiative transitions in semiconductors*, J. of Luminescence **12/13**, 47 (1976).

Hess K. *Advanced Theory of Semiconductors*. Englewood Cliffs NJ: Prentice Hall, 1988.

Hiramoto H., Yoshimura K., Yokoyama M., *Photo-modulation of light up conversion in light transducer using high gain photoresponsive amorphous silicon carbide combined with organic electroluminescent diode*, Appl. Phys. Lett. **60** (3), 324 (1992).

Hjalmarson H., Vogl P., Wolford D., Dow J., *Theory of substitutional deep traps in covalent semiconductors*, Phys. Rev. Lett. **44** (12), 810 (1980).

Holzlein K., Pensl G., Schulz M., Stolz P., *Fast computer controlled deep level transient spectroscopy system for versatile applications in semiconductors*, Rev. Sci. Instrum. **57** (7), 1373 (1986).

Hong R-D., Jenkins D., Ren S-Y., Dow J., *Hydrostatic pressure dependencies of deep impurity levels in zinc-blende semiconductors*. Phys. Rev. B **38** (17), 12549 (1988).

Hovel H. Semiconductors and Semimetals. Edited by R.K. Willardson and A.C. Beer, Academic Press:New York, 1975.

Hull A., *The crystal structure of carborundum*, Phys. Rev. 13, 292 (1919).

Humphreys R., Bimberg D., Choyke W., *Wavelength modulated absorption in SiC*, Solid State Comm. **39**, 163 (1981).

Hurkx G.A.M., Klaassen D.B.M., Knuvers M.P.G., *A New Recombination Model for Device Simulation Including Tunneling*, IEEE Trans. Elect. Dev. **39** (2), 331 (1992).

Ikeda M., Matsunami H., Tanaka T., *Site-dependent donor and acceptor levels in 6H-SiC*, J. of Luminescence **20**, 111 (1979).

Ingham Edward A. Parameter Estimation for Superimposed Weighted Exponentials. PhD Dissertation. School of Engineering, Air Force Institute of Technology (AU), Wright-Patterson AFB OH, December 1996.

Ingham E., Scofield J., Pachter M., *Improved linear prediction for deep level transient spectroscopy analysis*, J. Appl. Phys. **80** (5), 2805 (1996).

Ivashchenko A., Kopanskaya F., Solomonov A., Tarchenko V., *Some complications of the DLTS technique caused by non-exponential relaxation of barrier capacitance*, Sov. Phys. Tech. Phys. **38** (2), 1590 (1993).

Jagodzinski J. *Polytypism in SiC*, Acta. Cryst. **7**, 300 (1954).

Jang S., Kimoto T., Matsunami H., *Deep levels in 6H-SiC wafers and step controlled epitaxial layers*, Appl. Phys. Lett. **65** (5), 581 (1994).

Jansen A., Orazem M., *Identification of deep level states in electronic materials by optically stimulated deep level impedence spectroscopy*, J. Electrochem. Soc. **139** (5), 1463 (1992).

Jaros M., *A case for large Auger recombination cross sections associated with deep centers in semiconductors*, Solid State Comm. **25**, 1071 (1977).

Jenny J., Skowronski J., Mitchel W., Hobgood H., Glass R., Augustine G., Hopkins R., *Deep level transient spectroscopic and Hall effect investigation of the position of the vanadium acceptor level in 4H and 6H-SiC.*, Appl. Phys. Lett. **68** (14), 1963 (1996).

Jenny J., Skowronski J., Mitchel W., Hobgood H., Glass R., Augustine G., Hopkins R., *Vanadium related near-band-edge absorption bands in three SiC polytypes.*, J. Appl. Phys. **78** (5), 3160 (1995).

Jenny J., Skowronski J., Mitchel W., Hobgood H., Glass R., Augustine G., Hopkins R., *On the compensation mechanism in high-resistivity 6H-SiC doped with vanadium.*, J. Appl. Phys. **78** (6), 3839 (1995).

Johnson N., *Measurement of semiconductor-insulator interface states by constant-capacitance deep-level transient spectroscopy*, J. Vac. Sci. Technol. **21** (2), 303 (1982).

Johnstone D.K., Electrical characterization of GaSb-based semiconductors for 2-4 μm diode laser applications. PhD Dissertation. School of Engineering, Air Force Institute of Technology (AU), Wright-Patterson AFB OH, June 1996.

Jones H. The Theory of Brillouin Zones and Electronic States in Crystals. North Holland Publishing:Amsterdam, 1960.

Joosen W., Schoemaker D., *Behavior type method: symmetry and structure of point defects in cubic crystals derived from polarized Raman scattering*, J. Phys. Chem. Solids **51** (7), 821 (1990).

Kal'nin A., Pasynkov V., Tairov Y., Yas'kov D., *Photoluminescence of silicon carbide with berryllium impurity*, Sov. Phys. Solid State **8** (10), 2381 (1967).

Kane E.O., *Theory of Tunneling*, J. Appl. Phys. **32** (1), 83 (1960).

Karmann S., Haberstroh C., Engelbrecht F., Suttrop W., Schoner A., Schadt M., Helbig R., Penal G., Stein R., Leibenzeder S., *CVD growth and characterization of single crystalline 6H SiC*, Physica B **185**, 75 (1993).

Kay S. Modern Spectral Estimation. Prentice Hall:Englewood Cliffs NJ, 1988.

Kay S. Fundamentals of Statistical Signal Processing. Prentice Hall:Englewood Cliffs NJ, 1993.

Kearney M., Kelly M., Condie A., Dale I., *Temperature dependent barrier heights in bulk unipolar diodes leading to improved temperature stable performance*, Electronics Letters **26** (10), 671 (1990).

Kelner G., Binari S., Shur M., Palmour J., *High temperature operation of α-SiC buried gate junction field effect transistors*, Electronics Letters **27** (12), 1038 (1991).

Kelner G., Binari S., Shur M., Sleger K., Palmour J., Kong H., *α-SiC buried gate junction field effect transistors*, Mat. Sci.and Egr., **B11**, p121 (1992).

Kemenade A., Hagen S., *Proof of the involvement of Ti in the low temperature ABC luminescence spectrum of 6H-SiC*, Solid State Commun. **14**, 1331 (1974).

Kholuyanov G., *The roles of boron, nitrogen, and gallium in the electroluminescence of silicon carbide p-n junctions*, Sov. Phys. Solid-State **7** (11), 2620 (1966).

Kimerling L., *New developments in defect studies in semiconductors*, IEEE Trans. on Nuclear Science **NS-23** (6), 1497 (1976).

Kimerling L.C., *Defect characterization by junction spectroscopy*, in Defects in Semiconductors, Narayan and Tan eds., North-Holland, p85 (1981).

Kittel C. *Introduction to Solid State Physics*. New York: John Wiley, 1986.

Knippenberg W., *Growth phenomenon in SiC*, Philips Res. Repts. **18** (3), 161 (1963).

Knippenberg W., Verspui G., *The preparation of large single crystals of SiC polytypes by precipitation from solutions*, Philips Res. Repts. **21**, 113 (1966).

Kohn W., Solid State Physics **5**, 257 (1957)

Konstantinov A.O., *Influence of temperature on impact ionization and avalanche breakdown in silicon carbide*, Sov. Phys. Semicond. **23** (1), 31 (1989).

Kornilov B., *Carrier recombination at zinc atoms in n-silicon*, Sov. Phys. Solid State **7**, 1446 (1965).

Kroemer H., Chien W., *On the theory of Debye averaging in the C-V profiling of semiconductors*, Solid State Electronics **24**, 655 (1981).

Kroger F., *Point defect thermodynamics of compound semiconductors and their alloys*, Mat. Res. Soc. Symp. Proc. **14**, 207 (1983).

Kukimoto H., Henry C., Merritt F., *Photocapacitance studies of the oxygen donor in GaP. I. Optical cross sections, energy levels, and concentration*, Phys. Rev. B **7** (6) 2486 (1973).

Kunzer M., Kaufmann U., Maier K., Schneider J., *Magnetic circular dichroism and electron spin resonance of the A^- acceptor state of vanadium, V^{3+}, in 6H-SiC*, Mat. Sci. Egr. **B29**, 118 (1995).

Lanczos C., Applied Analysis, Englewood Cliffs:Prentice Hall, 1956.

Landsberg P., *Non-radiative transitions in semiconductors*, Phys. Stat. Sol. **41**, 457 (1970).

Lang D., Henry C., *Nonradiative recombination at deep levels in GaAs and GaP by lattice relaxation multiphonon emission*, Phys. Rev. Lett. **35** (22), 1525 (1975).

Lang D., Kimerling L., *Observation of recombination enhanced defect reactions in semiconductors*, Phys. Rev. Lett. **33** (8), 1863 (1974).

Lang D.V., *Deep level transient spectroscopy: A new method to characterize traps in semiconductors*, J. Appl. Phys. **45** (7), 3023 (1974).

Lang D.V., *Fast capacitance transient apparatus Application to ZnO and O centers in GaP p-n junctions*, J. Appl. Phys. **45** (7), 3014 (1974).

Lang D.V., Kimerling L.C., *A new technique for defect spectroscopy in semiconductors: application to 1 MeV electron-irradiated GaAs*, Inst. Phys. Conf. Ser. No. 23 Ch. 10, p581 (1975).

Lang D.V., Logan R.A., *A study of deep levels in GaAs by capacitance spectroscopy*, J. of Elec. Mat. **4** (5), 1053 (1975).

Lax M., *Cascade Capture of Electrons in Solids*, Phys. Rev. **119** (5), 1502 (1960).

Lee K., Dang L., Watkins G., Choyke W., *Optically detected magnetic resonance study of SiC:Ti*, Phys. Rev. B **32** (4), 2273 (1985).

Lee W., Borrego J., *Minority carrier emission effects in deep level transient spectroscopy measurements on Schottky diodes*, J. Appl. Phys. **63** (11), 5357 (1988).

Lely J. *Darstellung von Einkristallen von Silicium carbid und Beherrschung von Art und Menge der eingebautem Verunreingungen*, Ber. Deut. Keram. Ges. **32**, 229 (1955).

Loeb J., Cahen G., *More about process identification*, IEEE transactions on automatic control, p359 July 1965.

Lomakina G., Sokolov V., Vodakov Y., *Photoconductivity and luminescence of the 4H and 6H polytypes of n-type SiC doped with Sc*, Sov. Phys. Semicond. **16** (7), 795 (1982).

Lourdes P., Orantes J., Vincent J., Bailon L., Barbolla J., *The Poole-Frenkel Effect in 6H-SiC Diode Characteristics*, IEEE Trans. Elect. Dev. **41** (4), 587 (1994).

Madelung E.O., Semiconductors Group IV Elements and III-V Compounds, in *Data in Science and Technology*, Editor R. Poerschke, Berlin:Springer-Verlag, 1991.

Maier K., Schneider J., Wilkening W., Leibenzeder S., Stein R., *Electron spin resonance studies of transition metal deep level impurities in SiC*, Mat. Sci. and Eng. **B11**, 27 (1992).

Mayur A., Sciacca M., Ramdas A., Rodriguez S., *Redetermination of the valley orbit (chemical) splitting of the 1s ground state of group V donors in Si*, Phys. Rev. B **48** (16), 10893 (1993).

Mazzola M.S., Saddow S.E., Neudeck P.G., Lakdawala V.K., We S., *Observation of the D-Center in 6H-SiC p-n diodes grown by chemical vapor deposition*, Appl. Phys. Lett. **64** (20), 2730 (1994).

McKelvey J. Solid State and Semiconductor Physics. Malabar FL:Robert Krieger Publish., 1986.

Mehdi I., Haddad G., Mains R., *Microwave and millimeter-wave power generation in silicon carbide avalanche devices*, J. Appl. Phys. **64** (3), 1533 (1988).

Miller G.L., Lang D.V., Kimerling L.C., *Capacitance Transient Spectroscopy*, in the Ann. Rev. Mat. Sci. Edited by Huggins R.A., Bube R.H., Roberts R.W., p377-447 (1977).

Milnes A. *Deep Impurities in Semiconductors*. New York:John Wiley, 1973.

Moll J.L. *Physics of Semiconductors*. New York:McGraw-Hill, Physical and Quantum Electronics Series, 1964.

Mooney P., *Photo-deep level transient spectroscopy: A new technique to study deep levels in heavily compensated semiconductors*, J. Appl. Phys. **54** (1), 208 (1983).

Morimoto J., Kida T., Miyakawa T., *Multi-exponential analysis of DLTS by CONTIN*, Appl. Phys. A **39**, 197 (1986).

Morkoc H., Strite S., Gao G., Lin M., Sverdlov B., Burns M., *Wide bandgap SiC, III-V nitride, II-VI ZnSe based semiconductor device technologies*, J. Appl. Phys. **76** (3), 1363 (1994).

Muehlhoff L., Choyke W., Bozack M., Yates J., *Comparative electron spectroscopic studies of surface segregation on SiC (0001) and SiC (000-1),* J. Appl. Phys. **60** (8), 2842 (1986).

Myles C., Sankey O., *Deep levels associated with vacancy, impurity pairs in covalent semiconductors*, Phys. Rev. B **29** (12), 6810 (1984).

Neudeck P.G., Fazi C., *High-field fast-risetime pulse failures in 4H- and 6H-SiC pn junction diodes*, preprint of accepted article , J. Appl. Phys. (to be published in July 1996).

Neumark G., *Auger theory at defects-Application to states with two bound particles in GaP*, Phys. Rev. B **7** (8), 3802 (1972).

Niilisk A., Laisaar A., Gorban I., Slobodyanyuk A., *Large pressure effect on photoluminescence lines in 6H-SiC:Ti crystal*, Solid State Commun. **88** (7), 537 (1993).

Nishino S., Powell J., Will H., *Production of large area single crystal wafers of cubic silicon carbide for semiconductor devices*, Appl. Phys. Lett. **42** (5), 460 (1982).

Ott H., *Die gitter des karborunds (SiC),* Z. Krist. 61, 515 (1925).

Palmour J., *A high temperature silicon carbide differential amplifier*, Quarterly technical progress report TR 911011-1, USAF Contract F33615-89-C-2978, May 1991.

Palmour J., Kong H., Carter C., *Field effect transistors in 6H-SiC,* Proc. 1st Int. Conf. Hi. Temp. Elec., D.B. King F. Thome Eds., Albuquerque NM, p491 June 1991.

Pankove J. Optical Processes in Semiconductors. New York: Dover Publications, 1971.

Pantelides S.T., Lipari N.O., Bernholc J., *The effective mass nature of deep level point defect states in semiconductors*, Solid State Comm. **33**, 1045 (1979).

Papoulis A. Probability, Random Variables, and Stochastic Processes. New York:McGraw Hill, 1991.

Partin D., Chen J., Milnes A., Vassamillet L., *Deep level transient spectroscopy studies of Ni- and Zn-diffused vapor-phase-epitaxy n-GaAs*, J. Appl. Phys. **50** (11), 6845 (1979)

Patrick L., Choyke W., *Photoluminescence of radiation defects in ion-implanted 6H-SiC*, Phys. Rev. B **5** (8), 3253 (1972).

Patrick L., *Inequivalent sites and multiple donor and acceptor levels in SiC polytypes*, Phys. Rev. **127** (6), 1878 (1962).

Pavlichenko V., Ryzhikov I., Suleimanov Y., Shvaidak Y., *Blue photo- and electroluminescence of epitaxial silicon carbide films*, Sov. Phys. Solid-State **10** (9), 2205 (1969).

Pensl G., Choyke W., *Electrical and optical characterization of SiC*, Physica B **185**, 264 (1993).

Pfirsch F., Ruff M., *Note on charge conservation in the transient semiconductor equations*, IEEE Trans. Elec. Dev. **40** (11), 2085 (1993).

Potter R., *Cathodoluminescence measurements on a silicon carbide light-emitting diode*, J. Appl. Phys. **43** (2), 721 (1972).

Prins J., *Residual defect control when doping thin layers in diamond*, Physica B. **185**, 132 (1993).

Przylbylko S., *High temperature electronics for aircraft engines*, Proc. 26th AIAA Joint Prop. Conf., Orlando FL p1 (1990).

Przylbylko S., Calculations and figure courtesy of Mr. S. Przybylko of USAF Wright Laboratory turbine Engine division, WPAFB OH.

Rahman M., Furukawa S., *Silicon carbide turns on its power*, IEEE Circuits and Devices, p23 (1993).

Ramsdell L., *Studies on silicon carbide*, Am. Mineralogist **32**, 64 (1947).

Ransom C., Chappell T., Freeouf J., Kirchner P., *Modulating Functions Waveform analysis of multi-exponential transients for deep level transient spectroscopy*, Mat. Res. Symp. Proc. **69**, 337 (1986)

Raynaud C., Richier C., Brounkov P., Ducroquet F., Guillot G., Porter L., Davis R., Jaussaud C., Billon T., *Determination of donor and acceptor level energies by admittance spectroscopy in 6H-SiC*, Mat. Sci. Egr **B29**, 122 (1995).

Reinhardt K., Yeo Y., Hengehold R., *Junction characteristics of $Ga_{0.5}$ $In_{0.5}$ P n+p diodes and solar cells*, J. Appl. Phys. **77** (11), 5763 (1995).

Rhoderick E., Metal Semiconductor Contacts. Oxford:Clarendon Press, 1978.

Riben A., Feucht D., Solid State Electronics **9**, 1055 (1966).

Ringel S., Rohatgi A., Tobin S., IEEE Trans. Electron Devices **36**, 1230 (1989).

Robbins D., Dean P., *The effects of core structure on radiative and non-radiative recombinations at metal ion substituents in semiconductors and phosphors*, Advances in Physics **27** (4), 499 (1978).

Rosencher E., Coppard R., Bois D., *Probing of impurity potential well at the Si/SiO$_2$ interface by electric field enhanced emission,* J. Appl. Phys. **57** (8), 2823 (1985).

Sacchini J., Romano A., Steedly W., in Proceedings of the SPIE (SPIE, Orlando, FL, 1994), Vol. **2234**, pp91-105.

Sah C., Noyce R., Schockley W., *Carrier generation and recombination in P-N junctions and p-n junction characteristics*, Proceedings of the IRE **45**, 1228 (1957).

Sah C.T., *Bulk and interface imperfections in semiconductors*, Solid State Electronics **22**, 975 (1976).

Sah C.T., Forbes L., Rosier L.L., Tasch A.F., *Thermal and optical emission and capture rates and cross sections of electrons and holes at imperfection centers in semiconductors from photo and dark junction current and capacitance measurements*, Solid State Electronics **13**, 759 (1969).

Scharf L. Statistical Signal Processing. Reading MA:Addison Wesley 1990.

Schneider J., Maier K., *Point defects in silicon carbide*, Physica B **185**, 199 (1993).

Schneider J., Muller H., Maier K., Fuchs F., Dornen A., Leibenzeder S., Stein R., *Infrared spectra and electron spin resonance of vanadium deep level impurities in silicon carbide*, Appl. Phys. Lett. **56** (12), 1184 (1990).

Schottky W., *Halbleitertheorie der sperrschicht*, Naturwissenschaften, **26**, 843 (1938).

Schroder D., *The concept of generation and recombination lifetimes in semiconductors*, IEEE Trans. Elec. Dev. **ED-29** (8), 1336 (1982).

Schroder C., Heiland W., Held R., Loose W., *Analysis of reverse current-voltage characteristics of Ti/6H-SiC Schottky diodes*, Appl. Phys. Lett. **68** (14), 1957 (1996).

Schuster A., *On unilateral conductivity*, Phil. Mag. **48**, 251 (1874).

Scofield J., Yeo Y., Hengehold R., *Deep level investigation of bulk and epitaxial 6H-SiC at high temperatures*, Inst. Phys. Conf. Ser. No 145, Ch 3, IOP Publishing Bristol UK, (1995).

Scofield J., Yeo Y., Hengehold R., *Deep level study of as-grown and ion implanted bulk and MOCVD grown epitaxial 6H-SiC*, Inst. Phys. Conf. Ser. No 145, Ch 2, IOP Publishing Bristol UK, (1995).

Scofield J., Dunn M., Reinhardt K., Yeo Y., Hengehold R., *Defect dominant junction characteristics of 4H-SiC p+/n diodes*, Proc. Mat. Res. Soc. Spring Meeting, vol * (San Francisco CA), (1996).

Scofield J., Yeo Y.K., Hengehold R., *Deep level studies specific to the SiC polytypes 6H and 4H*, To be published in Physics of Semiconductors, Proc. International Conf. Phys. Semiconductors, Presented at the conference in Berlin, Germany, (July 1996).

Scofield J., Ingham E., Yeo Y.K., Pachter M., *Observation of inequivalent lattice site energies for deep level traps in 6H-SiC by isothermal deep level transient spectroscopy*, Submitted J. Appl. Phys. July 1996.

Scofield J., Ingham E., Yeo Y.K., Pachter M., *Evidence for nonradiative carrier capture by multi-phonon emission in hexagonal SiC polytypes 4H and 6H*, Submitted J. Appl. Phys. Oct 1996.

Scofield J., Wiemeri J., Dunn M., Reinhardt K., Yeo Y.K., Hengehold R., *Comparative study of the junction characteristics and performance of SiC p+/n and Schottky power rectifiers*, Inst. Phys. Conf. Ser. No, IOP Publishing Bristol UK, (1996).

Shah N., Rohr K., *More electric F-18 cost benefits study*, WL-TR-91-2093, 1992, Northrop Corporation, Aircraft Division, 90250.

Shapiro F.R., Senturia S.D., Adler D., *The use of linear predictive modeling for the analysis of transients from experiments on semiconductor defects*, J. Appl. Phys. **55** (10), 3453 (1984).

Shaw G., Messenger S., Walters R., Summers G., *Electrical characterization of InGaAs photodiodes*, J. Appl. Phys. **73**, 7244 (1993).

Sheni K., Scott R., Baliga J., *Optimum semiconductors for high-power electronics*, IEEE Trans. on Elec. Dev. **36** (9), 1811 (1989).

Sheinkman M., *On a possible recombination mechanism at multi-charged centers in semiconductors*, Sov. Phys. Solid State **5**, 2035 (1964).

Shockley W., Electrons and Holes in Semiconductors, New York:D. van Nostrand Co., Inc., 1950.

Shockley W., Pearson G., *Modulation of conductance of thin films of semiconductors by surface charges*, Phys. Rev. **74**, 233 (1948).

Shockley W., Read W., *Statistics of recombination of electrons and holes*, Phys. Rev. **87**, 835 (1952).

Smith R.A. Semiconductors. London:Cambridge University Press, 1978.

Sommerfeld A., Z. Phys. **47**, 1 (1928).

Son N.T., Sorman E., Chen W.M., Kordina O., Monemar B., Janzen E., *Possible lifetime limiting defect in 6H-SiC*, Appl. Phys. Lett. **65** (21), 2687 (1994).

Spencer M., Stall R., Eastman L, Wood C., *Characterization of grain boundaries using deep level transient spectroscopy*, J. Appl. Phys. **50** (12), 8006 (1979).

Spitzer W., Kleinman D., Walsh D., *Infrared properties of hexagonal silicon carbide*, Phys. Rev. **113** (1), 127 (1959).

Stallinga P., Gregorkiewicz T., Ammerlaan C., *Electron paramagnetic resonance study of new centers in SiC*, Mat. Sci. Egr. **B11**, p35 (1992).

Sugii T., Ito T., Furumura Y., Daki M., Mieno F., Maeda M., *Si heterojunction bipolar transistors with single crystallline β-SiC emitters*, J. Electrochem. Society **134** (10) 2545, (1987).

Suttrop W., Pensl G., Choyke W., Dornen A., Leibenzeder S., Stein R., *Hall effect and infrared absorption measurements on nitrogen donors in 6H-SiC*, Proc. Amorph. and Cryst. Silicon Carb. IV, Yang C., Rahman M., Harris G. eds., Springer-Verlag p129 (1992).

Suttrop W., Pensl G., Lanig P., *Boron Related Deep Centers in 6H-SiC*, Appl. Phys. A **51**, 231 (1990).

Sze S. Physics of Semiconductor Devices. New York: John Wiley, 1981.

Tachibana T., Kong H., Wang Y., Davis R., *Hall measurements as a function of temperature on monocrystalline SiC thin films*, J. Appl. Phys. **67** (10), 6375 (1990).

Tairov Y., Vodakov Y., *Group IV Materials Mainly SiC*, in Electroluminescence. eds Pankove J., Topics in Applied Physics, vol. **17**. Berlin: Springer-Verlag 1977.

Talwar D., Feng Z., *Tight-binding description for the bound electronic states of isolated single and paired native defects in β-SiC*, Phys. Rev. B **44** (7), 3191 (1991).

Tansley T., Egan R., *Point defect energies in the nitrides of aluminum, gallium, and indium*, Phys. Rev. B **45** (19), 10942 (1992).

Taschek W., *Military needs for high temperature electronics*, Proc. 1st Int. Conf. Hi. Temp. Elec., D.B. King F. Thome Eds., Albuquerque NM, p3 June 1991.

Thome F., King D., *High temperature electronics survey*, Internal memo, Sandia National Laboratory, Albuquerque NM 1988.

Thurber W., Forman R., Phillips W., *A novel method to detect non-exponential transients in deep level transient spectroscopy*, J. Appl. Phys. **53** (11), 7397 (1982).

Townsend P., Kelly J., Colour Centres and Imperfections in Insulators and Semiconductors. New York:Crane, Russak & Company, Inc., 1973.

Uddin A., Uemoto T., *Observation of deep level in p-n junction diode of 6H:SiC*, Jpn. J. Appl. Phys. **32** (2), 1670 (1993).

Uddin A., Mitsuhashi H., Uemoto T., *Investigation of Deep Levels and Residual Impurities in Sublimation Grown SiC Substrates*, Jpn. J. Appl. Phys. **33** (7A), 908 (1994).

Vainer V.,Il'in V., *ESR of close nitrogen-vacancy pairs in n-type 6H-SiC*, Sov. Phys. Solid State **23** (8), 1432 (1981).

Vainer V., Il'in V., Karachinov V., Tairov Y., *Electron spin resonance of $(TiN)^0$ impurity pairs in the 6H polytype of silicon carbide*, Sov. Phys. Solid-State **28** (2), 201 (1986).

van Daal H., Knippenberg W., Wasscher J., *On the electronic conduction of α-SiC crystal between 300 and 1500 K*, Phys. Chem. Solids **24**, 109 (1963).

Verma A., Krishna P. Polymorphism and polytypism in crystals. New York:John Wiley & Sons Inc., 1966.

Villeret M., Rodriguez S., Kartheuser E., *Optical absorption and Zeeman effect of Cu^{2+} in tetrahedrally coordinated crystals*, Phys. Rev. B **43** (17), 14115 (1991).

Vincent G., Chantre A., Bois D., *Electric field effect on the thermal emission of traps in semiconductor junctions*, J., Appl. Phys. **50** (8), 5484 (1979).

Violin E., Kholuyanov G., *On the electroluminescence and photoluminescence of diffused p-n junctions in SiC,* Sov. Phys. Solid-State **6** (6), 1331 (1964).

Vishnevskaya B., Dmitriev V., Kovalenko I., Kogan L., Morozenko Y., Rodkin V., Syrkin A., Taarenkov B., Chelnokov V., *Silicon carbide diodes emitting blue light*, Sov. Phys. Semicond. **22** (4), 414 (1988).

Vodakov Y., Vol'fson A., Mal'tsev A., *Cathode amplification in silicon carbide p-n junctions*, Sov. Phys. Tech. Phys. **32** (12), 1460 (1987).

Waldrop J., Grant R., Wang Y., Davis R., *Metal Schottky barrier contacts to alpha 6H-SiC*, J. Appl. Phys. **72** (10), 4757 (1992).

Waldrop J., *Schottky barrier height of metal contacts to p-type alpha 6H-SiC*, J. Appl. Phys. **75** (9) 4548 (1994).

Watkins G., *Defects in irradiated silicon: electron paramagnetic resonance and electron nuclear double resonance of the aluminum vacancy pair*, Phys. Rev. **155** (3), 802 (1968).

Watts R. Point Defects in Crystals. New York: John Wiley, 1977.

Wei Z., Bo Z., Ming N., *Cubic zero field splitting and site symmetry of Mn^{2+} in ZnS*, Phys. Rev. B **43** (4), 3712 (1991).

Wilson A.H., Proc. Roy. Soc. A **133**, 458 (1931).

Woodbury H., Ludwig G., *Electron spin resonance studies in SiC,* Phys. Rev. **124** (4), 1083 (1961).

Yariv A. Quantum Electronics. New York: John Wiley, 1989.

Yu P., Mahalingam K., Mitchel W., Roth M., Fischer D., *Characterization of boron in 6H-SiC using optical absorption*, Inst. Phys. Conf. Ser. No 145, Ch 3, IOP Publishing Bristol UK, (1995).

Zhao J., Lee C., Fang Z., Schlesinger T., Milnes A., *Theoretical and experimental determination of deep trap profiles in semiconductors*, J. Appl. Phys. **61** (3), 1063 (1986).

Zohta Y., *A new method for determination of deep level impurity centers in semiconductors*, Appl. Phys. Lett. **17** (7), 284 (1970).

Zylbersztein A., *Trap depth and electron capture cross section determination by trap refilling experiments in Schottky diodes*, Appl. Phys. Lett. **33** (2), 200 (1978).

REPORT DOCUMENTATION PAGE

Form Approved
OMB No. 0704-0188

Public reporting burden for this collection of information ... searching existing data sources, gathering and maintaining the data needed ... comments regarding this burden estimate or any other aspect of this collection of information ... Operations and Reports, 1215 Jefferson ... 20503.

1. AGENCY USE ONLY | 2. REPORT DATE: December 1996 | 3. REPORT TYPE AND DATES COVERED: Doctoral Dissertation 1993-1996

4. TITLE AND SUBTITLE
Electrical Characterization of Intrinsic and Induced Deep Level Defects in Hexagonal SiC

5. FUNDING NUMBERS

6. AUTHOR(S)
James D. Scofield

7. PERFORMING ORGANIZATION NAME(S) AND ADDRESS(ES)
Air Force Institute of Technology
2950 P Street
Wright Patterson AFB OH 45433-7765

8. PERFORMING ORGANIZATION REPORT NUMBER
AFIT/DS/ENP/96-08

9. SPONSORING/MONITORING AGENCY NAME(S) AND ADDRESS(ES)
M. Braydich, Lt. Col.
WL/POO
Air Force Wright Laboratory
Wright Patterson AFB OH 45433-7251

10. SPONSORING/MONITORING AGENCY REPORT NUMBER

11. SUPPLEMENTARY NOTES

12a. DISTRIBUTION/AVAILABILITY STATEMENT
Approved for Public Release; Distribution Unlimited

12b. DISTRIBUTION CODE

13. ABSTRACT *(Maximum 200 words)*
Deep level defects in hexagonal SiC were studied using digital deep level transient spectroscopy (DLTS) methods over the temperature range of 100 to 800 K. New centers were found in bulk and epitaxial 6H-SiC with ionization energies between 0.38 to 1.3 eV, and levels from 0.2 to 0.856 eV were identified in 4H-SiC epitaxy. Direct correlation between inequivalent lattice sites was identified for energetic pairs associated with both vanadium and ion implanted Mg impurities. Non-radiative carrier capture mechanisms were studied and deep level trapping was found to proceed via lattice relaxation multi-phonon emission, indicating efficient electronic-lattice coupling in the wide bandgap material. Junction transport characteristics of 4H-SiC p+/n bipolar devices were observed to be dominated by deep level defects in the epitaxial layers. Significant tunneling conduction in both forward and reverse bias conditions was directly correlated to deep level centers in these devices. Additionally, a negative temperature coefficient of reverse breakdown voltage was identified and related to deep level assisted tunneling. Vacancy or other lattice structural damage related center was identified as an acceptor-like luminescence activator in diodes exhibiting a bright green (2.4 eV) luminescence.

14. SUBJECT TERMS
DLTS, SiC, deep level, non-radiative capture, parameter estimation, linear prediction, multi-phonon emission, junction transport.

15. NUMBER OF PAGES
392

16. PRICE CODE

17. SECURITY CLASSIFICATION OF REPORT	18. SECURITY CLASSIFICATION OF THIS PAGE	19. SECURITY CLASSIFICATION OF ABSTRACT	20. LIMITATION OF ABSTRACT
Unclassified	Unclassified	Unclassified	UL